Investigation of Calcium Oxalate Crystallization under Microfluidic Conditions for the Understanding of Urolithiasis

Karol Rakotozandriny

Sorbonne Université

Ecole doctorale 397 : Physique et Chimie des Matériaux

Laboratoire de Chimie de la Matière Condensée de Paris

Laboratoire de Physicochimie des Electrolytes et Nanosytèmes InterfaciauX

Investigation of Calcium Oxalate Crystallization under Microfluidic Conditions for the Understanding of Urolithiasis

Etude de la Cristallisation des Oxalates de Calcium en Conditions Microfluidiques pour la Compréhension de l'Urolithiase

Par **Karol Rakotozandriny**

Thèse de doctorat de Physique et Chimie des Matériaux

Dirigée par Christian Bonhomme et Ali Abou Hassan

Présentée et soutenue publiquement le 27 septembre 2019

Devant un jury composé de :

M. Bruno BUJOLI	Directeur de Recherche	Rapporteur
Mme Fabienne TESTARD	Chercheur CEA	Rapporteure
M. Karim BENZERARA	Directeur de Recherche	Examinateur
Mme Christèle COMBES	Professeur des Universités	Examinatrice
Mme Annette F. TAYLOR	Professeur des Universités	Examinatrice
Mme Florence BABONNEAU	Directrice de Recherche	Membre invité
M. Ali ABOU HASSAN	Maître de Conférences	Co-directeur de thèse
M. Christian BONHOMME	Professeur des Universités	Directeur de thèse

Table of content

Table of abbreviations

ACO:	Amorphous calcium oxalate
CAOnh:	Anhydrous calcium oxalate
CaOx:	Calcium Oxalate
CaP:	Calcium Phosphate
CCM:	Constant Composition Method
COD:	Calcium Oxalate Dihydrate
COM:	Calcium Oxalate Monohydrate
COT:	Calcium Oxalate Trihydrate
EDS:	Energy-dispersive X-ray
FMCG:	Flow Model of Crystallization in Gels
GT:	Green tea
HAp:	Hydroxyapatite
KS:	Kidney Stone
$K_{sp(CaOx)}$:	Solubility product constant of Calcium Oxalate
MSMPR:	Mixed Suspension Mixed Product Removal
OCP:	Octacalcium Phosphate
P_e:	Péclet number
R_e:	Reynolds number
RP:	Randall's plaque
SBF:	Simulated Body Fluid
SEM:	Scanning Electron Microscopy
SS:	Supersaturation
XRD:	X-ray Diffraction

General introduction

Urolithiasis, else known as the kidney stone disease, is the cascade of events occuring in the kidney leading to the pathological formation of solid concretions in the urinary tracts. This disease has been a plague for mankind throughout history[1]. From ancient Egypt to modern age, major figures experienced the disease such as Ramesses II, Isaac Newton, Charles Darwin or Benjamin Franklin. Over the past fifty years, the kidney stone disease has affected about 10% of the industrialized populations with a global increase in prevalence[2]. A prevalence study, launched in 2012 in the United States of America, pointed out that men were more likely to develop kidney stones compared to women (10.6% *vs.* 7.1%)[3]. Moreover, the same study showed that overweight persons were more affected than normal-weight ones (11.2% *vs.* 6.1%). The etiology of the disease is complex and can be due to various causes such as low diuresis or imbalance diet[4-6]. Yet, treatments have been rapidly developed to counter-act the occurrence of kidney stones, *e.g.* ureteroscopy, shockwave lithotripsy or open surgery. Nevertheless, these treatments represent a physical burden for the patients and an economic one for the health insurance[7].

Kidney stones are known to exhibit a heterogeneous chemical composition with organic and inorganic species. In-depth chemical characterization of the inorganic compounds showed that calcium oxalate (CaOx) and calcium phosphate (CaP) crystals stand for ≈ 70% and ≈ 14% of the kidney stones, respectively[8]. As the main inorganic components among kidney stones, correlative studies were carried out to associate the occurrence of CaOx stones to abnormal urinary analyses[9,10]. Interestingly, most CaOx-based kidney stones appear to exhibit a CaP umbilication at their surface. Nowadays known as the Randall's plaque (*i.e.* after Alexander Randall who reported it first[11]), this CaP umbilication initially originates in the kidney at the thin basement of the loop of Henle[12] or in the ducts of Bellini[13]. It is broadly assumed that the Randall's plaque acts as an initiator regarding the growth of CaOx-based kidney stones. However, most *in vivo* studies accounting for the initiating role of the Randall's plaque or the formation of kidney stones in general rely on *indirect* evidences[14].

To improve knowledge on the growth of CaOx-based kidney stones, numerous *in vitro* studies have been conducted to better understand the kidney stone disease. Noteworthy, *in vitro* crystallizers have been developped in an attempt to study the growth of CaOx stones under stone promoting conditions (*e.g.* Mixed Suspension Mixed Product Removal (MSMPR)[15,16] crystallizer or Flow Model of Crystallization in Gels (FMCG)[17] crystallizer). Although valuable, these crystallizers all lack of accounting for the renal *confinement* and associated urinary *laminar-flow*. Indeed, the nephron (*i.e.* the functional unit of the kidney) is constituted of micro-

tubular structures through which urine flows at slow velocity. Several numerical studies tried to investigate the formation of calcium-based kidney stones throughout the nephron[18-21]. Yet, few experimental studies have correlated the numerical models and, *in fine*, the pathological formation of kidney stones in the nephron.

For example, CaOx-based kidney stones are highly suspected to form within the collecting duct of the nephron in response to abnormally high and pathological concentrations in urinary calcium and oxalate. The collecting duct[22] is a tubular structure with a diameter of ≈ 100 *µm* through which the urine flows at ≈ 10.0 $nL.min^{-1}$. *In vitro* crystallizers such as the MSMPR or FMCG systems are not capable of dealing with such physical constraints. To address these issues, we decided to rely on a microfluidic strategy (supported by the lab-on-a-chip technology[23-27]) to investigate the formation of CaOx stones under a micro-confinement akin to the collecting duct. This physical constraint enables to establish flow behaviors likewise encountered in the collecting duct. Associated to chemical conditions similar to pathological stone promoting conditions, we aim at contributing to a better understanding regarding the formation of CaOx kidney stones from a physicochemical point of view.

The present work is divided into **four distinctive** chapters.

In **Chapter 1**, we established an extensive literature review regarding the study of the kidney stone disease with an in-depth focus on CaOx stones. Therefore, we defined the CaOx systems with respect to the context of our study, the physicochemistry and the *in vivo* and *in vitro* studies accounting for their growth. First, we emphasized the microfluidic technology as a valuable tool to partially re-create the environment of the nephron (*i.e.* nephron-on-a-chip technology).

In **Chapter 2**, we introduced the collecting duct-on-a-chip device as a continuous-flow microfluidic platform capable of investigating CaOx crystallization under physicochemical conditions akin to stone promoting conditions. Serving as proof-of-concept, we studied the formation of CaOx crystals under the co-laminar mixing of Ca^{2+} and Ox^{2-} ions. We looked at the CaOx crystalline phases and crystal shapes, to correlate our results with medical observations. Compared to other *in vitro* crystallizers, we also investigated the *in situ* and *in real time* growth kinetics of CaOx crystals to propose a potential growth mechanism for CaOx stones enlargement.

In **Chapter 3**, we presented a new strategy to study the reactive role of the Randall's plaque with respect to the formation of CaOx kidney stones. We synthetized an apatitic layer with comparable chemical and morphological features of the Randall's plaque. This model system was suitable for subsequent microfluidic investigations using the collecting duct-on-a-chip device. Therefore, we explored *in vitro* the initiating role of the Randall's plaque regarding

CaOx crystallization by accounting for the micro-confinement and fluid-flow encountered in the nephron.

In **Chapter 4**, we explored the modulating effect of additives from green tea on CaOx crystals in the collecting duct-on-a-chip device. We supported the influence of gren tea in favoring COD crystallization compared to COM crystals. Moreover, this last chapter enables to open the way to more complex experimental and biomimietic conditions in order to investigate CaOx crystallization by using the collecting duct-on-a-chip device.

References

(1) Daudon, M.; Jungers, P.; Traxer, O. *Lithiase urinaire*; Lavoisier, Médecine Sciences publications, 2012.

(2) Romero, V.; Akpinar, H.; Assimos, D. G. Kidney Stones: A Global Picture of Prevalence, Incidence, and Associated Risk Factors. *Reviews in Urology* **2010,** *12* (2-3), e86.

(3) Scales, C. D.; Smith, A. C.; Hanley, J. M.; Saigal, C. S. Prevalence of Kidney Stones in the United States. *European Urology* **2012,** *62* (1), 160.

(4) Siener, R. Impact of dietary habits on stone incidence. *Urological Research* **2006,** *34* (2), 131.

(5) Asselman, M.; Verkoelen, C. F. Fructose intake as a risk factor for kidney stone disease. *Kidney international* **2008,** *73* (2), 139.

(6) Taylor, E. N.; Fung, T. T.; Curhan, G. C. DASH-style diet associates with reduced risk for kidney stones. *Journal of the American Society of Nephrology : JASN* **2009,** *20* (10), 2253.

(7) Raheem, O. A.; Khandwala, Y. S.; Sur, R. L.; Ghani, K. R.; Denstedt, J. D. Burden of Urolithiasis: Trends in Prevalence, Treatments, and Costs. *European Urology Focus* **2017,** *3* (1), 18.

(8) Daudon, M. [Epidemiology of nephrolithiasis in France]. *Ann Urol (Paris)* **2005,** *39* (6), 209.

(9) Daudon, M.; Letavernier, E.; Frochot, V.; Haymann, J.-P.; Bazin, D.; Jungers, P. Respective influence of calcium and oxalate urine concentration on the formation of calcium oxalate monohydrate or dihydrate crystals. *Comptes Rendus Chimie* **2016,** *19* (11), 1504.

(10) Daudon, M.; Traxer, O.; Jungers, P.; Bazin, D. Stone Morphology Suggestive of Randall's Plaque. *AIP Conference Proceedings* **2007,** *900* (1), 26.

(11) Randall, A. The Origin and Growth of Renal Calculi. *Annals of Surgery* **1937,** *105* (6), 1009.

(12) Evan, A. P.; Lingeman, J. E.; Coe, F. L.; Parks, J. H.; Bledsoe, S. B.; Shao, Y.; Sommer, A. J.; Paterson, R. F.; Kuo, R. L.; Grynpas, M. Randall's plaque of patients with

nephrolithiasis begins in basement membranes of thin loops of Henle. *The Journal of Clinical Investigation* **2003,** *111* (5), 607.

(13) Daudon, M.; Bazin, D.; Letavernier, E. Randall's plaque as the origin of calcium oxalate kidney stones. *Urolithiasis* **2015,** *43* (1), 5.

(14) Evan, A. P.; Coe, F. L.; Lingeman, J. E.; Shao, Y.; Sommer, A. J.; Bledsoe, S. B.; Anderson, J. C.; Worcester, E. M. Mechanism of Formation of Human Calcium Oxalate Renal Stones on Randall's Plaque. *The Anatomical Record* **2007,** *290* (10), 1315.

(15) Garside, J.; Brečević, L.; Mullin, J. W. The effect of temperature on the precipitation of calcium oxalate. *Journal of Crystal Growth* **1982,** *57* (2), 233.

(16) Bretherton, T.; Rodgers, A. Crystallization of calcium oxalate in minimally diluted urine. *Journal of Crystal Growth* **1998,** *192* (3), 448.

(17) Achilles, W.; Freitag, R.; Kiss, B.; Riedmiller, H. Quantification of Crystal Growth of Calcium Oxalate in Gel and its Modification by Urinary Constituents in a New Flow Model of Crystallization. *The Journal of Urology* **1995,** *154* (4), 1552.

(18) Finlayson, B.; Reid, F. The expectation of free and fixed particles in urinary stone disease. *Investigative urology* **1978,** *15* (6), 442.

(19) Kok, D. J.; Khan, S. R. Calcium oxalate nephrolithiasis, a free or fixed particle disease. *Kidney international* **1994,** *46* (3), 847.

(20) Robertson, W. G. Kidney models of calcium oxalate stone formation. *Nephron. Physiology* **2004,** *98* (2), p21.

(21) Rodgers, A. L.; Allie-Hamdulay, S.; Jackson, G.; Tiselius, H.-G. Simulating calcium salt precipitation in the nephron using chemical speciation. *Urological Research* **2011,** *39* (4), 245.

(22) Vize, P. D.; Woolf, A. S.; Bard, J. B. L. *The Kidney: From Normal Development to Congenital Disease*; Elsevier Science, 2003.

(23) Essig, M.; Terzi, F.; Burtin, M.; Friedlander, G. Mechanical strains induced by tubular flow affect the phenotype of proximal tubular cells. *American Journal of Physiology-Renal Physiology* **2001,** *281* (4), F751.

(24) Jang, K.-J.; Mehr, A. P.; Hamilton, G. A.; McPartlin, L. A.; Chung, S.; Suh, K.-Y.; Ingber, D. E. Human kidney proximal tubule-on-a-chip for drug transport and nephrotoxicity assessment. *Integrative Biology* **2013,** *5* (9), 1119.

(25) Jang, K.-J.; Suh, K.-Y. A multi-layer microfluidic device for efficient culture and analysis of renal tubular cells. *Lab Chip* **2010,** *10* (1), 36.

(26) Laffite, G.; Leroy, C.; Bonhomme, C.; Bonhomme-Coury, L.; Letavernier, E.; Daudon, M.; Frochot, V.; Haymann, J. P.; Rouziere, S.; Lucas, I. T.et al. Calcium oxalate precipitation by diffusion using laminar microfluidics: toward a biomimetic model of pathological microcalcifications. *Lab Chip* **2016,** *16* (7), 1157.

(27) Wei, Z.; Amponsah, P. K.; Al-Shatti, M.; Nie, Z.; Bandyopadhyay, B. C. Engineering of polarized tubular structures in a microfluidic device to study calcium phosphate stone formation. *Lab Chip* **2012,** *12* (20), 4037.

CHAPTER 1.

LITERATURE REVIEW

Chapter 1 Literature review

Table of contents

1. The context of the study

Over the past decades, the prevalence of urolithiasis, else known as kidney stone disease, has increased worldwide to affect up to 10.0 % of the industrialized populations. Medical procedures exist to treat people suffering from this condition. Yet, lacking pieces remain and prevent from exhaustively understanding the series of events that cause the disease in first place. Even nowadays, no universal answer prevails despite the investigations and progresses made in the field. In that context, we aim at contributing to the knowledge of kidney stone disease. Herein, we will present the key considerations that have motivated our work. This requires to introduce the vital function of the human kidney, the existing strategies to reproduce its functionality and finally, the microfluidic approach we have decided to follow to answer our questionings.

a. The nephron: the functional unit of the kidney

i. Anatomical description

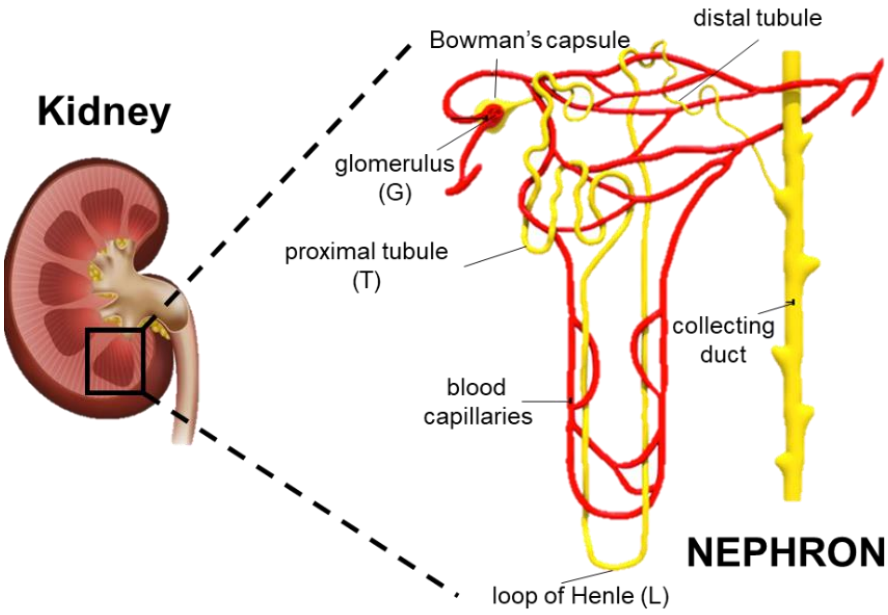

Figure 1. Anatomical illustration of one nephron (*i.e.* renal functional unit) and its location in the kidney. The image is adapted from the Internet.

The kidneys are two bean-shaped organs of ≈ 12 × 6.0 × 3.0 cm filtering the blood to help the body to pass wastes as urine. Crucial functions are the maintenance of fluid balance, regulation and filtration of minerals from blood, filtration of waste materials from food/medication/toxic substances, regulation of hormones all ensured by the nephron (*i.e.* the basic functional unit in the kidney). Each kidney contains about 1 million nephrons, each being constituted of several sub-structures and fulfilling specific functions (**Figure 1**): the renal corpuscle

(glomerulus (G) and Bowman's capsule) and the renal tubules (proximal tubule (T), loop of Henle (L), distal tubule and collecting duct).

In the nephron, the regulation of water, calcium and oxalate (from diet) takes place at different places[1]: the proximal tubule, the descending limb of the loop of Henle and the collecting duct are the segments where water is reabsorbed. Calcium is reabsorbed in the proximal tubule, the ascending limb of the loop of Henle and the distal tubule. Lastly, the proximal tubule reabsorbs oxalate at its early segment whereas it re-secretes oxalate at its late segment. Other electrolytes are also filtered throughout the nephron for maintaining body homeostasis (*e.g.* Mg^{2+}, Na^{+}, Cl^{-} *etc*…).

ii. Kidney disease

Due to the vital functions that the kidneys carry, these organs are susceptible of various failures such as their progressive and irreversible destruction (*i.e.* chronic kidney disease), the loose of filtration ability (*i.e.* kidney failure), the formation of solid concretions (*i.e.* kidney stone disease), the formation of fluid-filled cysts in the kidneys (*i.e.* polycystic kidney disease) *etc*… These conditions come with a wide range of symptoms (fatigue, increased or decreased urination, blood in urine, acute pain…) and represent an economic burden to the society. For instance, the Haute Autorité de Santé (HAS) estimated that in 2007 the French National Health Insurance spent more than 4.0 billion € to treat 61,000 patients with chronic kidney disease (https://www.has-sante.fr). Regarding this disease, treatments are heavy procedures and mainly consist of kidney transplants or hemodialysis. Hence, there is a real need of model systems to better understand the renal function. Currently, model systems are being developed to address the problematic. One promising approach relies on the use of nephron-on-a-chip devices, coming from the microfluidic technology.

b. Development of nephron-on-a-chip technology to mimic the renal function

i. Microfluidic organ-on-a-chip

Organ-on-chips are advanced microfluidic platforms designed to mimic physiological structures of an organ and reproduce a primary (yet precise) functionality. The fabrication technique mainly relies on the principle of photolithography from the electronic microchip manufacturing industry[2,3] for transferring geometric and micrometric patterns from a photomask to a light-sensitive chemical photoresist on a substrate. Photolithography being an expensive process and requiring specific facilities/equipment (*e.g.* clean room), soft lithography represents an alternative for rapid and affordable prototyping of microscale structures, devices on planar, curved, flexible and soft substrates[4]. Generally, soft lithography

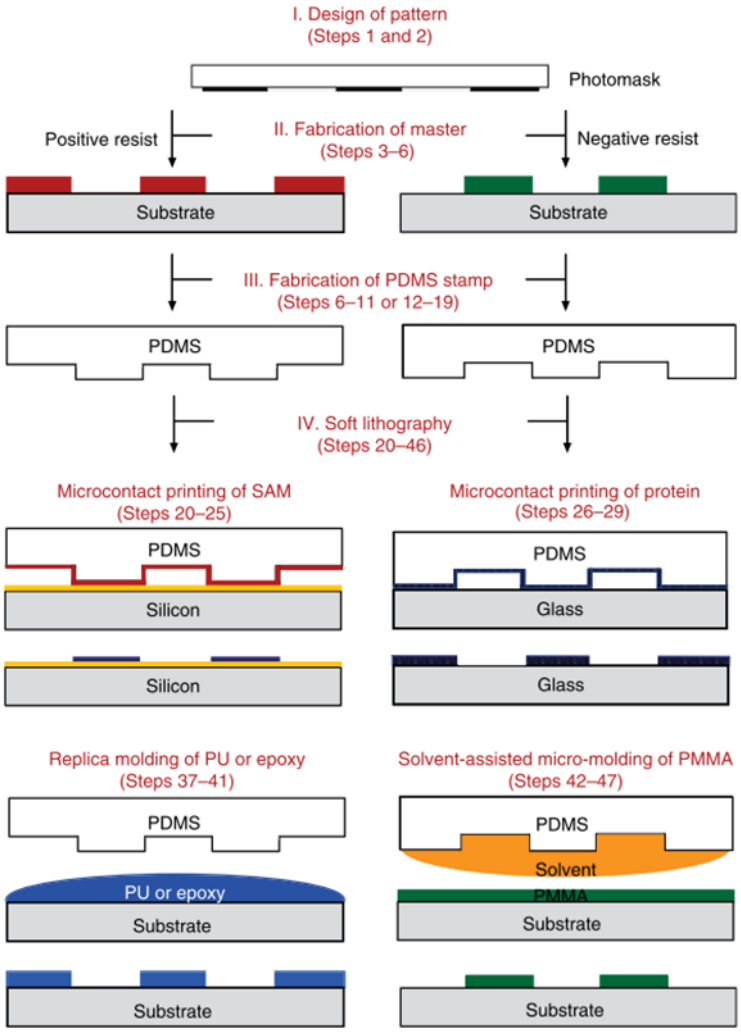

Figure 2. The four major steps involved in soft lithography. From top to bottom: I. Design of pattern, II. Fabrication of master, III. Fabrication of PDMS stamp and IV. Soft lithography. Thereafter are presented the main soft lithographic techniques, *i.e.* microcontact printing of self-assembled monolayer or protein, replica molding and solvent-assisted micro-molding. For example, from the design of a micropattern to its microcontact printing of self-assembled monolayer onto a substrate, it takes 16 steps of fabrication in total. Figure is reproduced from Qin *et al.*[4] with permission from Springer Nature.

procedure consists in the design of a micrometric pattern with a computer-aided design (CAD) software that is used to fabricate a mask then a master (**Figure 2**). Thereafter, the master enables to fabricate a stamp that finally serves to create the microchip. Several patterning techniques form the basis of soft lithography (*e.g.* microcontact printing (μCP)[5], microtransfer molding[6], micromolding in capillary[7] or solvent-assisted micromolding (SAMIM)[8]), yet replica molding (REM)[9] for the fabrication of microfluidic devices for biological and biomedical applications has proven to be particularly adapted.

Thanks to attractive features, polydimethylsiloxane (PDMS) is widely used as an elastomeric matrix for REM technique[10]. Besides of being suitable for biological applications, PDMS such as Sylgard® 184 has the mechanical properties of a moderately stiff elastomer[11], is optically transparent through a large range of wavelengths[12] and can ensure either irreversible or

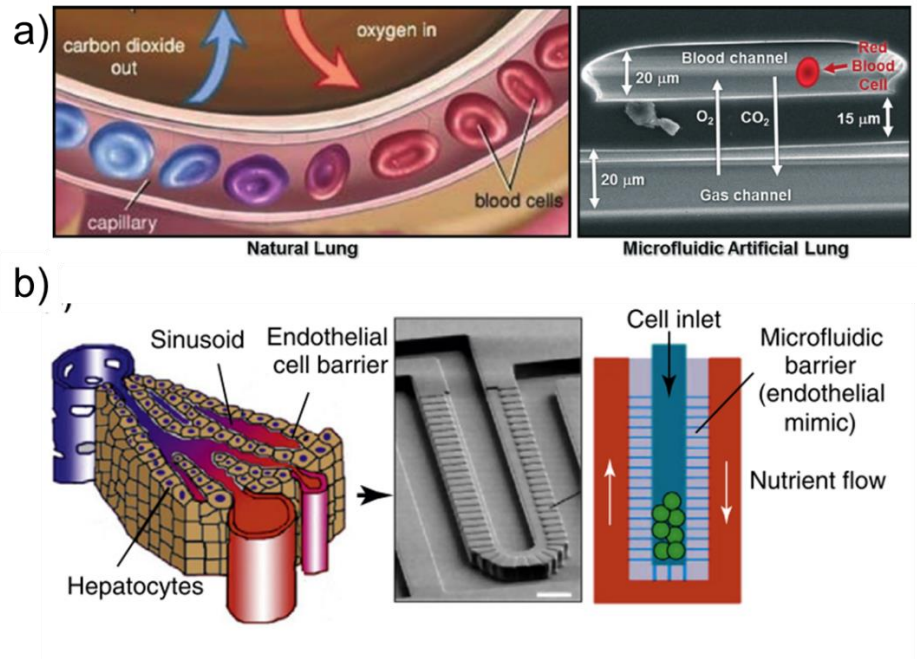

Figure 3. Towards the development of organ-on-a-chip bioreactors: a) lung-on-a-chip system proposed by Potkay *et al.*[13] enabling gas exchange. Cartoon on the right serves as comparison to microfluidic model; b) microfluidic endothelial-like platform developed by Lee *et al.*[14] exhibiting hepatic microarchitecture and function. All figures are reproduced with permission from RSC and John Wiley and Sons, respectively.

reversible sealing to different substrates after specific treatments (surface oxidation[15] or carbonyl iron-PDMS mixing[16,17], respectively).

As the most common microfluidic platforms, microchannels enable a large range of applications such as the synthesis and control of nanoparticle nucleation and growth[18,19], drug compounds screening[20,21] or gradients generators[22,23]. Furthermore, microfluidic cell culture has become a promising method compared to conventional cell culture (*e.g.* fine control over temperature, nutrients supply, automation of cell culture tasks…)[24] setting the stage for tissue modelling[25] and organ-on-a-chip development[13,14,26,27] as illustrated in **Figure 3**. Therefore, research studies focusing on the development of artificial organs such as artificial kidneys[27], lungs[13] or liver[14] help providing reliable model systems in fields like cancer research, drugs testing *etc.*

ii. Mimicking the renal function

As already briefly introduced, microfluidic organ-on-a-chip technology has widen the scope with respect to the understanding of organ function by providing reliable model systems. In that prospect, the development of nephron-on-chips have gain attention for the biomimicry of renal function. The first noticeable attempt to reproduce the kidney functional unit was conducted by Essig and collaborators in 2001[28]. By shear-stressing Mouse Proximal Tubule (MPT) cells in

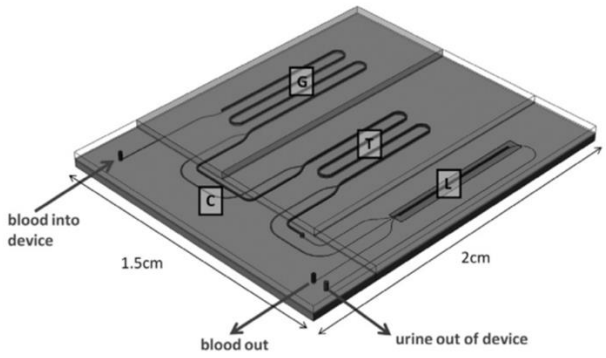

	Component		
	G	T	L
L, cm	10.00	5.30	4.00
W, μm	70.00	35.00	25.00
D_B, μm	40.00	40.00	25.00
D_F, μm	50.00	15.00	25.00

Figure 4. Complete nephron-on-a-chip platform designed by Weinberg *et al.*[29]. (G), (T) and (L) stand for glomerulus, proximal tubule and loop of Henle , respectively with their dimensions given in the table below. (C) represents the interface that connects each segment with one another and with the blood and waste streams. Figure is adapted with permission from SAGE Publishing.

a microfluidic chamber (0.5 x 20 x 70 *mm*) at various laminar flow conditions, they assessed the reorganization of the cytoskeleton of MPT cells in a flow-dependent fashion.

Later on, Baudoin *et al.*[27] developed a PDMS renal microchip to model the distal tubule of the nephron. The setup consisted in functional living cell microchambers interconnected by a microfluidic network and enabled continuous renal tubular cell feeding and control over waste removal by fluid microflow. Using a computational approach, Weinberg and collaborators contributed to the design of a bioartificial nephron-on-a-chip consistent with the anatomy and the physiology of human beings[29]. As shown in **Figure 4**, they computed a device capable of replicating the function of the glomerulus (G), the proximal tubule (T) and the loop of Henle (L) (see **Figure 1**). Moreover, they stated that the device could be constructed using current microfabrication technologies and seeded with various renal cell types.

Towards the culture and analysis of inner medullary collecting duct (IMCD) cells, Jang and Suh developed a simple multi-layer microfluidic device[30]. As shown in **Figure 5a**, a porous membrane divided the two compartments device (one channel-flow and one static chamber) within which renal cells were cultured under appropriate fluidic shear stress. The authors were confident in presenting their construct as a resembling *in vivo* renal tubule system suitable for drug screening application and advanced tissue engineering. To demonstrate and study the role of human renal proximal tubule epithelial cells (RPTECs) in molecular transport process,

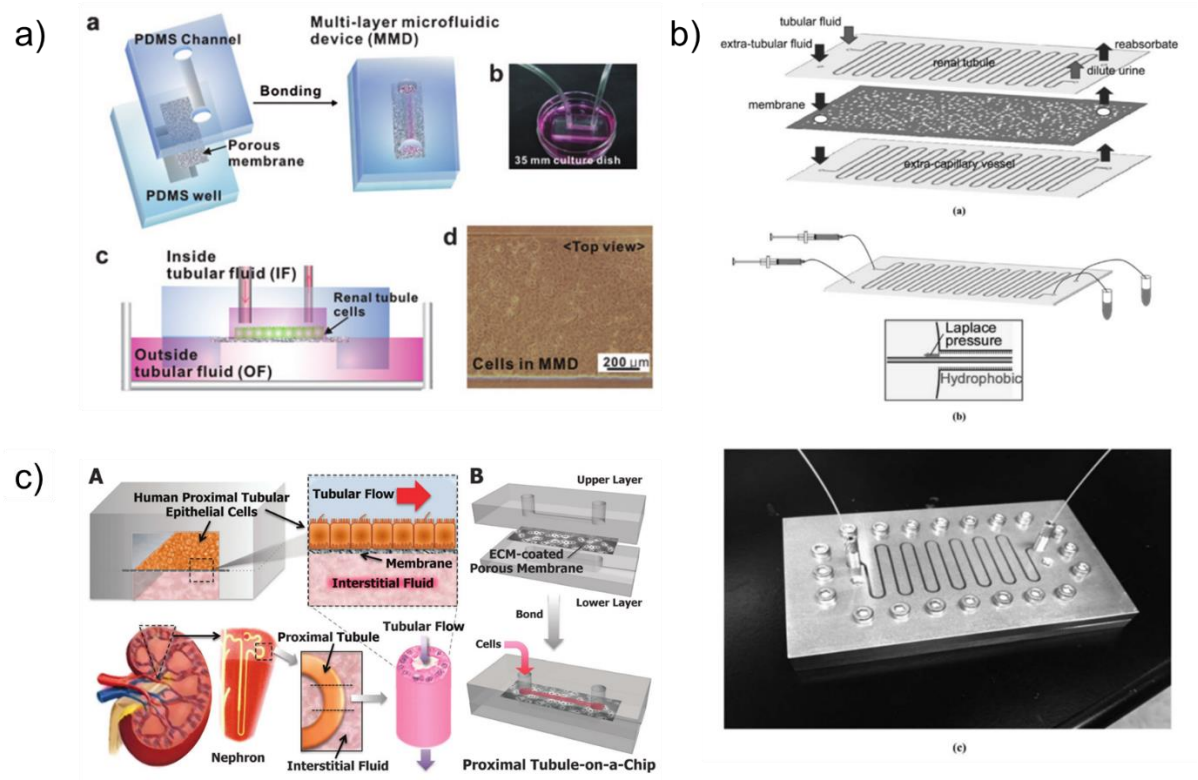

Figure 5. Microfluidic reactors for the study of renal function: a) multi-layer microfluidic platform developed by Jang and Suh[30] for the culture and analysis of inner medullary collecting duct cells; b) microdevice capable of nutrients and waste separation by Gao *et al.*[31]; c) proximal tubule-on-a-chip for nephrotoxicity assessment by Jang *et al.*[32]. All figures are reproduced with permission from RSC and The Japan Society for Analytical Chemistry.

Gao and collaborators reported on the construction of a cell-based separation microdevice on a etched glass substrate as a model for bioartificial renal tubule[31] (**Figure 5b**). They addressed the necessity to build up a chip capable of nutrients/waste separation for medical care or cell research. Kidney toxicity being one of the most frequent adverse events occurring during drug development, Jang *et al.* devised a human proximal tubule-on-a-chip capable of nephrotoxicity assessment[32]. In a multi-layer microfluidic device lined with proximal tubular epithelial cells (**Figure 5c**), they monitored the cells' ability to secrete cisplatin that is a chemotherapeutic drug albeit a proximal tubule nephrotoxin causing cells injury.

Although used to treat patients with chronic renal failure, hemodialysis (*i.e.* blood filtration) is a heavy procedure and is unable to substitute for the absorptive, metabolic, endocrine and immunological functions of a kidney. Hence, bioartificial renal tubule device (BRTD) capable of hemofiltration could offer a wearable and continuous renal replacement therapy as supported by Ng and collaborators[33]. The BRTD consisted of a lab-on-a-chip bioreactor system with a fibrin coated hollow fiber membrane, seeded with RPTECs and assembled in between a PDMS chamber and a glass substrate (**Figure 6a**). The authors assessed the proper organization in monolayer of the RPTECs with correct cell polarization. On one hand, RPTECs

were capable of solutes reabsorption from the glomerulus to the blood. Additionally, RPTECs exhibited correct transport functionalities. Lastly, it is worth pointing out that the rise of 3D printing has also provided a brand-new method for creating 3-dimensional models of human kidney tissue like 3D renal convoluted proximal tubules (PT)[34]. The 3D convoluted PT consisted of an open lumen architecture lined with RPTECs, embedded in an extracellular matrix and housed within a perfusable tissue-chip (**Figure 6b**). RPTECs inside the construct exhibited morphological features and functional markers akin to native cells *in vivo* that supported the use of 3-D bioprinting as a novel method towards finer replication of *in vivo* renal microenvironment.

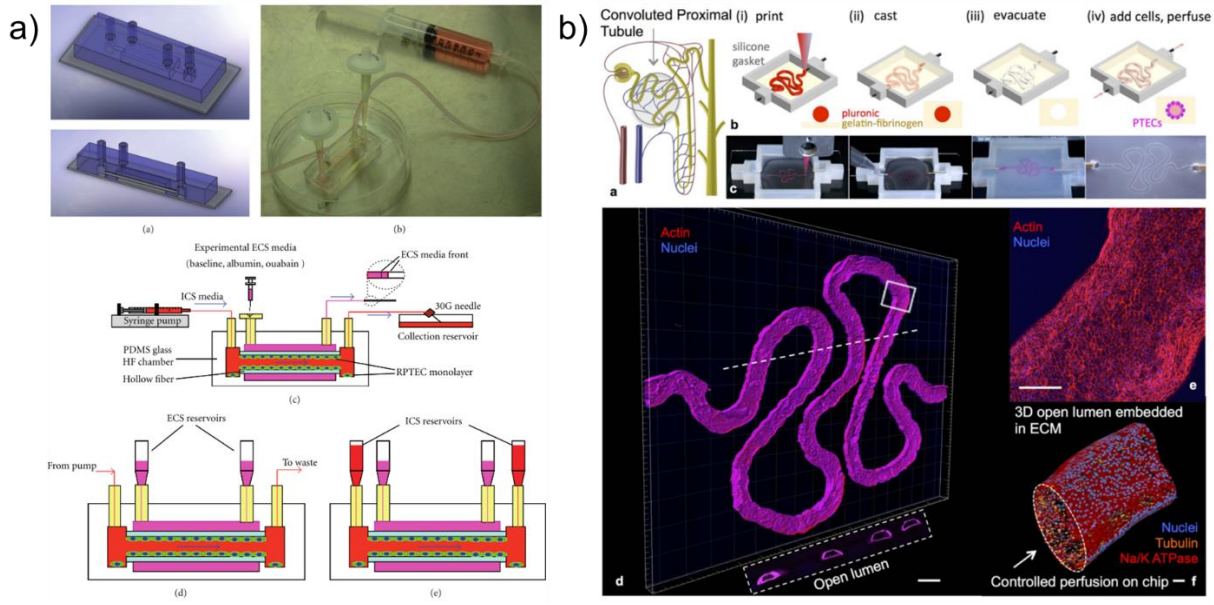

Figure 6. Tubule-on-a-chip systems: a) bioartificial renal tubule device designed for hemofiltration by Ng *et al.*[33]; b) 3-D printed proximal tubule colonized with renal cells and exhibiting morphological and functional renal features by Homan *et al.*[34]. Figure 6a is reproduced with permission from Hidawi and Figure 6b is under Creative Commons license.

c. The kidney stone disease: a microfluidic strategy

i. Kidney stone: epidemiology and structural aspects

The kidney stone (KS) disease, *i.e.* nephrolithiasis, affects about 10% of the industrialized populations[35] with a worldwide prevalence that has been increasing over the past fifty years[36]. The etiology of the disease is multifactorial (*e.g.* low diuresis or imbalance in diet[37-39]) and represents an economic burden for the society[40]. Yet, treatments have evolved rapidly offering invasive (*e.g.* ureteroscopy, percutaneous nephrolithotomy and open surgery) and non-invasive (shockwave lithotripsy) procedures to remove idiopathic KS[40]. Non-conventional

strategies have also been explored like riding a roller coaster to facilitate the evacuation of renal calculi[41].

Table 1. Main chemical species observed in renal calculi over the past decades in France from Daudon[36]. Table translated and reproduced with permission from Elsevier.

Main components	Frequency (%)
Calcium oxalate (CaOx)	**70.3**
whewellite	48.3
weddellite	22.0
Calcium phosphate (CaP)	**13.8**
carbonated apatite	11.4
brushite	1.8
octacalcium phosphate	0.3
amorphous calcium phosphate	0.2
whitlockite	0.1
Struvite (Magnesium Ammonium Phosphate)	**1.6**
presence of MAP	5.7
Purines	**9.7**
anhydrous acid urate	7.9
dihydrated acid urate	1.5
ammonium acid urate	0.2
other urates	0.1
other purines	< 0.05
uric acid	11.8
Cystine	**1.0**
Proteins	**1.7**
Drugs	**0.8**
Various	**1.1**

Even though KS exhibit a heterogeneous chemical composition (**Table 1**), calcium oxalate (CaOx) crystals often represent the predominant mineral component of these stones (70 %) and can be sub-divided into two crystalline phases, respectively the whewellite ($CaC_2O_4 \cdot H_2O$, COM) phase and the weddellite ($CaC_2O_4 \cdot 2H_2O$, COD) one[36]. Calcium phosphate (CaP) minerals are also non-negligible and found under various crystalline phases like carbonated apatite, brushite, octacalcium phosphate, amorphous CaP or whitlockite. For practical purposes, most studies only focus on the mineral composition of KS. Yet, these stones are also composed of an organic phase that might contain purines, proteins and even drugs. Consequently, it is more accurate to consider KS as hybrid organic-inorganic materials.

In the United States of America, a prevalence study launched in 2012 attempted to describe and identify the factors associated with kidney stones occurrence[42]. Results pointed out higher predominance of KS among men (10.6 %) rather than women (7.1 %). Besides, overweight persons were more affected than normal-weight ones were (11.2 % compared to 6.1 %). With similar results across the globe, we can understand the increasing interest of the scientific community in the deciphering of kidney stone disease (**Figure 7**).

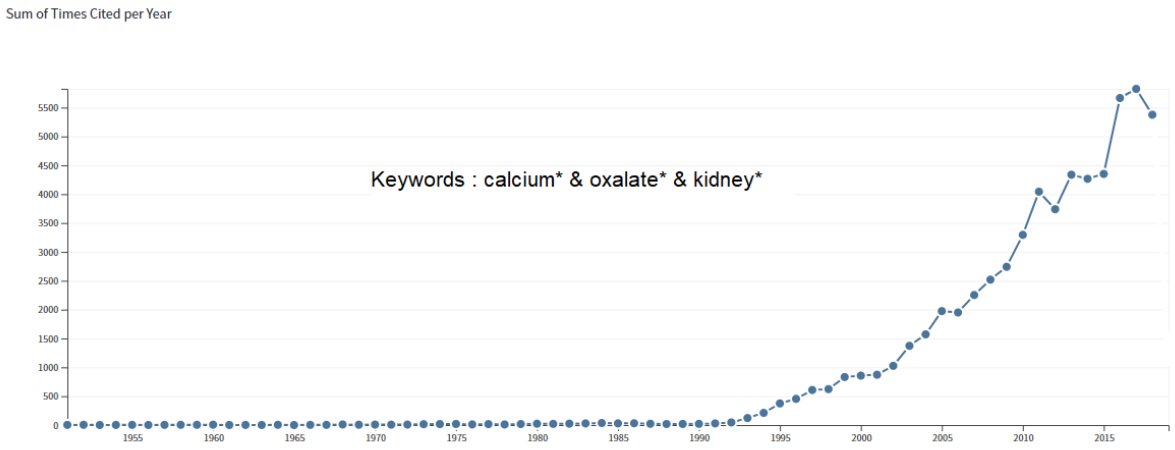

Figure 7. Citation report from Web of Science Core Collection between 1950 and 2018.

ii. Towards a biomimetic approach for kidney stone biomineralization

As previously presented, the increase in prevalence of nephrolithiasis has brought attention on the need of model systems to understand the mechanism responsible for kidney stone formation. *In vitro* model systems have been proposed to explain the possible reasons for KS formation along with the effect on cellular integrity but without fully accounting for the fluid flow and tubular confinement in the nephron. Consequently, the development of lab-on-a-chip bioreactor systems could overcome these limitations.

In 2012, Wei and collaborators reported on the dynamic formation of CaP stones in a circular cross-section microchannel ($Ø$ = 400 μm) mimicking the renal proximal tubule[43]. First, the

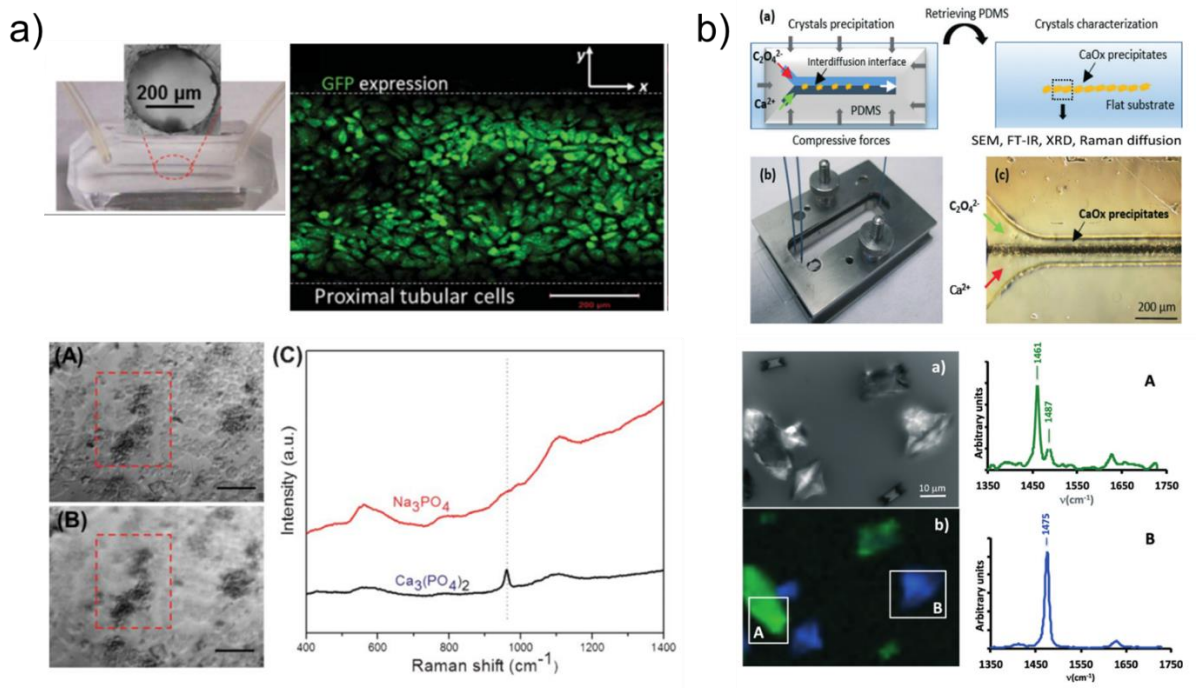

Figure 8. Microfluidic approach of the kidney stone disease: a) circular cross-section microchannel mimicking the renal proximal tube colonized with appropriate cells by Wei *et al.*[43]. Calcium phosphate stone deposition was assessed by microscopy and Raman spectroscopy. Scale bars are 200 *µm*; b) microchannel device for the precipitation of calcium oxalate crystals under laminar flow conditions by Laffite *et al.*[44]. All figures are adapted with permission from RSC.

microchannel was colonized with RPTECs (top in **Figure 8a**) that exhibited proper renal epithelium polarization. Thereafter, the *in situ* deposition of CaP stones on the cellular walls was assessed after the introduction and rapid mixing of $CaCl_2$ and Na_3PO_4 in Hank's Buffered Salt Solution (HBSS, pH 7.4). The experiment could be monitored by confocal *Raman* microscopy (bottom in **Figure 8a**). Additionally, the deposition of other calcium stones on the cellular walls was investigated (*i.e.* CaOx stones and $CaHPO_4$ stones). Therefore, the authors supported the use of the platform for real time observation of the kinetics of kidney stones formation.

A second study conducted by Laffite and collaborators proposed to follow the formation of calcium oxalate stones using a 100 × 100 *µm* microchannel mimicking the collecting duct's dimensions (*i.e.* the most distal tubular structure of the nephron in **Figure 1**)[44]. To initiate CaOx precipitation, solutions of $CaCl_2$ ($[Ca^{2+}]_{(aq)}$ = 12.0 $mmol.L^{-1}$) and $Na_2C_2O_4$ ($[C_2O_4^{2-}]_{(aq)}$ = 0.4 $mmol.L^{-1}$) were prepared accordingly to stone promoting concentrations measured in the urine (hypercalciuria and moderate hyperoxaluria, respectively) and continuously injected at 1.0 µ$L.min^{-1}$ each within the microchannel. Following the co-laminar mixing of $Ca^{2+}_{(aq)}$ and $C_2O_4^{2-}{}_{(aq)}$ ions, CaOx crystals precipitated in a "conical-shape" due to the establishment of concentration gradients perpendicular to the dynamical interface (top in **Figure 8b**). Scanning electron microscopy and *Raman* spectroscopy (bottom in **Figure 8b**)

identified calcium oxalate monohydrate (COM) as the dominant crystalline phase with a fewer amount of calcium oxalate dihydrate (COD) as expected with respect to the initial concentrations in $Ca^{2+}_{(aq)}$ and $C_2O_4^{2-}{}_{(aq)}$ ions. Worth mentioning, the absence of renal cells within the microchannel did not prevent the CaOx crystallization and enabled to focus solely on the inorganic chemistry behind the biomineralization. Furthermore, the microfluidic approach was also anticipated as an opportunity to study kidney stone growth kinetics, in a state of continuous flow and constant supply in calcium and oxalate solutions to understand the formation of pathological microcalcifications.

In the kidney, the nephron is the functional unit in charge of maintaining fluid balance, regulation and filtration of minerals from blood, filtration of waste materials from food/medication/toxic substances or regulation of hormones. All these vital functions make the nephron susceptible of failures towards the development of kidney diseases. To mimic the renal function, the microfluidic nephron-on-a-chip technology has proven to be a valuable approach[28-30,32]. In the particular context of kidney stone disease, continuous-flow microchannels of similar dimension to tubules in the nephron have served as valid candidates to investigate calcium-based kidney stones formation (*e.g.* calcium oxalate or calcium phosphate stones) under stone promoting conditions[43,44].

2. The crystal growth of calcium oxalate systems

Kidney stones are hybrid organic-inorganic materials, though CaOx minerals stand as their dominant inorganic constituent. Thereby, intensive studies have been conducted to characterize CaOx crystals. Herein, we intend to present an exhaustive overview of the studies accounting for its chemical identity, the physicochemical features impacting its occurrence and the main *in vitro* crystallizers used to study CaOx crystal growth and kinetics under similar conditions to the ones found in the kidney.

a. The calcium oxalate crystals, $CaC_2O_4 \cdot nH_2O$

i. Calcium oxalate monohydrate (COM): whewellite (n = 1)

Thermodynamically stable, calcium oxalate monohydrate ($CaC_2O_4 \cdot H_2O$, COM) or whewellite (after William Whewell) is a crystalline system exhibiting a monoclinic structure (space group $P2_1/c$) as depicted in **Figure 9.**

COM crystal morphology has been extensively studied in the literature[45,46] (**Figure 10**). COM crystal exhibits numerous shapes, *e.g.* monoclinic prismatic (A in **Figure 10a** and **Figure 10b**), twins (D-E in **Figure 10b**), dendrites (F-H in **Figure 10b**), flower-like (N-P in **Figure 10b**) *etc.* Millan determined, theoretically and experimentally, the crystal growth of whewellite shapes[47]. The study aimed at showing that the crystal shape could provide clues about the growth conditions of natural renal calculi. Albeit whewellite is the most abundant crystal among the idiopathic renal microcalcifications[36], it can also be encountered in breast calcifications[48] or (unexpectedly) considered for concrete constructions due to waterproof properties[49].

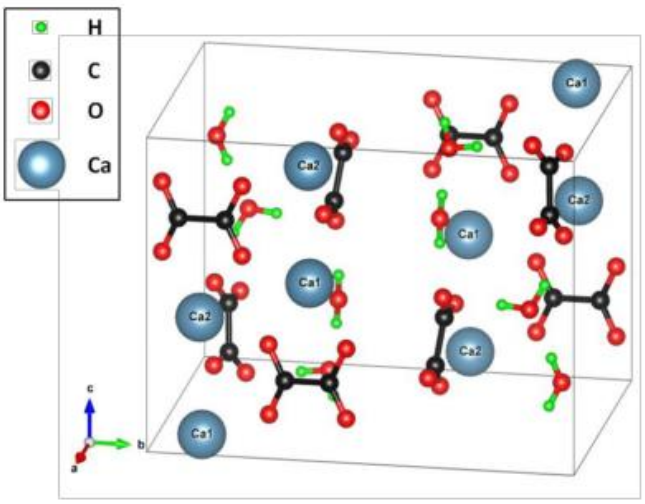

Figure 9. Crystalline structure of whewellite ($CaC_2O_4 \cdot H_2O$, COM).

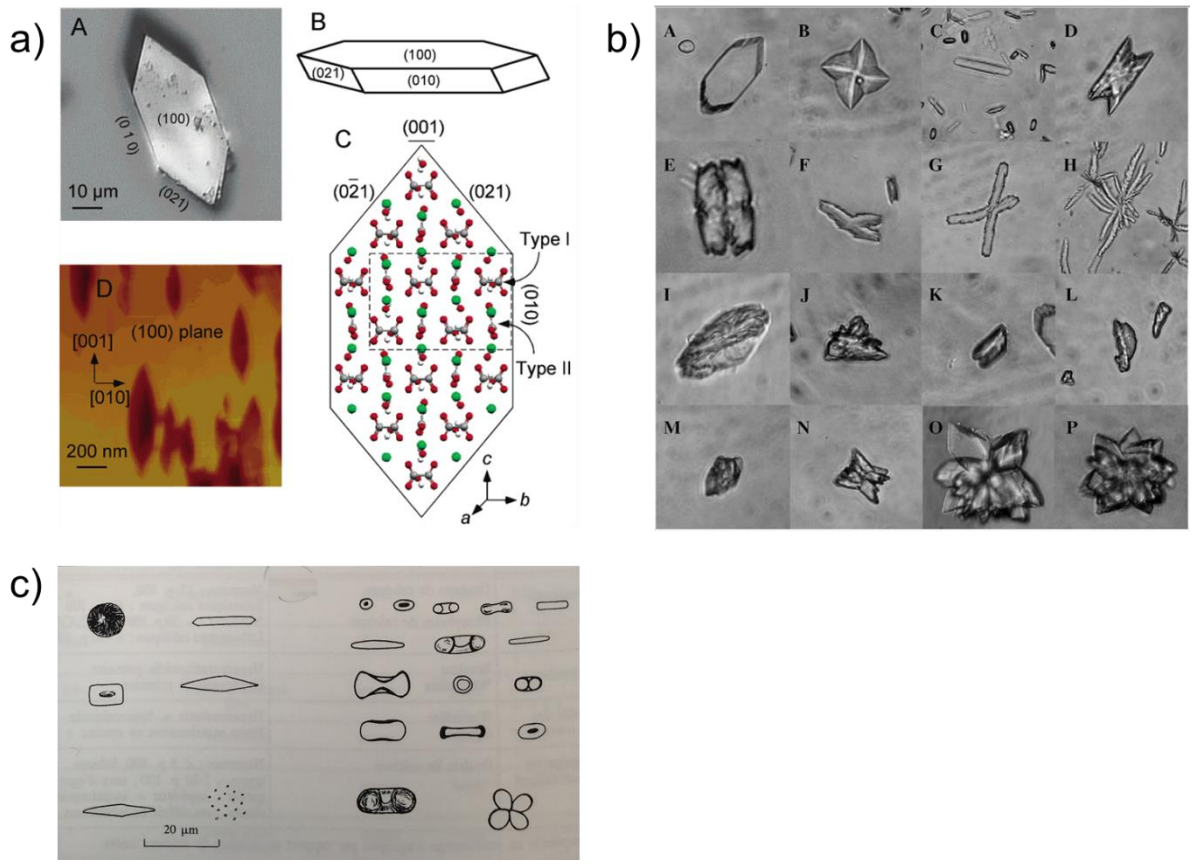

Figure 10. Morphologies of calcium oxalate monohydrate COM crystals: a) habit of monoclinic prismatic COM crystal with plane assignments and molecular arrangement in the crystal by Guo *et al.*[45]; b) COM crystal habits based on the work of Thongboonkerd *et al.*[46]. A, D-E, F-H, N-P images stand for monoclinic prismatic, twins, dendritic and flower-like COM crystals, respectively while B image represents COD crystal; drawing of reported morphologies in kidney stones of c) catalogue of COM crystals from the book Lithiase urinaire from Daudon and *et al.*[50]. All figures are reproduced with permission from ACS, Elsevier and Lavoisier - Médecine sciences, respectively.

Calcium oxalate monohydrate is not uncommon in the vegetal reign neither, where it fulfils calcium regulation in cell or protection against herbivory[51]. Actually, COM crystals extracted from plants allowed Arnott and collaborators to propose a structure based on X-ray diffraction in 1965[52]. In a book firstly published in 1989, Daudon, Jungers and Traxer introduced an extensive catalogue of COM crystal morphologies (**Figure 10c**) with emphasis on the stone disease conditions[50] (**Table 2**). Noteworthy, presence of whewhellite in kidney stones was related to abnormally high oxalate concentration in urine (*i.e.* hyperoxaluria).

ii. Calcium oxalate dihydrate (COD): weddellite (n = 2)

Calcium oxalate dihydrate ($CaC_2O_4 \cdot 2H_2O$, COD) or weddellite is a tetragonal crystal system (space group I4/m)[53] as shown in **Figure 11** and often found in urines of healthy persons[54]. Closer attention to COD crystal shows zeolites structure, *i.e.* channels containing water molecules (right in **Figure 11**). Therefore, the amount of water molecules into the structure can

vary inducing $CaC_2O_4 \cdot (2 + x)H_2O$ with $x < 1$ as the real chemical formula. Noteworthy, the number of water molecules occupying the pores is still under debate among the community.

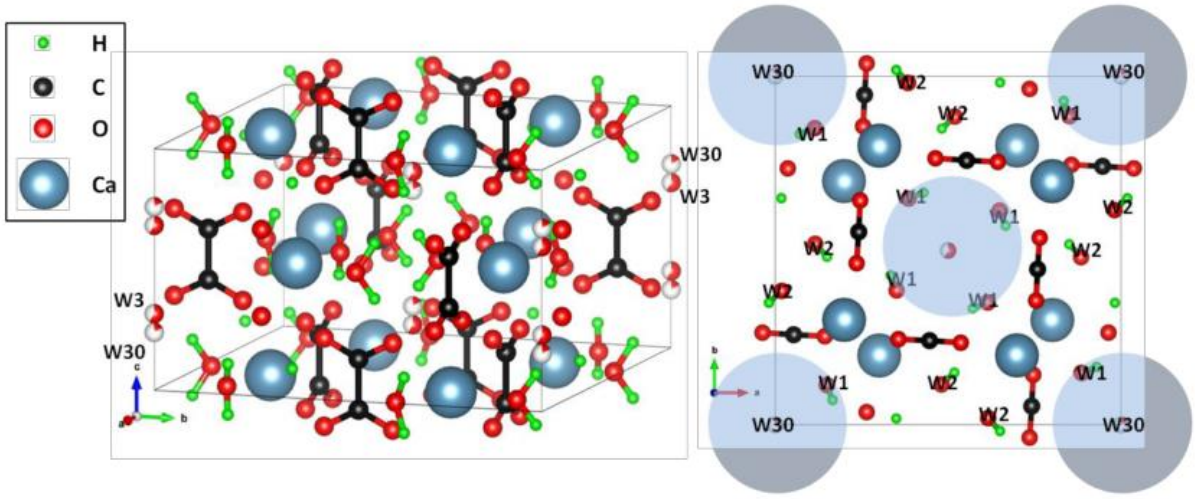

Figure 11. Crystalline structure of weddellite ($CaC_2O_4 \cdot 2H_2O$, COD).

Suspected to have protective effects against stone formations due to weak renal adhesion[55], COD crystals can also be lithogenic[36] given specific renal conditions (*e.g.* excess in urinary calcium concentration). Likewise COM crystals, Daudon *et al.* listed the various morphologies of weddellite crystals (**Figure 12a**) according to the disease conditions[50] (**Table 2**). Compare to whewellite, weddellite is thermodynamically metastable and tends to retransform to stable COM[56]. I*n vitro* COD crystallization in batch is uneasy and often requires additives[57]. Yet, Stankovic and collaborators recently published on the precipitation of sole COD crystals in aqueous solutions by sonication to study crystal growth and conduct kinetic analyses[58] (**Figure 12b**).

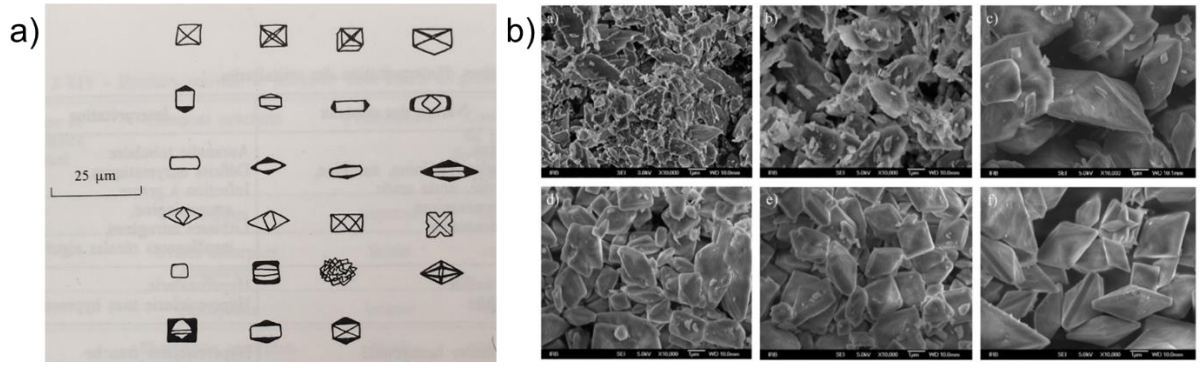

Figure 12. Morphologies of calcium oxalate dihydrate COD crystals: a) catalogue of COD crystals from the book Lithiase urinaire from Daudon *et al.*[50]; b) Scanning Electron Microscopy (SEM) images of COD crystals from Stankovic *et al.*[58]. Figure is reproduced with permission from Lavoisier - Médecine sciences and Elsevier, respectively.

Table 2. Relationship between type of morphologies, composition of calcium oxalate crystals and renal conditions. Ia-Id and IIa-IIc stand as naming for the type of CaOx kidney stone under scrutiny. Table adapted from the book Lithiase Urinaire of Daudon *et al.*[50] with permission from Lavoisier – Médecine sciences.

Type of morphology	Description of the surface	Usual composition	Common causes
Ia	More or less mammillary-shaped, presence of an umbilication, brown	whewellite (C1)	Intermittent hyperoxaluria – Cacchi-Ricci disease
Ib	Rough and mammillary-shaped, no umbilication, dark brown	whewellite	Hyperoxaluria – stasis (C2 to C1 conversion)
Ic	Smooth or sprouting, cream-colored, locally translucent especially for small calculi	whewellite	Primary hyperoxaluria
Id	Smooth, brownish-yellowish	whewellite	Hyperoxaluria
IIa	Flatted bipyramid embedded, translucent, sharp edges, brownish-yellowish to cream-colored	weddellite (C2)	Hypercalciuria
IIb	Crystal in spicule, embedded, thick, dense, blunt edges, silk to cream-colored	C2 + C1 due to water loss or mix crystallization	Hypercalciuria + intermittent hyperoxaluria
IIc	Rough, microcrystalline, silk-colored to brownish-yellowish	weddellite	Hypercalciuria

iii. The other calcium oxalate minerals: calcium oxalate trihydrate (n = 3, COT), amorphous (ACO) and anhydrous (COAnh)

Calcium oxalate trihydrate ($CaC_2O_4 \cdot 3H_2O$, COT) or caoxite[59] is a triclinic structure (space group $P\bar{1}$) as defined by Deganello *et al.*[60] and Echigo *et al.*[61]. Although much less common in kidney stones, heterogeneous nucleation of COT crystals in artificial urine was studied[62] since it was hypothesized that caoxite acted as an intermediate for the formation of COM and COD crystals[63]. The idea was abandoned with new evidences that amorphous calcium oxalate could play this role. Amorphous calcium oxalate (ACO) is uneasy to synthesize and extract from aqueous solution since it can transform to a more stable crystalline counterpart once back in solution. Yet, several syntheses have been proposed to precipitate ACO either in absolute ethanol[64], aqueous solution[65] or ionic liquid[66]. Known to be a potential intermediate for calcium

oxalate monohydrate in the vegetal reign[67], ACO seems to play a similar role in the formation of kidney stones as suggested by Xie *et al.*[68] (**Figure 13**). Briefly, their findings supported that early aggregation of ACO onto the CaP Randall's plaque in the kidney promoted the nucleation and growth of COM-based stone. Last, anhydrous calcium oxalate (CaC_2O_4, COAnh) has a monoclinic structure (space group P2/m). It is not reported in kidney stone, yet its study provides thermal data about the other CaOx polyhydrates[69,70].

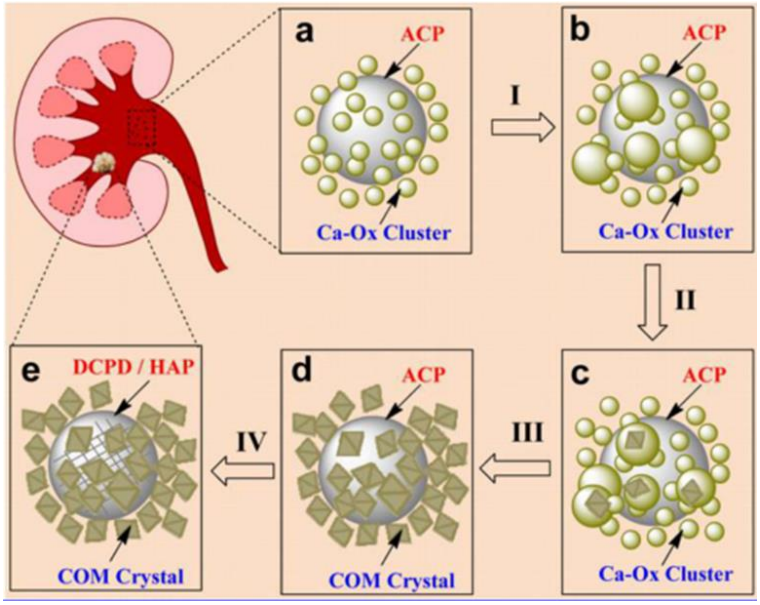

Figure 13. Proposition for the nucleation mechanism of COM crystals in presence of calcium phosphate (ACP) presented by Xie *et al.*[68]. Figure is reproduced with permission from ACS.

b. The origin of calcium oxalate stone formation

i. The "free-particle" model vs. the "fixed-particle" model

Regarding the initiation of calcium oxalate stone formation in the urinary tract, two dominant models currently exist that were defined by Finlayson and Reid as the "free-particle" model and the "fixed-particle" model[71]. In the "free-particle" model, it was assumed that stone formation was triggered by tubular fluid being supersaturated in calcium oxalate particles. Hence, *de novo* nucleation of calcium oxalate tended to occur at some point in the nephron towards the nuclei growth, aggregation and entrapment while traveling through the section. However, Finlayson and Reid determined by mathematical modelling that this pathway was unlikely to happen due to insufficient transit time in the nephron preventing from individual crystals to grow large enough and end up trapped. In contrary, they proposed the alternate "fixed-particle" model suggesting that excessive supersaturation of the tubular fluid resulted in the formation of small calcium oxalate nuclei. These nuclei became attached to the epithelial cells in the tubule where damages had occurred leading to crystal growth and agglomeration. Finlayson and Reid's later model remained uncontested for decades until Kok and Khan's

work[72]. In their publication, they tried to reconcile the free- and fixed-particle mechanisms on the basis that both healthy subjects and stone formers experienced crystalluria in the urine with stone formers excreting larger and more agglomerated particles. Therefore, they calculated the likelihood of stone formation based on the free-particle model used by Finlayson and Reid with the incorporation into the model of the size increasing effect of crystal agglomeration. In essence, they still agreed with Finlayson and Reid regarding the "fixed-particle" mechanism. Yet, they argued that crystalline particles could still grow large enough during normal transit time, be retained due to their size at some point in the nephron and consequently act as a site for stone formation with the highest risk at the end of the collecting ducts.

Lastly, Robertson also supported that the "free-particle" model could still be possible with crystal aggregation taking place if passage in the tubules was delayed[1]. Therefore, he mathematically introduced three new hydrodynamic factors accounting for crystal passage delay. First, particles travelling close to the tubule walls might be moving much slower than at the tubule's central axis due to the flow velocity profile in a pipe structure. Thus, it would significantly delay the transit time through a given segment of tubule. Then, a second potential drag effect on particles could come from the tubule walls themselves. In fact, an increasing effect on a particle velocity in the fluid flow could happen if the diameter of the particle approached the inner diameter of the tubule. Finally, particular spatial orientation of collecting ducts (*i.e.* upward-draining tubules) within the kidney could add additional transit time for crystal passage since crystals could be subject to gravity force. Hence, it could promote crystal growth alongside aggregation. Robertson's work predicted that calcium oxalate crystals could form *de novo* at the end of the descending limb of the loop of Henle and/or at the collecting duct prevailing the concentration in oxalate in the tubular fluid. In the collecting ducts, crystallization of small particles would follow small increase in tubular oxalate concentration. In contrary, larger increase in tubular oxalate concentration would promote crystallization of large crystals coming from the descending loop of Henle and small crystals from collecting ducts.

Recent studies tried to provide experimental investigations with respect to free- and fixed-particle models leading to the conclusion that both could occur in human and animal models[73,74]. In particular, Kok and collaborators reported on the time-dependency involved in both mechanisms[74]. They concluded that the "fixed-particle" mechanism was a slow process whereas the "free-particle" one was a rather fast one. Their assertions were based on the examination of two stones timelines. The first stone (**Figure 14**), suspected to describe the fixed-particle model, originated from a prior renal trauma and grew slowly (yet surely) for over

two decades. The second stone, describing the free-particle model, started from a situation of urinary tract infection and grew within 6 years (**Figure 15**).

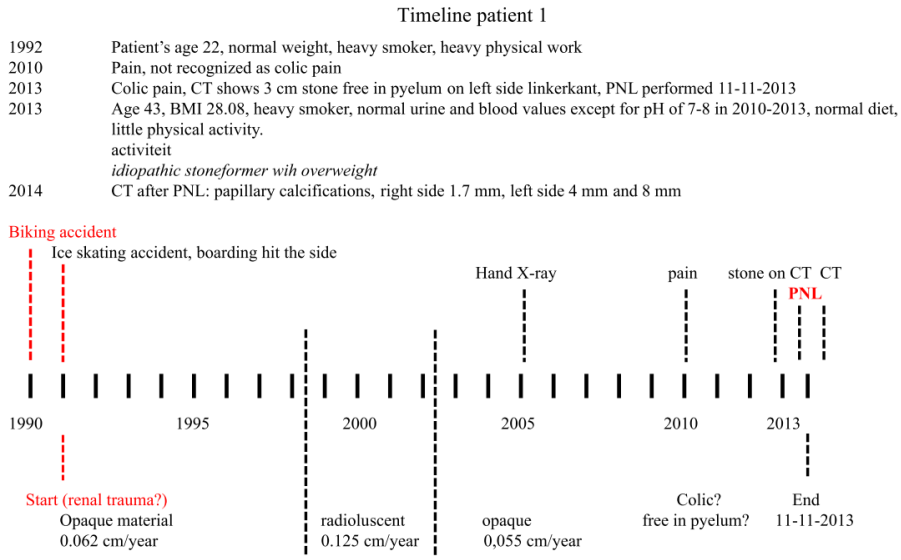

Figure 14. Effect of time regarding the evolution of stone formation suspected to grow according to the fixed-particle theory. Figure is reproduced from Kok *et al.*[74] with permission from Springer.

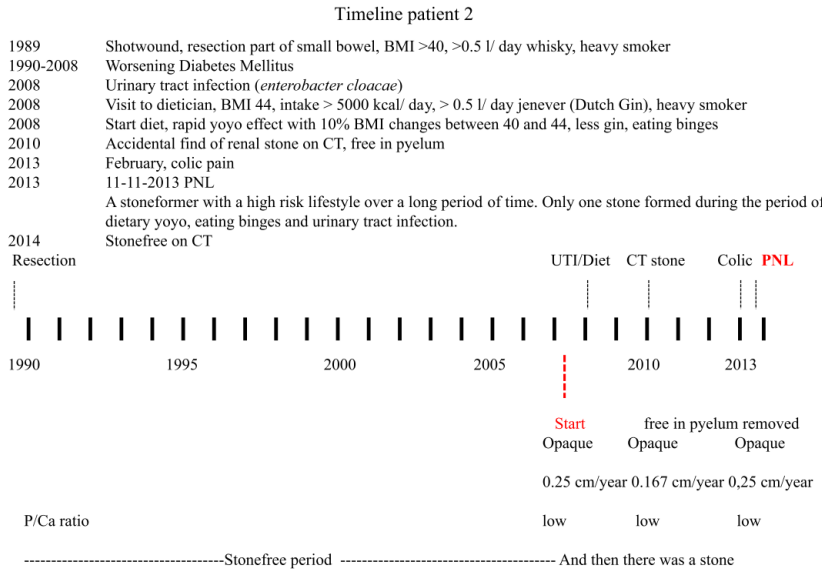

Figure 15. Effect of time regarding the evolution of stone formation suspected to grow according to the free-particle theory. Figure is reproduced from Kok *et al.*[74] with permission from Springer.

ii.Physicochemical aspects

With respect to urolithiasis, Finlayson listed the physicochemical features known to intervene in the formation of CaOx stones[75]. First was the supersaturation of urine as the thermodynamic driving force. This driving force, related to concentration in electrolytes, measured whether particles might precipitate or grow due to sufficient energy present in the medium. The second

feature was the nucleation as the initial event in stone precipitation. The onset was governed by the balance between the energy spent to form a new phase volume versus the required energy to expand its surface. Second to last aspect, the growth of crystals and particles was studied thanks to experimental methods likewise: single crystals size measurement, spontaneous precipitation in unstable supersaturated solution, seeded crystals added to supersaturated solution, continuous crystallizer and crystal growth in gels. Importantly, crystal growth had to be properly discriminated from crystal aggregation that was the last physicochemical factor from Finlayson's list. *In fine*, all combined parameters should provide a comprehensive thermodynamics and kinetics picture of CaOx stone formation. Additionally, Daudon *et al.* added three more mechanisms that could further depict kidney stone formation[50]: the presence of urinary macromolecules (*e.g.* Tamm-Horsfall protein) could result in CaOx crystal agglomeration to form a bigger calculus. Moreover, the crystal could be blocked at some point in the nephron. This could be due to (i) direct adhesion to the renal epithelium, (ii) an important increasing size, (iii) the anchoring through an (inorganic or organic) intermediate or (iv) potential entrapment within a cavity. Last, kidney stone would just grow within the kidney until its natural elimination or after medical procedures (*i.e.* drugs or surgery).

In a review published in 2011, Tiselius presented an overview of how CaOx stone formation was initiated for important growth and aggregation in the urinary tract[76]. Basic observations agreed with CaOx stones having their origin on CaP precipitates. The cascade of events leading to CaOx stones seemed to imply the concerted CaP dissolution due to low urine pH, high Ca and Ox concentrations in urine and low inhibitory activity with respect to growth/aggregation. Yet, precipitation of CaOx stone in absence of a CaP initiator seemed feasible in case of exceptionally large excretion of oxalate. It would lead to high peak levels of urine supersaturation and appeared to be encountered only in the distal collecting duct and caliceal urine. Rodgers and collaborators proposed a theoretical modeling of the risk of crystallization throughout the nephron and over a large range of pH values[77]. Using real urinary data, the computational approach relied on the software Join Expert Speciation System (JESS) to calculate the speciation in Ca stones (**Figure 16a**) and urine saturation index (SI), equivalent to the relative supersaturation. Additionally, JESS enabled to report on the influence with respect to the precipitation of one Ca stone on the others in the distal part of the collecting duct (**Figure 16b**). Noteworthy, the model never predicted the formation of pure CaOx stone but resulting from prior precipitation of brushite or hydroxyapatite. Authors acknowledged the limitations of the model (*i.e.* data dependent, sole thermodynamics consideration), yet they

believed that it could initiate insightful discussion and debate about the mechanisms of Ca stones formation.

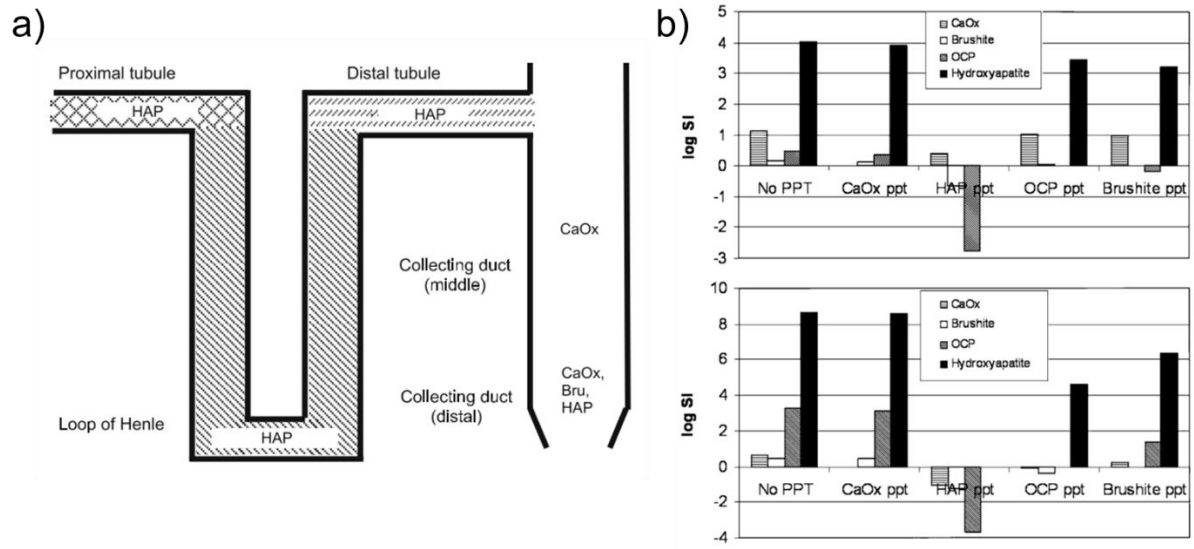

Figure 16. Chemical speciation of Ca salts simulated by JESS software: a) supersaturated salts in the different regions of the nephron at the lower end of pH ranges; b) effect of precipitation on saturation index SI values of each Ca salts in the distal region of the collecting duct at the lower end (top) and upper end (bottom) of the pH ranges. Figures are adapted from Rodgers *et al.*[77] with permission from Springer.

iii. Influence of calcium and oxalate concentrations in urine

Even among healthy persons, urine is supersatured (SS) in the thermodynamically metastable region of stone formation with its susceptibility to induce calcium oxalate crystallization if not well balanced by inhibitors. It underlies the importance of faithfully depicting all the urinary compounds in their native concentration and "chemical environment" for each individual and clinical profile. For instance, subjects with increasing urinary risk factors (*e.g.* renal excretion, urinary pH and urine volume voided in 24 hours) do not necessarily form stones whereas stone formers could present normal urine analyses. To bridge the gap between the complex *in vivo* formation of CaOx (or CaP…) crystals and the standard strategy using risk factor analyses, extensive studies have been required to help with the etiology of stone formation. In 2010, He and collaborators described the morphology, size, aggregation and crystalline phase of nanocrystallites from freshly collected urine samples of 85 health persons with respect to 65 lithogenic patients[54]. In healthy urine samples, they observed smooth spheroidal nanocrystallites, more often COD than COM particles that were well dispersed, with a size distribution from about 20 to 350 *nm*. In contrast, particles in lithogenic urines had sharply angled edges and tips, were aggregated, with a broader size distribution (from ≈ 1.0 to 1000 *nm*) and with COM phase more present compared to healthy urines. The study suggested that the rounder the particles, the less aggregated they were preventing stone formation.

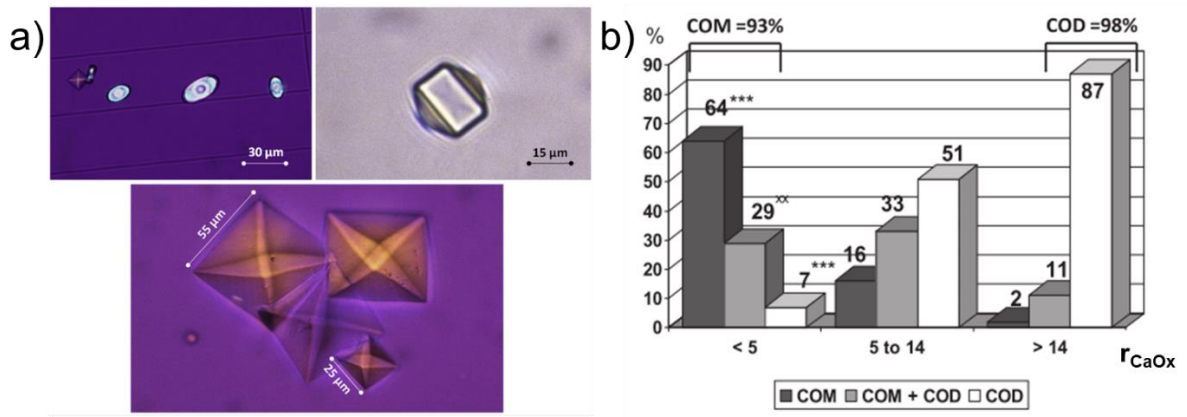

Figure 17. CaOx crystallization with respect to urinary concentrations in calcium and oxalate ions: a) CaOx crystals found in urines of different stone formers. Images on top describe (left) CaOx crystal mixture of COM crystals and octahedral COD crystal and (right) elongated COD crystal usually observed in the case of heavy hypercalciuria. At the bottom, the image depicts large octahedral COD crystals suggesting coupled hyperoxaluria and hypercalciuria; b) influence of $r_{CaOx} = Ca^{2+} / Ox^{2-}$ on the crystalline phases of CaOx observed in urine samples. Figures are adapted from Daudon *et al.*[78] with permission from Elsevier.

Furthermore, they concluded with the presence of COD crystallites in healthy urines as being relatively more favorable in preventing stone formation as proposed by Sheng and collaborators previously[55]. The authors supported that COD crystals formed less stable aggregates, had a poorer adhesion contact to renal epithelial cells leading to a protective effect against stone formation.

Among idiopathic stone formers, Daudon *et al.* examined the relationship between the concentrations in calcium and oxalate ions with respect to the type of COM and/or COD crystals present in the associated urine samples[78]. While the ionic product of concentrations measured in urine $[Ca^{2+}]\times[Ox^{2-}]$ (p_{CaOx}) stood as the driving force for CaOx crystallization, they used the Ca^{2+}/Ox^{2-} molar ratio (r_{CaOx}) as an empirical parameter to correlate with the CaOx crystalline phases found in the collected urine samples (**Figure 17a**). As shown in **Figure 17b**, low values of r_{CaOx} (< 5.0) were associated with high occurrence of COM crystals whereas at high values of r_{CaOx} (> 14), COD crystals were observed mostly. When $5.0 < r_{CaOx} < 14$, CaOx crystal mixture of both crystalline phases were obtained. With respect to the data, Daudon and collaborators showed the oxalate- (respectively calcium-) dependency for COM (respectively COD) crystal formation. Additional urine examinations enabled to construct a monogram depicting r_{CaOx} against p_{CaOx} and to assess the risk extent of individuals for CaOx crystal

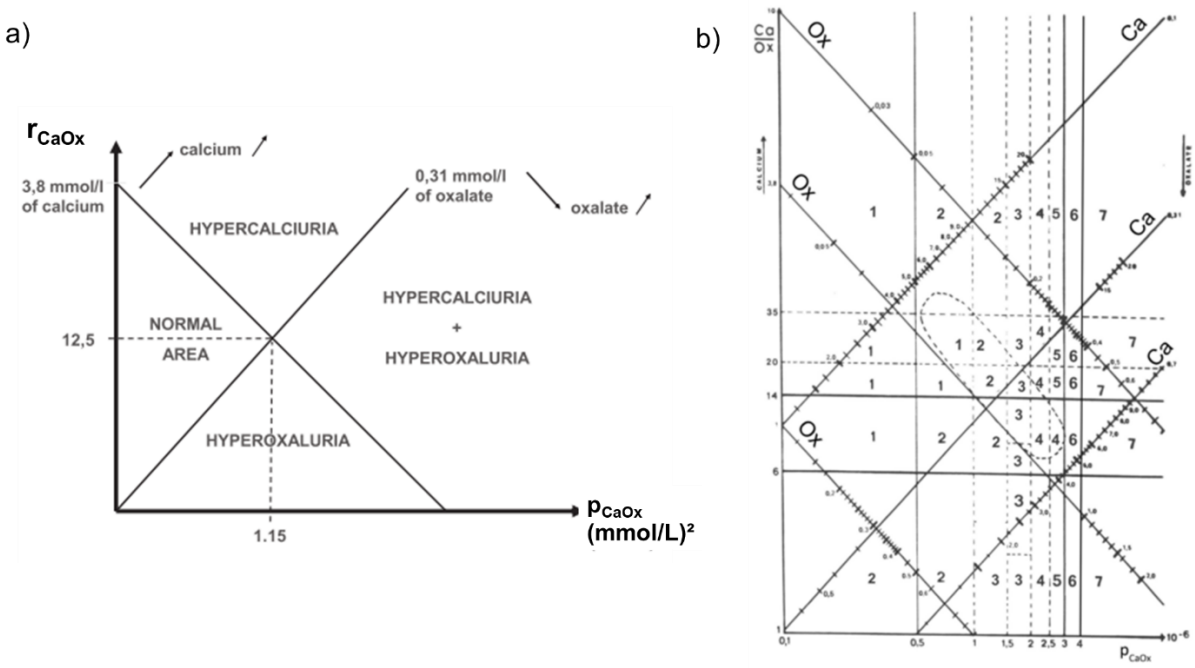

Figure 18. Relationship between calcium and oxalate concentrations in urine and CaOx crystallization: a) simplified representation of the different areas on the calcium oxalate crystallization monogram according to calcium (*e.g.* 3.8 *mmol.L*$^{-1}$) and oxalate (*e.g.* 0.31 *mmol.L*$^{-1}$) concentrations in the urine of stone formers; b) extended crystallization monogram depicting the clinical risk of stone formation as defined in **Table 3**. Figures are adapted from Daudon *et al.*[78] with permission from Elsevier.

formation. With respect to urinary concentrations in Ca^{2+} and Ox^{2-} ions, individuals were categorized under either normal, hypercalciuria, hyperoxaluria or coupled hypercalciuria and hyperoxaluria conditions (*e.g.* case scenario for patient with [Ca^{2+}] = 3.8 *mmol.L*$^{-1}$ and [Ox^{2-}] = 0.31 *mmol.L*$^{-1}$ in **Figure 18a**). Within a condition area, CaOx crystallization scores (**Table 3**) were attributed to predict the clinical risk of stone formation (**Figure 18b**). At p_{CaOx} > 2.0 (*mmol.L*$^{-1}$)², data reported a higher risk of favoring stone recurrence since crystallization score was above 4.0. Finally, Daudon and collaborators concluded with the clinical relevance to distinguish COM from COD crystalluria to help finding out the etiology of renal stone disease (**Figure 17a**). For instance, abundant COM crystals in urine reflected lithogenic process towards the clinical diagnosis of primary hyperoxaluria. Even though COD crystals in urine had less specific diagnostic value (lesser adhesion onto renal walls than COM crystals), it still accounted for high calcium concentration. Interestingly, COD crystals found under elongated shape (top right in **Figure 17a**) could be associated to severe (and idiopathic) case of hypercalciuria (> 7.0 *mmol.L*$^{-1}$) while large octahedral COD crystals (bottom in **Figure 17a**) were correlated to combined hyperoxaluria and hypercalciuria.

Table 3. Crystallization score related to the frequency of CaOx crystallization (fc). Table reproduced from Daudon *et al.*[78] with permission from Elsevier.

Frequency (%) of CaOx crystalluria	Crystallization score	Clinical risk of stone formation
0 ≤ **fc** ≤ 10	1	Very low
10 ≤ **fc** ≤ 25	2	Low
25 ≤ **fc** ≤ 40	3	Medium
40 ≤ **fc** ≤ 60	4	Moderately increased
60 ≤ **fc** ≤ 75	5	High
75 ≤ **fc** ≤ 90	6	Very high
90 ≤ **fc** ≤ 100	7	Maximum

Research teams also tried to correlate Ca^{2+} and Ox^{2-} ionic concentrations in urine and CaOx crystallization. For instance, Borghi and collaborators studied the effect on CaOx crystallization of reduced SS in urine due to drinking therapy among 12 normal subjects versus 15 recurrent stone formers[79]. Worth mentioning, none of the stone formers presented common urinary risks, *e.g.* hypercalciuria or hyperoxaluria. Before and after water consumption, the research group measured the oxalate tolerance in urine and the upper limit of metastability (both terms define afterwards). First, increasing amounts of $Na_2C_2O_4$ were added to urine aliquots and calcium concentration in supernatant was measured afterwards. Once plotted against the concentrations of added oxalate, it allowed extrapolating the permissible increment in oxalate, *i.e.* the maximal load of oxalate added without measurable crystallization. Thereafter, the upper limit of metastability (point of CaOx precipitation) was determined by adding the initial oxalate concentration in urine to the permissible increment in oxalate. In both groups, the water load (*i.e.* decrease in CaOx SS) resulted in an increase in the permissible increment in oxalate, without significant changes in the upper limit of metastability. Additionally, the induced dilution did not affect the inhibitory activity of urinary macromolecules with respect to CaOx crystallization. Authors concluded with a protective effect of water load with respect to CaOx crystallization in stone formers without common urinary risk factors. More than ever, this rises the importance in fully characterizing the native concentration and "chemical environment" of urinary compounds with respect to CaOx crystallization.

In a recent contribution, Laube and collaborators proposed the BONN-Risk-Index (BRI) as an *in vitro* method to measure the extent of urinary samples for stone formation/inhibition and associated growth kinetics[80]. As described in **Figure 19a**, urine's relative light transmissivity (RLT) was measured during induced crystallization between native free urinary calcium ions

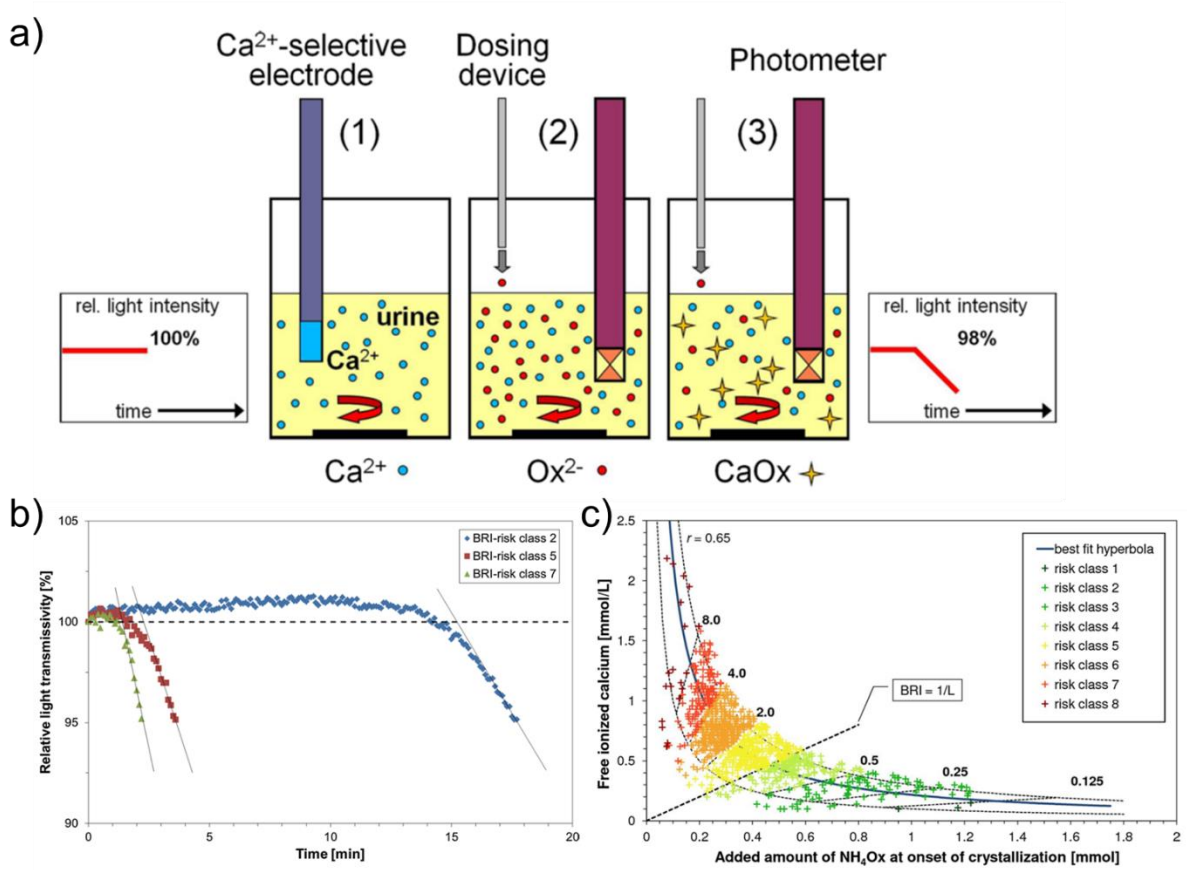

Figure 19. Description of the BRI-method: a) schematic illustration of the system; b) titration curves of urines according to risk class of stone formers; c) results of BRI measurement of urine samples. Figures are adapted from Laube *et al.*[80] with permission from Springer.

$[Ca^{2+}]$ and oxalate ions (Ox^{2-}) from added $(NH_4)_2C_2O_4$. Set to 100 % at the start of titration, RLT was continuously recorded until a decrease to 95 % indicating the onset of crystallization (**Figure 19b**) and BRI = $[Ca^{2+}]/(Ox^{2-})$ was calculated (**Figure 19c**). In a given urine sample, $[Ca^{2+}]$ stood for a significant lithogenic estimate while (Ox^{2-}) indirectly measured the inhibitory activity with respect to stone formation. In conclusion, Laube and collaborators showed that the BRI method described the imbalance between inhibitors and promotors of crystal formation and enabled to monitor the behavior of crystal growth right after nucleation. They were confident that these two factors could provide with a more complete picture of *in vivo* stone formation.

c. *In vitro* calcium oxalate crystallization methods

i. Factors determining types and morphologies

In vitro crystallization of calcium oxalate systems is highly influenced by the experimental conditions. For instance, Brecevic and collaborators investigated factors that could influence the crystalline phase distribution of hydrates in CaOx precipitation[81]. Experiments were conducted in a batch crystallizer by mixing equal volumes (100 mL) of $CaCl_2$ and $Na_2C_2O_4$

(25°C, pH 6). As reported in **Table 4**, mixing process demonstrated that pouring simultaneously calcium (5.3 $mmol.L^{-1}$) and oxalate (6.0 $mmol.L^{-1}$) solutions into the crystallizer induced the precipitation of COM crystals as major component with a significant amount of COD crystals.

Table 4. Distribution of hydrates under various experimental conditions from Brecevic *et al.*[81]. Table partially reproduced with permission from Elsevier.

	COT (%wt / wt)	COD (%wt / wt)	COM (%wt / wt)
Simultaneous mixing	-	19	81
Ox^{2-} into Ca^{2+}	54	-	46
Ca^{2+} into Ox^{2-}	65	-	35
2 x Ca^{2+} ions	-	25	75
2 x Ox^{2-} ions	-	11	89
2 x (Ca^{2+} + Ox^{2-}) ions	-	7	93

If calcium (oxalate, respectively) solution was poured into oxalate (calcium, respectively), no COD crystals were detected at the expense of COT crystals with a large amount of COM crystals. The authors also varied the initial solution composition fed into the system. They concluded with COM crystals remaining the major crystalline phase with respect to COD crystals. Moreover, they observed that COM crystal morphology was concentration-dependent. Effect of stirring on the distribution of CaOx hydrates was under scrutiny too. The induction time (*i.e.* the point at which a precipitate first became visible) dramatically varied if reactant solutions were unstirred (20 min), magnetically (2 min) or mechanically (3-4 min) stirred right after mixing. With unstirred solutions, the relative proportions of COM and COD crystals remained constant around 3:1. Under magnetic stirring, precipitates primary consisted of COT crystals and decayed as a function of time in favor of COM crystals. Mechanical stirring induced the precipitation of all three hydrates with COT crystalline phase being the major component. Finally, the effects of mechanical grinding (*i.e.* crystal breakage likely due to stirring) and applied magnetic field were investigated. While grinding increased the amount of COT into the crystallizer, the presence of a magnetic field did not have an influence on the distribution of all three CaOx hydrates. To conclude, the authors agreed on the appearance of a particular hydrate being the result of combined thermodynamic and kinetics factors.

In a more recent contribution, Thongboonkerd and collaborators evaluated factors affecting crystalline phases and morphologies of CaOx crystal generated *in vitro*[46]. Into a 24-well plate,

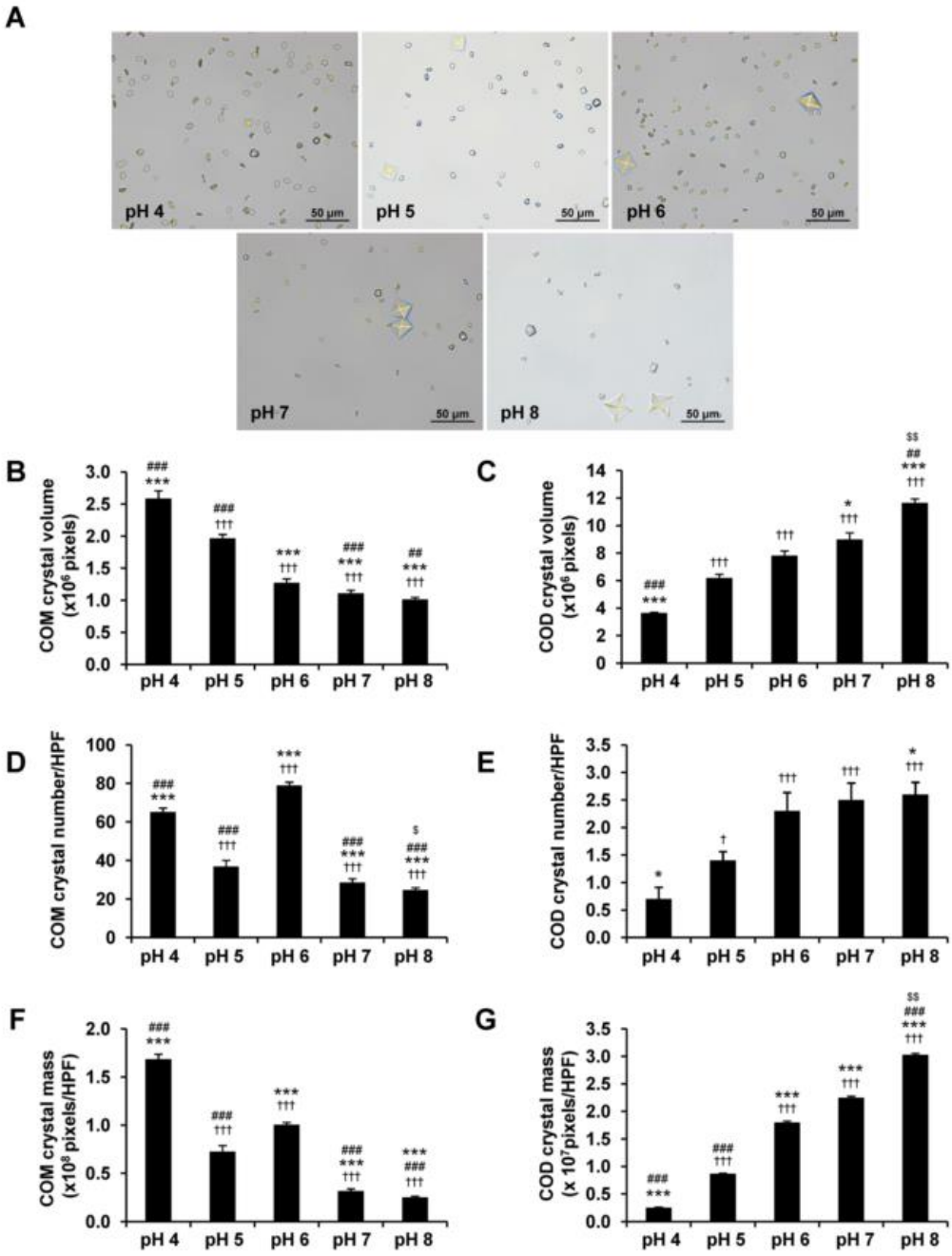

Figure 20. Effect of urine pH on CaOx crystallization. (A) Morphology of the resulting CaOx crystals (original magnification 400×). (B) COM crystal size (volume) measured. (C) COD crystal size measured. (D,E) Number of COM and COD crystals, , respectively, counted. (F,G) COM and COD crystal masses. Figure reproduced from Manissorn *et al.*[82] and under Creative Commons license.

$CaCl_2$ and $Na_2C_2O_4$ solutions were mixed under 78 different conditions taking into account molar concentrations, buffering, pH, stirring and temperature. With respect to molar concentrations, COM crystal morphology (*i.e.* the most observed crystalline phase throughout all conditions) varied in a concentration-dependent manner while COD crystals precipitated after using 5.0 $mmol.L^{-1}$ $CaCl_2$ and 0.5 $mmol.L^{-1}$ $Na_2C_2O_4$. The use of a 10 $mmol.L^{-1}$ Tris-HCl buffer solution (pH 7.3) enhanced the growth and aggregation of COM crystal. The pH also affected CaOx crystallization since at pH > 5.0, COD crystallization was favored. While

magnetic stirring resulted in a reduction of size crystallites, CaOx crystallization at 4°C was more efficient than at higher temperature (25 and 37°C). *In fine*, the authors presented their work as a valuable catalogue (**Figure 10b** in section **2.a.i**) for further study on modulation of CaOx crystals and kidney stone disease.

In 2017, Manissorn and collaborators studied the systematic influence of urine pH on CaOx crystallization[82]. Briefly, 10 $mmol.L^{-1}$ $CaCl_2.2H_2O$ and 10 $mmol.L^{-1}$ $Na_2C_2O_4$ were used to crystallize CaOx in artificial urine with pH ranging from 4.0 to 8.0 in 24-well plate. The results (**Figure 20**) showed that the most acidic pH 4.0 favored monoclinic-prismatic COM crystallization whereas bipyramid-shaped COD crystals formed at pH 8.0. In between, they observed a CaOx crystal mixture with COM (COD, respectively) crystals being dominant at acidic (basic, respectively) urine pH. Importantly, the group also evaluated the effect of pH on crystal-cell adhesion and internalization. They demonstrated that crystal-cell adhesion was maximal (minimal, respectively) at the most acidic (basic, respectively) pH and internalization had a peak activity at pH 7.0. The study suggested a promoting effect of acidic urine pH on CaOx kidney stone formation whereas basic pH seemed to prevent the formation of pathogenic crystals.

A gel medium rather than a classical aqueous medium also demonstrated to influence *in vitro* CaOx crystallization. Bisaillon and Tawashi grew CaOx crystals in two distinct gel systems, respectively silica and gelatin[83] (**Figure 21**). A U-shaped tube (**Figure 21a**) was filled with each gel. Prior to crystallization, additives could be incorporated in the gel medium to modify crystal growth. Slow diffusion of the reacting ions was completed by the addition of 10 mL of $CaCl_2$ (0.5 $mol.L^{-1}$) and 10 mL of oxalic acid (0.5 $mol.L^{-1}$) solutions on the gel surface of each side of the U-tube. The results showed that CaOx crystallization in silica gel enabled the growth of single crystals (**Figure 21b**). COM crystals were twins- or rosette-shaped while COD crystals exhibited bipyramidal shaped similar to those present in the urine of stone formers. In contrary, CaOx crystals grew into aggregates in gelatin gel, but phase identification based on crystal habit was not possible (**Figure 21c**). The report demonstrated that the gel structure and composition was able to control the nucleation, growth and orientation of CaOx crystals.

The effect of temperature on CaOx crystals grown in silica gel systems was investigated as well[84]. At temperature varying from 7.0°C to 67.0°C, 5.0 mL of $CaCl_2$ (0.5 $mol.L^{-1}$) and 5.0 mL of $Na_2C_2O_4$ (0.2 $mol.L^{-1}$) were added at each limb of a U-tube to enable CaOx crystallization. With respect to crystalline phases and morphology, Ouyang and collaborators showed that low temperature (*i.e.* 7.0°C) increased the content of COD crystals while decreasing the crystal size. Higher temperatures induced COM crystallization in rosettes at 27°C and with encrustations at 57°C likewise second-nucleation occurred at the crystal surface. In terms of crystal growth rate, the results supported an increase in crystal size accordingly to the increase

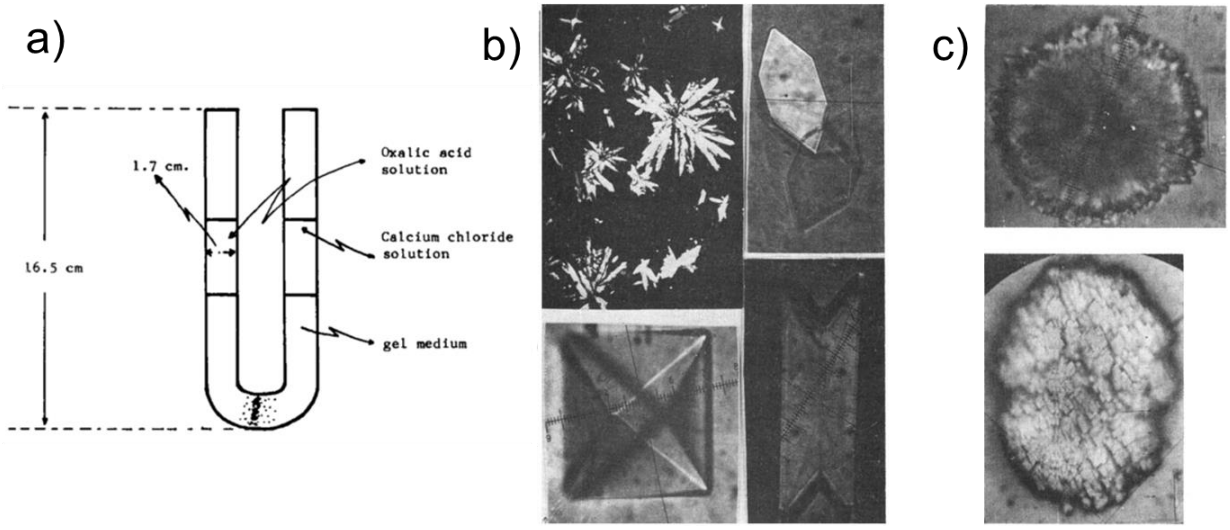

Figure 21. Growth of CaOx crystals in gel systems: a) schematic illustration of the U-shaped tube selected for the gel growth studies; b) CaOx crystals grown in silica gel. All presented crystals apart from the one at the left bottom (COD crystal) are COM crystals; c) CaOx crystals grown in gelatin exhibiting aggregated organization. Figure is adapted from Bisaillon and Tawashi[83] with permission from Elsevier.

in temperature. The authors also demonstrated an increase in weight of CaOx crystals along with a decrease in time induction, supposedly caused by an enhanced diffusion rate of reagents in gel system at higher temperature.

Finally, molecular additives are known to modulate *in vitro* CaOx crystallization. For instance, an AFM investigation showed that citrate modulation on COM crystallization relied on selective bindings between $–COO^-$ of citrate and calcium in the CaOx lattice along with H-bond between the –OH group of citrate and an oxalate from the matrix[85]. A study involving osteopontin supported that the protein affected COM crystal morphologies in a concentration-dependent fashion[86] (**Figure 22a**). Besides, catechins (*i.e.* polyphenolic compounds represented in **Figure 22b**) from green tea extract appeared effective in directing CaOx crystallization from COM to elongated COD crystals[57] (**Figure 22c**). Previous studies on animal models supported the preventive effect of green tea on renal stones[87,88]. An *in vitro* study conducted on renal tubular cells demonstrated the ability of one catechin of interest (the epigallocatechin gallate or EGCG) to decrease the binding of COM crystals from the cells[89]. Knowing that green tea is one of the most drank beverage worldwide, these results could provide with an interesting and natural solution to treat and prevent kidney stones[90].

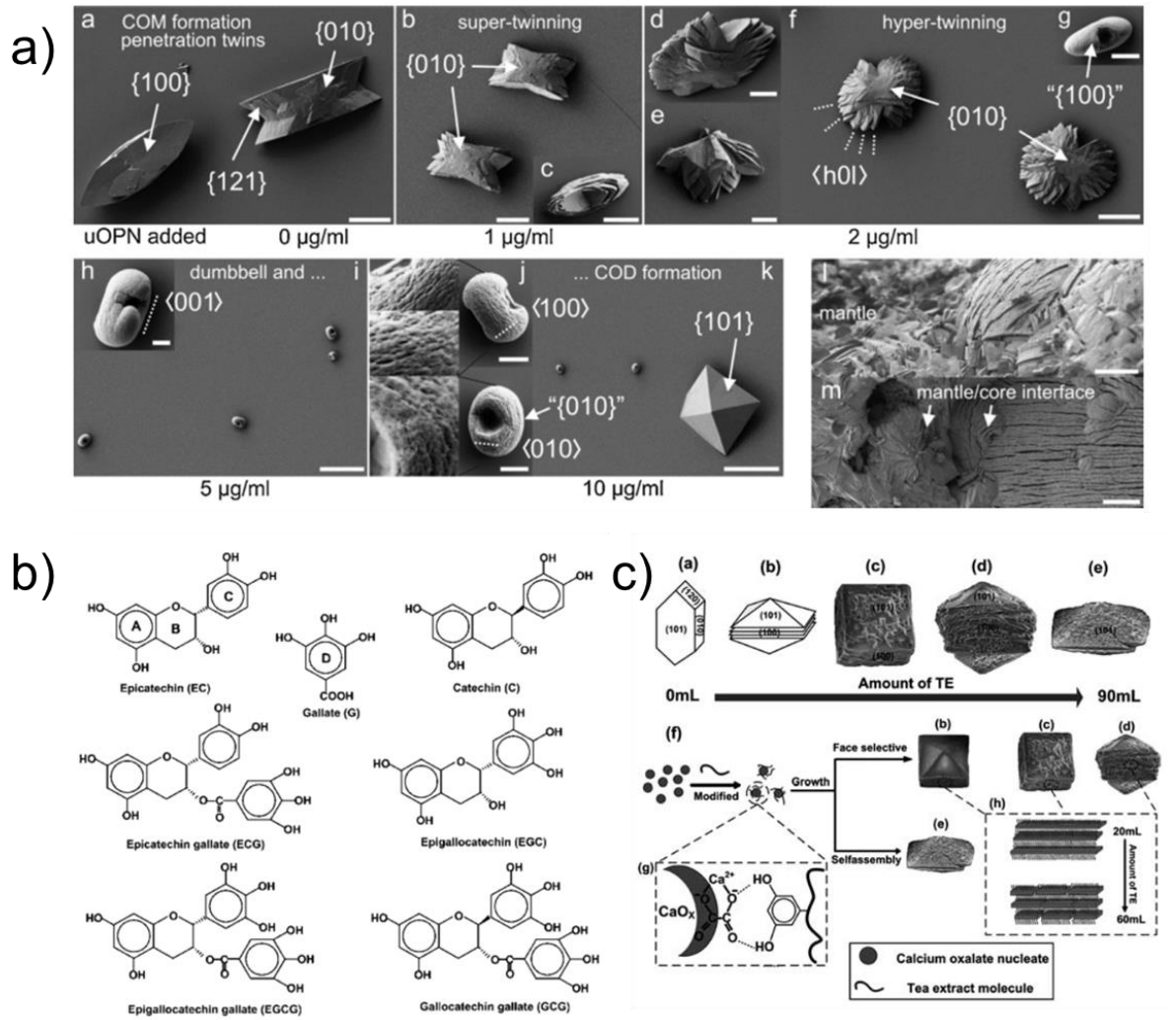

Figure 22. Modulation effect of molecular additives on CaOx crystallization: a) SEM images of COM crystals precipitated at different concentrations of osteopontin; b) structure of main catechins in green tea extract. A, B, C and D are identifiers for the basic ring frame of polyphenols; c) schematic representation of CaOx crystals obtained at increasing amount of green tea extract with potential crystallization pathway. **Figure 22a** is reproduced from Langdon *et al.*[86] and **Figure 22b-c** are adapted from Chen *et al.*[57] with permission from Elsevier and RSC, respectively.

ii.*In vitro* crystallization systems

In vitro crystallizers are often used for the study of urinary stone formation. In a review published in 1997, Achilles compared the most important systems against each other yet with respect to their potential importance and similarity to the intrarenal mechanisms of stone formation[91]. Yet, we arbitrary decided to focus on three of the reviewed *in vitro* crystallizer systems: the Constant Composition Method (CCM), the Mixed Suspension Mixed Product Removal crystallization (MSMPR) and the Flow Model of Crystallization in Gels (FMCG).

In the Constant Composition Method (CCM), where a metastable solution is incubated with well-characterized seed crystals of CaOx, a calcium-selective electrode monitors the decline of Ca^{2+} ions. The change in potential induces the automatic addition of equivalent amount of

Ca^{2+} and Ox^{2-} ions to maintain supersaturation (SS) of solution at constant level. Crystal growth rates are derived from the rate of addition of the titrating solution against the surface area of the crystals present. CCM enables high reproducibility of the measurement of crystal growth rates along with the determination of growth inhibition at constant SS. Yet, the simultaneous quantification of thermodynamic (*i.e.* change of SS) and kinetic (*e.g.* inhibitor of crystallization) effects on CaOx crystallization is uneasy and measurements in (nearly) undiluted urine is not possible. Kolbach-Mandel and collaborators, using a CCM approach, addressed the separate effects of growth rate, nucleation and aggregation in COM crystal formation, by combining the system with particle size determination and separate aggregation experiment[92]. Calcium and oxalate solutions were allowed to equilibrate prior to seed crystal addition into a thermostated reaction vessel. Two Dosimats maintained the reaction solution at constant composition, one filled with calcium solution and the other with oxalate solution. They showed that the COM growth rate was influenced by secondary nucleation (*i.e.* creation of new and smaller crystals) at low seed crystal additions into the *in vitro* system, while at higher seed crystal densities growth-related aggregation occurred (*i.e.* fusion of newly formed and preexisting crystals into larger aggregates). Additionally, Kolbach-Mandel and collaborators studied the effect of inhibitors such as citrate, Mg^{2+} ion or osteopontin on COM crystallization at constant SS to broaden the understanding of kidney stone formation.

The Mixed Suspension Mixed Product Removal (MSMPR) crystallization is a continuous-flow technique that enables to estimate kinetics parameters of crystallization (*i.e.* nucleation and growth rates) based on crystal size distribution. The experimental setup (**Figure 23**) consists of a chamber containing a well-mixed crystal suspension. Two separate feed lines (filled with $CaCl_2$ and $Na_2C_2O_4$ solutions, respectively) deliver the chamber at equal flow rates with the CaOx crystal phase component, while the product is removed through an output line. Although it is largely accepted that MSMPR simulates crystallization processes occurring in the pelvis (i.e. in the urinary tracts below the kidney), numerous applications are noticeable such as the work of Garside and collaborators who reported on the effect of temperature on the precipitation of CaOx[93].Precipitation experiments were conducted in a MSMPR crystallizer over a large range of temperature (from 9°C up to 45°C) using aqueous $CaCl_2$ and $Na_2C_2O_4$ solutions with each CaOx hydrate being identified at specific temperature range. Later on, Bertherton and Rodgers studied the crystallization of CaOx in minimally diluted urine (92 %) using a MSMPR crystallizer combined with a Malvern particle sizer cell into the flow system[94]. Thereby it permitted direct, non-invasive crystal counting and sizing to account for CaOx thermodynamic and kinetic factors. They investigated the effects of exogenous sodium oxalate and temperature on CaOx nucleation and growth rate. While nucleation and growth rate were dependent on SS levels inside the crystallizer, the authors showed that COM formed at 58°C,

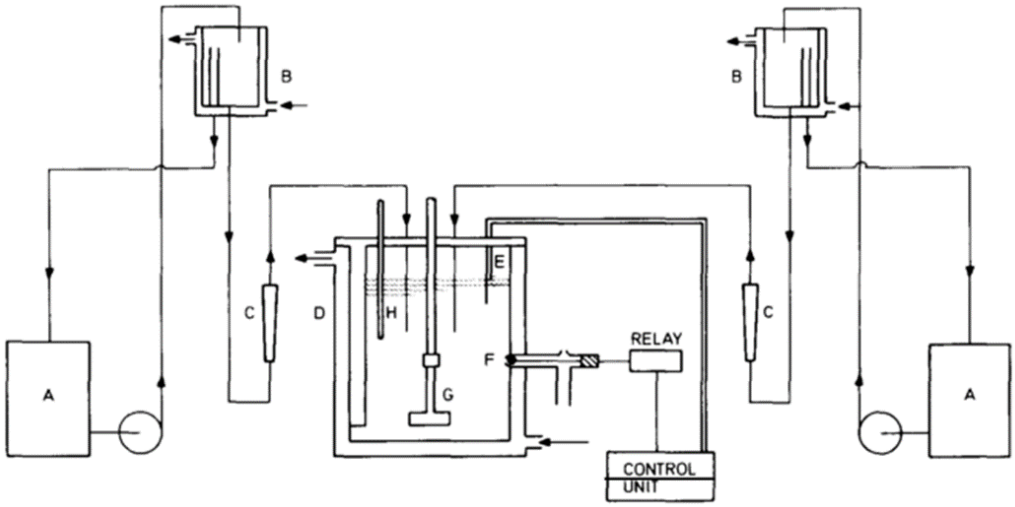

Figure 23. Illustration of a Mixed Suspension Mixed Product Removal (MSMRP) crystallizer from the work of Garside *et al.*[93]. The system consists of a thermostated bath (A), a constant level tank (B), a rotameter (C), the crystallizer (D), a level control (E), an outlet valve (F), a stirrer (G) and a thermometer (H). Figure is reproduced with permission from Elsevier.

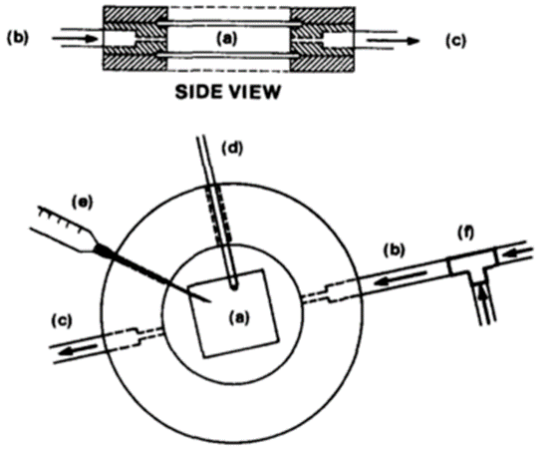

Figure 24. Schematic illustration of the isothermal growth cell from DeLong *et al.*[95]: setup consists of an observation chamber (a), the solution inlet (b) and outlet (c), a temperature monitor (d), a seed injection syringe (e) and a T-junction (f). Figure is reproduced with permission from Elsevier.

COD at 38°C and COT at 18°C in agreement with previously reported results[81,93].

In one last noteworthy contribution, DeLong and Briedis utilized an isothermal growth cell in a continuous-flow system to study the growth of COM under either MSMPR or CCM approaches[95] (**Figure 24**).The cell was equipped with a glass window allowing microscopic viewing (**Figure 24a**). Additionally, it enabled exact and direct means of measuring the linear growth rates of crystals at controlled temperature and solution SS. Growth rates of COM appeared to be constant at constant SS, showed little evidence of growth rate dispersion with

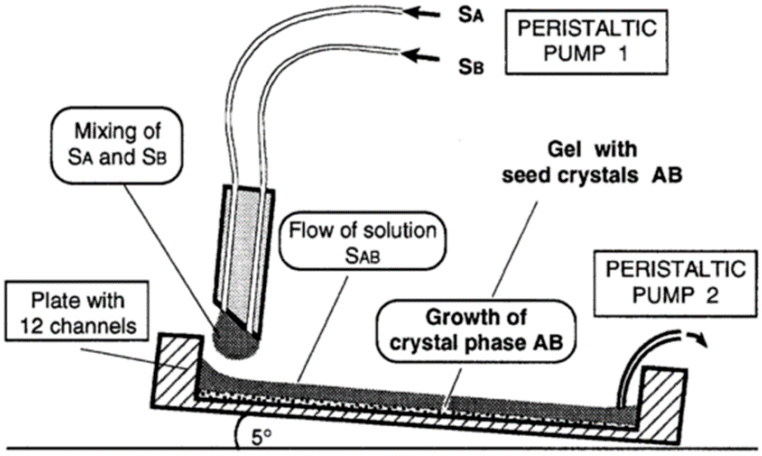

Figure 25. Illustration of the flow model of crystallization in gel (FMCG). Two feeding solutions, S_A and S_B, containing the soluble components A and B of a crystal phase AB, are mixed at a special mixing tip. The resulting supersaturated solution S_{AB} is conducted over a gel layer through a channel. Crystallization of AB proceeds in the gel matrix and can be observed or quantified by optical devices. Figure is reproduced from Achilles *et al.*[96] with permission from Springer.

to the conditions tested and indicated that growth kinetics of COM crystal obeyed surface-reaction kinetics.

Among all *in vitro* systems, Achilles described the Flow Model of Crystallization in Gels (FMCG) as the most relevant flow model for closely simulating intrarenal mechanisms of urolithiasis with respect to the fixed-particle theory[1,71,72,91]. In an earlier work, Achilles' research group utilized a FMCG system to investigate the crystal growth of COM crystals in a gel from a flow of supersaturated artificial urine[96] (**Figure 25**). Seed crystals of COM were generated within an agar-agar gel matrix, then feed solutions were conducted through channels (size: $70 \times 4 \times 12$ *mm*) over the surface at flow rate of 0.5 m*L.min*$^{-1}$ (mean urinary flow rate for one kidney) at nearly constant SS. The crystallization model was found to be relevant for investigating the effect of urinary parameters (*e.g.* drinking therapy or oxalate excretion) on CaOx stone formation under physiopathological conditions.

Other *in vitro* flow models appear significant for the study of stone formation likewise the use of a reverse osmosis hollow-fiber membrane connected to a flow system by Azoury and collaborators[97]. With the plug-flow system, they simulated the early stages of CaOx precipitation occurring in the distal convoluted tubule and the collecting system of the kidney. The experimental setup, fed at 0.5 or 1.5 *L.min*$^{-1}$ with $CaCl_2$ (1.75 *mmol.L*$^{-1}$) and $Na_2C_2O_4$ (0.14 *mmol.L*$^{-1}$), enabled water reabsorption and SS generation for residence time comparable to the one in urinary tract (*i.e.* approximately 3 min). Particle analysis showed the formation of 1500 particles.mL^{-1} (mean size of 5.1 *µm*) corresponding to CaOx dihydrate crystalline phase.

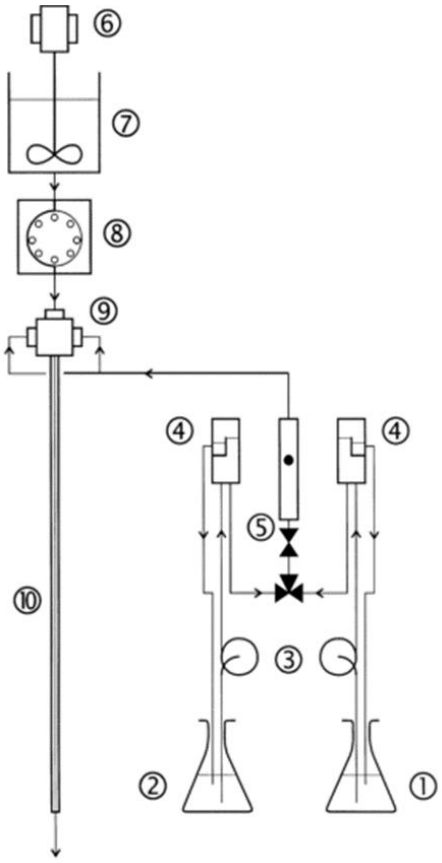

Figure 26. Schematic illustration of the Poiseuille-Flow Crystallizer (PFC): each individual part stands for the saturated solution reservoir (1), metastable solution reservoir (2), centrifugal pumps (3), head tanks (4), flow meter (5), overhead stirrer (6), seed reservoir (7), peristaltic pump (8), mixing adapter (9) and glass capillary (10), respectively. Figure is reproduced from Mumtaz and Hounslow[98] with permission from Elsevier.

Azoury's results suggested that the crystallization of COD played a role in stone formation in the renal tubules. In 2000, Mumtaz and Hounslow investigated the effect of hydrodynamics and solution composition on the aggregation of COM crystals using a Poiseuille Flow Crystallizer (PFC) made of a vertically oriented glass capillary associated with pumps and storage reservoirs[98] (**Figure 26**). The PFC was operated at steady state with pre-mixed feed particles and solution fed to the top and samples of the effluent were collected at the bottom. They successfully characterized the role of fluid shear rate on aggregation rate constants and predicted collision rates for further understanding of the aggregation mechanism during COM precipitation. With respect to the role of solution composition on aggregation, they found that the aggregation rate was independent of the calcium and oxalate ions ratio. In later contributions, the same research group presented a model of aggregation kinetics accounting for the fluid shear stress, polydisperse size and linear contact of colliding particles[99]. Afterwards, they implemented it within the PFC system[100] for further complexity with respect to COM aggregation mechanism[101].The same year, the precipitation kinetics of CaOx was studied using a continuous Draft Tube Baffled (DTB) precipitation reactor operated at different

residence times, feed concentrations and stirrer speeds[102]. The DBT reactor was made of a jacket glass reactor equipped with a polyethylene draft tube and four baffles. The contents were stirred using a three-blade marine-type propeller with motor pumping the suspension upward in the annulus and downward inside the draft tube. The feed tubes and withdrawal tube could be precisely positioned in the reactor to maintain accurate SS profile in the system. While a Coulter counter was used to determine particle size distribution, crystals could be withdrawn from reactor for morphology examination using light or electron microscopies. The results indicated that crystal growth rates were controlled by a surface-reaction mechanism with a second-order dependence on absolute SS (i.e. $\propto SS^2$). Additionally, the nucleation rates were dependent on the flow rate input and the feed point position suggesting a mixing-controlled nucleation process.

iii. The growth kinetics of calcium oxalate systems

For the development of suitable models for stone removal, knowledge on the dissolution kinetics of calcium oxalate hydrates could be worthwhile. To address the question, Tomazic and Nancollas carried out dissolution experiments of either COM or COT in a thermostated glass vessel at temperature from 15°C to 50°C[63]. A weighted amount of seed crystals in solution (NaCl or KCl) was stirred in the dissolution cell under nitrogen atmosphere. Then, the rate of reaction was monitored periodically by the analysis of both solid and solution phases. Tomazic and Nancollas concluded that the dissolution of COM and COT was diffusion controlled and dissolution rates were proportional to the undersaturations. Nancollas and Gardner studied the growth kinetics of COM crystals in supersaturated solutions[103]. Well-characterized seed crystals of CaOx were stirred into a thermostated conductivity cell filled with supersaturated solutions in calcium and oxalate under stoichiometric concentrations. The growth rate was monitored against time by calcium conductivity and modelled following the equation

$$-\frac{d[Ca^{2+}]}{dt} = k\,S\,([Ca^{2+}] - [Ca^{2+}]_0)^2 \quad (1.1)$$

(with $[Ca^{2+}]$ = ionic concentration of calcium ions at time t, $[Ca^{2+}]_0$ = ionic solubility under the experimental conditions, S = surface area of added seed crystals and k = observed rate constant for crystal growth). The quadratic dependency in the kinetic equation implied that crystal growth was controlled by a surface-limited reaction rather than diffusion-limited with ions incorporating into CaOx matrix from bulk solution. The authors evocated several plausible scenarii to depict the chemical reactions occurring at the crystal surface. If a monolayer of water was surrounding the crystal surface, growth would occur through simultaneous dehydration of pairs of calcium and oxalate growth sites due to ionic bulk concentrations.

Another hypothesis would rely on ionic adsorption on the crystal surface with partial or complete dehydration and subsequent surface diffusion to active growth sites. At low SS, the dislocation model for crystal growth as originally proposed (originally in vapor phase but thereafter extended to growth in solution) by Burton, Cabrera and Frank[104] could also be consistent with the kinetic equation given above.

Later on, Nielsen and Toft also reported on the growth kinetics in supersaturated solutions of COM crystals along with other binary electrolyte crystals[105]. They compared the electrolytes based on whether the growth rate $\frac{dr}{dt}$ was transport- or surface-controlled. In the case of transport-controlled kinetics, the growth rate would be limited by the combined convection and diffusion of ions within the crystal matrix. In the latter case, surface-controlled kinetics would be governed by the saturation ratio in electrolytes S around the growing crystal. Based on the relationship between $\frac{dr}{dt}$ and S, the rate law could be discriminated as linear, parabolic or exponential. Experimentally, chemical reactants were dissolved in distilled water, mixed together (at 25°C and 1.0 atm) and the course of the reaction followed throughout the experiment. As reported by Nancollas and Gardner, the results supported CaOx monohydrate to grow accordingly to surface-controlled kinetics, more specifically following a parabolic rate law,

$$\textit{i.e.}\ \frac{dr}{dt} \propto (S-1)^2 \quad (\mathbf{1.2})$$

at moderate SS. To describe the "cementing" process (*i.e.* transport of solute by diffusion followed by surface reaction of the two colliding particles) occurring during COM aggregation, Hounslow and collaborators developed a pore-diffusion reaction model[106]. The precipitation of COM crystals was conducted in metastable aqueous solutions using a batch precipitation system. While initial SS was maintained constant, COM seed crystals were added to the metastable solutions at varying $CaCl_2$ and $Na_2C_2O_4$ concentration ratios and the resulting suspension was analyzed with a particle size analyzer. The results concluded that the aggregation rate constant depended only on the "cementing" rate, which in turn depended on the solution composition.

For the development of a quantitative growth model, Ananth and collaborators studied the enlargement of the stone fragments to clinically significant size using a MSMPR crystallizer[107]. Three patients underwent surgical procedure to retrieve eight CaOx fragments of initial weights from 30 to 240 mg. Once suspended in the crystallizer, fragments were supplied with artificial urine from two feed solutions pumping in $Na_2C_2O_4$ (2.4 *mmol.L*$^{-1}$) and $CaCl_2$ (12 *mmol.L*$^{-1}$) solutions at 0.32 *mL.min*$^{-1}$. At intervals of 24 h and until they reached 500 *mg*, stones were

removed, dried and weighted. Throughout the experiment (> 12 weeks), weight was plotted against time to finally best fit a surface area-dependent growth model described as

$$w = k\,t^{3/2} + c \quad (1.3)$$

(with w = weight, k = growth rate constant, t = time, c = constant corresponding to the weight of the initial fragment) and illustrated by the green solid line in **Figure 27.**

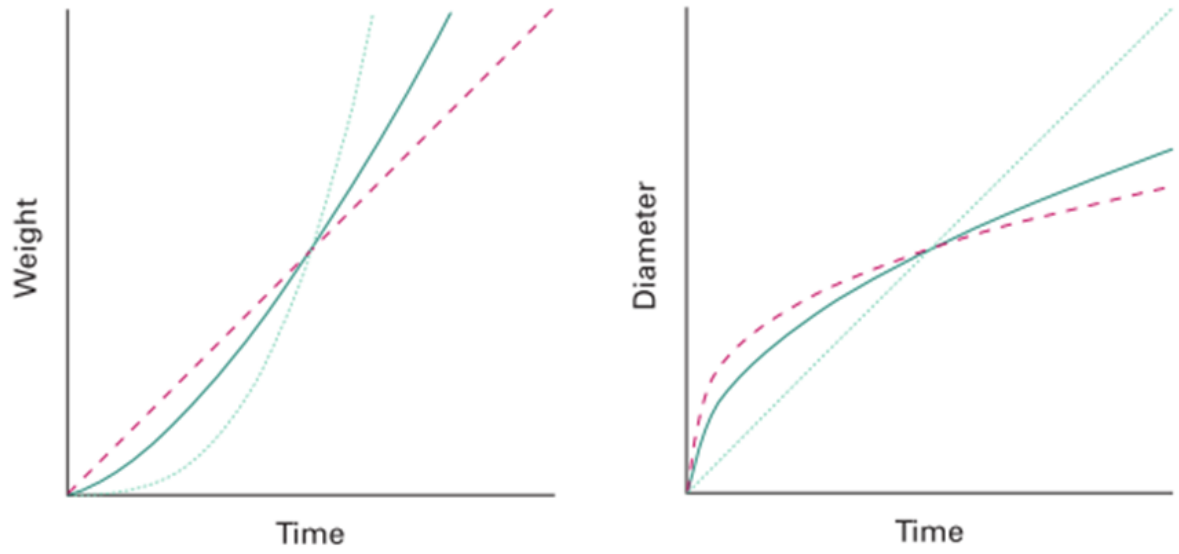

Figure 27. Illustration of the curve shapes of the three growth mechanisms investigated by Ananth *et al.*[107]. Weight (w) and extrapolated diameter (d) of a kidney stone are plotted against experiment time. Red dashed trace fits the crystal growth model of constant deposition ($w \propto t$, $d^3 \propto t$); green solid line, surface area-dependent ($a \propto t$, $d^2 \propto t$, $d \propto t^{1/2}$, $d^3 \propto t^{3/2}$, $w \propto t^{3/2}$); green dotted line, linear growth in diameter ($d \propto t$, $d^3 \propto t^3$, $w \propto t^3$). w = weight, t = time, d = diameter and a = surface area. For the purpose of illustration, the units are arbitrary and proportionality constants are chosen to make each curve pass through the central coordinate. Figure is reproduced with permission from John Wiley and Sons.

The growth rate of these fragments was suspected to be dependent on their surface area, but no clear and direct evidences supported this suggestion until Ananth and collaborators' contribution. Worth keeping in mind, the developed model could only be considered analogous to a stone growing in a calyx or pelvis of a kidney. Saw and Kavanagh conducted further investigations to study the influence of CaOx crystallization kinetics and variations of calcium and oxalate concentrations on *in vitro* stone using the same crystallizer system[108]. Fragments of calcium carbonate core material received continuous (yet at various flow rates) supply in calcium (6.0 $mmol.L^{-1}$) and oxalate (1.2 $mmol.L^{-1}$) solutions in artificial urine for 5 to 7 weeks and stone masses were plotted against the experiment duration. Stone growth rate was calculated based on the surface area-dependent model proposed by Ananth and collaborators[107]. The results supported the growth rate to be positively correlated to the number of crystals in suspension around the growing stone at the expense of growth of individual

crystals. The authors concluded with aggregation of crystals from surrounding suspension to be the dominant mechanism for stone enlargement.

Kassemi and collaborators developed an algorithm that coupled effects of transport- and surface-controlled kinetics at the surface of the crystal to depict CaOx growth model[109]. With surface-controlled reaction being dictated by the integration of ions in the kinks of CaOx crystal, they used the Damköhler dimensionless number, D_a = surface reaction kinetics/transport rate, and the solution SS as criteria to describe the growth rate of CaOx crystal. At low Da and low SS, surface concentrations in Ca and Ox approached their bulk concentrations in solution. It led to growth rate likely limited by the surface reaction kinetics. At high D_a and high SS, Ca and Ox surface concentrations shifted towards their equilibrium or saturation values and the growth rate tended to be limited by the transport through the medium. In any case, the authors observed that as the stone size increased, the reaction inevitably shifted towards a transport-limited growth.

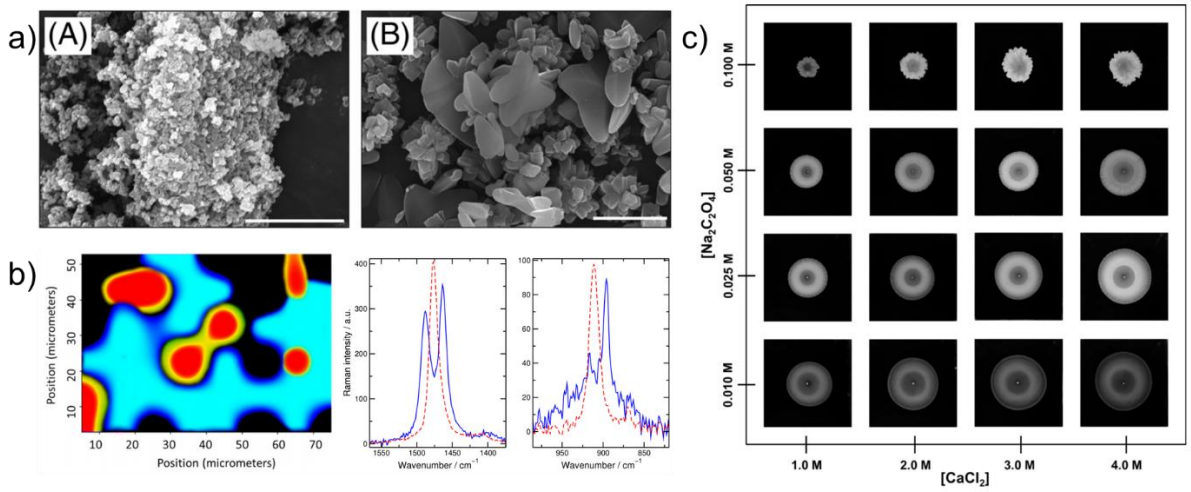

Figure 28. CaOx precipitation in presence of spatial gradients in Ca^{2+} and Ox^{2-} ions: a) SEM images of COM aggregates formed in a well-stirred crystallizer (left) and COD crystals formed in the flow-driven system (right). Scale bars represent 5.0 *µm*; b) characterization of the CaOx precipitation pattern using Raman spectroscopy to determine the spatial distribution (left) and spectral (right) of COM (blue) and COD (red) crystals; c) phase diagram showing the CaOx precipitate pattern. Figure 28a is reproduced from Bohner *et al.*[110] and Figure 28b-c are adapted from Bohner *et al.*[111] with permission from RSC and AIP, respectively.

The precipitation reaction of calcium oxalate was studied experimentally in the presence of spatial gradients by controlled flow of calcium into oxalate solution[110,111]. First, Bohner and collaborators assessed the formation of the thermodynamically unstable calcium oxalate dihydrate in presence of concentration gradients[110]. Briefly, $CaCl_2$ solution (4.00 $mol.L^{-1}$) was flowed into $Na_2C_2O_4$ solution (0.025 $mol.L^{-1}$, pH 9.0) at 20 $mL.h^{-1}$ and calcium oxalate dihydrate crystals were discriminated under rose- and butterfly-shaped crystals larger than 5.0 *µm* (B in **Figure 28a**). In contrary, the calcium oxalate crystals resulting from the dropwise addition of

calcium chloride solution into well-stirred sodium oxalate solution led to the formation of the thermodynamically stable crystalline phase, smaller than 1.0 *µm* and aggregated to form larger particles (A in **Figure 28a**). There, they concluded that in system characterized with fast kinetics (such as calcium oxalate system), the existence of spatial gradients could provide pathways in producing unstable chemical structures without any additional stabilizers. It was confirmed in a second study that detailed the calcium oxalate precipitate pattern formation by systematically varying parameters that affected the gravity current (*i.e.* fluid motion)[111]. The same research group showed that enhancing the gravity flow by either increasing the flow rate or the density difference between the reagent solutions (*i.e.* concentrations) could control the composition of the calcium oxalate product (**Figure 28b**) and the spatial spreading of precipitate pattern (**Figure 28c**).

In kidney stones, calcium oxalate (CaOx) crystals stand as the main inorganic mineral (> 70 %). Commonly found under CaOx monohydrate (COM) or CaOx dihydrate (COD) crystalline phase, they have been extensively studied in the literature with respect to their morphologies in kidney stones[50] and the physicochemical and urinary features affecting their occurrence among stone formers (*e.g.* urinary pH[82], excess in Ca^{2+} and/or Ox^{2-} ions[78], catechins[57] *etc*…). Currently, two theories exist to depict the series of events leading to kidney stone formation. Whether a stone grows freely into the tubular flowing-fluid of the nephron (the free-particle model) or grows attached onto the tubular walls (the fixed-particle theory)[1,71,72,74]. Furthermore, *in vitro* investigations have been conducted to build a model system accounting for the growth kinetics of CaOx crystals. In that context, noteworthy *in vitro* continuous-flow crystallizers have been utilized such as the Mixed Suspension Mixed Product Removal (MSMPR)[93] or the Flow Model of Crystallization in Gel (FMCG)[112]. These crystallizers aim at experimentally simulating CaOx crystal growth at physicochemical conditions similar to encountered in the kidney. Current growth models tend to support CaOx crystal growing based on a surface dependent kinetics, *i.e.* depending on the bulk concentrations in Ca^{2+} and Ox^{2-} ions surrounding the growing particle[107]. However, the transport-limited kinetics (*i.e.* reagents supplied rate to the growing particle) cannot be neglected with respect to CaOx crystal growth under continuous-flow[109].

3. The hydroxyapatite: a calcium phosphate mineral of interest

Kidney stone examination strongly suggests that stones originate in the nephron from the Randall's plaque, *i.e*. a hydroxyapatite deposit. Studies have been trying to explain the occurrence of Randall's plaque in the kidney along with its reactive role with respect to renal calculi. In the coming section, we will present the hydroxyapatite system in terms of the chemical structure and the strategies to obtain a biomimetic composite. Then, a review regarding the Randall's plaque characterization will be proposed. Finally, we will present relevant attempts to build up an *in vitro* model system of the Randall's plaque for the study of kidney stone formation.

a. The calcium phosphates in the field of biomineralization

i. Description of the calcium phosphate systems

Calcium phosphate (CaP) minerals are materials containing Ca^{2+} ions together with tetrahedral PO_4^{3-} ions to form various crystalline phases (**Table 5**) extensively studied in several fields of science. In food chemistry for example, calcium bioavailability from tricalcium phosphate (TCP) was investigated in case of a dairy-free diet[113]. Regarding biomineralization, the hydroxyapatite ($Ca_{10}(PO_4)_6(OH)_2$, HAp) has been also studied. HAp is a crystalline structure exhibiting mainly a hexagonal (**Figure 29a**) and occasionally a monoclinic (**Figure 29b**) symmetry (space groups $P6_3/m$ and $P2_1/b$, respectively)[114].

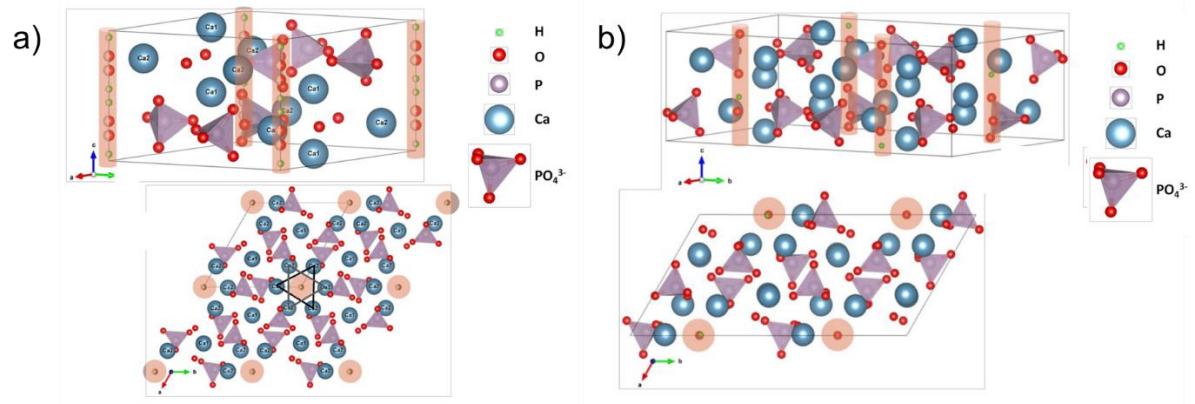

Figure 29. Representation of hydroxyapatite: hexagonal (a) and monoclinic (b) structures.

As the main mineral constituent in bones and teeth, HAp has been under scrutiny for tissue engineering[115] or dentistry[116]. Methodologies have been developed to obtain HAp under suitable structure and morphology for the fabrication of biomaterials. For instance, controlled crystallization was proposed to synthetize HAp powder either using calcium nitrate tetrahydrate

$Ca(NO_3)_2{\cdot}4H_2O$ and diammonium hydrogen phosphate $(NH_4)_2HPO_4$[117,118] or calcium dichloride $CaCl_2$, calcium nitrate $Ca(NO_3)_2$ and potassium dihydrogen phosphate KH_2PO_4[119]. The HAp powder would require post-processing to obtain the final material (*e.g.* pelletizing). On the other hand, HAp coating onto substrates was also prepared. Kokubo and collaborators firstly developed an acellular Simulated Body Fluid (SBF) solution matching the ion concentrations of the human blood plasma (**Table 6**) to carry out the formation of HAp onto bioactive glass-ceramic[120]. Thereafter, the protocol for the preparation of SBF was modified to a solution with ion concentrations 1.5 times those of SBF (1.5 SBF) in order to lower the induction period for the apatite nucleation on the substrate[121]. Although under constant modification, the use of SBF solution has remained one standard to prepare biomimetic apatite coating on substrate like titanium for surgical implant purpose[122]. However, some controversy still remains regarding the use of SBF solution to prepare HAp and test its bioactivity[123].

Table 5. Main calcium phosphate minerals.

Name		Formula	Ca/P ratio
Monocalcium phosphate	MCPM	$Ca(H_2PO_4)_2{\cdot}H_2O$	0.5
Monohydrate or Anhydrous	MCPA	$Ca(H_2PO_4)_2$	0.5
Monetite	DCP	$CaHPO_4$	1
Brushite	DCPD	$CaHPO_4{\cdot}2H_2O$	1
Octacalcium phosphate	OCP	$Ca_8H_2(PO_4)_6{\cdot}5H_2O$	1.33
Tricalcium phosphate	TCP	$Ca_3(PO_4)_2$	1.5
Hydroxyapatite	HAp	$Ca_{10}(PO_4)_6(OH)_2$	1.67
Tetracalcium phosphate	TTCP	$Ca_4(PO_4)_2O$	2

Table 6. Ion composition and associated concentrations of blood plasma, Simulated Body Fluid (SBF) and 1.5 SBF solutions (*mmol.L*$^{-1}$).

Ions	Na^+	K^+	Mg^{2+}	Ca^{2+}	Cl^-	HCO_3^-	HPO_4^{2-}	SO_4^{2-}
Blood plasma	142.0	5.0	1.5	2.5	103.0	27.0	1.0	0.5
SBF	142.0	5.0	1.5	2.5	147.8	4.2	1.0	0.5
1.5 SBF	213.0	7.5	2.3	3.8	221.7	6.3	1.5	0.8

ii.The hydroxyapatite: the second most abundant phase in kidney stones

Over the past decades, CaP minerals have stood for the second most recurrent species in kidney stones after CaOx crystals[36] as illustrated in **Table 1** section **1.c.i** (13.8 %). In France, in-depth characterization showed that CaP was present under carbonated apatite (11.4 %), brushite (1.8 %), octacalcium phosphate (0.3 %), amorphous CaP (0.2 %) and whitlockite ($Ca_9(Mg,Fe)(PO_4)_6(PO_3OH)$, 0.1 %). With a specific interest in carbonated apatite, this crystalline phase stood for the non-stoichiometric HAp (Ca/P ratio ≠ 1.67) and was substituted with carbonate (CO_3^{2-}) groups among other substituents (**Figure 30**). In a way similar to what was done for CaOx kidney stones, Daudon *et al.* listed the type of carbonated apatite-based kidney stones with a focus on the disease conditions[50] (**Table 7)**. Interestingly, the presence of an apatitic deposit on CaOx-based stones was often noted[124] and was addressed as the Randall's plaque.

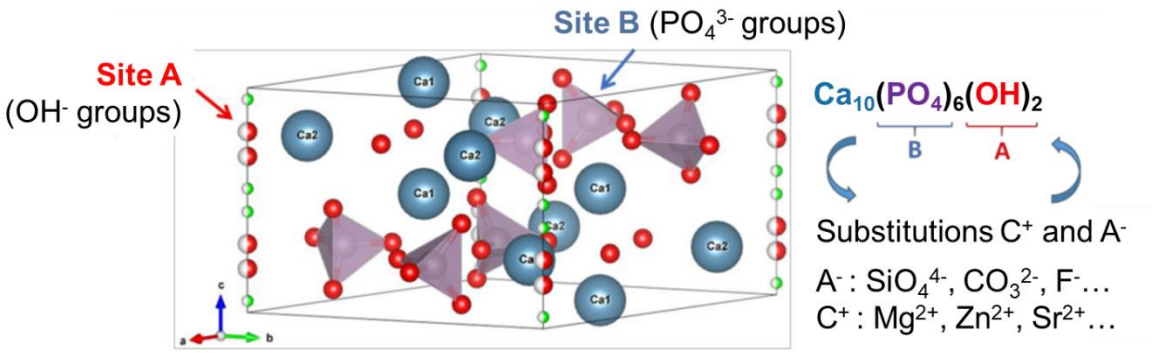

Figure 30. Cationic and anionic substitutions for stoichiometric hydroxyapatite (hexagonal structure).

Table 7. Relationship between morphologies, composition of CaP stones and renal conditions. Table adapted from the book "Lithiase Urinaire" by Daudon *et al.*[50] with permission from Lavoisier – Médecine sciences.

Type of morphology	Description of the surface	Usual composition	Common causes
IVa1	Homogeneous, crystalline, rough or subtly uneven, whitish to beige	carbonated apatite ± struvite ($NH_4MgPO_4.6H_2O$)	Urinary tract infection
IVa2	Homogeneous, crystalline, glazed, roughness, brownish-yellowish	carbonated apatite	Tubular acidosis - Cacchi-Ricci disease
IVb	Heterogeneous, rough with porosity, microcrystalline deposit, whitish to brownish-yellowish	carbonated apatite ± struvite	Urinary tract infection due to urease germs – Primary hyperparathyroidism
IVc	Homogeneous, crystalline, blunt edges, whitish	struvite	Urinary tract infection due to urease germs
IVd	Homogeneous, subtly rough, lightly translucent, cream to silk-colored	brushite	Primary hyperparathyroidism – hypercalciuria - diabetes
Ia + IIa + IVa	-	whewellite + weddellite + carbonated apatite	Intermittent hyperoxaluria + hypercalciuria – Cacchi-Ricci disease + hypercalciuria
IIa + IVa	-	weddelite + carbonated apatite	Hypercalciuria – hyperparathyroidism
Ia + IVa	-	whewellite + carbonated apatite	Cacchi-Ricci disease – intermittent hyperoxaluria + urinary tract infection

b. The Randall's plaque

i. The formation of the Randall's plaque

In 1937, Alexander Randall conducted the post-mortem examination of 429 pairs of kidneys and correlated the presence of kidney stones with the deposition of a CaP plaque on the renal papilla due to prior cellular lesions[125]. Nowadays known as the Randall's plaque (RP), chemical analysis showed that it was made of hydroxyapatite[126] or carbonated hydroxyapatite[127].

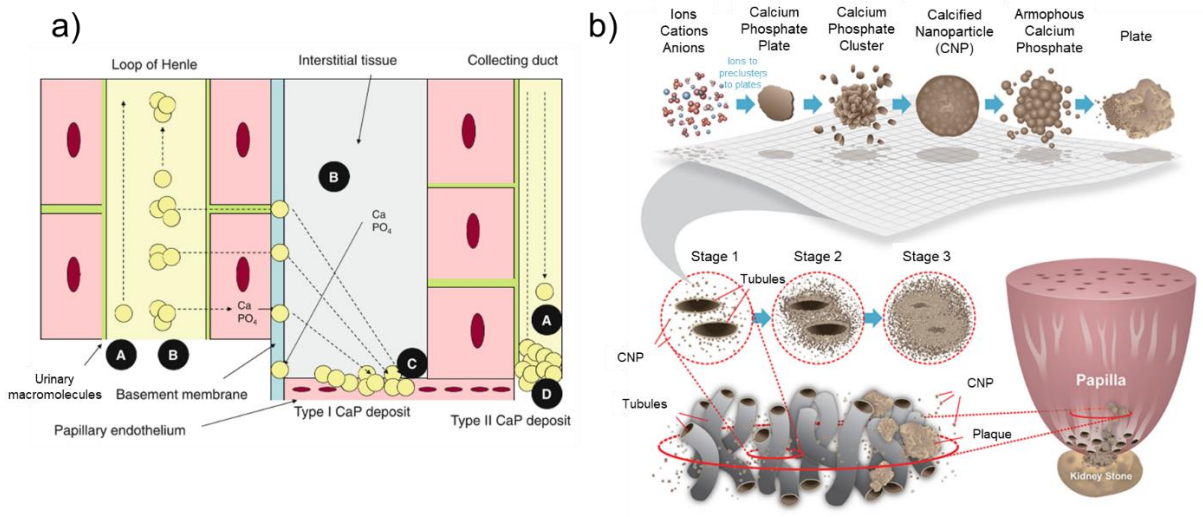

Figure 31. Schematic illustration depicting the formation of the Randall's plaque: a) Possible mechanisms either at the basement of the loop of Henle (Type I deposit) or in the duct of Bellini (Type II deposits) from Tiselius[128]; b) progression of the Randall's plaque in the distal renal papilla from Sherer *et al.*[129]. Top row, ions coalesce to form pre-clusters and calcified nanoparticles that agglomerate into higher ordered calcium phosphate phases (*e.g.* amorphous CaP) and eventually form full developed RP. Bottom row, the progression of interstitial mineral deposit is illustrated schematically (stage 1) to agglomerates surrounding tubules (stage 2) to advanced RP (stage 3) that emerge from the papillary tip. Figures reproduced with permission from Springer and Elsevier, respectively.

Furthermore, RP was either located at the basement membranes of the thin loops of Henle[126] as scattered apatite (Type I deposits) or in the ducts of Bellini as tubular plugs[127] (Type II deposits). Tiselius proposed a model to account for the formation of Type I and Type II deposits[128] (**Figure 31a**). In case of Type I deposits, CaP would be internalized in cells and dissolved for the release of calcium and phosphate ions. Afterwards, these ions would be excreted in the interstitial tissue to recrystallize at sufficient supersaturation with CaP. Kuo and collaborators hypothesized on the driving forces leading to Type I deposits[130]. They suggested that the excretion of low urine volume, important calcium concentration and decreased pH raised higher coverage among stone formers compared to control subjects. Regarding Type II deposits, CaP particles that avoided internalization in the loop of Henle would form agglomerates large enough to be trapped in the narrow opening of the duct of Bellini (*i.e.* the most distal part of the collecting duct in **Figure 33a**).

Recently, Sherer and collaborators carried out a correlative microscopy study to describe the progressive formation of RP[129]. As shown in **Figure 31b**, the results concluded with the pre-formation of interstitial calcified nanoparticles of CaP agglomerating into higher ordered aggregates that could eventually spread to dense interstitial RP near the tip of the papilla. Further morphological characterization enabled to discriminate RP as spheroidal units of 1.0 to 5.0 *μm* diameter (*i.e.* spherulites) closely associated with collagen fibers and membrane vesicles[131] (**Figure 32a**), glycosaminoglycans[132] or even osteopontin and Tamm-Horsfall protein[133]. Additionally, X-ray micro-diffraction (*μ*XRD) analysis on human RP showed a

relatively sharp (002) diffraction peak at $2\theta = 26°$ and a broader peak between $30° < 2\theta < 35°$ enabling to conclude that RP was made of crystalline HAp nanoparticles[134] (**Figure 32b**).

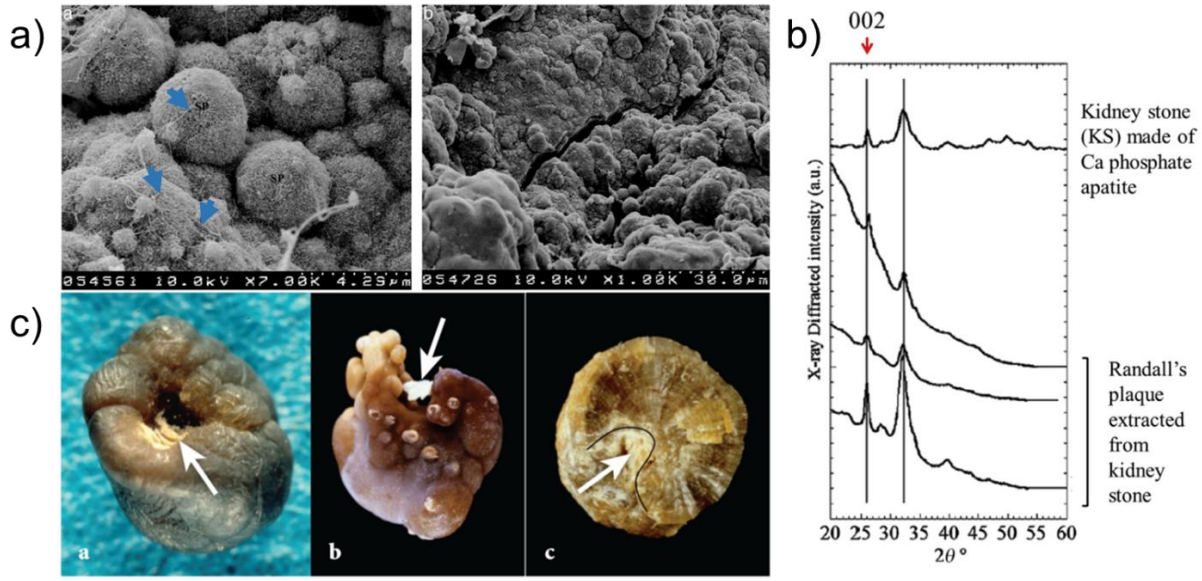

Figure 32. Characterization of the Randall's plaque: a) Scanning electron microscopy images of (left) RP spherulites with fibers embedded inside (blue arrow) and (right) surface of internal layer of fused spherulites from Khan *et al.*[131]; b) XRD patterns of extracted RP and kidney stone from Rouzière *et al.*[134]; c) Whewellite (COM) stones with a Randall's plaque (white arrows) from Daudon *et al.*[124]. Figures reproduced with permission from Elsevier and AIP, respectively.

ii.A growing site for calcium oxalate stones

CaOx renal stones often exhibit a RP umbilication[124] (**Figure 32c**) that strongly suggests a supporting role as nidus for CaOx stone formation. With this aim in mind, Evan and collaborators suggested a sequence of events leading to formation of human CaOx stones on RP[133]. The loss of papillary epithelial integrity exposes RP to urine proteins (*e.g.* osteopontin and Tamm-Horsfall protein). These proteins, having affinity for apatite crystals, cover the plaque to form a new hybrid matrix. Driven by urine supersaturation for CaP species, amorphous apatite crystals form within the matrix layer onto which additional urine proteins continue to adsorb. Bursts of crystallization and coating periodically repeat over the tissue plaque to the point that crystallization overcomes the moderating effect of urine proteins towards the final formation of CaOx stones. Afterwards, further investigations enabled to detail the interface area between the RP and CaOx stones[135,136]. Scanning electron microscopy depicted the organization at the mesoscopic scale of CaOx crystals entrapped in the carbonated apatite spherulites of RP[135] (**Figure 33b**). Extensive examinations demonstrated that COM crystalline phase on RP was associated with hyperoxaluria while COD crystalline phase on RP was correlated to hypercalcuria[136].

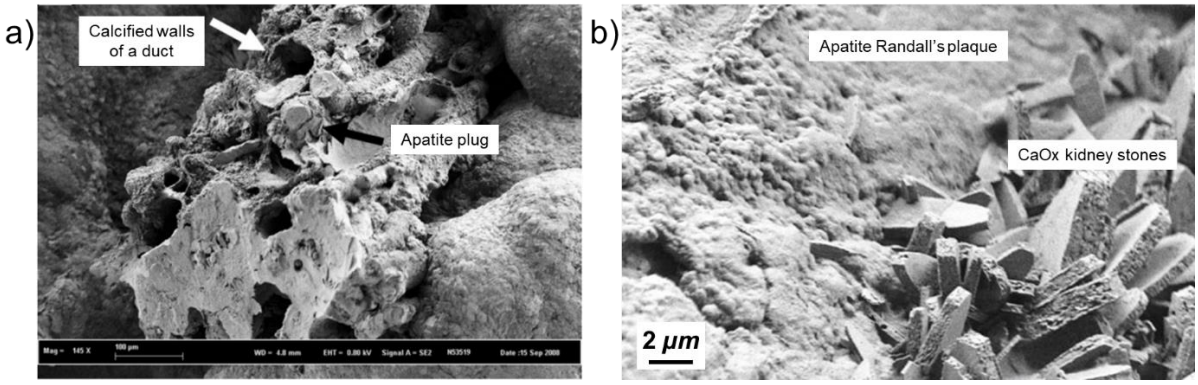

Figure 33. Scanning electron microscopy images of a) Randall's plaque made of a mixing of tubules with calcified walls and of tubules obstructed by calcium phosphate plugs[127] and b) interface area between Randall's plaque and CaOx stones[135]. Figures reproduced with permission from Springer and ACS, respectively.

Although recent advances have been achieved, unanswered questions still remain like what environmental factors may disturb the urine composition to promote Randall's plaque formation or what physicochemical mechanisms underlie CaOx crystallization on the plaque[137]? Thereby, *in vitro* models would be of great interest to understand the multiscale interactions between the Randall's plaque and CaOx kidney stones.

iii. *In vitro* approach of the Randall's plaque

Few models in bulk exist regarding *in vitro* approach of the Randall's plaque. In the early 90's, Achilles and collaborators generated CaP spherulites in a FMCG system (**Figure 25** in section **2.c.ii**) to induce thereafter the growth of CaOx crystals[138]. In agar-agar gel matrix, CaP spherulites had a size up to 200 *µm* in diameter and were organized in a microcrystalline core surrounded by a radially oriented sheet-like shell (**Figure 34a-c**). Later contribution discriminated the core as carbonated apatite while the shell consisted of octacalcium phosphate (OCP)[112]. The passage of a supersaturated solution in calcium oxalate induced the heterogeneous growth of CaOx crystals predominantly around the CaP spherulites (**Figure 34d-f**). Morphological examination demonstrated the growth of monoclinic prismatic COM crystals directly out of the sheet-like shell (**Figure 34f**). Albeit uneasy to confirm, this observation raised the possible transition phase from CaP phase to CaOx phase and emphasized with the reactive role of CaP in the genesis of CaOx formation.

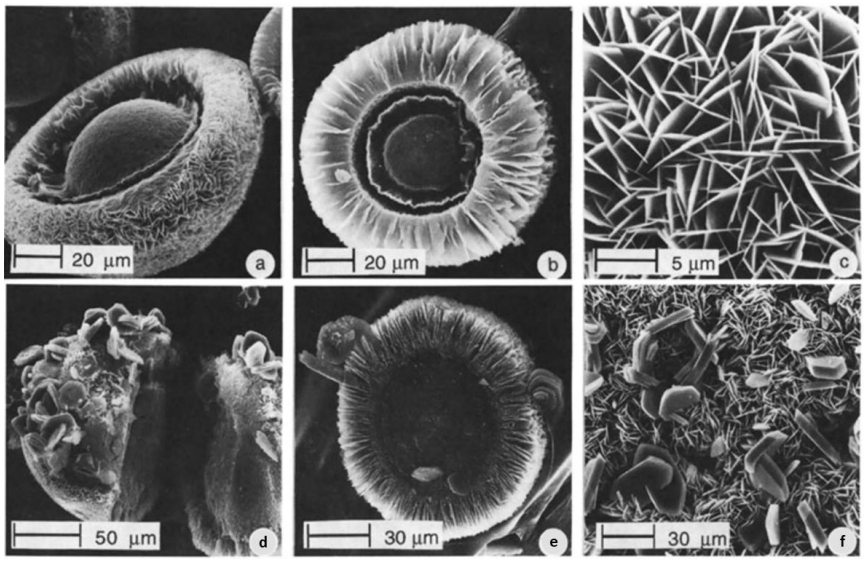

Figure 34. SEM images of CaP spherulites generated using a FMCG system: images from a-c) stand for a mushroom-like whole spherulite with microcrystalline core and incomplete grown shell (a), fractured spherulite showing the radially oriented sheet-like shell (b) and detailed sheet-like shell (c); images from d-f) represent CaP spherulites overgrown with CaOx crystals. Figure is adapted from Achilles *et al.*[138] with permission from Springer.

Amos and collaborators reported on the formation of multi-laminated CaP spherules via a Polymer-Induced Liquid-Precursor (PILP) process similar to the structure of Randall's plaque[139]. A solution of $NaH_2PO_4.H_2O$ (12 $mmol.L^{-1}$) was slowly added dropwise into an equal volume of $Ca(CH_3COO)_2.H_2O$ solution (12 $mmol.L^{-1}$). Prior to the addition, different amount of poly-L-aspartic acid additives were added to the Ca^{2+} containing solution. The synthesis is promoted the precipitation of liquid-like amorphous CaP in presence of additives for the formation of globules that later crystallized into spherulites. During crystallization, additives along with water were excluded from the material with yet some polymer becoming entrapped within it. X-ray diffraction analysis demonstrated that an increasing amount of polymer directed the crystallization of OCP with respect to HAp (**Figure 35a**) and influenced the final morphology of the spherulites (**Figure 35b**). Based on the similar structure of the multi-lamellar spherulites compared to RP, authors suggested that *in vivo* formation of the plaque occurred via a PILP route. They argued that various anionic proteins in the urinary environment (*e.g.* osteopontin) might associate with CaP to form the plaque. Although they did not carry out the overgrowth of CaOx crystals onto the spherulites, they remained confident with the supportive role of the material to induce CaOx heterogeneous crystallization. In a later contribution, the same research group improved the model system by integrating an organic matrix (*i.e.* Matrigel™) in order to mimic the tissue environment of the kidney[140]. Using the PILP process, they

succeeded to mineralize the tissue matrix with CaP spherulites to, *in fine*, induce the overgrowth of CaOx crystals.

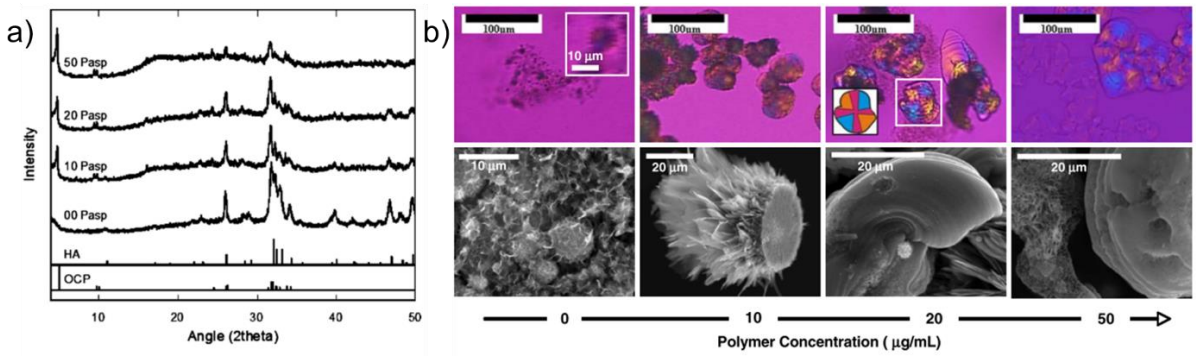

Figure 35. Influence of increasing amount of poly-L-aspartic acid on CaP crystalline phase (a) and spherules morphology (b). Figure is adapted from Amos *et al.*[139] with permission from Springer.

The Randall's plaque, a hydroxyapatite (HAp) deposit at the loop of Henle or plug in the duct of Bellini, seems to act as a growing site for CaOx crystals. Its formation would be in final response of an excretion of low urine volume, important calcium concentration and decreased pH along with cellular internalization towards HAp entrapment[130]. As the second most abundant mineral phase in kidney stones, HAp has drawn attention among the community. In a recent contribution, Sherer and collaborators attempted to propose experimental evidences of the cascade of events towards the Randall's plaque formation[129]. On the other hand, few models in bulk exist regarding *in vitro* approach of the Randall's plaque with the most noticeable one being the utilization of Flow Model of Crystallization in Gel (FMCG) crystallizer by Achilles and collaborators[96,138]. In-depth knowledge about this biomineral would provide with valuable insights with respect to kidney stone formation.

4. Conclusion

With the prevalence of kidney stone disease increasing worldwide, it is of prime importance to well understand the stone composition, the factors affecting the crystalline phases and morphologies, and the cascade of events leading to urolithiasis. Thereby, we reviewed the current state-of-the-art regarding research on kidney stone disease. CaOx crystals being the predominant species in renal calculi, extensive *in vitro* studies have been conducted regarding the crystallization and growth kinetics akin to conditions found in the kidney. For instance, investigations involving MSMPR (section **2.c.ii**) system tended to support that CaOx crystal growth obeyed a surface-reaction kinetics. Therefore, the incorporation process into the CaOx matrix from the bulk solution would only depend on the supersaturation state in ionic species at the crystal surface. On the other hand, FMCG (section **2.c.ii**) system provided with insightful information regarding the growth of CaOx crystals at the interface of an organic or inorganic

supporting matrix. Albeit operating under continuous-flow, *in vitro* crystallizers such as MSMPR and FMCG systems lack to take into account the microscale environment and associated micro-flow encountered in the micro-tubular structures of the nephron. To address this issue, a microfluidic strategy (supported by the nephron-on-a-chip technology) appears as a promising approach. Current fabrication techniques alongside experimental setup enable to simulate the renal function for specific *in vitro* investigations. With that in mind, we propose to explore the crystallization of CaOx microcalcifications under continuous-flow in a microfluidic platform. At microscale similar to tubules in the nephron, such device allows to investigate features like the influence of hydrodynamics on crystal growth, phase and morphology, the screening of molecules of interest regarding modulation effect on crystallization, the role of a supporting matrix with respect to the CaOx formation and even the growth of CaOx crystals on deposits such HAp. As a result, we hope to contribute towards an in-depth understanding of *in vitro* CaOx crystallization. In collaboration with physicians, it would provide with further and valuable clues for kidney stone formation.

References

(1) Robertson, W. G. Kidney models of calcium oxalate stone formation. *Nephron. Physiology* **2004,** *98* (2), p21.

(2) Moreau, W. M. *Semiconductor lithography : principles, practices, and materials*; New York : Plenum Press, 1988.

(3) Mazurek, J. *Making microchips: policy, globalization, and economic restructuring in the semiconductor industry*; Mit Press, 1998.

(4) Qin, D.; Xia, Y.; Whitesides, G. M. Soft lithography for micro- and nanoscale patterning. *Nature Protocols* **2010,** *5*, 491.

(5) Kumar, A.; Whitesides, G. M. Features of gold having micrometer to centimeter dimensions can be formed through a combination of stamping with an elastomeric stamp and an alkanethiol ‘‘ink’’ followed by chemical etching. *Applied Physics Letters* **1993,** *63* (14), 2002.

(6) Zhao, X.-M.; Xia, Y.; Whitesides, G. M. Fabrication of three-dimensional micro-structures: Microtransfer molding. *Adv Mater* **1996,** *8* (10), 837.

(7) Kim, E.; Xia, Y.; Whitesides, G. M. Polymer microstructures formed by moulding in capillaries. *Nature* **1995,** *376* (6541), 581.

(8) King, E.; Xia, Y.; Zhao, X.-M.; Whitesides, G. M. Solvent-assisted microcontact molding: A convenient method for fabricating three-dimensional structures on surfaces of polymers. *Adv Mater* **1997,** *9* (8), 651.

(9) Xia, Y.; McClelland, J. J.; Gupta, R.; Qin, D.; Zhao, X.-M.; Sohn, L. L.; Celotta, R. J.; Whitesides, G. M. Replica molding using polymeric materials: A practical step toward nanomanufacturing. *Adv Mater* **1997,** *9* (2), 147.

(10) McDonald, J. C.; Duffy, D. C.; Anderson, J. R.; Chiu, D. T.; Wu, H.; Schueller, O. J. A.; Whitesides, G. M. Fabrication of microfluidic systems in poly(dimethylsiloxane). *Electrophoresis* **2000,** *21* (1), 27.

(11) Johnston, I. D.; McCluskey, D. K.; Tan, C. K. L.; Tracey, M. C. Mechanical characterization of bulk Sylgard 184 for microfluidics and microengineering. *Journal of Micromechanics and Microengineering* **2014,** *24* (3), 035017.

(12) Zahid, A.; Dai, B.; Hong, R.; Zhang, D. Optical properties study of silicone polymer PDMS substrate surfaces modified by plasma treatment. *Materials Research Express* **2017,** *4* (10), 105301.

(13) Potkay, J. A. The promise of microfluidic artificial lungs. *Lab Chip* **2014,** *14* (21), 4122.

(14) Lee, P. J.; Hung, P. J.; Lee, L. P. An artificial liver sinusoid with a microfluidic endothelial-like barrier for primary hepatocyte culture. *Biotechnology and Bioengineering* **2007,** *97* (5), 1340.

(15) Bhattacharya, S.; Datta, A.; Berg, J. M.; Gangopadhyay, S. Studies on surface wettability of poly(dimethyl) siloxane (PDMS) and glass under oxygen-plasma treatment and correlation with bond strength. *Journal of Microelectromechanical Systems* **2005,** *14* (3), 590.

(16) Rasponi, M.; Piraino, F.; Sadr, N.; Laganà, M.; Redaelli, A.; Moretti, M. Reliable magnetic reversible assembly of complex microfluidic devices: fabrication, characterization, and biological validation. *Microfluidics and Nanofluidics* **2011,** *10* (5), 1097.

(17) Li, J.; Zhang, M.; Wang, L.; Li, W.; Sheng, P.; Wen, W. Design and fabrication of microfluidic mixer from carbonyl iron–PDMS composite membrane. *Microfluidics and Nanofluidics* **2011,** *10* (4), 919.

(18) Natalia, H.; Felipe, O.-A.; Pablo, L.; Simón, G.; Valérie, C.; Ali, A.-H.; Marcelo, J. K. Flow Chemistry to Control the Synthesis of Nano and Microparticles for Biomedical Applications. *Current Topics in Medicinal Chemistry* **2014,** *14* (5), 676.

(19) Sounart, T. L.; Safier, P. A.; Voigt, J. A.; Hoyt, J.; Tallant, D. R.; Matzke, C. M.; Michalske, T. A. Spatially-resolved analysis of nanoparticle nucleation and growth in a microfluidic reactor. *Lab Chip* **2007,** *7* (7), 908.

(20) Goyal, S.; Thorson, M. R.; Zhang, G. G. Z.; Gong, Y.; Kenis, P. J. A. Microfluidic Approach to Cocrystal Screening of Pharmaceutical Parent Compounds. *Crystal Growth & Design* **2012,** *12* (12), 6023.

(21) Thorson, M. R.; Goyal, S.; Schudel, B. R.; Zukoski, C. F.; Zhang, G. G. Z.; Gong, Y.; Kenis, P. J. A. A microfluidic platform for pharmaceutical salt screening. *Lab Chip* **2011,** *11* (22), 3829.

(22) Dertinger, S. K. W.; Chiu, D. T.; Jeon, N. L.; Whitesides, G. M. Generation of Gradients Having Complex Shapes Using Microfluidic Networks. *Analytical Chemistry* **2001,** *73* (6), 1240.

(23) Atencia, J.; Morrow, J.; Locascio, L. E. The microfluidic palette: A diffusive gradient generator with spatio-temporal control. *Lab Chip* **2009,** *9* (18), 2707.

(24) Mehling, M.; Tay, S. Microfluidic cell culture. *Current Opinion in Biotechnology* **2014,** *25*, 95.

(25) van Duinen, V.; Trietsch, S. J.; Joore, J.; Vulto, P.; Hankemeier, T. Microfluidic 3D cell culture: from tools to tissue models. *Current Opinion in Biotechnology* **2015,** *35*, 118.

(26) Huh, D.; Hamilton, G. A.; Ingber, D. E. From 3D cell culture to organs-on-chips. *Trends in Cell Biology* **2011,** *21* (12), 745.

(27) Baudoin, R.; Griscom, L.; Monge, M.; Legallais, C.; Leclerc, E. Development of a Renal Microchip for In Vitro Distal Tubule Models. *Biotechnology Progress* **2007,** *23* (5), 1245.

(28) Essig, M.; Terzi, F.; Burtin, M.; Friedlander, G. Mechanical strains induced by tubular flow affect the phenotype of proximal tubular cells. *American Journal of Physiology-Renal Physiology* **2001,** *281* (4), F751.

(29) Weinberg, E.; Kaazempur-Mofrad, M. R.; Borenstein, J. Concept and computational design for a bioartificial nephron-on-a-chip. *The International Journal of Artificial Organs* **2008,** *31* (6), 508.

(30) Jang, K.-J.; Suh, K.-Y. A multi-layer microfluidic device for efficient culture and analysis of renal tubular cells. *Lab Chip* **2010,** *10* (1), 36.

(31) Gao, X.; Tanaka, Y.; Sugii, Y.; Mawatari, K.; Kitamori, T. Basic structure and cell culture condition of a bioartificial renal tubule on chip towards a cell-based separation microdevice. *Anal. Sci.* **2011,** *27* (9), 907.

(32) Jang, K.-J.; Mehr, A. P.; Hamilton, G. A.; McPartlin, L. A.; Chung, S.; Suh, K.-Y.; Ingber, D. E. Human kidney proximal tubule-on-a-chip for drug transport and nephrotoxicity assessment. *Integrative Biology* **2013,** *5* (9), 1119.

(33) Ng, C. P.; Zhuang, Y.; Lin, A. W. H.; Teo, J. C. M. A Fibrin-Based Tissue-Engineered Renal Proximal Tubule for Bioartificial Kidney Devices: Development, Characterization and In Vitro Transport Study. *International Journal of Tissue Engineering* **2013,** *2013*, 10.

(34) Homan, K. A.; Kolesky, D. B.; Skylar-Scott, M. A.; Herrmann, J.; Obuobi, H.; Moisan, A.; Lewis, J. A. Bioprinting of 3D Convoluted Renal Proximal Tubules on Perfusable Chips. *Scientific Reports* **2016,** *6*, 34845.

(35) Romero, V.; Akpinar, H.; Assimos, D. G. Kidney Stones: A Global Picture of Prevalence, Incidence, and Associated Risk Factors. *Reviews in Urology* **2010,** *12* (2-3), e86.

(36) Daudon, M. [Epidemiology of nephrolithiasis in France]. *Ann Urol (Paris)* **2005,** *39* (6), 209.

(37) Siener, R. Impact of dietary habits on stone incidence. *Urological Research* **2006,** *34* (2), 131.

(38) Asselman, M.; Verkoelen, C. F. Fructose intake as a risk factor for kidney stone disease. *Kidney international* **2008,** *73* (2), 139.

(39) Taylor, E. N.; Fung, T. T.; Curhan, G. C. DASH-style diet associates with reduced risk for kidney stones. *Journal of the American Society of Nephrology : JASN* **2009,** *20* (10), 2253.

(40) Raheem, O. A.; Khandwala, Y. S.; Sur, R. L.; Ghani, K. R.; Denstedt, J. D. Burden of Urolithiasis: Trends in Prevalence, Treatments, and Costs. *European Urology Focus* **2017,** *3* (1), 18.

(41) Mitchell, M. A.; Wartinger, D. D. Validation of a Functional Pyelocalyceal Renal Model for the Evaluation of Renal Calculi Passage While Riding a Roller Coaster. *The Journal of the American Osteopathic Association* **2016,** *116* (10), 647.

(42) Scales, C. D.; Smith, A. C.; Hanley, J. M.; Saigal, C. S. Prevalence of Kidney Stones in the United States. *European Urology* **2012,** *62* (1), 160.

(43) Wei, Z.; Amponsah, P. K.; Al-Shatti, M.; Nie, Z.; Bandyopadhyay, B. C. Engineering of polarized tubular structures in a microfluidic device to study calcium phosphate stone formation. *Lab Chip* **2012,** *12* (20), 4037.

(44) Laffite, G.; Leroy, C.; Bonhomme, C.; Bonhomme-Coury, L.; Letavernier, E.; Daudon, M.; Frochot, V.; Haymann, J. P.; Rouziere, S.; Lucas, I. T.et al. Calcium oxalate precipitation by diffusion using laminar microfluidics: toward a biomimetic model of pathological microcalcifications. *Lab Chip* **2016,** *16* (7), 1157.

(45) Guo, S.; Ward, M. D.; Wesson, J. A. Direct Visualization of Calcium Oxalate Monohydrate Crystallization and Dissolution with Atomic Force Microscopy and the Role of Polymeric Additives. *Langmuir* **2002,** *18* (11), 4284.

(46) Thongboonkerd, V.; Semangoen, T.; Chutipongtanate, S. Factors determining types and morphologies of calcium oxalate crystals: Molar concentrations, buffering, pH, stirring and temperature. *Clinica Chimica Acta* **2006,** *367* (1–2), 120.

(47) Millan, A. Crystal Growth Shape of Whewellite Polymorphs: Influence of Structure Distortions on Crystal Shape. *Crystal Growth & Design* **2001,** *1* (3), 245.

(48) Tornos, C.; Silva, E.; El-Naggar, A.; Pritzker, K. Calcium oxalate crystals in breast biopsies. *Am J Surg Pathol* **1990,** *14* (10), 961.

(49) Arvaniti, E. C.; Lioliou, M. G.; Paraskeva, C. A.; Payatakes, A. C.; Østvold, T.; Koutsoukos, P. G. Calcium oxalate crystallization on concrete heterogeneities. *Chemical Engineering Research and Design* **2010,** *88* (11), 1455.

(50) Daudon, M.; Jungers, P.; Traxer, O. *Lithiase urinaire*; Lavoisier, Médecine Sciences publications, 2012.

(51) Franceschi, V. R.; Nakata, P. A. Calcium oxalate in plants: formation and function. *Annu. Rev. Plant Biol.* **2005,** *56*, 41.

(52) Arnott, H.; Pautard, F.; Steinfink, H. Structure of calcium oxalate monohydrate. *Nature* **1965,** *208* (5016), 1197.

(53) Sterling, C. Crystal Structure of Weddellite. *Science* **1964,** *146* (3643), 518.

(54) He, J. Y.; Deng, S. P.; Ouyang, J. M. Morphology, Particle Size Distribution, Aggregation, and Crystal Phase of Nanocrystallites in the Urine of Healthy Persons and Lithogenic Patients. *IEEE Transactions on NanoBioscience* **2010,** *9* (2), 156.

(55) Sheng, X.; Ward, M. D.; Wesson, J. A. Crystal surface adhesion explains the pathological activity of calcium oxalate hydrates in kidney stone formation. *Journal of the American Society of Nephrology* **2005,** *16* (7), 1904.

(56) Conti, C.; Casati, M.; Colombo, C.; Realini, M.; Brambilla, L.; Zerbi, G. Phase transformation of calcium oxalate dihydrate–monohydrate: Effects of relative humidity and new spectroscopic data. *Spectrochimica Acta Part A: Molecular and Biomolecular Spectroscopy* **2014,** *128*, 413.

(57) Chen, Z.; Wang, C.; Zhou, H.; Sang, L.; Li, X. Modulation of calcium oxalate crystallization by commonly consumed green tea. *CrystEngComm* **2010,** *12* (3), 845.

(58) Stanković, A.; Kontrec, J.; Njegić Džakula, B.; Kovačević, D.; Marković, B.; Kralj, D. Preparation and characterization of calcium oxalate dihydrate seeds suitable for crystal growth kinetic analyses. *Journal of Crystal Growth* **2018,** *500*, 91.

(59) Basso, R.; Lucchetti, G.; Zefiro, L.; Palenzona, A. *Caoxite, $Ca(H_2O)_3(C_2O_4)$, a new mineral from the Cerchiara mine, northern Apennines, Italy*, 1997.

(60) Deganello, S.; Kampf, A. R.; Moore, P. B. The crystal structure of calcium oxalate trihydrate: Ca $(H_2O)_3(C_2O_4)$. *American Mineralogist* **1981,** *66* (7-8), 859.

(61) Kyono, A.; Kimata, M.; Shimizu, M.; Echigo, T.; Hatta, T. Re-investigation of the crystal structure of whewellite [$Ca(C_2O_4)\cdot H_2O$] and the dehydration mechanism of caoxite [$Ca(C_2O_4)\cdot 3H_2O$]. *Mineralogical Magazine* **2005,** *69* (1), 77.

(62) Opalko, F. J.; Adair, J. H.; Khan, S. R. Heterogeneous nucleation of calcium oxalate trihydrate in artificial urine by constant composition. *Journal of Crystal Growth* **1997,** *181* (4), 410.

(63) Tomazic, B.; Nancollas, G. H. The kinetics of dissolution of calcium oxalate hydrates. *Journal of Crystal Growth* **1979,** *46* (3), 355.

(64) Hajir, M.; Graf, R.; Tremel, W. Stable amorphous calcium oxalate: synthesis and potential intermediate in biomineralization. *Chemical Communications* **2014,** *50* (49), 6534.

(65) Ihli, J.; Wang, Y.-W.; Cantaert, B.; Kim, Y.-Y.; Green, D. C.; Bomans, P. H. H.; Sommerdijk, N. A. J. M.; Meldrum, F. C. Precipitation of Amorphous Calcium Oxalate in Aqueous Solution. *Chemistry of Materials* **2015,** *27* (11), 3999.

(66) Gehl, A.; Dietzsch, M.; Mondeshki, M.; Bach, S.; Häger, T.; Panthöfer, M.; Barton, B.; Kolb, U.; Tremel, W. Anhydrous Amorphous Calcium Oxalate Nanoparticles from Ionic Liquids: Stable Crystallization Intermediates in the Formation of Whewellite. *Chemistry – A European Journal* **2015,** *21* (50), 18192.

(67) Weber, E.; Verch, A.; Levy, D.; Fitch, A. N.; Pokroy, B. Amorphous biogenic calcium oxalate. *ChemistrySelect* **2016,** *1* (2), 132.

(68) Xie, B.; Halter, T. J.; Borah, B. M.; Nancollas, G. H. Aggregation of Calcium Phosphate and Oxalate Phases in the Formation of Renal Stones. *Crystal Growth & Design* **2015,** *15* (1), 204.

(69) Kutaish, N.; Aggarwal, P.; Dollimore, D. Thermal analysis of calcium oxalate samples obtained by various preparative routes. *Thermochimica Acta* **1997,** *297* (1), 131.

(70) Hourlier, D. Thermal decomposition of calcium oxalate: beyond appearances. *Journal of Thermal Analysis and Calorimetry* **2019,** *136* (6), 2221.

(71) Finlayson, B.; Reid, F. The expectation of free and fixed particles in urinary stone disease. *Investigative urology* **1978,** *15* (6), 442.

(72) Kok, D. J.; Khan, S. R. Calcium oxalate nephrolithiasis, a free or fixed particle disease. *Kidney international* **1994,** *46* (3), 847.

(73) Khan, S. R. Histological aspects of the "fixed-particle" model of stone formation: animal studies. *Urolithiasis* **2017,** *45* (1), 75.

(74) Kok, D. J.; Boellaard, W.; Ridwan, Y.; Levchenko, V. A. Timelines of the "free-particle" and "fixed-particle" models of stone-formation: theoretical and experimental investigations. *Urolithiasis* **2017,** *45* (1), 33.

(75) Finlayson, B. Physicochemical aspects of urolithiasis. *Kidney international* **1978,** *13* (5), 344.

(76) Tiselius, H.-G. A hypothesis of calcium stone formation: an interpretation of stone research during the past decades. *Urological Research* **2011,** *39* (4), 231.

(77) Rodgers, A. L.; Allie-Hamdulay, S.; Jackson, G.; Tiselius, H.-G. Simulating calcium salt precipitation in the nephron using chemical speciation. *Urological Research* **2011,** *39* (4), 245.

(78) Daudon, M.; Letavernier, E.; Frochot, V.; Haymann, J.-P.; Bazin, D.; Jungers, P. Respective influence of calcium and oxalate urine concentration on the formation of calcium oxalate monohydrate or dihydrate crystals. *Comptes Rendus Chimie* **2016,** *19* (11), 1504.

(79) Borghi, L.; Guerra, A.; Meschi, T.; Briganti, A.; Schianchi, T.; Allegri, F.; Novarini, A. Relationship between supersaturation and calcium oxalate crystallization in normals and idiopathic calcium oxalate stone formers. *Kidney international* **1999,** *55* (3), 1041.

(80) Laube, N.; Klein, F.; Bernsmann, F. Kinetics of calcium oxalate crystal formation in urine. *Urolithiasis* **2017,** *45* (2), 151.

(81) Brečević, L.; Kralj, D.; Garside, J. Factors influencing the distribution of hydrates in calcium oxalate precipitation. *Journal of Crystal Growth* **1989,** *97* (2), 460.

(82) Manissorn, J.; Fong-ngern, K.; Peerapen, P.; Thongboonkerd, V. Systematic evaluation for effects of urine pH on calcium oxalate crystallization, crystal-cell adhesion and internalization into renal tubular cells. *Scientific Reports* **2017,** *7*.

(83) Bisaillon, S.; Tawashi, R. Growth of Calcium Oxalate in Gel Systems. *Journal of Pharmaceutical Sciences* **1975,** *64* (3), 458.

(84) Ouyang, J.; Deng, S.; Li, X.; Tan, Y.; Bernd, T. Effects of temperature and sodium carboxylate additives on mineralization of calcium oxalate in silica gel systems. *Science in China Series B: Chemistry* **2004,** *47* (4), 311.

(85) Qiu, S. R.; Wierzbicki, A.; Salter, E. A.; Zepeda, S.; Orme, C. A.; Hoyer, J. R.; Nancollas, G. H.; Cody, A. M.; De Yoreo, J. J. Modulation of calcium oxalate monohydrate crystallization by citrate through selective binding to atomic steps. *Journal of the American Chemical Society* **2005,** *127* (25), 9036.

(86) Langdon, A.; Grohe, B. The osteopontin-controlled switching of calcium oxalate monohydrate morphologies in artificial urine provides insights into the formation of papillary kidney stones. *Colloids and Surfaces B: Biointerfaces* **2016,** *146*, 296.

(87) Itoh, Y.; Yasui, T.; Okada, A.; Tozawa, K.; Hayashi, Y.; Kohri, K. Preventive Effects of Green Tea on Renal Stone Formation and the Role of Oxidative Stress in Nephorlithiasis. *The Journal of Urology* **2005,** *173* (1), 271.

(88) Jeong, B. C.; Kim, B. S.; Kim, J. I.; Kim, H. H. Effects of green tea on urinary stone formation: an in vivo and in vitro study. *Journal of endourology* **2006,** *20* (5), 356.

(89) Kanlaya, R.; Singhto, N.; Thongboonkerd, V. EGCG decreases binding of calcium oxalate monohydrate crystals onto renal tubular cells via decreased surface expression of alpha-enolase. *JBIC Journal of Biological Inorganic Chemistry* **2016,** *21* (3), 339.

(90) Benzerara, Y.; Daudon , M.; Bazin , D.; Haymann, J. P.; Rode, J. In *WIPO*; A61K 31/353 (2006.01), A61P 13/04 (2006.01) ed., 2015; Vol. WO/2015/025294

(91) Achilles, W. In vitro crystallisation systems for the study of urinary stone formation. *World Journal of Urology* **1997,** *15* (4), 244.

(92) Kolbach-Mandel, A. M.; Kleinman, J. G.; Wesson, J. A. Exploring calcium oxalate crystallization: a constant composition approach. *Urolithiasis* **2015,** *43* (5), 397.

(93) Garside, J.; Brečević, L.; Mullin, J. W. The effect of temperature on the precipitation of calcium oxalate. *Journal of Crystal Growth* **1982,** *57* (2), 233.

(94) Bretherton, T.; Rodgers, A. Crystallization of calcium oxalate in minimally diluted urine. *Journal of Crystal Growth* **1998,** *192* (3), 448.

(95) DeLong, J. D.; Briedis, D. A technique for the study of growth rates of single crystals of sparingly soluble salts. *Journal of Crystal Growth* **1985,** *71* (3), 689.

(96) Achilles, W.; Freitag, R.; Kiss, B.; Riedmiller, H. Quantification of Crystal Growth of Calcium Oxalate in Gel and its Modification by Urinary Constituents in a New Flow Model of Crystallization. *The Journal of Urology* **1995,** *154* (4), 1552.

(97) Azoury, R.; Garside, J.; Robertson, W. Calcium oxalate precipitation in a flow system: an attempt to simulate the early stages of stone formation in the renal tubules. *The Journal of urology* **1986,** *136* (1), 150.

(98) Mumtaz, H. S.; Hounslow, M. J. Aggregation during precipitation from solution: an experimental investigation using Poiseuille flow. *Chemical Engineering Science* **2000,** *55* (23), 5671.

(99) Hounslow, M. J.; Wynn, E. J. W.; Kubo, M.; Pitt, K. Aggregation of growing crystals in suspension: I. Mumtaz revisited. *Chemical Engineering Science* **2013,** *101*, 731.

(100) Pitt, K.; Hounslow, M. J. Aggregation of growing crystals in suspension: II. Poiseuille flow crystalliser. *Chemical Engineering Science* **2015,** *122*, 384.

(101) Pitt, K.; Hounslow, M. J. Aggregation of growing crystals in suspension: III. Accounting for adhesion and repulsion. *Chemical Engineering Science* **2015,** *133*, 148.

(102) Zauner, R.; Jones, A. G. Determination of nucleation, growth, agglomeration and disruption kinetics from experimental precipitation data: the calcium oxalate system. *Chemical Engineering Science* **2000,** *55* (19), 4219.

(103) Nancollas, G. H.; Gardner, G. L. Kinetics of crystal growth of calcium oxalate monohydrate. *Journal of Crystal Growth* **1974,** *21* (2), 267.

(104) Burton, W. K.; Cabrera, N.; Frank, F. C. The Growth of Crystals and the Equilibrium Structure of their Surfaces. *Philosophical Transactions of the Royal Society of London. Series A, Mathematical and Physical Sciences* **1951,** *243* (866), 299.

(105) Nielsen, A. E.; Toft, J. M. Electrolyte crystal growth kinetics. *Journal of Crystal Growth* **1984,** *67* (2), 278.

(106) Hounslow, M. J.; Bramley, A. S.; Paterson, W. R. Aggregation During Precipitation from Solution. A Pore Diffusion–Reaction Model for Calcium Oxalate Monohydrate. *Journal of Colloid and Interface Science* **1998,** *203* (2), 383.

(107) Ananth, K.; Kavanagh, J. P.; Walton, R. C.; Rao, P. N. Enlargement of calcium oxalate stones to clinically significant size in an in-vitro stone generator. *BJU International* **2002,** *90* (9), 939.

(108) Saw, N. K.; Rao, P. N.; Kavanagh, J. P. A nidus, crystalluria and aggregation: key ingredients for stone enlargement. *Urological Research* **2008,** *36* (1), 11.

(109) Kassemi, M.; Brock, R.; Nemeth, N. A combined transport-kinetics model for the growth of renal calculi. *Journal of Crystal Growth* **2011,** *332* (1), 48.

(110) Bohner, B.; Schuszter, G.; Berkesi, O.; Horváth, D.; Tóth, Á. Self-organization of calcium oxalate by flow-driven precipitation. *Chemical Communications* **2014,** *50* (33), 4289.

(111) Bohner, B.; Endrődi, B.; Horváth, D.; Tóth, Á. Flow-driven pattern formation in the calcium-oxalate system. *The Journal of chemical physics* **2016,** *144* (16), 164504.

(112) Achilles, W.; Jöckel, U.; Schaper, A.; Burk, M.; Riedmiller, H. In vitro formation of 'urinary stones': Generation of spherulites of calcium phosphate in gel and overgrowth with calcium oxalate using a new flow model of crystallization. **1995,** *9*, 577.

(113) Heaney, R. P.; Dowell, M. S.; Rafferty, K.; Bierman, J. Bioavailability of the calcium in fortified soy imitation milk, with some observations on method. *The American Journal of Clinical Nutrition* **2000,** *71* (5), 1166.

(114) Elliott, J. C. Monoclinic Space Group of Hydroxyapatite. *Nature Physical Science* **1971,** *230* (11), 72.

(115) Rosa, A. L.; Beloti, M. M.; Oliveira, P. T.; Van Noort, R. Osseointegration and osseoconductivity of hydroxyapatite of different microporosities. *Journal of Materials Science: Materials in Medicine* **2002,** *13* (11), 1071.

(116) Sanosh, K. P.; Chu, M.-C.; Balakrishnan, A.; Lee, Y.-J.; Kim, T. N.; Cho, S.-J. Synthesis of nano hydroxyapatite powder that simulate teeth particle morphology and composition. *Current Applied Physics* **2009,** *9* (6), 1459.

(117) Rodríguez-Lorenzo, L. M.; Vallet-Regí, M. Controlled Crystallization of Calcium Phosphate Apatites. *Chemistry of Materials* **2000,** *12* (8), 2460.

(118) Chaudhry, A. A.; Haque, S.; Kellici, S.; Boldrin, P.; Rehman, I.; Khalid, F. A.; Darr, J. A. Instant nano-hydroxyapatite: a continuous and rapid hydrothermal synthesis. *Chemical Communications* **2006**, DOI:10.1039/B518102J 10.1039/B518102J(21), 2286.

(119) Koutsopoulos, S. Synthesis and characterization of hydroxyapatite crystals: a review study on the analytical methods. *Journal of Biomedical Materials Research Part A* **2002,** *62* (4), 600.

(120) Kokubo, T.; Kushitani, H.; Sakka, S.; Kitsugi, T.; Yamamuro, T. Solutions able to reproduce in vivo surface-structure changes in bioactive glass-ceramic A-W3. *Journal of Biomedical Materials Research* **1990,** *24* (6), 721.

(121) Tanahashi, M.; Yao, T.; Kokubo, T.; Minoda, M.; Miyamoto, T.; Nakamura, T.; Yamamuro, T. Apatite Coating on Organic Polymers by a Biomimetic Process. *Journal of the American Ceramic Society* **1994,** *77* (11), 2805.

(122) Liu, Q.; Ding, J.; Mante, F. K.; Wunder, S. L.; Baran, G. R. The role of surface functional groups in calcium phosphate nucleation on titanium foil: a self-assembled monolayer technique. *Biomaterials* **2002,** *23* (15), 3103.

(123) Bohner, M.; Lemaitre, J. Can bioactivity be tested in vitro with SBF solution? *Biomaterials* **2009,** *30* (12), 2175.

(124) Daudon, M.; Jungers, P.; Bazin, D. Stone Morphology: Implication for Pathogenesis. *AIP Conference Proceedings* **2008,** *1049* (1), 199.

(125) Randall, A. The Origin and Growth of Renal Calculi. *Annals of Surgery* **1937,** *105* (6), 1009.

(126) Evan, A. P.; Lingeman, J. E.; Coe, F. L.; Parks, J. H.; Bledsoe, S. B.; Shao, Y.; Sommer, A. J.; Paterson, R. F.; Kuo, R. L.; Grynpas, M. Randall's plaque of patients with nephrolithiasis begins in basement membranes of thin loops of Henle. *The Journal of Clinical Investigation* **2003,** *111* (5), 607.

(127) Daudon, M.; Bazin, D.; Letavernier, E. Randall's plaque as the origin of calcium oxalate kidney stones. *Urolithiasis* **2015,** *43* (1), 5.

(128) Tiselius, H.-G. The role of calcium phosphate in the development of Randall's plaques. *Urolithiasis* **2013,** *41* (5), 369.

(129) Sherer, B. A.; Chen, L.; Kang, M.; Shimotake, A. R.; Wiener, S. V.; Chi, T.; Stoller, M. L.; Ho, S. P. A continuum of mineralization from human renal pyramid to stones on stems. *Acta Biomaterialia* **2018,** *71*, 72.

(130) Kuo, R. L.; Lingeman, J. E.; Evan, A. P.; Paterson, R. F.; Parks, J. H.; Bledsoe, S. B.; Munch, L. C.; Coe, F. L. Urine calcium and volume predict coverage of renal papilla by Randall's plaque. *Kidney international* **2003,** *64* (6), 2150.

(131) Khan, S. R.; Rodriguez, D. E.; Gower, L. B.; Monga, M. Association of Randall Plaque With Collagen Fibers and Membrane Vesicles. *The Journal of Urology* **2012,** *187* (3), 1094.

(132) Reid, D. G.; Jackson, G. J.; Duer, M. J.; Rodgers, A. L. Apatite in Kidney Stones is a Molecular Composite With Glycosaminoglycans and Proteins: Evidence From Nuclear Magnetic Resonance Spectroscopy, and Relevance to Randall's Plaque, Pathogenesis and Prophylaxis. *The Journal of Urology* **2011,** *185* (2), 725.

(133) Evan, A. P.; Coe, F. L.; Lingeman, J. E.; Shao, Y.; Sommer, A. J.; Bledsoe, S. B.; Anderson, J. C.; Worcester, E. M. Mechanism of Formation of Human Calcium Oxalate Renal Stones on Randall's Plaque. *The Anatomical Record* **2007,** *290* (10), 1315.

(134) Rouzière, S.; Bazin, D.; Daudon, M. In-lab X-ray fluorescence and diffraction techniques for pathological calcifications. *Comptes Rendus Chimie* **2016,** *19* (11), 1404.

(135) Bazin, D.; Daudon, M.; Combes, C.; Rey, C. Characterization and Some Physicochemical Aspects of Pathological Microcalcifications. *Chemical Reviews* **2012,** *112* (10), 5092.

(136) Daudon, M.; Traxer, O.; Jungers, P.; Bazin, D. Stone Morphology Suggestive of Randall's Plaque. *AIP Conference Proceedings* **2007,** *900* (1), 26.

(137) Letavernier, E.; Bazin, D.; Daudon, M. Randall's plaque and kidney stones: Recent advances and future challenges. *Comptes Rendus Chimie* **2016,** *19* (11), 1456.

(138) Achilles, W.; Jöckel, U.; Schapers, A.; Ulshöfer, B.; Riedmiller, H. In *Urolithiasis 2*; Ryall, R.;Bais, R.;Marshall, V. R.;Rofe, A. M.;Smith, L. H.;Walker, V. R., Eds.; Springer US: Boston, MA, 1994, DOI:10.1007/978-1-4615-2556-1_55 10.1007/978-1-4615-2556-1_55.

(139) Amos, F. F.; Dai, L.; Kumar, R.; Khan, S. R.; Gower, L. B. Mechanism of formation of concentrically laminated spherules: implication to Randall's plaque and stone formation. *Urological Research* **2009,** *37* (1), 11.

(140) Chidambaram, A.; Rodriguez, D.; Khan, S.; Gower, L. Biomimetic Randall's plaque as an in vitro model system for studying the role of acidic biopolymers in idiopathic stone formation. *Urolithiasis* **2015,** *43* (1), 77.

CHAPTER 2.

CALCIUM OXALATE CRYSTALLIZATION IN A MICROFLUIDIC PLATFORM: PROOF-OF-CONCEPT

Chapter 2 Calcium oxalate crystallization in a microfluidic platform: proof-of-concept

Table of contents

1. Inducing calcium oxalate crystallization under microfluidic confinement

As described in **Chapter 1** section **2.c.**, numerous *in vitro* crystallizers aim at improving knowledge with respect to CaOx formation (*e.g.* Mixed-Suspension Mixed Removal Product (MSMPR) system), though they lack of accounting for the effect of *confinement* and associated *fluid-flow* encountered in the nephron. Thanks to a microfluidic approach that we will develop hereafter, we intend to address the two previous issues. In the coming section, we will present a 2D continuous-flow microchannel as a "proof-of-concept" towards the investigation of CaOx crystallization akin to renal physiopathological conditions. Beforehand, preliminary basis will set the scene with respect to fluid mechanisms at microscopic scale.

a. The microfluidic methodology

i. Hydrodynamics at the microfluidic scale

In the field of microfluidics, microchannels have been considered as micro-reactors for conducting chemical reactions[1,2]. Fluid mechanics has to be taken into consideration to describe the physicochemical phenomena occurring in the micro-systems. For simplicity, we will illustrate it with a pipe system of circular section. A fluid continuously entering at a defined flow rate Q in a pipe behaves according to the laws of hydrodynamics[3] (**Figure 1**). The fluid is characterized by its velocity profile $\vec{u}$ (*m.s*$^{-1}$) and flows differently according to the radial location in a pipe. Friction along the pipe walls tends to slow the fluid, whereas at its axis the fluid is at its maximal speed. The average fluid velocity is defined as $\bar{u}$ (*m.s*$^{-1}$)

$$\bar{u} = \frac{Q}{S} \quad (2.1)$$

with Q = the flow rate (*m*^{3}*.s*$^{-1}$) and S = the pipe cross-section (*m*²). In the particular case of a Newtonian fluid (*i.e.* fluid density ρ_0 = constant), its motion is described by the Navier-Stokes equation

$$\frac{\partial \vec{u}}{\partial t} + \vec{u} \cdot \nabla \vec{u} = \frac{\rho}{\rho_0}\vec{g} - \frac{\nabla p}{\rho_0} + \nu \nabla^2 \vec{u} \quad (2.2)$$

with $\vec{g}$ = the g-force applied to the fluid (*N*), p = the pressure (*Pa*) and $\nu = \mu / \rho$ the fluid kinematic viscosity (*m*².*s*$^{-1}$). The previous equation (**2. 2**) is the application of the second Newton's law to a fluid. In case of an incompressible fluid (*i.e.* $\vec{u} \cdot \nabla \vec{u} = 0$), fluid motion is

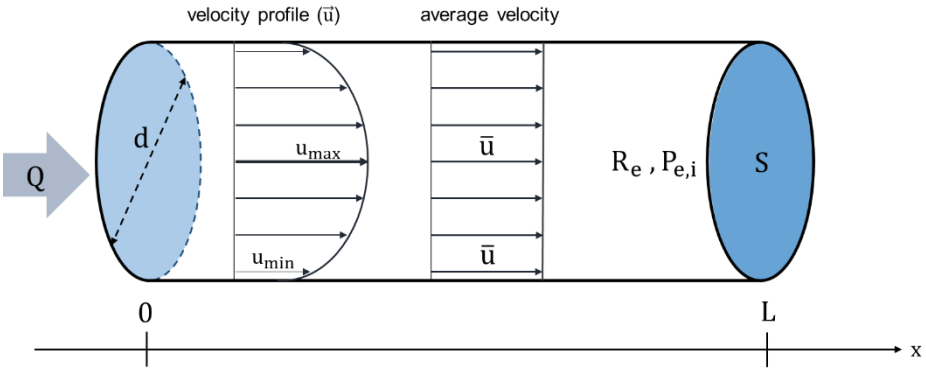

Figure 1. Schematic illustration of the hydrodynamic parameters of interest in a pipe of total length L, diameter d and cross-section S. When a fluid is continuously injected at a given flow rate Q, the average fluid velocity $\bar{u}$, the Reynolds number R_e and the Péclet number P_e can be defined and calculated. The present scheme has illustrative purposes only.

subject to the sum of external forces (herein absent), a convective term and a diffusing viscous term. From this equation, other hydrodynamic parameters can be defined.

In a pipe, the Reynolds number R_e (dimensionless) defines the fluid flow regime

$$R_e = \frac{\bar{u}\, d}{\nu} = \frac{\text{convection}}{\text{viscosity}} \quad (2.3)$$

with $\bar{u}$ = the average flow velocity as defined in equation (**2. 1**) ($m.s^{-1}$), d = the diameter of the pipe (m) and ν = the kinematic viscosity of the fluid ($m^2.s^{-1}$). By comparing the inertial forces to the viscous forces in the fluid, the flow regime at a microfluidic scale (*i.e.* herein the scale of interest with respect to the nephron) is said to be either *laminar* when $R_e \ll 1$ or *turbulent* when $R_e \gg 1$. A laminar flow regime is characterized by smooth streamlines and highly ordered fluid motion while a turbulent regime is described by fluid velocity fluctuations and disordered motion.

Another parameter of interest with respect to fluid mechanics is the Péclet number $P_{e,i}$ (dimensionless)

$$P_{e,i} = \frac{\bar{u}\, d}{D_i} = \frac{\text{convection}}{\text{diffusion}} \quad (2.4)$$

with D_i = the diffusion coefficient of chemical species i ($m^2.s^{-1}$). The parameter is relevant in the study of transport phenomena, *e.g.* to measure the ratio of the convection rate of a molecule (by the flow) to its molecular diffusion rate by a gradient. In the field of microfluidics, it is uneasy to give a precise characteristic order of magnitude regarding the Péclet number. Nevertheless, a high (respectively low) Péclet number indicates a strong (respectively low) influence of the molecular convection along the pipe compared to diffusion.

To summarize, some parameters of interest have to be considered with respect to hydrodynamics in a microchannel. From the Navier-Stokes equation, dimensionless features such as the Reynolds and the Péclet numbers (*i.e.* R_e and P_e,, respectively) enable to characterize the fluid flow behavior in a microchannel. In the context of the present study, these features are important when using a micro-reactor to conduct chemical reactions. Compared to batch syntheses, controlling the fluid behavior in the micro-reactor permits a finer control of the diffusion of ions in the confined medium towards synthesis reproducibility.

ii. The collecting duct: a tubular micro-reactor

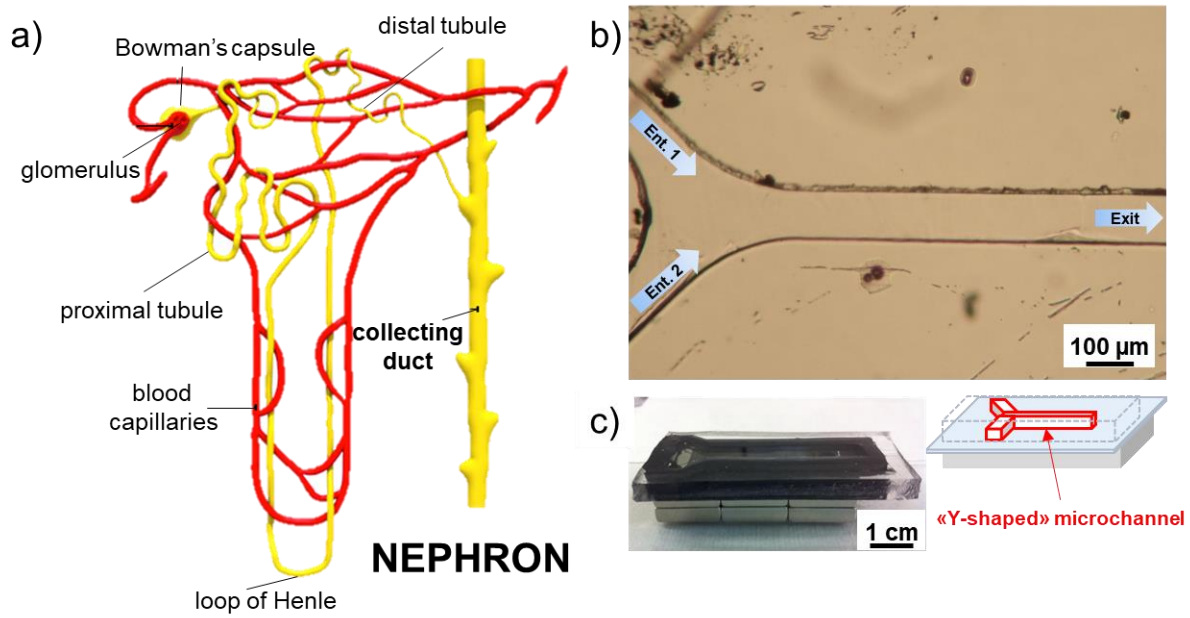

Figure 2. Overview of the collecting duct-on-a-chip device: a) schematic illustration of one nephron, the functional unit of the kidney, with an emphasis on the collecting duct; b) light micrograph in top view of the 100 × 100 µm square section tubular micro-reactor casted in polydimethylsiloxane (PDMS) polymer. The "Y-shaped" structure exhibits two inlets and one outlet referred as Entrance 1, Entrance 2 and Exit respectively; c) image of the final microfluidic assembly and corresponding scheme showing from top to bottom a PDMS piece with the casted "Y-shaped" microchannel, a glass coverslip and sealing magnets.

In the nephron, the collecting duct (**Figure 2a**) is a tubular micro-structure of ≈ 100 *µm* in diameter with urine flowing at ≈ 10 $nL.min^{-1}$ under laminar regime (*i.e.* Re ≈ 0.0021)[4]. Within this structure, CaOx stones might form due to supersaturated concentrations in Ca^{2+} and Ox^{2-} ions. In the context of the present work, we made the decision to use the microfluidic technology to build up a microchannel operating under continuous-flow conditions. A previous contribution from our research group showed that such microfluidic system allows the study of CaOx crystallization[5]. Compared to classical crystallization in batch, the microchannel aimed at mimicking the tubular micro-confinement and associated fluid-flow of a single collecting duct. Therefore, a "Y-shaped" channel with a 100 × 100 *µm* square section and of 2.5 *cm* in length from the Y-junction was designed and casted in a polydimethylsiloxane (PDMS) matrix (**Figure 2b**). Worth pointing out, the length of 2.5 *cm* in our design was consistent with the

dimensions of one collecting duct as used by Roberston to model mathematically CaOx stone formation[6] (refer to **Chapter 1** section **2.b.i**). The tubular structure was assembled with a bare glass slide using a compressive metallic holder. Consequently, Laffite *et al*.[5] obtained a mechanically and reversibly sealed microfluidic platform. The platform served as a *collecting duct-on-a-chip* device to induce CaOx stone crystallization akin to conditions promoting pathological kidney stone formation. It enabled to investigate the precipitation of CaOx crystals at the mixing micro-interface of Ca^{2+} and Ox^{2-} ions. Nevertheless, the fully assembled device was too thick. Therefore, the platform was unsuitable for investigating CaOx crystallization using microscopy for *in situ* characterization, for example.

In the present work, we modified the previous collecting duct-on-a-chip device to allow magnetic and reversible sealing of the platform[7] (**Figure 2c** and **Appendix** for *further technical description*). Briefly, iron carbonyl micro-particles are added to the PDMS polymer matrix to make the edges magnetic and induce reversible sealing/unsealing using magnets. Hereafter, we will demonstrate that this modification did not affect the ability of the collecting duct-on-a-chip device to act as a CaOx crystallizer. In contrary, the reversible property provided with an easy-to-use microfluidic platform for later structural and spectroscopic characterization unlike usual PDMS microchips irreversibly sealed using O_2 plasma treatment.

b. The physicochemical strategy for calcium oxalate crystalluria

i. CaOx crystallization under co-laminar flow of $Ca^{2+}_{(aq)}$ and $Ox^{2-}_{(aq)}$ ions in aqueous solution

As previously introduced, concentrations of Ca^{2+} and Ox^{2-} ions associated to significant ion product Q_{CaOx}

$$\textit{i.e.}\ Q_{CaOx} = [Ca^{2+}]_{(aq)} \times [Ox^{2-}]_{(aq)} > K_{sp(CaOx)} = 2.32 \times 10^{-9} \text{ at } 25°C^{8}$$

might lead to idiopathic CaOx crystallization. To induce *in vitro* crystallization of CaOx stones, we operated the collecting duct-on-a-chip device with aqueous solutions at pathological concentrations in Ca^{2+} and Ox^{2-} ions as measured in urines of stone formers. Thereby, calcium aqueous solution was used at concentration $[Ca^{2+}]_{(aq)} = 12.0$ *mmol.L*$^{-1}$ while oxalate aqueous solution was at concentration $[Ox^{2-}]_{(aq)} = 0.4$ *mmol.L*$^{-1}$ (**Table 1**). From a physiological viewpoint, such chemical conditions are similar to stone promoting conditions of patients diagnosed with combined hypercalciuria and moderate hyperoxaluria[9].

Table 1. Summary of the chemical conditions used to induce CaOx crystallization at room temperature.

Ion species (reagents)	Concentration	Medical condition[9]	$[Ca^{2+}]_{(aq)} \times [Ox^{2-}]_{(aq)}$	Self-diffusion coefficient in water at 25°C[10]
Ca^{2+} ($CaCl_2$)	12.0 *mmol.L*$^{-1}$	Hypercalciuria	4.8×10^{-6}	7.92×10^{-10} *m².s*$^{-1}$
Ox^{2-} ($Na_2C_2O_4$)	0.40 *mmol.L*$^{-1}$	Moderate hyperoxaluria		9.87×10^{-10} *m².s*$^{-1}$

Thereafter, co-laminar flow mixing of aqueous solutions of Ca^{2+} and Ox^{2-} ion induced CaOx crystallization. As already mentioned above, some parameters are worth keeping in mind when considering hydrodynamics. Obviously, the main one is the flow rate (Q) that enables to define the average flow velocity ($\bar{u}$), the flow regime (R_e) and the magnitude of convection over diffusion (P_e) in the channel. To illustrate our point, **Table 2** summarizes the hydrodynamic parameters of interest in case of the Ca^{2+} and Ox^{2-} aqueous solutions injected at equal flow rate of 1.0 *µL.min*$^{-1}$ inside the 100 × 100 *µm* "Y-shaped" microchannel of 2.5 *cm* length. At this point, it is important to point out that Q = 1.0 *µL.min*$^{-1}$ is ≈ 100 times higher compared to the urinary flow condition in a single collecting duct.

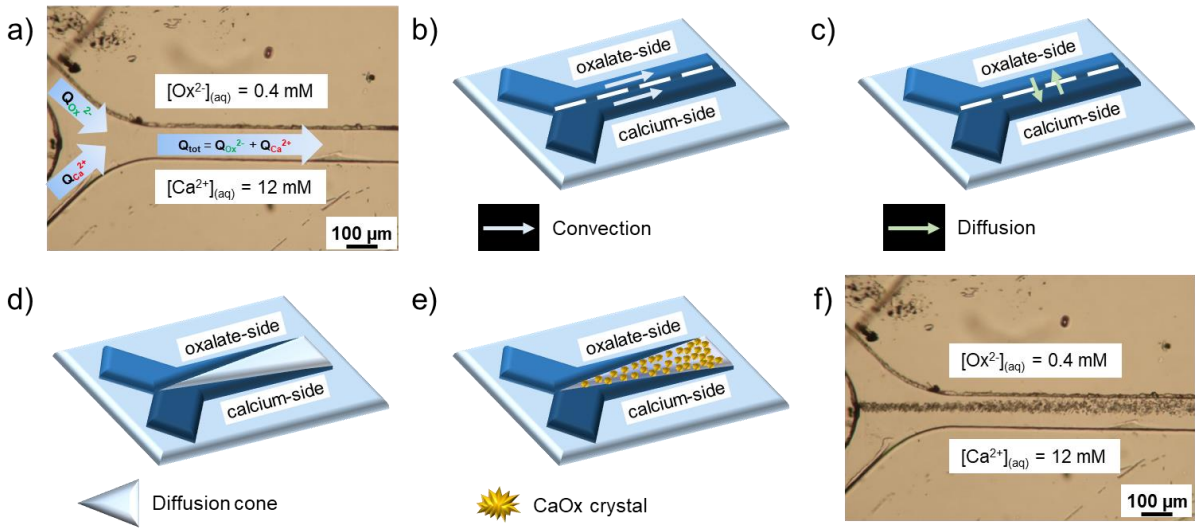

Figure 3. Illustrative description of the events leading to calcium oxalate (CaOx) crystallization in the tubular micro-reactor under co-laminar mixing of Ca^{2+} and Ox^{2-} solutions: a) both solutions are injected at equal flow rates for two hours; b) a liquid-liquid interface separates Ca^{2+} and Ox^{2-} ions; c) the interface is dynamic and enables diffusion of Ca^{2+} and Ox^{2-} ions; d) it results in the appearance of a cone of diffusion due to concentration gradients; e) finally, CaOx crystals precipitate; f) optical image shows the resulting CaOx crystallization within the microfluidic device for $Q_{Ca^{2+}} = Q_{Ox^{2-}} = 1.0$ *µL.min*$^{-1}$. Attention is drawn to the asymmetric shape of the cone of CaOx crystallization after two hours of co-laminar mixing in Ca^{2+} and Ox^{2-} solutions.

Table 2. Illustrative hydrodynamic parameters for equal flow rate of 1.0 *µL.min*$^{-1}$ in Ca^{2+} and Ox^{2-} ion solutions. The Reynolds number (**R_e**) and Péclet number (**P_e**) are calculated according to section **1.a.i**.

$Q_{Ca^{2+}} = Q_{Ox^{2-}}$	$\bar{u}$	R_e	P_e
1.00 *µL.min*$^{-1}$	3.33×10^3 *µm.s*$^{-1}$	0.37	374

In these conditions, R_e = 0.37 ($\ll$ 1) indicated a laminar flow regime in the microchannel as well. Regarding P_e = 374, it emphasized the relative importance of convection *vs.* diffusion of ions in the system.

Crystallization occurred following several steps as described in **Figure 3**. First, both ion precursors were injected with a syringe pump at same flow rates, *i.e.* $Q_{Ca^{2+}} = Q_{Ox^{2-}}$, inside the micro-reactor for two hours (**Figure 3a**). While convection occurred along the flow direction in the channel (**Figure 3b)**, Ca^{2+} and Ox^{2-} ions diffused through the dynamical liquid-liquid interface (dashed line in **Figure 3c**). As shown in **Figure 3d**, this phenomenon created a diffusion cone where the two ion precursors mixed leading to the precipitation of CaOx crystals (**Figures 3e-f**). **Figure 3f** underscored the asymmetric geometry of the CaOx precipitation cone. CaOx precipitation appeared shifted towards the oxalate-rich side of the microchannel.

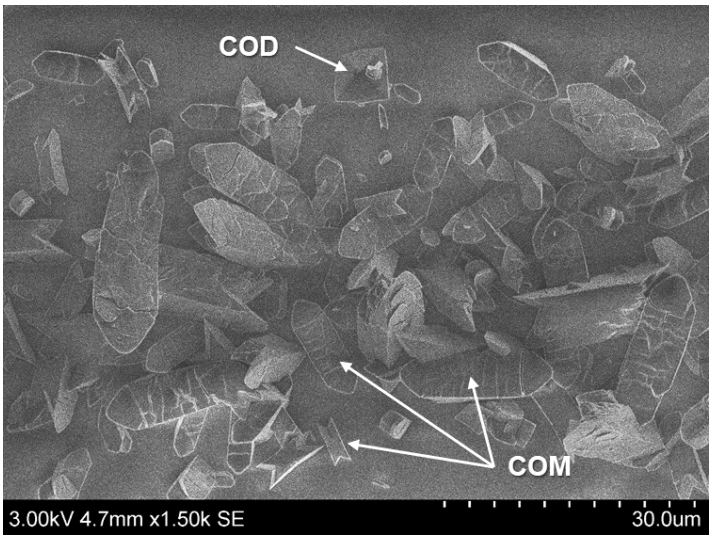

Figure 4. Scanning Electron Microscopy (SEM) image of CaOx crystal mixture resulting from the co-laminar mixing of Ca^{2+} and Ox^{2-} ions at equal flow rate of 1.0 *µL.min*$^{-1}$. The image is obtained after disassembling the collecting duct-on-a-chip device to enable visualization of the mixture of predominant COM and rare COD crystals that precipitated onto the glass coverslip. The present micrograph can be considered as representative of CaOx crystallization within the collecting duct-on-a-chip device.

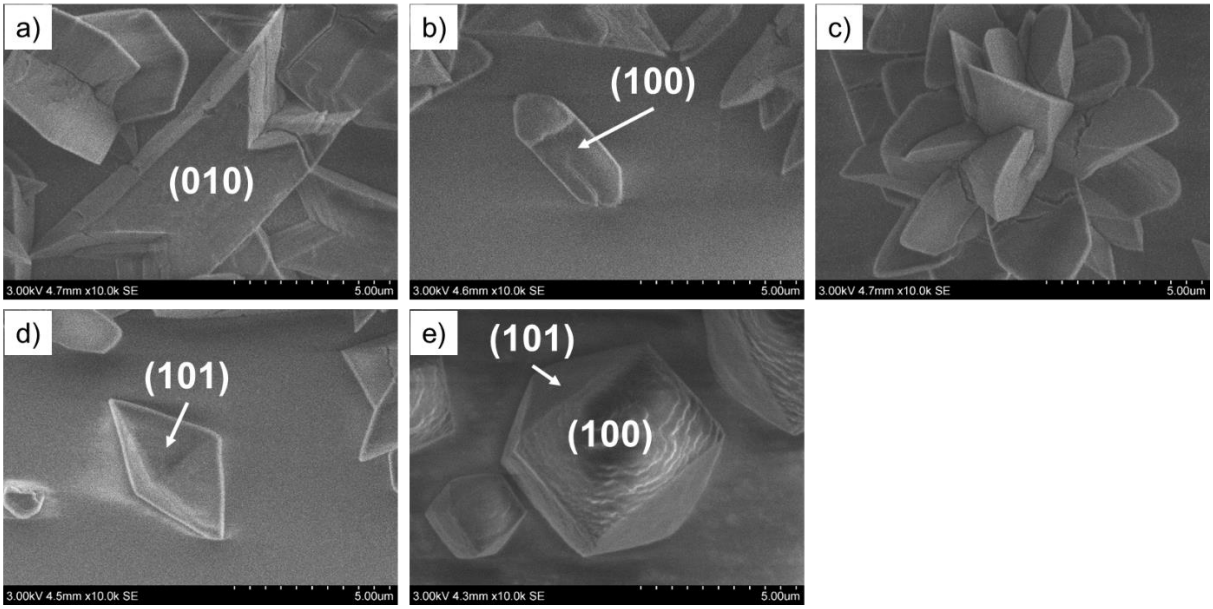

Figure 5. Magnified SEM images of isolated CaOx crystals resulting from the co-laminar mixing of Ca^{2+} and Ox^{2-} ions. Images a) – c) stand for calcium oxalate monohydrate (COM) under twins (a), prismatic (b) and "flower-like" morphologies. Images d) – e) stand for calcium oxalate dihydrate (COD) crystals under flatted bipyramid (d) and elongated bipyramid (e) crystal habits.

This observation was simply due to higher concentration in Ca^{2+} ions ($[Ca^{2+}]_{(aq)}$ = 12.0 *mmol.L*$^{-1}$) present in the micro-reactor compared to Ox^{2-} ions ($[Ox^{2-}]_{(aq)}$ = 0.4 *mmol.L*$^{-1}$). If we consider the 1st Fick's law of diffusion

$$\vec{j}_i = -D_i \nabla c \quad (2.5)$$

(with $\vec{j}_i$ = the diffusion of chemical species i in *m².s*$^{-1}$, D_i = the diffusion coefficient of chemical species i in *m².s*$^{-1}$ and ∇c = the concentration gradient), we can state that at comparable self-diffusion coefficient Ca^{2+} ions (D_{Ca}^{2+} = 7.92 × 10^{-10} *m².s*$^{-1}$) will diffuse faster towards the Ox^{2-} rich-side (D_{Ox}^{2-} = 9.87 × 10^{-10} *m².s*$^{-1}$).

Based on crystal habit examination, Scanning Electron Microscopy (SEM) revealed that CaOx crystals precipitate on the sealing glass coverslip in a mixture of predominant CaOx monohydrate whewellite ($CaC_2O_4{\cdot}H_2O$, COM) form and occasional CaOx dihydrate weddellite ($CaC_2O_4{\cdot}2H_2O$, COD) ones (**Figure 4**). SEM examination *along* the microchannel demonstrated that COM crystals remained dominant compared to COD crystals. Moreover, we observed the overall decrease in CaOx crystal size with respect to the distance away from the channel "Y-junction". Each CaOx hydrate exhibited various morphologies with discernable crystallographic faces (**Figure 5**). Based on data from the literature, COM crystals were found under twins (**Figure 5a**), prismatic (**Figure 5b**) or "flower-like" (**Figure 5c**) habits while COD crystals were bipyramid-shaped either flatted (**Figure 5d**) or elongated under very specific chemical conditions (*e.g.* **Figure 5e** in addition of green tea). It is worth mentioning that we did not report the precipitation of other CaOx hydrates such as trihydrate caoxite ($CaC_2O_4{\cdot}3H_2O$,

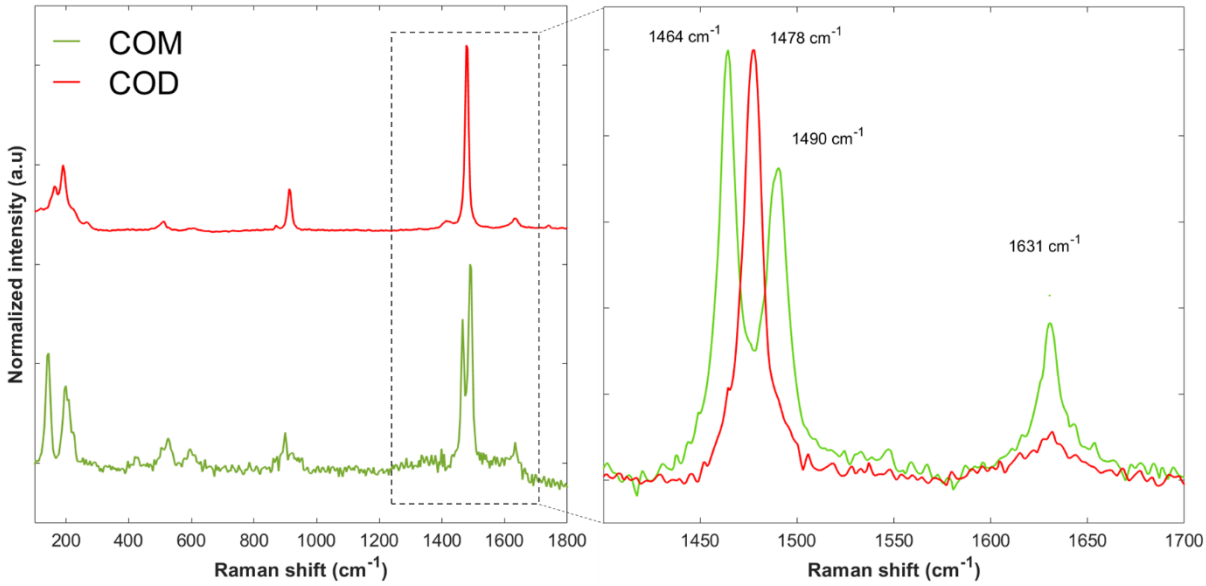

Figure 6. *Raman* spectra for isolated COM and COD crystals. Left: 100 to 1800 cm^{-1} range. Right: 1300 and 1700 cm^{-1} range. All spectra were baseline corrected.

COT), amorphous ($CaC_2O_4 \cdot nH_2O$, ACO) or anhydrous (CaC_2O_4, COAnh) CaOx crystals. This observation supported the use of the collecting duct-on-a-chip platform to mimic CaOx kidney stone crystallization. Indeed, COT crystalline phase is almost never observed in kidney stones. ACO is suspected to be an intermediate phase for kidney stone formation[11] but there is a lack of clear evidence and COAnh was never reported.

Due to the small amount of precipitated materials, standard X-Ray Diffraction (XRD) analysis could not be carried out to discriminate CaOx crystalline phases. Numerically, if CaOx crystals precipitated to entirely fill the microchannel ($V = 2.5 \times 10^{-4}\ cm^3$) then $m_{CaOx,max} = 0.53\ mg$ ($\rho_{COM} = 2.12\ g.cm^{-3}$ at 20°C). To confirm the formation of either COM or COD crystals, we conducted *Raman* spectroscopy instead (**Figure 6**) at the spatial resolution of a unique crystal. Therefore, each morphology could be correlated to the specific spectral signature of either COM or COD crystals[5,12,13]. As shown in the right part of **Figure 6**, COM crystal (in green) exhibited *characteristic* peaks at 1464 and 1490 cm^{-1} while COD crystal (in red) exhibited its *characteristic* peak at 1478 cm^{-1}. These peaks correspond to a double symmetric C-O bending vibration for COM and a single symmetric C-O bending vibration for COD[13], respectively. Interestingly, the relative intensities of the two characteristic peaks for COM crystals varied with respect to one another and seemed to depend on the crystallographic face under scrutiny. Additional investigation will be considered to support this statement.

Finally, we collected and analyzed the reagents solution at the end of the micro-reactor. It enabled to determine the concentration of remaining Ca^{2+} ions along with the type of crystals exiting the microchannel. After two hours of continuous injection of reagents, the concentration

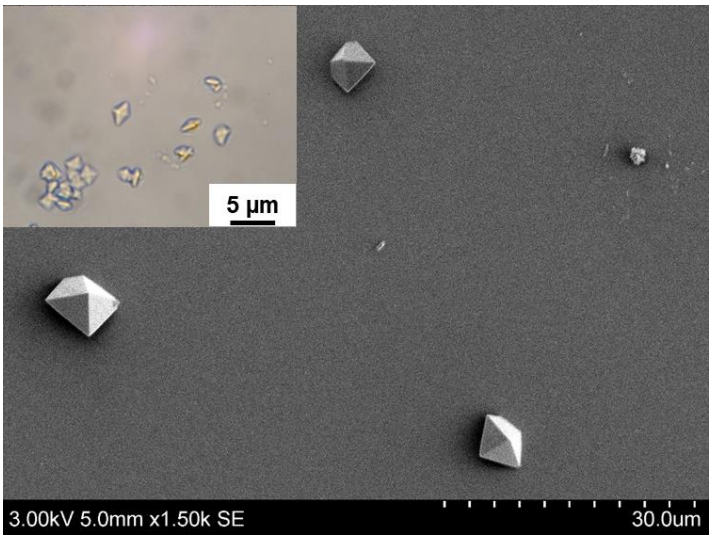

Figure 7. Optical and electronic microscopies images of flatted bipyramid-shaped COD crystals collected at the end of the collecting duct-on-a-chip device in the reagents solution.

in Ca^{2+} ions was $[Ca^{2+}]_{(eq)}$ = 11.5 ± 0.2 *mmol.L*$^{-1}$ (measured with a HORIBA Ca^{2+} selective electrode). **Figure 7** shows that the reagents solution coming out of the collecting duct-on-a-chip device contained only flatted bipyramid-shaped COD crystals.

We want to point out the consistency of the experimental observations compared to the previous contribution in our research group[5]. To study CaOx crystallization, Laffite and collaborators utilized a mechanically sealed PDMS microfluidic chip and obtained majority of COM and occasional COD crystal mixtures at flow rate 1.0 *µL.min*$^{-1}$. Yet possible, retrieving CaOx precipitates might be difficult to handle preventing from in-depth characterization of CaOx crystals. Indeed, a magnetic PDMS micro-reactor presents noteworthy advantages with respect to a mechanically sealed PDMS microchip. The first and obvious one is the facile and rapid sealing/unsealing of the platform with magnets. It enables to retrieve easily the CaOx crystals. Furthermore, the same ion concentrations and flow rates led to comparable results regarding CaOx crystallization as supported by SEM imaging and *Raman* spectroscopy. Albeit the sealing method differed between the two microfluidic platforms, the collecting duct-on-a-chip device stands for a robust tool to investigate CaOx crystallization.

Herein, we introduced our “proof-of-concept” of an engineered collecting duct-on-a-chip platform where CaOx crystallization can take place. Our platform allowed interfacial characterization using approaches such as SEM imaging or *Raman* spectroscopy. CaOx crystals were found exclusively under COM or COD crystalline phases, both CaOx hydrates exhibiting various morphologies. The robustness of CaOx crystallization inside the micro-reactor was tested with respect to sealing considerations. At same initial conditions (*i.e.* Ca^{2+} and Ox^{2-} ion concentrations and flow rates), CaOx crystallization occurred following the same pattern[5] already observed in the literature.

Nevertheless, it is important to confront the results with medical observations to conclude with the consistency of the microfluidic device to serve as a model system for idiopathic CaOx crystallization.

ii. Relevancy with respect to medical considerations

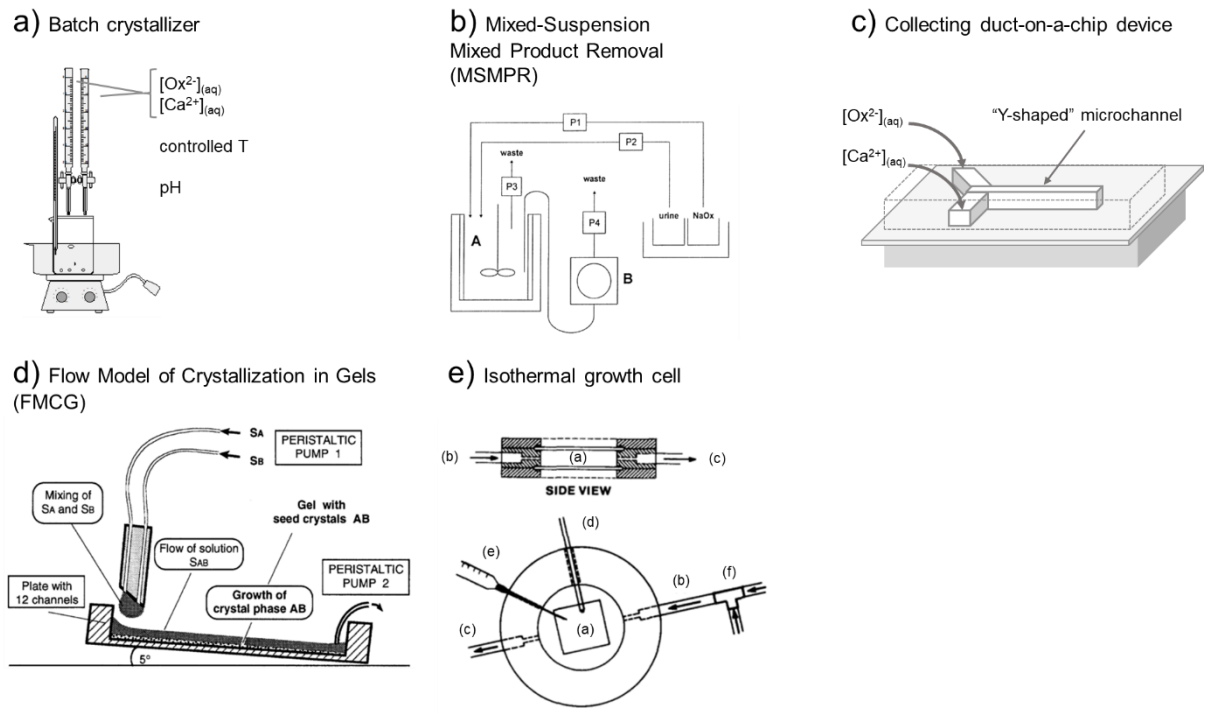

Figure 8. *In vitro* CaOx crystallizers: a) CaOx co-precipitation by dropwise addition of Ca^{2+} and Ox^{2-} aqueous solutions; b) continuous-flow system for the controlled growth of CaOx seed crystals. Figure reproduced from Bretherton *et al*.[14] with permission from Elsevier; c) continuous-flow operating microchannel aiming at mimicking the dimensions of one collecting duct of the nephron to induce CaOx crystallization[5]; d) continuous-flow system for the growth of CaOx crystals in gel state from Achilles *et al.*[15] with permission from Springer; e) circular cross-section chamber of 30 *mm* (capacity 5 *mL*) with observation chamber (a), solution inlet (b) and outlet (c), temperature monitor (d), seed injection syringe (e) and T-junction from DeLong *et al*.[16] with permission from Elsevier.

In our study, the concentrations of calcium and oxalate ions matched the stone promoting conditions of a patient experiencing hypercalciuria ($[Ca^{2+}]_{(aq)}$ = 12.0 $mmol.L^{-1}$) and moderate hyperoxaluria ($[Ox^{2-}]_{(aq)}$ = 0.4 $mmol.L^{-1}$) at the same time. Several *in vitro* strategies could be considered to investigate this medical condition (see **Chapter 1** section **2.c.ii**). However, not all these crystallizers suit the problematic. Although $Q_{CaOx} > K_{sp(CaOx)}$, these chemical conditions are not sufficient to induce CaOx precipitation using a standard batch crystallizer (**Figure 8a**) due to a lack of control over diffusion and mixing phenomena. Using a Mixed Suspension Mixed Product Removal (MSMPR) crystallizer (**Figure 8b**) could be considered since it is broadly utilized to study kidney stone growth under stone promoting conditions[14]. However, the setup requires few liters of reagent solutions to operate. To overcome the previous issues, a micro-reactor of dimensions akin to one collecting duct can be considered (**Figure 8c**)[5]. Microfluidics allows reproducing the laminar flow regime (R_e = 0.37) as encountered in a single

collecting duct. In addition, it permits an accurate control over the concentration gradients generated due to coupling of the molecular diffusion and convection (P_e = 374). Finally, small volume of solutions are required to induce crystallization (*e.g.* 120 *µL* of each reagent at equal flow rate of 1.0 $\mu L.min^{-1}$ for 2 hours). Crystallizers presented in **Figure 8d-e** will be discussed later on in section **2.b.i**.

Based on experimental observations, we assessed that CaOx crystallization occurred within the microchannel, either *onto the glass coverslip* (**Figure 4**) or *within the continuous flow* of the solution (**Figure 7**). Under simplified assumption, the CaOx crystals *inside* the microchannel could be regarded as similar to those attached on the surface of the collecting duct. On the other hand, the crystals collected *in the reagents solution* (*i.e*. at the exit of the flow) could be considered as a simplified model of CaOx crystals in urine of stone formers. Such comparison could be envisaged, especially when thinking about the fixed- and free-particle theories as introduced by Finlayson and Reid[17] (see **Chapter 1** section **2.b.i**). On one hand, the fixed-particle theory supports that CaOx stones can develop once attached to the epithelial cells in the tubules. The second model, *i.e.* the free-particle theory, suggests a crystallization of CaOx stones within the tubular flow. Nowadays, no net consensus exists to conclude with a gold standard theory. Kok and Khan[18] or Robertson[6] tried to reconcile the fixed- and free-particle theories using mathematical modelling. More recently, Kok suggested that both could be valid based on human model examinations[19]. As described in **Chapter 1** section **2.b.i**, they investigated the timelines of two patients having kidney stone from its formation to its surgical removal and concluded that both theories were plausible. Yet valuable, their respective contributions relied on indirect observations. With that in mind, the collecting duct-on-a-chip platform would stand for an experimental setup for CaOx crystallization following fixed- and free-particle theories at the same time.

As introduced in **Chapter 1** section **2.b.ii**, Daudon *et al.* investigated CaOx crystalline phases with respect to the concentrations of free Ca^{2+} and Ox^{2-} ions measured in the urine samples of a large group of stone formers[8]. In turn, they considered the molar ratio r_{CaOx}

$$r_{CaOx} = \frac{[Ca^{2+}]_{(eq)}}{[Ox^{2-}]_{(eq)}} \quad (2.6)$$

with $[Ca^{2+}]_{(eq)}$ and $[Ox^{2-}]_{(eq)}$ ($mmol.L^{-1}$) standing as the concentrations of free Ca^{2+} and Ox^{2-} at equilibrium with the CaOx solid phase in the *urine* sample. The authors established a catalogue of CaOx crystals in urine with various crystalline phases and morphologies (**Figure 9a**). Besides, they correlated the urinary occurrence of CaOx crystalline phases to r_{CaOx} (**Figure 9b**). Consequently, COM crystals were mainly reported in urine samples when $r_{CaOx} < 5$. In contrary, COD crystals became the dominant crystalline phase in case of

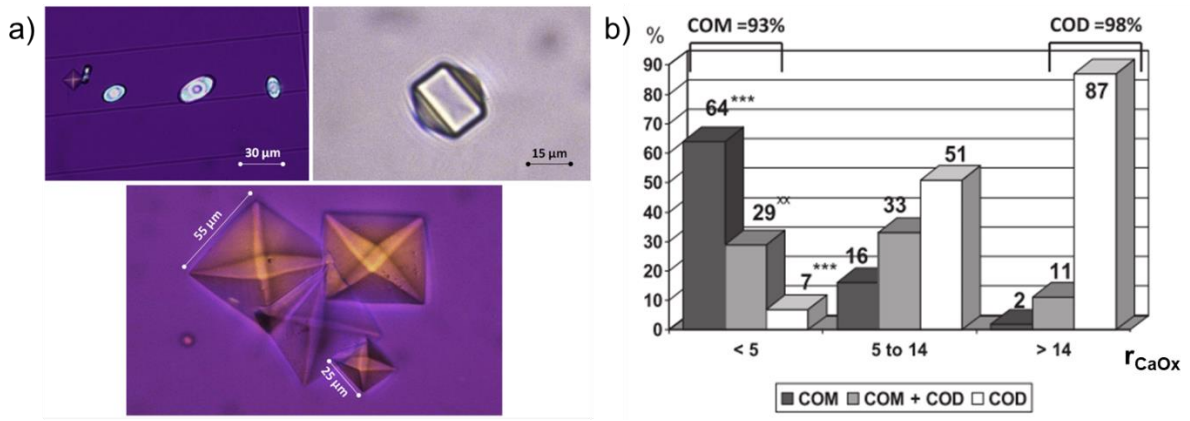

Figure 9. CaOx crystallization with respect to urinary concentrations in Ca^{2+} and Ox^{2-} ions: a) CaOx crystals reported in urines of different stone formers. Images on top describe (left) CaOx crystal mixture of COM and COD crystals and (right) elongated COD crystal. At the bottom, the picture depicts large bipyramid COD crystals suggesting combined hyperoxaluria and hypercalciuria; b) influence of the molar ratio $r_{CaOx} = [Ca^{2+}]_{(eq)} / [Ox^{2-}]_{(eq)}$ on the crystalline phases of CaOx observed in urine samples. Figures are reproduced from Daudon *et al.*[8] with permission from Elsevier.

r_{CaOx} > 14. For 5 < r_{CaOx} < 14, a crystal mixture of COM and COD crystals were identified in urine samples. With respect to **Table 1**, it could be tempting to define a molar ratio of r_{CaOx} = 30 in the present work. It follows that CaOx crystallization in the collecting duct-on-a-chip device should lead to the favored formation of COD crystals. Yet, it is important to specify that r_{CaOx} = 30 herein stands for a molar ratio prior to CaOx crystallization in the microfluidic platform. Consistent comparisons to the work of Daudon *et al.* would imply to redefine r_{CaOx} after CaOx crystallization in the micro-reactor. To this end, means to measure $[Ca^{2+}]_{(eq)}$ and $[Ox^{2-}]_{(eq)}$ would enable to determine an effective molar ratio r_{CaOx} at equilibrium with the CaOx crystals from the micro-reactor. Therefore, we want to notify the readers that we are aware of the reasoning limitations we are about to propose.

Whether CaOx crystallization takes place inside the microchannel or within the continuous flow, the resulting CaOx crystalline phases and morphologies are influenced by the boundary conditions. *Inside the microchannel*, CaOx crystals precipitated in a mixture of COM and COD (**Figure 4**) with various shapes (**Figure 5**). Albeit usually obtained in batch (*e.g.* in a 24-well plate crystallizer[20,21]), the twins COM crystal morphology (**Figure 5a**) was never reported *in vivo*[9]. *In the reagents solution*, it was interesting to note that CaOx crystals exiting the microchannel were only flatted bipyramid COD crystals. The sole identification of COD crystals in our highly simplified model of urine supported the finding of Daudon and collaborators[8]. Nevertheless, **Figure 4** indicated a different behavior inside the microchannel with respect to CaOx crystallization. Interestingly, COM crystals were clearly favored with respect to the concentration in Ca^{2+} and Ox^{2-} ions. However, the authors only studied CaOx particles from the urine samples of stone formers. They did not directly investigate the relationship between the CaOx stones attached in the kidney and r_{CaOx}. Therefore, we could not objectively compare

the crystal mixture of COM and COD within the microchannel to the chemical conditions used in their work. Nonetheless, we can hypothesize on a favored crystalline phase in the collecting duct whether it happens at the tubular wall or in the tubular flow.

The collecting duct-on-a-chip device presented several advantages. The microfluidic approach enabled to mimic the tubular confinement and laminar flow regime encountered in a single collecting duct[5]. Therefore, CaOx crystallization was investigated at pathological concentrations in Ca^{2+} and Ox^{2-} ions[9]. In a highly simplified approach, the CaOx particles were considered to form either at the surface of the collecting duct (*i.e.* on the glass coverslip) or in the tubular flow (*i.e.* very simplified model of urine). Additionally, CaOx crystalline phases and morphologies could be studied with respect to the physicochemical conditions. Moreover, the results could be confronted to medical observations[8] taking into account some limitations. Indeed, Daudon and collaborators correlated the occurrence of CaOx crystalline phases in urines of patients to the molar ratio $r_{CaOx} = [Ca^{2+}]_{(eq)} / [Ox^{2-}]_{(eq)}$ (*i.e*. urinary concentration in free Ca^{2+} and Ox^{2-} ions). They observed that COM crystals in urines of stone formers were associated to $r_{CaOx} < 5$ while COD crystals were associated to $r_{CaOx} > 14$. However, we wanted to point out that their study only accounted for the CaOx stones observed in urines. No similar correlative study was conducted regarding CaOx stones attached in the nephron. It is probably due to invasive procedures the patients should have to undergo (*e.g*. surgery). From this point of view, our collecting duct-on-a-chip stood for a valuable platform since it enabled to study CaOx crystallization either *in the tubular flow* or *inside the micro-reactor*. With the proper tools of investigation, similar correlations could be made to associate CaOx crystalline phase to Ca^{2+} and Ox^{2-} ion concentrations in our model system.

Nonetheless, we would like to draw attention to the used flow rate of 1.0 $\mu L.min^{-1}$. With respect to *in vivo* urine flow, the flow rate used here was 100 times higher and could not be considered as biomimetic. Thereby, we could not neglect the possible role of hydrodynamics on CaOx crystallization. We will be focusing on this parameter of interest in the following part.

2. Influence of hydrodynamics on calcium oxalate crystallization

We have demonstrated that the collecting duct-on-a-chip device is a robust platform for the investigation of CaOx crystallization. The *in vitro* micro-reactor operates at concentrations in Ca^{2+} and Ox^{2-} ions matching human stone promoting concentrations. Furthermore, our microfluidic approach enables to conduct investigations at low fluid-flow conditions. In consequence, the influence of hydrodynamics cannot be disregarded with respect to the cascade of events leading to CaOx crystallization. Herein, we will address the role of flow conditions regarding mixing of reagents and the subsequent CaOx crystallization.

a. The effect of the hydrodynamics

i. Homogeneous *vs.* heterogeneous crystallization of CaOx hydrates

As introduced in section **1.a.i,** a flowing fluid is characterized by specific hydrodynamic parameters such as the fluid velocity, the Reynolds and the Péclet numbers. Therefore, in a collecting duct, where urine flows at ≈ 10.0 $nL.min^{-1}$, we cannot expect to observe the same fluid behavior as in a microchannel operating at 1.0 $\mu L.min^{-1}$. CaOx crystallization should be conducted in the micro-device at lower flow rates to match the flow conditions encountered in a single collecting duct. In total, two different flow conditions, *i.e.* 1.00 and 0.10 $\mu L.min^{-1}$, were investigated experimentally and numerically. To anticipate on section **2.a.ii**, we want to notify that we attempted to conduct CaOx crystallization at an ultra-low flow rate (i.e. 0.01 $\mu L.min^{-1}$). Unfortunately, we did not succeed in inducing CaOx crystallization *experimentally* at the lowest flow rate due to technical limitations (*i.e*. inappropriate syringes for the setup). However, we believed that the *numerical* investigation of Q = 0.01 $\mu L.min^{-1}$ in the channel was worth studying.

A given flow rate, *e.g.* 1.00 $\mu L.min^{-1}$, stands for the flow rate of *one* reagent in solution. In consequence, the total flow rate in the microchannel is $Q_{tot} = Q_{Ca^{2+}} + Q_{Ox^{2-}} = 2 \times Q_{Ca^{2+}}$ as shown in **Figure 3a**. For each flow rate, the corresponding hydrodynamic parameters were calculated for an averaged self-diffusion coefficient $D_{average} = 0.5 \times (D_{Ca^{2+}} + D_{Ox^{2-}}) = 8.89 \times 10^{-10}\ m^2.s^{-1}$ and the kinematic viscosity of water $\nu = 0.893 \times 10^{-6}\ m^2.s^{-1}$ at 25°C (**Table 3**).

Table 3. Comparison of the average flow velocity ($\bar{u}$), the Reynolds number (R_e) and the Péclet number (P_e), the measured angle of diffusion cone (α), size range of CaOx particles (l_{CaOx}) in the channel and the concentration in Ca^{2+} ion at equilibrium ($[Ca^{2+}]_{(eq)}$) after CaOx crystallization in the collecting duct-on-a-chip platform at all flow rates. Hydrodynamic parameters are calculated according to the series of equations in **1.a.i**.

$Q_{Ca^{2+}} = Q_{Ox^{2-}}$	$\bar{u}$	R_e	P_e	α	l_{CaOx}	$[Ca^{2+}]_{(eq)}$
1.00 *µL.min^{-1}*	3.33×10^3 *µm.s^{-1}*	0.37	374	3.41 ± 0.11 °	$1.0 < l_{CaOx} < 25$ *µm*	11.5 ± 0.2 *mmol.L^{-1}*
0.10 *µL.min^{-1}*	333 *µm.s^{-1}*	0.037	37.4	5.21 ± 0.18 °	$1.0 < l_{CaOx} < 15$ *µm*	n/a
0.01 *µL.min^{-1}*	33.3 *µm.s^{-1}*	0.0037	3.74	n/a	n/a	n/a

As expected, the flow regime was always *laminar* regardless of the hydrodynamic flow rate, *i.e.* $R_e \ll 1$, while P_e decreased with the flow rate. Again, P_e describes the capacity of a molecule to be transported along the microchannel by convection compared with its perpendicular diffusion due to a concentration gradient (**Figures 3b**, **3c** in section **1.b.i,** respectively). Low P_e indicated the gradual take-over of the inter-diffusion of Ca^{2+} and Ox^{2-} ions along the liquid-liquid interface compared to their respective convection. The molecular mixing of reagents was likely to take place "sooner" in the microchannel, *i.e.* spatially closer to the first contact zone between Ca^{2+} and Ox^{2-} solutions.

Alike section **1.b.i**, CaOx crystallization was investigated according to the flow rate using the collecting duct-on-a-chip platform. Regardless of the flow condition, the initial chemical conditions remained unchanged (see **Table 1** in section **1.b.i**). Hence, calcium and oxalate solutions were initially at $[Ca^{2+}]_{(aq)} = 12.0$ *mmol.L^{-1}* and $[Ox^{2-}]_{(aq)} = 0.40$ *mmol.L^{-1}*, respectively. Due to a decrease in flow rate, *i.e.* decrease in average flow velocity $\bar{u}$, the experiment time had to be adapted to study CaOx crystallization in the micro-reactor. Arbitrary, we set the complete experiment duration at 2 hours, 2.5 hours and 16 hours for each flow rate condition (*i.e.* 1.00, 0.10 and 0.01 *µL.min^{-1}*, respectively). As said previously, we have not been successful in carrying out CaOx crystallization at Q = 0.01 *µL.min^{-1}*. Nevertheless, the experimental investigations are still in progress to complete the present study.

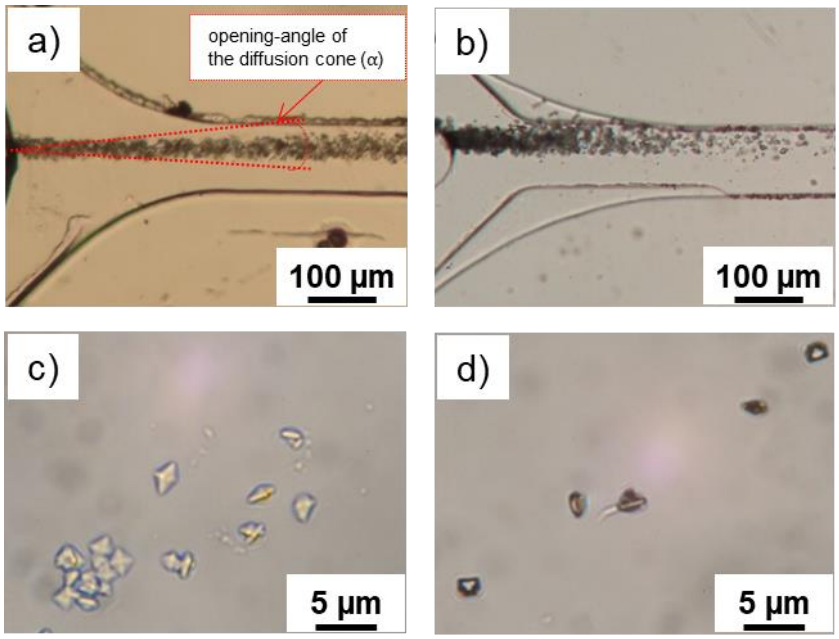

Figure 10. CaOx crystallization under co-laminar mixing of Ca^{2+} and Ox^{2-} aqueous solutions at 1.00 and 0.10 *µL.min*$^{-1}$. **Figures 10a-b)** precipitation of CaOx crystals in the collecting duct-on-a-chip device after the complete experiment duration for each flow rate; **Figures 10c-d)** COD crystals collected at the exit of the microchannel for each flow condition.

The co-laminar mixing of Ca^{2+} and Ox^{2-} aqueous solutions in the microchannel enabled CaOx crystallization at 1.00 *µL.min*$^{-1}$ as already demonstrated (**Figure 10a**), but also at 0.10 *µL.min*$^{-1}$ (**Figure 10b**). Similarly to section **1.b.i**, the reagents solutions at the end of the microfluidic device were collected to identify their content in CaOx crystals (**Figures 10c-d**) and to measure $[Ca^{2+}]_{(eq)}$. Additional measurements such as the shape of the diffusion cone (quantified by the angle α as illustrated in **Figure 10a**) and the size range of CaOx crystals (l_{CaOx}) within the microchannel are gathered in **Table 3**. These parameters served as a qualitative overview regarding the influence of hydrodynamics on CaOx crystallization.

The images in **Figures 10a-b** pointed out that CaOx crystals precipitated into a conical shape at all flow rates. Further discussion will be initiated in the next section regarding this experimental observation.

At the exit of the microchannel, **Figures 10c-d** revealed the sole presence of flatted bipyramid-shape COD crystals. With respect to the chemical conditions, this finding was in accordance with the molar ratio $r_{CaOx} > 14$[8] (**Figure 9b**). As already mentioned, cautiousness had to be used when reasoning with r_{CaOx}. To further support **Figures 10c-d**, we already showed in our research group that a large excess of Ca^{2+} ion *vs.* Ox^{2-} ion can direct CaOx crystals to COD phase in *batch*[21]. With respect to the concentration in Ca^{2+} and Ox^{2-} ions (**Table 1**), the initial ion product of concentrations $Q_{CaOx} = 4.8 \times 10^{-6} \gg K_{sp(CaOx)} = 2.32 \times 10^{-9}$ led to CaOx crystallization. Since $[Ca^{2+}] / [Ox^{2-}] \gg 1$, we can hypothesize that COD nuclei will likely result

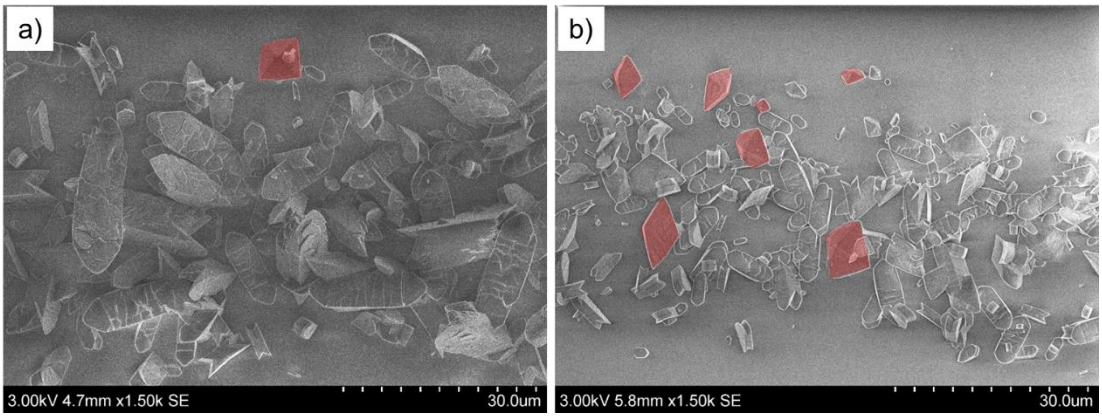

Figure 11. SEM images of CaOx crystallization in mixture of COM and COD crystals inside the microfluidic device at 1.00 *µL.min*$^{-1}$ (**a**) and 0.10 *µL.min*$^{-1}$ (**b**). To ease identification, some flatted bipyramid COD crystals are colored in red "false-color". Additionally, SEM images are taken at the same position in the channel (≈ 300 *µm* away from "Y-junction").

Table 4. Volume **V** and total amount of substance in reagents injected in the collecting duct-on-a-chip device as a function of the flow rate (1.00 and 0.10 *µL.min*$^{-1}$) and its corresponding complete experiment duration (2 hours and 2.5 hours). Amount of substance values do not consider the happening of CaOx crystallization inside the micro-reactor.

$Q_{Ca^{2+}} = Q_{Ox^{2-}}$	V	$n(Ca^{2+})$	$n(Ox^{2-})$
1.00 *µL.min*$^{-1}$	120 *µL*	1.44 *µmol*	0.048 *µmol*
0.10 *µL.min*$^{-1}$	15 *µL*	0.18 *µmol*	0.0060 *µmol*

from the mixing of ions and *homogeneous* nucleation. In the flow, and until they exit the channel, these nuclei can be transported by convection and grow into crystals (identified as COD crystals at all flow rates). At least, we could say that P_e (*i.e.* extent of mixing) did not interfere with the formation and growth of COD crystals in the continuous flow of reagents and their transport to the end of the microchannel. However, the lack of suitable characterization techniques enabling to experimentally explore the nanoscale prevented the previous reasoning to be more than a hypothesis.

CaOx crystallization behaves differently inside the microchannel, *i.e.* specifically onto its sealing glass coverslip. Within the collecting duct-on-a-chip device (**Figure 11**), CaOx crystals precipitated in a mixture of predominant COM and minority of COD particles at all flow rates. Crystal habit examination showed that COM crystals exhibited twins, prismatic or sometimes "flower-like" shapes as in **Figures 5a-c** (section **1.b.i**). Besides, COD crystal only displayed the flatted bipyramid shape as in **Figure 5d**. Although not reported herein, *Raman* spectroscopy confirmed the crystal habit examination. As the flow rate decreased (from **Figures 11a-c**), the overall size of CaOx crystals decreased (see l_{CaOx} in **Table 3**) and the

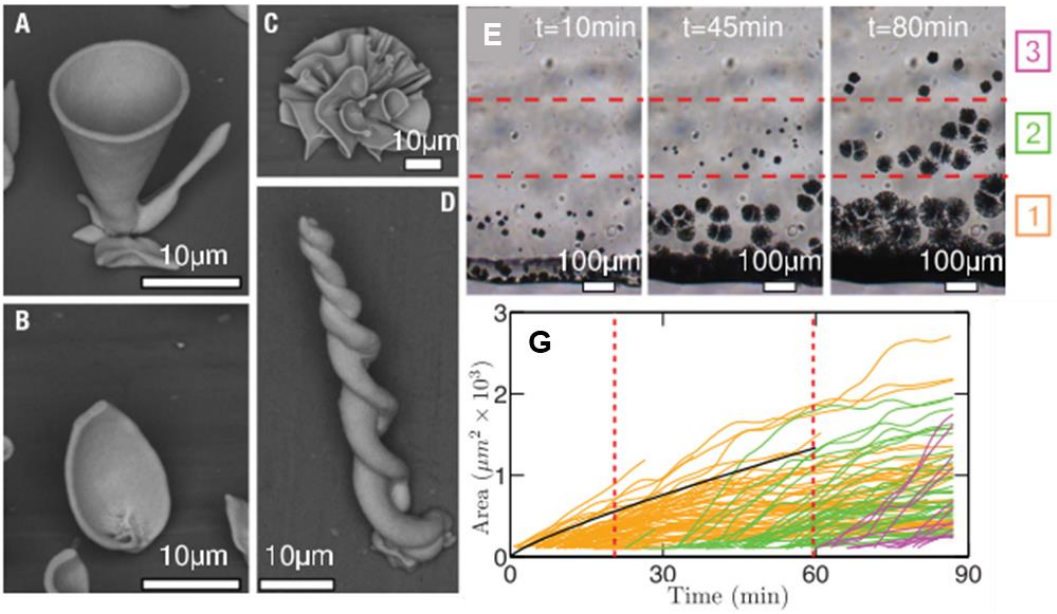

Figure 12. Carbonate-silica co-precipitation patterns[22]: (**A**) to (**D**) SEM images of the (**A**) vase-like, (**B**) petal-like, (**C**) coral-like and (**D**) helical microstructures; (**E**) growth of coral-like structures in a microfluidic reactor monitored in three distinct regions noted 1 in orange, 2 in green and 3 in purple, respectively; (**G**) projected circular area of growing corals as a function of time and the region (1, 2 or 3, respectively). Images are adapted with permission from the American Association for the Advancement of Science.

occurrence of COD crystals increased (in red in **Figure 11**). Nonetheless, COM crystals still stood for the dominant crystalline phase regardless of the flow condition. The global decrease in crystal size could be explained by less amount of substance in reagents transported during the complete experiment duration (**Table 4**). Furthermore, the increasing occurrence of COD crystals became more and more consistent with the effect of $[Ca^{2+}] / [Ox^{2-}] \gg 1$. An enhanced inter-diffusion of Ca^{2+} and Ox^{2-} ions, *i.e.* low P_e value, favored the formation of the expected COD crystals with respect to the initial chemical conditions.

Based on the literature, a discussion regarding the experimental results can be opened. Although the following crystalline systems to be discussed are different from the CaOx system, the underlying chemical principles will give insights regarding the understanding of our system. Kaplan and collaborators supported that the growth of a final crystalline microstructure was diffusion-controlled at the co-precipitation front in a microfluidic reactor[22]. To this end, they investigated the "three-steps" growth of carbonate-silica from CO_2, $BaCl_2$ and Na_2SiO_3. The final shape of carbonate-silica structures relied on the primary density in $BaCO_3$ nuclei starting from CO_2 and Ba^{2+} (pH 12). Actually, batch syntheses showed that high densities in $BaCO_3$ nuclei led to vase-like or petal-like carbonated-silica (**Figures 12a-b**). In contrary, low nucleation directed carbonated-silica growth to coral-like structures (**Figure 12c**). In the micro-reactor, the results enlightened a growth in coral-like microcrystals, in response to low nucleation in $BaCO_3$ (**Figure 12e**). Kaplan *et al.* explained it due to the limited diffusion of CO_2

at the precipitation front with Ba^{2+} ions. Zeng *et al.* went further by studying the formation of calcium carbonate $CaCO_3$ in laminar microfluidics[23]. In a "Y-shaped" microfluidic device, they induced $CaCO_3$ crystallization under co-laminar mixing of equimolar solutions of $CaCl_2$ and Na_2CO_3 injected at equal flow rates. They assessed the transient formation of amorphous $CaCO_3$ (ACC) prior to its transformation into crystalline $CaCO_3$ through dissolution-recrystallization mechanisms. They correlated it to the establishment in the channel of an asymmetric supersaturation ratio in Ca^{2+} and CO_3^{2-} ions. Mass transfer was diffusion-controlled and influenced the reaction phenomenon at the contact interface between the two fluids. ACC formed in the side where CO_3^{2-} ions were delivered whereas crystalline $CaCO_3$ crystals formed in the side of Ca^{2+} ions delivery. The growth of crystalline $CaCO_3$ caused the decrease in Ca^{2+} and CO_3^{2-} ions (*i.e.* decrease in supersaturation ratio), which were maintained by way of dissolution of ACC. Consecutively, it resulted in the promoted growth of $CaCO_3$. Therefore, Zeng and collaborators demonstrated as well that diffusion-controlled phenomena occurring in laminar microfluidics played a key role in directing the crystallization reaction.

In our study, the flow conditions limited the diffusion at the mixing interface. Thereby, an important flow rate (high P_e value) favored the transport of ions by convection in the flow direction rather than by diffusion. Nonetheless, Ca^{2+} and Ox^{2-} ions at the liquid-liquid interface can induced the *heterogeneous* nucleation of CaOx nuclei onto the coverslip surface. Because it is the thermodynamically stable phase, we could assume that COM nuclei would first form at high P_e although mixing was on progress. On the other hand, a decrease in flow rate facilitated Ca^{2+} and Ox^{2-} ions at the fluids contact interface. Enhanced diffusion resulted in "proper" mixing, towards *heterogeneous* nucleation of COD nuclei accordingly to $[Ca^{2+}] / [Ox^{2-}] \gg 1$. Consequently, this suggested the role of the flow rate in favoring one crystalline phase rather than another.

To summarize partially, the flow condition does not seem to alter the formation of COD crystals solely in the continuous reagents solution. Indeed, all exiting crystals correspond to COD crystals. On the other hand, the decrease in the flow rate influences CaOx crystallization on the supportive glass coverslip. In **Figure 11** in section **1.b.i**, preliminary results showed that CaOx crystallization occurred with the dominant occurrence of COM and the rare formation of COD crsytals onto the glass substrate. In the micro-reactor, a decrease in flow rate induces a decrease in P_e. It means that Ca^{2+} and Ox^{2-} diffusion at the co-precipitation front is the dominant phenomenon compared to the convection. In turn, Ca^{2+} and Ox^{2-} mixing is "properly" achieved and ultimately enhances the incidence of COD crystals with respect to CaOx crystallization. Therefore, the formation of COM and/or COD crystals is probably limited by diffusion phenomena at the co-laminar front of reagents regardless of the chemical conditions.

ii.The evolution of concentration gradients in $Ca^{2+}_{(aq)}$ and $Ox^{2-}_{(aq)}$ ions

When depicting CaOx crystallization, **Figure 3f** showed that the crystallization reaction occurred into a conical shape. Furthermore, the observations from the previous section strengthened this trend with respect to the studied flow rates (**Figures 10a-b**).

To support the experimental findings, numerical simulations of the transport phenomena occurring within the microchannel were run using COMSOL Multiphysics® software (version 4.2), for each flow condition (**Figures 13a**, **13d, 13g** for Q = 1.00 *µL.min*$^{-1}$, **Figures 13b**, **13e**, **13h** for Q = 0.10 *µL.min*$^{-1}$ and **Figures 13c**, **13f**, **13i** for Q = 0.01 *µL.min*$^{-1}$). At this point, we want to remind that the slowest flow rate, *i.e.* Q = 0.01 *µL.min*$^{-1}$, was aimed to be experimentally investigated and the work is still in progress. The objective of the numerical approach was to establish a relationship between CaOx crystallization and the state of mixing in Ca^{2+} and Ox^{2-} ions (*in fine* the supersaturation) in the microchannel. The concentration distribution of Ca^{2+} (**Figures 13a-c**) and Ox^{2-} (**Figures 13d-f**) species at 25°C in the channel was calculated in the convection and diffusion modes using the incompressible Navier-Stokes equation (**2. 2**) in steady-state mode.

The mass balance equation was implemented in the convection and diffusion application mode

$$\nabla . (- \mathrm{D_i} \nabla \mathrm{c_i}) = - \vec{\mathrm{u}} \nabla . \mathrm{c_i} \quad (2.7)$$

with $\mathrm{D_i}$ = the self-diffusion coefficient (*m².s*$^{-1}$) of species i (calcium or oxalate ions) in water at 25°C in **Table 1**, $\mathrm{c_i}$ = the concentration (*mmol.L*$^{-1}$) of species i and $\vec{\mathrm{u}}$ = the fluid velocity vector (*m.s*$^{-1}$). Finally, the supersaturation (SS) gradients were simulated at discrete locations in the microchannel (**Figure 13g-i**) using the following definition[24]

$$\mathrm{SS} = \frac{\mathrm{c_{oxalate}} \cdot \mathrm{c_{calcium}}}{\mathrm{c^{eq}_{oxalate}} \cdot \mathrm{c^{eq}_{calcium}}} \quad (2.8)$$

with $\mathrm{c^{eq}_{oxalate}}$ and $\mathrm{c^{eq}_{calcium}}$ = the concentrations of Ox^{2-} and Ca^{2+} ions at equilibrium, respectively (*i.e.* the solubility at 25°C about 3.1 × 10^{-2} *mmol.L*$^{-1}$)[25].

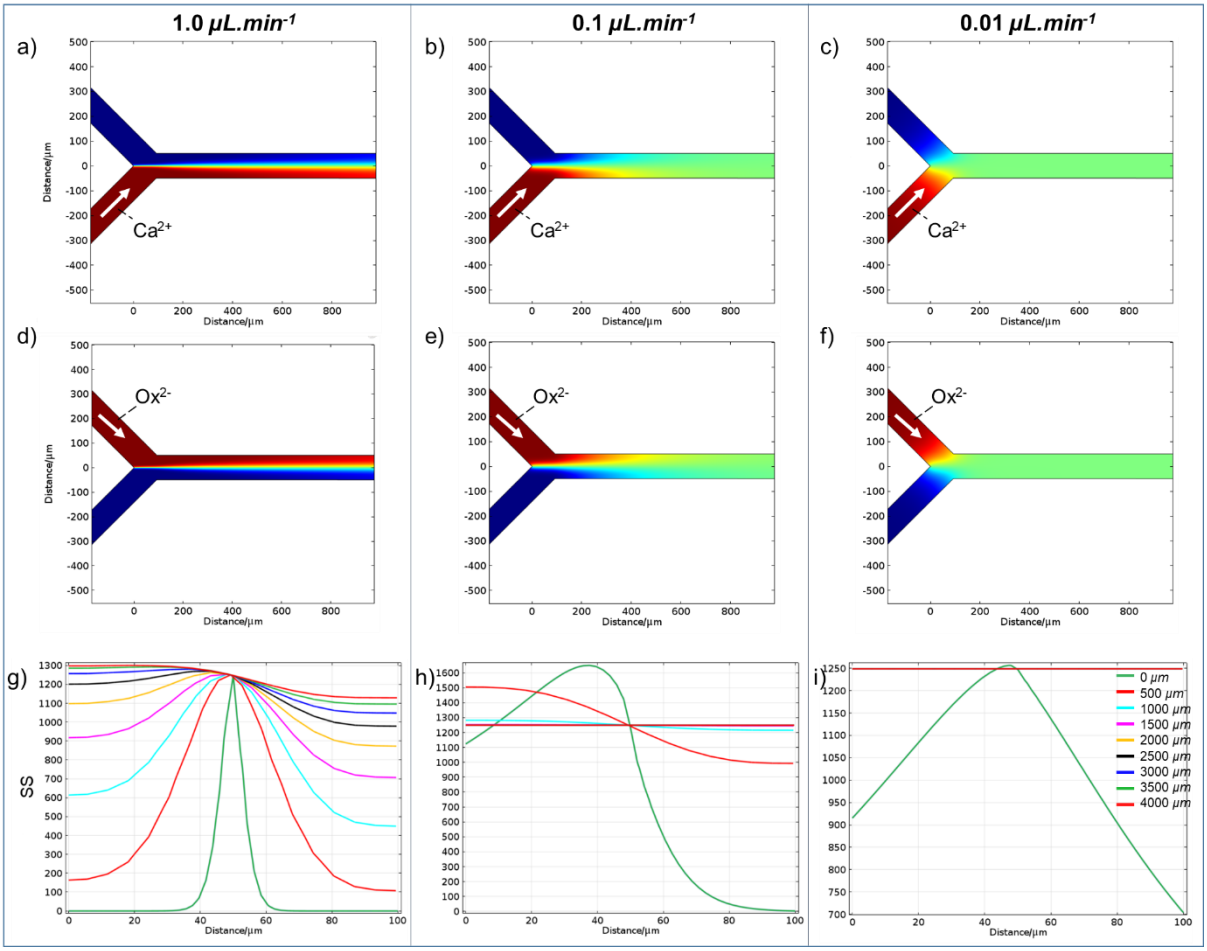

Figure 13. Numerical simulations of the convection and diffusion phenomena occurring in the micro-device *at equilibrium* for all flow rates of interest. The incompressible Navier-Stokes equation is solved in steady-state condition at 25°C. Results are displayed for the concentration distribution of Ca^{2+} species (**Figure 13a-c**) and Ox^{2-} species (**Figure 13d-f**) in the microchannel as a function of the molecular flow rate. For **Figure 13a-f**), the concentration gradient of the species under scrutiny is showed as a color gradient from blue (0) to red (maximal concentration). **Figure 13g-i**) supersaturation (SS) distribution profile during mixing in the microchannel at equal flow rates for Ca^{2+} and Ox^{2-} species at different distances from the channel "Y-junction" (distances from junction are given in **Figure 13i**).

Prior comments, it is important to specify that the numerical results are obtained *at infinite time* and consequently, *at equilibrium*. Therefore, the simulations did not inform about the kinetics acting in the microchannel. At all flow rates, Ca^{2+} ions (Ox^{2-} ions, respectively) could diffuse to the oxalate-rich side (calcium-rich side, respectively) as indicated by the color gradient from red to green to blue in **Figures 13a-f** (maximal to intermediate to zero concentration).

Along the microchannel, the concentration gradients in Ca^{2+} and Ox^{2-} ions transversally spread into the shape of a cone. The corresponding diffusion cones widened and shifted closer to the "Y-junction" as the flow rate, *i.e.* P_e, decreased. A low P_e value induced the slow convection of both Ca^{2+} and Ox^{2-} species in the microchannel, favoring the transversal diffusion. From the concentration distributions of Ca^{2+} (**Figures 13a-c**) and Ox^{2-} (**Figures 13d-f**), the influence of the flow rate (and ultimately P_e) on the molecular mixing could be deduced (**Figures 13g-i**). In the 100 × 100 *µm* square section plane of the microchannel, the ion product of concentrations

was simulated at different distances away from the junction for 1.00, 0.10 and 0.01 $\mu L.min^{-1}$ (**Figures 13g**, **13h** & **13i**, respectively). In the case of 1.00 $\mu L.min^{-1}$ (**Figure 13g**), the different curves depicting the transversal SS profiles lost their symmetry as a function of the distance from the junction. This observation was expected regarding an initial higher concentration in Ca^{2+} compared to Ox^{2-} ions. Furthermore, the slow evolution of the transversal SS zone indicated that SS was confined close to the liquid-liquid interface. Consequently, the complete molecular mixing was hardly reached even at 4000 μm from the junction. In contrary, the complete molecular mixing was achieved at shorter distance from the junction when decreasing the flow rate (**Figures 13h** & **13i**).

The conical shape of concentration gradients obtained by COMSOL simulations (**Figures 13a-f**) enlightened on the conical shape of CaOx crystallization (**Figures 10a-c**). Since the mixing in Ca^{2+} and Ox^{2-} ions occurred in the form of a cone, it was easy to understand that CaOx crystals would precipitate according to the shape of the mixing zone. The gradual decrease in the flow rate led to a widening of the CaOx precipitation cone as supported by α (**Table 3**). This parameter stood for an indirect evidence of the role of P_e on the mixing of Ca^{2+} and Ox^{2}. It induced an extended ion mixing zone in the width of the microchannel. Ultimately, it broadened the precipitation cone of CaOx crystals. Herein, mixing at the liquid-liquid interface was again diffusion-limited with respect to the flow rate.

The numerical simulations allowed predicting how CaOx crystallization would be affected by local hydrodynamics. The decrease in flow rate (and associated P_e) of chemical species resulted in “smooth” gradients facilitating Ca^{2+} and Ox^{2-} molecular diffusion at the liquid-liquid interface and broadening the diffusion cone. Such mixing in Ca^{2+} and Ox^{2-} species was fully achieved at a shorter distance from the microchannel junction. Accordingly, the supersaturation SS was attained across the entire channel. Although CaOx crystallization was likely to spread in the full width of the channel at slow flow rates, the reaction was expected to be delayed with respect to the flow conditions. In contrary, an increase in flow rate was expected to confine CaOx crystallization at the liquid-liquid interface. Consequently, CaOx crystallization was anticipated to occur faster in response to high SS in the thin fluid layers at the liquid-liquid interface. Noteworthy, the full mixing in Ca^{2+} and Ox^{2-} species would be obtained at a longer distance from the microchannel junction. In summary, the manipulation of hydrodynamics in the microchannel appeared as a promising strategy to influence CaOx crystallization.

b. The growth kinetics of calcium oxalate crystal

i. *In situ* and in real time monitoring of CaOx crystal growth

Studying CaOx crystal growth is of prime importance to understand kidney stone formation. Usually, *in vitro* crystallizers serve to incubate well-characterized CaOx seeds in metastable solutions of Ca^{2+} and Ox^{2-} ions[26]. It enables to quantify the thermodynamic and/or kinetic factors associated to CaOx crystallization. Each crystallizer presents, up to a certain extent, similarities to the intrarenal mechanisms of stone formation. Hereafter, a brief review will summarize the capacity of several *in vitro* crystallizers of interest. For further details, refer to **Chapter 1** section **2.c.ii**. For instance, the Constant Composition Method (CCM) is a steady-state approach using a crystallizer that measures the growth or inhibition rate of CaOx crystals at constant supersaturation (SS) in Ca^{2+} and Ox^{2-} ions[27]. Alternatively, the Mixed-Suspension Mixed Product Removal (MSMPR) crystallizer estimates the nucleation and growth rates of CaOx crystals at continuous feed in Ca^{2+} and Ox^{2-} solutions[14,28,29] (**Figure 8b** in section **1.b.ii**). This technique aims at imitating CaOx stone growth in the renal calyx. One interesting system is the Flow Model of Crystallization in Gels (FMCG) crystallizer[15] (**Figure 8d**). This method investigates the growth of CaOx crystals in a gel state from a flow of SS artificial urine (with respect to the fixed-particle theory)[17,18,26]. One last noteworthy system is the isothermal growth cell from DeLong and Briedis[16] (**Figure 8e**). This continuous-flow system enables the direct visualization and measurement of CaOx crystal growth through a transparent window.

Interestingly, all crystallizers operate at comparable concentrations in Ca^{2+} and Ox^{2-} ions to those of stone formers (≈ $mmol.L^{-1}$). Furthermore, the MSMPR and FMCG crystallizers are continuous-flow techniques used to depict the growth mechanisms in urinary tracts. However, the FMCG flow rate (0.5 $mL.min^{-1}$, *i.e.* mean urinary flow of one kidney) is ≈ 50×10^3 times higher than of one collecting duct (10 $nL.min^{-1}$). Similarly, the MSMPR flow rate is ≈ 40×10^5 times more important[14]. Besides, none of the *in vitro* crystallizers accounts for the micro-tubular confinement of the nephron. The isothermal growth cell developed by DeLong *et al.* consists of a circular chamber of 30 *mm*, yet it is 300 times larger than one single collecting duct (Ø = 100 *µm*)[16]. Last, growth rate measurements mainly relied on indirect measurements such as decrease in Ca^{2+} ions concentration in the reaction medium (CCM), CaOx crystal size distributions (MSMPR) or light scattering (FMCG).

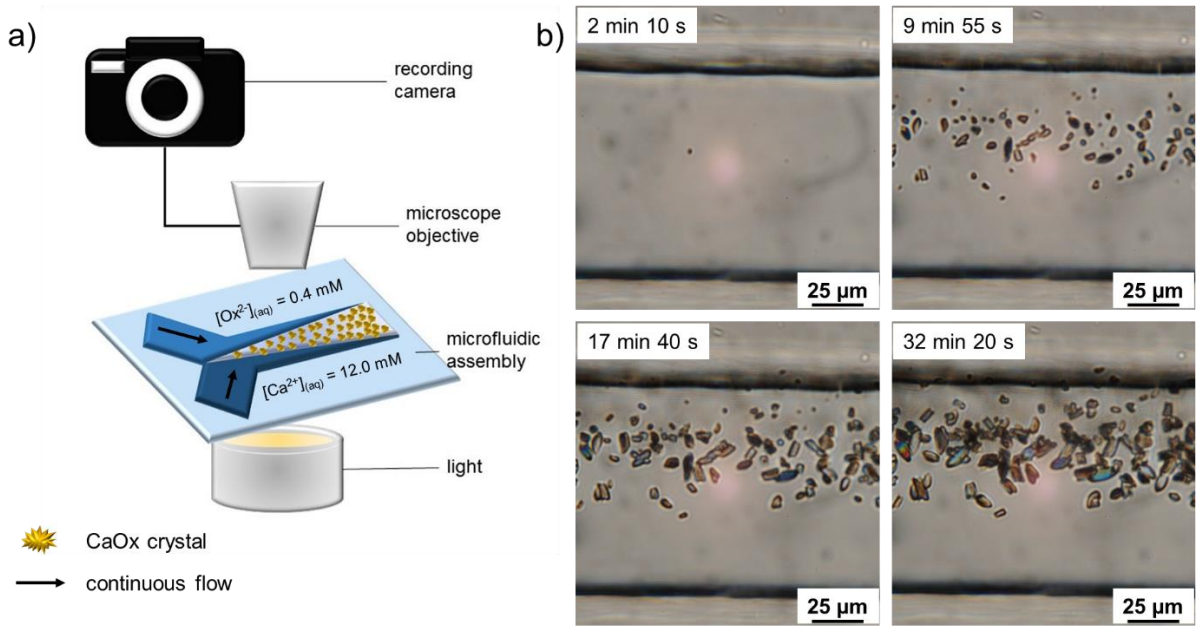

Figure 14. *In situ* monitoring of CaOx crystal growth as a function of time: a) illustrative scheme of the collecting duct-on-a-chip device adapted under a light microscope for monitoring CaOx crystal growth at continuous-flow condition; b) set of images depicting the growth of CaOx crystals within the micro-reactor at different times (magnification 400×). In the present example, crystallization is monitored at a distance of 300 *µm* from the microchannel "Y-junction" for a molecular flow rate of $Q_{Ca^{2+}} = Q_{Ox^{2-}} = 1.0$ *µL.min*$^{-1}$.

The collecting duct-on-a-chip device overcomes all these limitations for the investigation of CaOx crystallization at physiopathological concentrations in Ca^{2+} and Ox^{2-} ions, similar micro-confinement and flow-condition of a single collecting duct. Moreover, the device transparency permits direct visualization of CaOx crystal growth (alike the isothermal growth cell of DeLong and collaborators[16]). Under appropriate configuration (**Figure 14a**), the *in situ* and in real time study of the growth of a single CaOx particle is reached (**Figure 14b**). *For further specifications*, see **Appendix**.

The growth kinetics of CaOx crystals was investigated according to the flow conditions (*i.e.* 1.00 and 0.10 *µL.min*$^{-1}$). A parameter of interest is the macroscopic induction time of crystallization t_0, defined as follows. Starting from the time the reactor is filled entirely with the reagents, t_0 is the time required to observe the formation of the first CaOx micro-crystals (≈ 1.0 *µm*) in the microchannel. Consequently, events happening at the nanoscale (*e.g.* CaOx nucleation) are far below the spatial resolution limit. With respect to the flow condition, CaOx crystallization started at t_0 = 1.0 ± 0.5 and 8.0 ± 0.5 *min* for 1.0 and 0.1 *µL.min*$^{-1}$, respectively. The increase in t_0, associated to the decrease in the flow rate, suggested a *slow homogenization* of concentration gradients in Ca^{2+} and Ox^{2-} ions. As a reminder, such kinetics information was not accessible using COMSOL simulations since results were obtained *at equilibrium*. In consequence, the slow homogenization delayed the molecular mixing of reagents and subsequent CaOx crystallization in the microchannel. Thereby, the transversal

diffusion in Ca^{2+} and Ox^{2-} ions appeared to be a slow process, albeit favored compared to convection at low flow rate (*i.e*. low P_e).

The *in situ* visualization of CaOx crystallization provides with experimental evidence regarding the time needed to achieve molecular mixing along with the kinetics. Yet, the increase in induction time of crystallization t_0 shows that mixing is a slow phenomenon. In turn, we expect that the slow mixing of Ca^{2+} and Ox^{2-} ions will affect CaOx crystallization and ultimately the growth kinetics of CaOx crystals.

ii. Growth model: surface- or transport-limited kinetics?

From now on, it is important to notify that we will consider CaOx crystallization in terms of the crystal growth process only. We will not address or discuss phenomena related to CaOx nucleation process. As briefly mentioned before, the detection of crystallization events in the microchannel occurs at the microscale. In consequence, events happening to any nano-objects are out of reach. In addition, we will only focus on the growth of isolated CaOx crystal and will not account for the growth of crystal induced by secondary nucleation (although suspected to exist).

Towards in-depth understanding of the coming experimental observations, noteworthy contributions from the literature have to be taken into consideration. Nowadays, the prevailing model relies on the surface-reaction kinetics[16,29-31]. With respect to such model, the growth mechanism is governed by the saturation ratio Ca^{2+} and Ox^{2-} ions at the surface of the growing crystal. For instance, Nancollas and Gardner monitored the growth rate of COM seed crystals in supersaturated solutions[30]. In a static thermostated reaction vessel, they measured the calcium conductivity as a function of time and modelled CaOx growth kinetics as follows

$$-\frac{d[Ca^{2+}]}{dt} = k\,S\,([Ca^{2+}] - [Ca^{2+}]_0)^2 \quad (2.9)$$

with $[Ca^{2+}]$ = calcium concentration at time t, $[Ca^{2+}]_0$ = solubility under the experimental conditions, S = surface area of added seed crystals and k = observed rate constant for crystal growth. Ions incorporation at the crystal surface plausibly occurs based on simultaneous dehydration of pairs of calcium and oxalate growth sites due to the ion concentrations in the reaction medium. Another hypothesis relies on ion adsorption on the crystal surface with partial or complete dehydration and subsequent surface diffusion to active growth sites. Using the isothermal growth cell (*i.e.* continuous flow system), DeLong and Briedis also supported that COM crystal growth at constant SS obeyed surface-reaction kinetics[16].

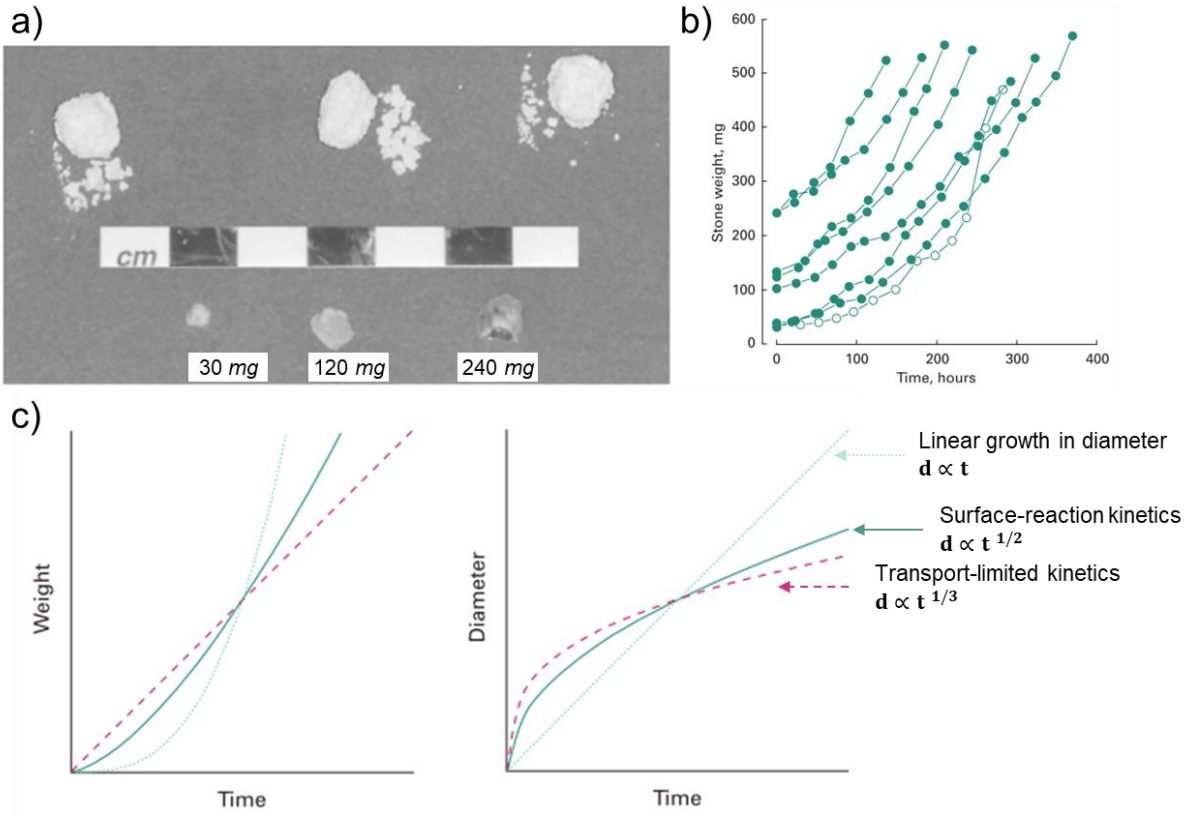

Figure 15. Enlargement of CaOx stones in a continuous-flow MSMPR crystallizer from Ananth *et al*.[29] with permission from John Wiley and Sons. Picture in (a) stands for representative examples of CaOx stones grown *in vitro* (upper three images) and example of three fragments used as initial core (lower). Graph in (b) presents *in vitro* growth curves for eight fragments of human calculi. Finally, graphs in (c) are illustrations of the curve shapes of the three growth mechanisms under scrutiny.

Ananth and collaborators made the same assertion after investigating the enlargement of CaOx stones in a MSMPR crystallizer[29] (**Figure 15**). Briefly, they retrieved CaOx fragments from patients (bottom in **Figure 15a**) and suspended them in a crystallizer. Afterwards, the CaOx fragments were supplied with $Na_2C_2O_4$ (2.4 $mmol.L^{-1}$) and $CaCl_2$ (12 $mmol.L^{-1}$) solutions at 0.32 $mL.min^{-1}$. For more than 12 weeks, the fragments were weighted until they reached 500 *mg* (upper part in **Figure 15a**) with the weight plotted against time t (**Figure 15b**). The authors processed the data according to three possible mechanisms depicting CaOx stone growth (**Figure 15c)**. One possible mechanism is the linear increase in diameter (*i.e.* diameter $d \propto t$, weight $w \cong d^3 \propto t^3$). Another one is the surface-reaction kinetics (*i.e*. surface-area $a \cong d^2 \propto t$, $d \propto t^{1/2}$, *in fine*, $w \cong d^3 \propto t^{3/2}$). Last is the transport-limited kinetics (*i.e*. $d \propto t^{1/3}$, $w \cong d^3 \propto t$). With respect to their experimental data, they concluded with the growth of the fragments being dependent on the surface-reaction kinetics.

Attention is drawn to the transport-limited process to enlarge CaOx stone. Such mechanism accentuates the importance of transport rate of electrolytes from the solutions to the emerging CaOx stone. Kassemi and collaborators suggested that this process could not be dissociated from the growth kinetics of CaOx stones[32]. To address the problematic, they developed an

algorithm coupling the effects of transport- and surface-controlled kinetics. They used the Damkohler dimensionless number D_a

$$D_a = \frac{K_v''}{K_m} \quad (2.10)$$

(with K_v'' = volumetric growth rate constant (*cm.s*$^{-1}$) and K_m = convective mass transfer coefficient (*cm.s*$^{-1}$)) and the solution *SS* as criteria to describe the growth rate of CaOx crystal. Briefly, D_a characterizes the ratio between surface-reaction and transport rate of electrolytes. At low Da and low SS, surface concentrations of Ca^{2+} and Ox^{2-} approached their concentrations in solution. In response, the growth rate was likely limited by the surface reaction kinetics. At high D_a and high SS, Ca^{2+} and Ox^{2-} surface concentrations shifted towards their equilibrium values. Thereby, the growth rate appeared to be limited by the transport of electrolytes. In any case, the increase in CaOx stone size *vs.* time shifted the growth reaction mechanism inevitably towards a transport-limited growth. Worth mentioning, the CaOx growth models throughout the different studies are consistent when accounting for CaOx crystals with a spherical geometry. One must bear this significant detail in mind when discussing the following experimental results.

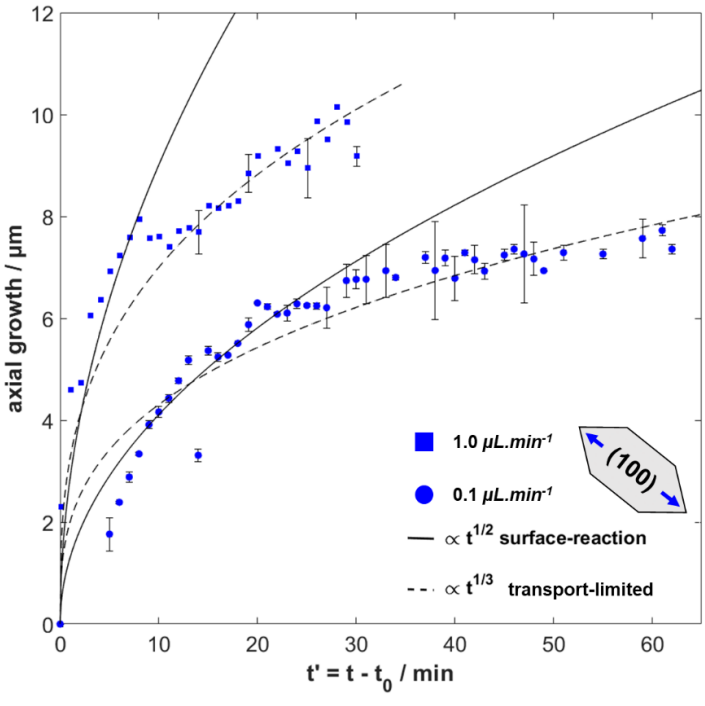

Figure 16. Time evolution of the axial growth of (100) crystallographic face for monoclinic prismatic COM crystal. Schematic illustration of a model COM crystal shows the (100) crystallographic face under scrutiny. Blue markers stand for the experimental data points monitored with respect to the flow conditions. Black lines (solid and dashed) are fitting models to describe the growth kinetics of COM crystals. The time $t' = t - t_0$ stands for a translated time between the induction time t_0 and the time t when the measurement is made.

To study the growth kinetics of CaOx crystals, monoclinic prismatic COM crystals (**Figure 5b** in section **1.b.i**) served as a model system due to its main occurrence. In particular, the growth of (100) crystallographic face was under scrutiny and referred as the axial growth hereafter. With respect to the flow condition, series of images such as in **Figure 14b** enabled to measure the axial growth of monoclinic prismatic COM crystal *vs.* time *t'* (blue markers in **Figure 16**). We want to specify that t' stands for a translated time between the CaOx induction time t_0 and the time t when the measurement is made. As the flow rate decreased, the axial growth decreased accordingly. For example, axial growth at t' = 20 *min* is ≈ 8.5 and 6.0 *µm* for 1.00 and 0.10 *µL.min*$^{-1}$, respectively and supported the overall decrease in CaOx size range l_{CaOx} (**Table 4**). Furthermore, a slow COM crystal growth agreed with a slow molecular mixing of Ca^{2+} and Ox^{2-} ions at low flow rate (section **2.b.i**). An estimate of $v_0(Q)$, the nominal growth rate in the linear part of data points, strengthened the assumption: $v_0(1.00\ \mu L.min^{-1})$ = 1.79 ± 0.04 *µm.min*$^{-1}$ and $v_0(0.10\ \mu L.min^{-1})$ = 0.41 ± 0.06 *µm.min*$^{-1}$.

At this point, further considerations have to be made regarding the collecting duct-on-a-chip device. The continuous-flow micro-reactor allows establishing concentration gradients in Ca^{2+} and Ox^{2-} ions as numerically illustrated in **Figures 13a-f** (section **2.a.ii**). In consequence, constant SS in electrolytes is ensured at discrete locations along the microchannel (**Figures 13g-i**). However, the state of constant SS depends on the continuous transport of Ca^{2+} and Ox^{2-} ions making the system in constant non-equilibrium. Under these circumstances and based on the experimental data points (**Figure 16**), we suggest the following model regarding the growth behavior of COM crystal

$$\text{axial growth}(t') = \begin{cases} a\, t'^{1/2} & \text{for axial growth} < \text{critical size} \\ b\, t'^{1/3} & \text{for axial growth} > \text{critical size} \end{cases} \quad (2.\ 11)$$

with a and b = growth constants in **Table 5**. Before going further, we want to remind that the power laws in equation (**2.** 11) apply to CaOx crystals with a spherical geometry leading to an isotropic growth. In the context of our study, the (100) crystallographic face of COM crystals grows in an anisotropic direction. As a first approach, we consider the monoclinic prismatic COM crystal written down in a circle whose diameter is roughly equal to the major axis of (100) crystallographic face.

Table 5. Constants associated to the growth model from eq. (**2. 11**).

$Q_{Ca^{2+}} = Q_{Ox^{2-}}$	a ($\mu m.min^{-1/2}$)	b ($\mu m.min^{-1/3}$)
1.00 $\mu L.min^{-1}$	2.8	3.2
0.10 $\mu L.min^{-1}$	1.3	2.0

The equation (**2.** 11) shows a growth behavior following two distinct regimes. In the beginning, the axial growth $\propto t'^{1/2}$ which stood for a surface-limited kinetics (solid line in **Figure 16**). The small yet emerging COM micro-crystal was affected solely by the state of SS in Ca^{2+} and Ox^{2-} ion concentrations at its surface. Then, the crystal reached a critical size (≈ 4 μm) and a take-over occurred between the power laws. Then, the axial growth $\propto t'^{1/3}$ and stood for a transport-limited kinetics (dashed line in **Figure 16**). The transport rate of reagents into the COM lattice limited the crystal growth. Interestingly, the kinetics in two regimes was valid at all flow conditions. Therefore, we could hypothesize that a decrease in flow rate would just delay the growth of COM crystal without affecting the inner mechanisms of its kinetics. Another evidence of delayed growth of CaOx crystal was shown in **Figure 17**. The surface state examination of the COM crystal showed the emergence of stratifications as the flow decreased. We assumed that these uneven planes exposed the sites where Ca^{2+} and Ox^{2-} ions insert to enlarge the CaOx crystal. As the flow decreased, insertion within the crystal matrix was delayed due to the limited transport of Ca^{2+} and Ox^{2-} ions from the solution.

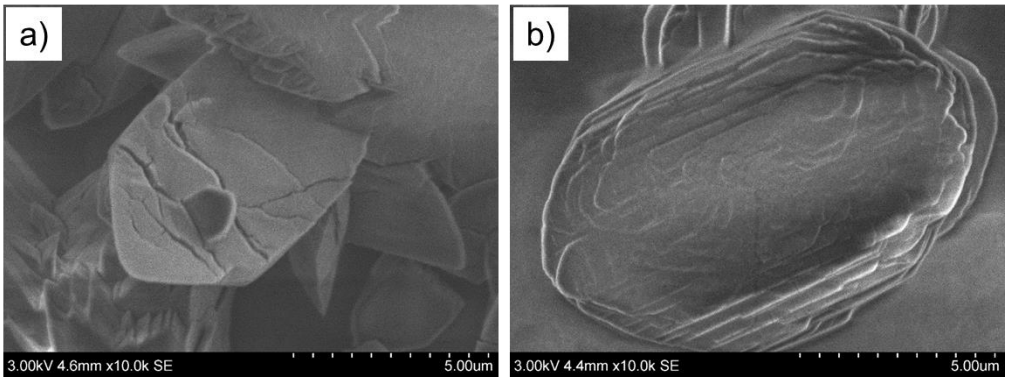

Figure 17. SEM images of the surface state of COM crystals against the flow condition. The flow rate decreases from a) to b) and account for 1.0 and 0.1 $\mu L.min^{-1}$, respectively.

In the collecting duct-on-a-chip platform, the state of constant SS rested on the continuous transport of Ca^{2+} and Ox^{2-} ions. Henceforth, CaOx crystal growth could not depend solely on the prevailing surface-reaction kinetics[16,29,30]. Crystal growth had to account for transport-limited kinetics[32]. Herein, we proposed a growth model involving at least two regimes. At first, an isolated COM particle grew according to the state of SS in electrolytes at its surface (growth $\propto t'^{1/2}$). Then, at a critical size the crystal growth relied on the transport-rate of precursors

(growth $\propto t'^{1/3}$). This model described the growth kinetics of COM crystal at all studied flow conditions. The take-over of the second growth regime was just being delayed as the flow rate decreased.

c. Numerical approach of calcium oxalate crystallization in a micro-reactor

i. Methodology

So far, we assess CaOx crystallization in the collecting duct-on-a-chip device under various experimental conditions. Crystal characterization shows the formation of COM and COD crystals such as in real kidney stones. Additionally, direct measurements enable to describe the growth behavior of CaOx particles. However, the investigation of crystallization at its primary stage lacks and limits the comprehension of CaOx reactivity under confinement. Numerical simulations from COMSOL Multiphysics® software demonstrate the establishment of concentration gradients in Ca^{2+} and Ox^{2-} ions. These gradients are flow-dependent and become “smoother” as the flow rate decreases. Consequently, the state of complete mixing is achieved at a shorter distance within the microchannel and affects CaOx crystallization. Nevertheless, the simulations are conducted at steady-state and the corresponding results are obtained at equilibrium. In turn, they do not account for the emergence of crystals in response to the concentration gradients and, *in fine*, the state of mixing. A model considering the chemical reactions of CaOx crystals in the state of continuous-flow, *i.e.* under non-equilibrium conditions, would be useful on two points. First, it would consolidate the understanding of the experimental findings. Then, it could help predicting the outcomes of future experiments. The creation of such model has been made possible in partnership with Pr. Ágota Tóth and Pr. Dezső Horváth from the University of Szeged in Hungary. The in-house code they have developed gives insights regarding CaOx crystallization under microfluidic confinement. The methodology used is presented hereafter for further understanding of the numerical approach.

In the modeling study, two miscible liquids were pumped into the microfluidic device. The laminar flow was governed by the Navier-Stokes equation for incompressible fluids as described in (**2. 2**) section **1.a.i**. The density was defined as a linear function of the chemical composition

$$\rho = \rho_0 + \sum_i \rho_i c_i \quad (\mathbf{2.\ 12})$$

with ρ_i = density of chemical species i ($kg.m^{-3}$) and c_i = concentration of species i ($mmol.L^{-1}$).

With respect to the reagents, the following reactions took place

$$CaCl_{2(aq)} + Na_2C_2O_{4(aq)} \rightarrow CaC_2O_{4(aq)} + 2NaCl_{(aq)} \quad (2.13)$$

$$CaC_2O_{4(aq)} \rightarrow CaC_2O_{4(s)} \quad (2.14)$$

providing that $[Ca^{2+}] \times [Ox^{2-}] > K_{sp(CaOx)}$ was respected. Noteworthy, $CaC_2O_{4(aq)}$ represents the colloidal CaOx prior to precipitation (≤ 1.0 *μm*). The mass balance equation was implemented with a new term compared to equation (**2. 7**) in section **2.a.ii** in order to complete the model

$$\frac{\partial c_i}{\partial t} + \vec{u} \cdot \nabla c_i = D_i \nabla^2 c_i + \nu_i r \quad (2.15)$$

and introduced the rate of reaction (r) for the species $CaCl_2$, NaC_2O_4, colloidal CaOx and NaCl. Herein, the rate of reaction accounted for both nucleation (r_n) and growth (r_g) acting simultaneously with respect to crystallization

$$r = r_n + r_g = (k_n + k_g \sum_i d_i^2)([CaCl_2][Na_2C_2O_4] - K_{sp(CaOx)}) \quad (2.16)$$

where k_n = rate coefficient for homogeneous nucleation, k_g = rate coefficient for growth and d_i = diameter of particles present within a cell volume ΔV. Noticeable, the reaction in (**2. 14**) was considered to occur *instantaneously* during the time scale of the transport processes. In turn, no colloidal CaOx accumulated unless there was not enough amount for the formation of a new particle with d > 1 *μm* via homogeneous nucleation (see below).

The governing equations (**2. 2**) and (**2. 15**) were solved by a finite volume method using the Open-FOAM package[33] with the microfluidic channel being represented by a volume with length of 25 *mm*, a cross-section of 100 × 100 *μm* and a T-shaped head for the two inlets. The in-house code of our collaborators, based on the PIMPLE algorithm[34], incorporated Lagrangian particle tracking for processing the formation of solid CaOx. At each iteration step, a particle with a diameter d_p in the volume ΔV increased its mass according to

$$\Delta m_p = \frac{k_g d_p^2}{k_n + k_g \sum_i d_i^2} M_r[CaC_2O_{4(aq)}]\Delta V \quad (2.17)$$

with M_r = molar mass of the crystalline CaOx. From the preceding equation, the size increase could be calculated as well. Additionally, homogeneous nucleation within the volume occurred

$$\Delta m_n = \frac{k_n}{k_n + k_g \sum_i d_i^2} M_r[CaC_2O_{4(aq)}]\Delta V > \frac{\rho\pi(1\ \mu m)^3}{6} \quad (2.18)$$

in which case, [$CaC_2O_{4(aq)}$] was set to zero. Otherwise, the concentration of colloidal calcium oxalate remained non-zero.

The numerical calculations were conducted with two sets of initial reagent concentrations, one with [$CaCl_2$] = [$Na_2C_2O_4$] = 12 $mmol.L^{-1}$ and the other [$CaCl_2$] = 12 $mmol.L^{-1}$ and [$Na_2C_2O_4$] = 4.0 $mmol.L^{-1}$. The initial concentration in sodium oxalate of [$Na_2C_2O_4$] = 0.4 $mmol.L^{-1}$ was not applied since it did not trigger CaOx crystallization in the time scale of the numerical experiments. Furthermore, two different flow rates were applied, *i.e.* 1.0 and 0.1 $\mu L.min^{-1}$. Worth mentioning, CaOx particles generated with the numerical model exhibited a spherical geometry in first approach for convenience purposes.

The model's introduction aimed at setting the scene for the comprehension of the physics at stake with respect to the reactivity of CaOx crystallization. The preliminary results hereafter illustrate the potential of such numerical tool.

ii. Simulating CaOx crystallization

Before discussing the upcoming results, it is worth pointing out that the next figures depict the case scenario of calcium chloride in large excess compared to sodium oxalate, *i.e*. second set of initial reagent concentrations previously introduced.

Alike the results from COMSOL Multiphysics® software, it was possible to emulate the concentration distributions in chemical species from equation (**2. 13**) within the microchannel (**Figure 18**). While the fluid flow dominated along the channel (x - axis), diffusion remained the main mode of transport in the transversal direction (y - axis). However, the model developed by our collaborators accounted for the precipitation of CaOx particles upon contact of reagents. Although $CaCl_2$ (**Figure 18a**) and $Na_2C_2O_4$ (**Figure 18b**) could diffuse within one another, $CaCl_2$ diffused to occupy the initial oxalate-side due to a higher concentration. It was mainly underlined with the asymmetric depletion in oxalate concentration in **Figure 18b**. In turn, precipitation took place to the oxalate-side as revealed by the concentration distribution of the by-product NaCl in **Figure 18c** (see equation (**2. 13**)). While the simulations carried out in section **2.a.ii** informed on the state of SS in the microchannel, the present results supported the reaction of precipitation in response to the mixing in Ca^{2+} and Ox^{2}- ions. Furthermore, they supported the experimental observations regarding the asymmetric formation of CaOx particles in the reactor. The emergence of CaOx particles began on the side where oxalate was injected to later spread to the entire width of the channel primary due to calcium chloride being in large excess.

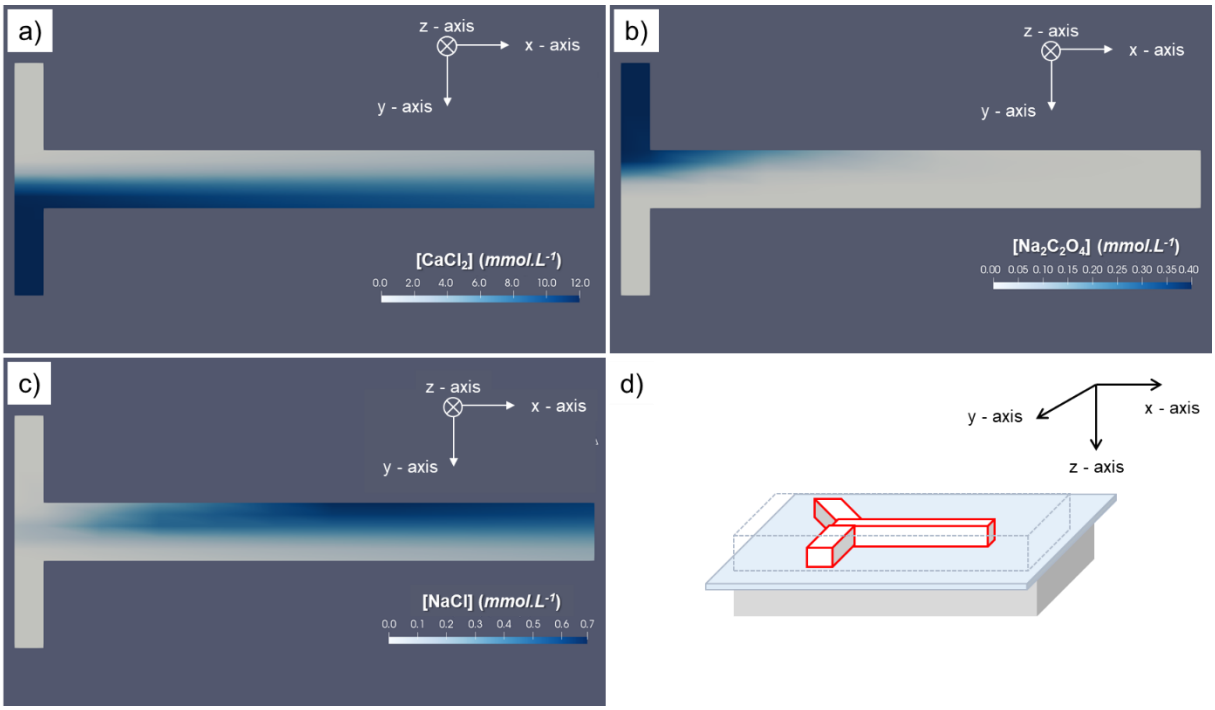

Figure 18. Concentration distribution calculated in case of sodium oxalate being the limiting reagent: a) concentration distribution for calcium chloride; b) concentration distribution for sodium oxalate; c) concentration distribution of soluble product sodium chloride acting as an indirect tracker regarding calcium oxalate reactivity; d) 3-D illustration of the microfluidic device with oriented axes.

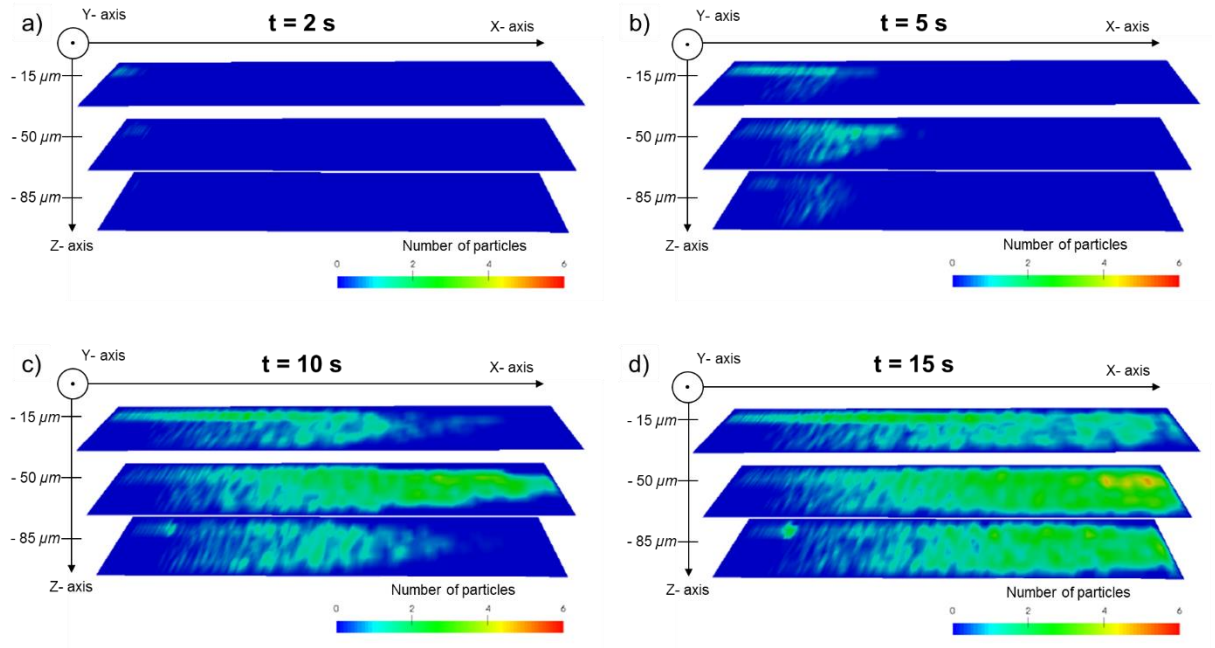

Figure 19. Time evolution of the amount of CaOx particles and corresponding propagation in the channel for the case scenario of sodium oxalate being the limiting reagent. Herein, time stands for the time increment to run the simulations. X-axis stands for the position along the flow-direction, Y-axis the transversal position and Z-axis represents the position from the channel's top to bottom.

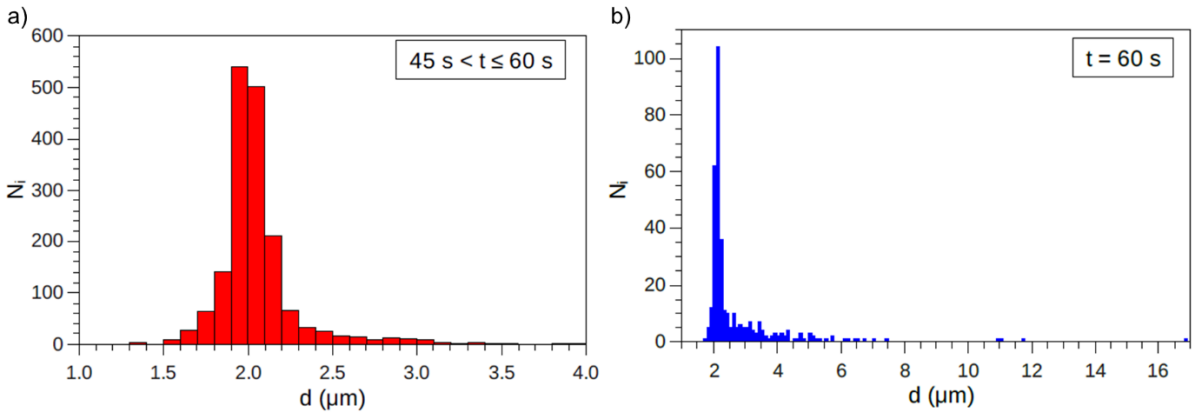

Figure 20. Size distribution of CaOx particles tracked at different positions in the micro-reactor for specific time intervals: a) CaOx particles exiting the microchannel at a time interval from 45 sec until 60 sec; b) CaOx particles that have settled down due to increase in density at 60 sec.

Moreover, it was possible to give an estimate of the amount of particles that formed in the microchannel against simulation time and the z-position (**Figure 19**). Worth mentioning, the z-axis stands for the microchannel depth with z = 0 *µm* and z = - 100 *µm* representing the top and bottom of the channel, respectively. Prior to any further discussion, we raise awareness on the model of reaction regarding CaOx particles. Herein, the reaction is triggered through *homogeneous* nucleation in solution. Consequently, the cascade of events leading to CaOx particles stands for one possible route with respect to crystallization in the micro-reactor. As shown in **Figure 19**, CaOx particles propagated and accumulated along the flow-direction against simulation time. This observation was in accordance with the previous **Figure 18c**. Worth pointing out, the number of particle was more important at z = - 50 *µm* at all time, though particles tended to accumulate more and more at z = - 85 *µm*. This was simply due to the settlement of CaOx particles in response to an increase in mass density as depicted in equation (**2. 17**). Thus, the simulations supported the formation of CaOx particles in the flow-direction. They mainly remained in the flow while a certain amount settled with time at the bottom of the channel.

Further investigations were conducted on the two populations of CaOx particles (settled *vs.* dragged by the flow) with a particular interest in their size distributions (**Figure 20**). With respect to the reaction model, it is interesting to note that again there were more CaOx particles emerging in the flow-direction ($N_i \approx 550$ in **Figure 20a**) rather than at the bottom of the channel ($N_i \approx 100$ in **Figure 20b**). Furthermore, CaOx particles that exited the micro-reactor exhibited a narrow size distribution (mean diameter around d = 2.0 *µm*). In contrary, settled CaOx particles showed a slightly more scattered size distribution starting from 2.0 *µm*. We want to insist on the notion of simulation time displayed in the figures. It is a different notion from all experiment times previously presented in this work. When working with a numerical model,

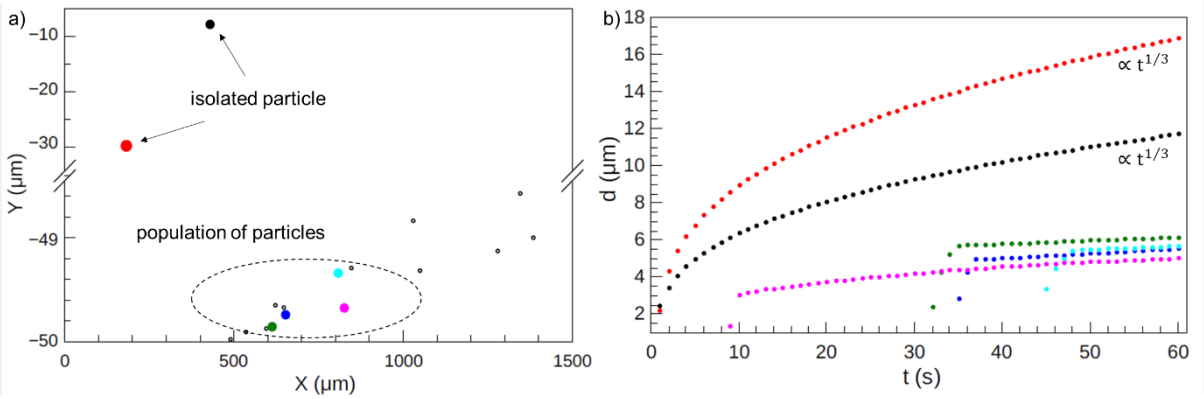

Figure 21. Tracking of individual CaOx particles in the channel: a) position of settled CaOx particles in a limited volume of the reactor. X-axis stands for the position along the flow-direction while Y-axis locates the particles at different positions away from the edge of the channel Y = - 50 *µm*; b) growth against simulation time of the CaOx particles in **Figure 21a**.

one is bound to the time it takes to run the calculations. Thereby, compromises have to be made to depict a faithful model to reality and, in consequence, the result interpretations shall be handled carefully.

Interestingly, it was possible to track the position of CaOx particles after settling in response to the flow-condition (*i.e.* on the XY plane). Pr. Tóth and Pr. Horváth showed that calcium chloride being denser, it tended to advance to the bottom of the channel and created a reverse flow on the top fluid-layer due to continuity. The transverse flow resulted in the accumulation of solid particles close to the edge (*i.e.* at Y = - 50 *µm* in **Figure 21a**). Once settled, the particles continued to grow as shown in **Figure 21b**. However, the growth rate of particles did not solely depend on the solution SS but on the occupancy of a local site. For individual particles, *e.g.* black and red ones in **Figure 21a**, the corresponding growth rate scaled $d \propto t^{1/3}$ in **Figure 21b**. On the other hand, the growth rate was significantly slower for crowded population of particles. Hence, the growth of one particle was correlated to the growth of its respective neighbors.

At this point, it is important to analyze the results from the numerical model with respect to the experimental findings. First, it was possible to account for the reaction of CaOx crystallization in the micro-reactor in the state of continuous-flow. The model even confirmed the asymmetric formation of CaOx particles in case of a large excess of calcium chloride compared to sodium oxalate. Interestingly, the becoming particles could be tracked with respect to the flow-conditions. It was possible to visualize the propagation and accumulation of the particles in the micro-reactor. Furthermore, the model permitted to estimate the size distribution of particles depending on their location in the channel. Regarding the CaOx particles leaving the channel, the narrow size distribution in **Figure 20a** matched the size of COD crystals of ≈ 3 – 5 *µm* in **Figure 7** (section **1.b.i**). At the bottom of the channel, the scattered size distribution of particles (**Figure 20b**) agreed with the various sizes of CaOx crystals observed after experimentations (**Table 3** in section **2.a.i**). Noteworthy, the difference in size range was attributed to the

difference in time definition to run the model and to carry out the experiment. Furthermore, the simulations enabled to predict the settlement of CaOx particles in response to the hydrodynamics. Besides, the growth behavior of particles could be modeled in interaction with surrounding neighbors. An isolated CaOx particle saw its growth rate scaling $d \propto t^{1/3}$, which supported part of the growth model for monoclinic prismatic COM crystal in section **2.b.ii**. Consequently, it seemed realistic to consider that CaOx crystal growth depended on the hydrodynamics with a focus on the transport rate in Ca^{2+} and Ox^{2-} ions. In the case of a population of particles, the model study showed the slowing down of particle growth in plausible response to a competitive growth behavior. Such phenomenon was suspected to occur, though complicated to experimentally investigate due to a lack of spatial resolution.

Herein, the numerical model supported the experimental observations and was valuable towards in-depth understanding of the CaOx crystallization under confinement. In implementing the reaction of CaOx crystallization, the simulations enabled to investigate phenomena experimentally out of reach. Furthermore, they provided with information regarding the physics of CaOx particles in response to the hydrodynamics. The model had its advantages providing that the results were handled with care. Nonetheless, we wanted to recognize some limitations such as the notion of simulation time or the current inability to predict a favored CaOx crystalline phase.

3. Conclusion

In the present chapter, a continuous-flow microchannel was developed as proof-of-concept to simulate the confinement and fluid-flow of one collecting duct in the nephron. This collecting duct-on-a-chip device enabled to induce CaOx crystallization under the co-laminar mixing of Ca^{2+} and Ox^{2-} ions at matching concentrations of patients undergoing kidney stone disease. In the case scenario of combined hypercalciuria and moderate hyperoxaluria condition (*i.e.* $[Ca^{2+}]_{(aq)}$ = 12.0 $mmol.L^{-1}$ and $[Ox^{2-}]_{(aq)}$ = 0.4 $mmol.L^{-1}$), the crystal examination showed that precipitates result in COM and COD crystals such as reported by physicians. Interestingly, a noticeable difference could be made regarding the crystalline phase of the CaOx crystals collected at the channel exit (*i.e.* COD crystals) and those sticking at the channel bottom (*i.e.* mixture of COM and COD crystals). Noteworthy, the facile sealing/unsealing of our micro-reactor permitted to probe CaOx crystals in state thanks to various characterization techniques (*e.g.* SEM or *Raman* spectroscopy).

Compared to other *in vitro* crystallizers, the collecting duct-on-a-chip enabled to study CaOx crystallization with respect to the flow-conditions. A particular focus was made on the role of the concentration gradients in Ca^{2+} and Ox^{2-} ions in the micro-reactor and how these gradients (proportional to the solution supersaturation) seemed to direct the favored emergence of one

crystalline phase or the other one. Considering our initial condition of large excess of Ca^{2+} ion compared to Ox^{2-} ions, it was expected to favor COD crystals at the expense of COM crystals. In the continuous-flow micro-reactor, the experimental observations showed that a high flow rate directed the formation of predominant COM crystals with rare COD crystals. Accordingly, a high flow rate corresponded to a limited inter-diffusion of Ca^{2+} and Ox^{2-} ions upon contact compared to the rapid transport along the channel through convection. It limited the mixing and induced high level of solution supersaturation. In contrary, the decrease in flow rate enhanced the emergence of COD crystals albeit COM ones remained dominant. In turn, the inter-diffusion was favored with respect to transport through convection. Albeit it was a slow process, the complete mixing occurred at a shorter distance in the micro-reactor and "smoothed" the solution supersaturation.

The collecting duct-on-a-chip device allowed the direct visualization and measurement of CaOx crystal growth against time. Being able to access these information provided with evidences regarding the mechanisms at stake regarding the stone enlargement. Nowadays, growth models for CaOx crystal are based on a surface-reaction kinetics, *i.e.* the bulk concentrations in Ca^{2+} and Ox^{2-} ions (*i.e.* the supersaturation) have a direct influence on the growth of the emerging CaOx particle. Nevertheless, most studies were carried out without studying the influence of ion transport in confined structures such as encountered in the nephron. The utilization of our micro-reactor enabled to address the question. Our experimental findings supported the growth of CaOx crystal following two distinct kinetic regimes. At first, the emerging particle grew against time in response to a surface-reaction kinetics (*i.e.* growth $\propto t^{1/2}$). Thereafter, a take-over occurred when the particle reached a critical size. From that moment, the transport rate of ions into the CaOx matrix influenced the particle growth (*i.e.* growth $\propto t^{1/3}$).

Towards further understanding of our experimental observations, we have carried out the numerical modeling of CaOx crystallization in a microchannel in partnership with Pr. Ágota Tóth and Pr. Dezső Horváth from the University of Szeged in Hungary. The implementation of CaOx reactivity in their in-house code permitted to understand the physics of CaOx crystallization under confinement and to confirm our findings regarding the growth kinetics of CaOx crystals. Alike all numerical models, the results had to be carefully interpreted. Nonetheless, the use of such powerful tool in parallel to experimental work allowed in-depth investigation regarding CaOx crystallization. CaOx particles propagated and accumulated along the flow-direction. Among these CaOx particles, some settled down due to gravity while the others were dragged out the micro-reactor by the flow. With respect to the settled particles, it was possible to monitor *vs.* time their growth with the corresponding growth rate scaling

$d \propto t^{1/3}$. This late result supported the growth model of CaOx crystal proposed based on the experimental data.

The collecting duct-on-a-chip device was a robust platform to investigate CaOx crystallization under continuous-flow conditions and at concentrations in Ca^{2+} and Ox^{2-} ions matching patients diagnosed with kidney stone disease. Although complicated, the scenario presented herein remains simple with respect to real life kidney stone formation. Indeed, medical investigations have shown that most kidney stones originate from a calcium phosphate deposit in the nephron, known as the Randall's plaque. Accounting for the influence of such deposit in our microfluidic device will prove valuable if we want to develop a platform as mimetic as possible.

References

(1) Natalia, H.; Felipe, O.-A.; Pablo, L.; Simón, G.; Valérie, C.; Ali, A.-H.; Marcelo, J. K. Flow Chemistry to Control the Synthesis of Nano and Microparticles for Biomedical Applications. *Current Topics in Medicinal Chemistry* **2014,** *14* (5), 676.

(2) Abou-Hassan, A.; Sandre, O.; Cabuil, V. Microfluidics in Inorganic Chemistry. *Angewandte Chemie International Edition* **2010,** *49* (36), 6268.

(3) Tabeling, P.; Oxford University Press on Demand, 2005.

(4) Vize, P. D.; Woolf, A. S.; Bard, J. B. L. *The Kidney: From Normal Development to Congenital Disease*; Elsevier Science, 2003.

(5) Laffite, G.; Leroy, C.; Bonhomme, C.; Bonhomme-Coury, L.; Letavernier, E.; Daudon, M.; Frochot, V.; Haymann, J. P.; Rouziere, S.; Lucas, I. T.et al. Calcium oxalate precipitation by diffusion using laminar microfluidics: toward a biomimetic model of pathological microcalcifications. *Lab Chip* **2016,** *16* (7), 1157.

(6) Robertson, W. G. Kidney models of calcium oxalate stone formation. *Nephron. Physiology* **2004,** *98* (2), p21.

(7) Rasponi, M.; Piraino, F.; Sadr, N.; Laganà, M.; Redaelli, A.; Moretti, M. Reliable magnetic reversible assembly of complex microfluidic devices: fabrication, characterization, and biological validation. *Microfluidics and Nanofluidics* **2011,** *10* (5), 1097.

(8) Daudon, M.; Letavernier, E.; Frochot, V.; Haymann, J.-P.; Bazin, D.; Jungers, P. Respective influence of calcium and oxalate urine concentration on the formation of calcium oxalate monohydrate or dihydrate crystals. *Comptes Rendus Chimie* **2016,** *19* (11), 1504.

(9) Daudon, M.; Jungers, P.; Traxer, O. *Lithiase urinaire*; Lavoisier, Médecine Sciences publications, 2012.

(10) Buffle, J.; Zhang, Z.; Startchev, K. Metal Flux and Dynamic Speciation at (Bio)interfaces. Part I: Critical Evaluation and Compilation of Physicochemical Parameters for Complexes with Simple Ligands and Fulvic/Humic Substances. *Environmental Science & Technology* **2007,** *41* (22), 7609.

(11) Xie, B.; Halter, T. J.; Borah, B. M.; Nancollas, G. H. Aggregation of Calcium Phosphate and Oxalate Phases in the Formation of Renal Stones. *Crystal Growth & Design* **2015,** *15* (1), 204.

(12) Petit, I.; Belletti, G. D.; Debroise, T.; Llansola-Portoles, M. J.; Lucas, I. T.; Leroy, C.; Bonhomme, C.; Bonhomme-Coury, L.; Bazin, D.; Daudon, M.et al. Vibrational Signatures of Calcium Oxalate Polyhydrates. *ChemistrySelect* **2018,** *3* (31), 8801.

(13) Bohner, B.; Endrődi, B.; Horváth, D.; Tóth, Á. Flow-driven pattern formation in the calcium-oxalate system. *The Journal of chemical physics* **2016,** *144* (16), 164504.

(14) Bretherton, T.; Rodgers, A. Crystallization of calcium oxalate in minimally diluted urine. *Journal of Crystal Growth* **1998,** *192* (3), 448.

(15) Achilles, W.; Freitag, R.; Kiss, B.; Riedmiller, H. Quantification of Crystal Growth of Calcium Oxalate in Gel and its Modification by Urinary Constituents in a New Flow Model of Crystallization. *The Journal of Urology* **1995,** *154* (4), 1552.

(16) DeLong, J. D.; Briedis, D. A technique for the study of growth rates of single crystals of sparingly soluble salts. *Journal of Crystal Growth* **1985,** *71* (3), 689.

(17) Finlayson, B.; Reid, F. The expectation of free and fixed particles in urinary stone disease. *Investigative urology* **1978,** *15* (6), 442.

(18) Kok, D. J.; Khan, S. R. Calcium oxalate nephrolithiasis, a free or fixed particle disease. *Kidney international* **1994,** *46* (3), 847.

(19) Kok, D. J.; Boellaard, W.; Ridwan, Y.; Levchenko, V. A. Timelines of the "free-particle" and "fixed-particle" models of stone-formation: theoretical and experimental investigations. *Urolithiasis* **2017,** *45* (1), 33.

(20) Thongboonkerd, V.; Semangoen, T.; Chutipongtanate, S. Factors determining types and morphologies of calcium oxalate crystals: Molar concentrations, buffering, pH, stirring and temperature. *Clinica Chimica Acta* **2006,** *367* (1–2), 120.

(21) Leroy, C. Ph.D thesis, Université Pierre et Marie Curie, 2016.

(22) Kaplan, C. N.; Noorduin, W. L.; Li, L.; Sadza, R.; Folkertsma, L.; Aizenberg, J.; Mahadevan, L. Controlled growth and form of precipitating microsculptures. *Science* **2017,** *355* (6332), 1395.

(23) Zeng, Y.; Cao, J.; Wang, Z.; Guo, J.; Lu, J. Formation of Amorphous Calcium Carbonate and Its Transformation Mechanism to Crystalline CaCO3 in Laminar Microfluidics. *Crystal Growth & Design* **2018,** *18* (3), 1710.

(24) Finlayson, B. Physicochemical aspects of urolithiasis. *Kidney international* **1978,** *13* (5), 344.

(25) Atanassova, S. S.; Gutzow, I. S. Hippuric acid as a significant regulator of supersaturation in calcium oxalate lithiasis: the physiological evidence. *Biomed Res Int* **2013,** *2013*, 374950.

(26) Achilles, W. In vitro crystallisation systems for the study of urinary stone formation. *World Journal of Urology* **1997,** *15* (4), 244.

(27) Kolbach-Mandel, A. M.; Kleinman, J. G.; Wesson, J. A. Exploring calcium oxalate crystallization: a constant composition approach. *Urolithiasis* **2015,** *43* (5), 397.

(28) Garside, J.; Brečević, L.; Mullin, J. W. The effect of temperature on the precipitation of calcium oxalate. *Journal of Crystal Growth* **1982,** *57* (2), 233.

(29) Ananth, K.; Kavanagh, J. P.; Walton, R. C.; Rao, P. N. Enlargement of calcium oxalate stones to clinically significant size in an in-vitro stone generator. *BJU International* **2002,** *90* (9), 939.

(30) Nancollas, G. H.; Gardner, G. L. Kinetics of crystal growth of calcium oxalate monohydrate. *Journal of Crystal Growth* **1974,** *21* (2), 267.

(31) Zauner, R.; Jones, A. G. Determination of nucleation, growth, agglomeration and disruption kinetics from experimental precipitation data: the calcium oxalate system. *Chemical Engineering Science* **2000,** *55* (19), 4219.

(32) Kassemi, M.; Brock, R.; Nemeth, N. A combined transport-kinetics model for the growth of renal calculi. *Journal of Crystal Growth* **2011,** *332* (1), 48.

(33) Weller, H. G.; Tabor, G.; Jasak, H.; Fureby, C. A tensorial approach to computational continuum mechanics using object-oriented techniques. *Computers in Physics* **1998,** *12* (6), 620.

(34) Issa, R. I. Solution of the implicitly discretised fluid flow equations by operator-splitting. *Journal of Computational Physics* **1986,** *62* (1), 40.

CHAPTER 3.

MICROFLUIDIC AND BIOMIMETIC APPROACHES OF THE RANDALL'S PLAQUE

Chapter 3 Microfluidic and biomimetic approaches of the Randall's plaque

Table of contents

1. The hydroxyapatite: a model system for the Randall's plaque

Medical observations have shown that kidney stones originate most probably from the so-called Randall's plaque, a calcium phosphate deposit in the nephron. In-depth characterization has demonstrated that carbonated hydroxyapatite is the recurrent crystalline phase of such deposit. Several studies have been trying to elucidate its cause *in vivo* and noteworthy *in vitro* approaches have investigated its reactive role regarding CaOx stone formation. Therefore, hydroxyapatite serves as the *in vitro* model system to simulate the Randall's plaque. In the coming section, we will present the strategy we have developed to obtain an *in vitro* and biomimetic Randall's plaque-like system suitable for a collecting duct-on-a-chip device. Beforehand, we will introduce the physicochemical characterization of this specific calcium phosphate mineral. Additionally, we will give some examples from the literature that have led to the need of our model system.

a. The Randall's plaque

i. At the origin of kidney stone formation

Kidney stones are known to exhibit a heterogeneous chemical composition. While CaOx crystals stand for ≈ 70% of the kidney stones, calcium phosphate (CaP) components represent ≈ 14% of the stones[1]. Interestingly, CaOx-based kidney stones often exhibit a CaP umbilication at their surfaces[2] as shown in **Figure 1a**. This deposit is known as the Randall's plaque (RP), after Alexander Randall who correlated the occurrence of kidney stones with CaP plaques on the renal papilla due to prior cellular lesion[3]. Nowadays, it is commonly assumed that CaOx stones can grow from such RP precipitates. Nonetheless, the mechanisms behind this overgrowth have remained an open question. Studies regarding the interface between CaOx stones and RP have provided with structural indications to support for the role of RP as nidus with respect to stone crystallization[4-7]. Evan and collaborators suggested a sequence of events responsible for the formation of CaOx stones on RP[4]. Briefly, the loss of papillary epithelial integrity exposes RP to urine protein such as osteopontin or Tamm-Horsfall protein. Worth mentioning, these two proteins are known to have preventive effect against CaOx stone formation[8,9]. Due to a high affinity to the deposit, the proteins cover the plaque to form a new hybrid matrix. Thereafter, the urine supersaturation in CaP species drives the formation of amorphous CaP within the matrix. Afterwards, bursts of crystallization and coating periodically repeat over the tissue plaque up to the point that crystallization overcomes the moderating effect of urine proteins regarding the formation of CaOx stones. As shown in **Figure 1b**, Scanning Electron Microscopy images (SEM) detail the organization of RP in spherulites with

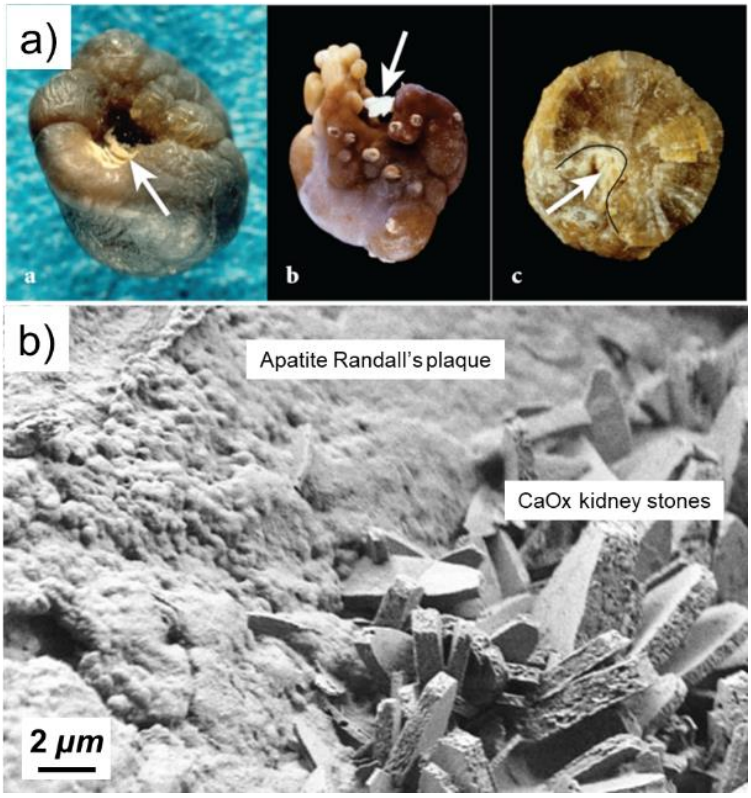

Figure 1. Relationship between Randall's plaque and CaOx kidney stones: a) CaOx monohydrate (COM) stones exhibiting a Randall's plaque deposit (white arrows)[2]; b) image of the interface area between Randall's plaque and COM stones[5]. Images reproduced with permission from AIP and ACS, respectively.

attached COM crystals[5] standing as the first layers surrounding RP[6]. Later contributions have associated the occurrence of COM crystalline phase on RP with hyperoxaluria while COD crystals have been correlated to hypercalciuria (*i.e.* excess of oxalate or calcium in urine, respectively)[10].

To understand the role of RP regarding CaOx stone formation, it is important to depict first this specific CaP mineral. The RP is a deposit that can be located either at the basement membranes of the thin loop of Henle as scattered apatite[11] or in the ducts of Bellini as tubular plugs[12]. Studies have tried to describe the cascade of events leading to the formation of both forms of RP[12-14]. At the loop of Henle, a low excretion of urine volume, an important calcium concentration and a decreased pH act as driving forces for CaP crystallization in contact to the altered epithelial surface[13]. In the ducts of Bellini, *i.e.* the most distal segment of the collecting duct, CaP particles appear to agglomerate and get trapped in the narrow opening[7,12,14] (**Figure 2a**). Extensive chemical analyses show that RP is made of (carbonated) hydroxyapatite[11] mainly, although its composition accounts for many other species[12] (**Table 1**). Furthermore, RP is known to be in strong association with components from the extra-cellular matrix such as collagen fibers[15] or glycosamynoglycans[16].

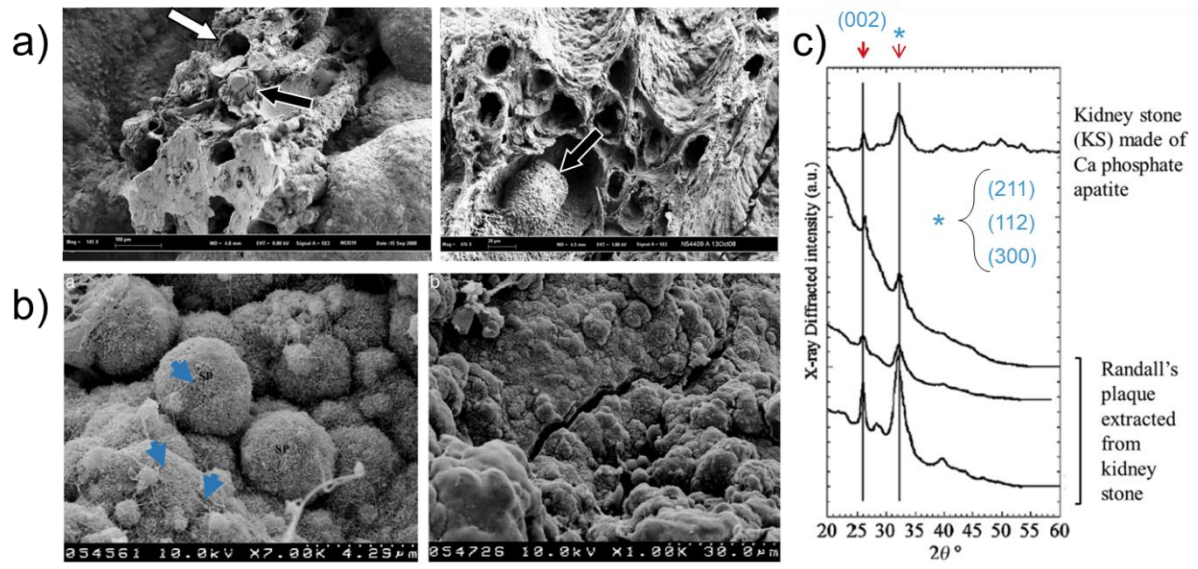

Figure 2. Characterization of the Randall's plaque: a) set of images showing the mixing of tubules with calcified walls (white arrow) or obstructed by calcium phosphate plugs (black arrow)[12]; b) Randall's plaque spherulites with fibers embedded inside (blue arrow in left image) and surface of internal layer of fused spherulites (right)[15]; c) XRD patterns of extracted Randall's plaques and kidney stones[17]. Figures are reproduced with permission from Springer and Elsevier, respectively.

As previously introduced in **Chapter 1** section **3.b.i**, the morphological characterization of RP enables to describe an organization in spherulites of 1.0 to 5.0 *μm* in diameter[15] (**Figure 2b**). X-ray diffraction (XRD) analysis has been conducted on human RP samples[17] as shown in **Figure 2c**. The patterns exhibit diffraction peaks at 2θ = 26° (sharp) and between 30° < 2θ < 45° (broad), which match with poorly crystalline HAp nanoparticles.

The Randall's plaque plays an important role regarding kidney stone formation. Its chemical characterization shows that it is mainly constituted of carbonated HAp, poorly crystalline[11,12], organized in spherulites[15] and in close relationship with proteins from the extra-cellular matrix[15,16]. Although highly valuable, most studies accounting for its role regarding CaOx crystallization are based on *indirect* evidences. Therefore, an *in vitro* model system would be interesting to support *in vivo* observations. As the main inorganic mineral in RP, HAp is used as the model candidate to simulate CaOx crystallization on a RP-like system.

Table 1. Occurrence of the different crystalline species founded in Randall's plaques at the surface of a series of kidney stones. The total number of samples is given in the bottom of the table. Table reproduced from Daudon *et al.*[12] with permission from Springer.

Components of papillary deposits	Main (%)	Minor (%)	Total occurrence (%)
Calcium phosphate (CaP)	10716 (97.3)	-	10894 (98.9)
carbonated apatite	10404 (94.4)	351 (3.2)	10755 (97.6)
amorphous carbonated CaP	264 (2.4)	629 (5.7)	893 (8.1)
whitlockite	30 (0.3)	87 (0.8)	117 (1.0)
octacalcium phosphate	3 (0.03)	13 (0.12)	16 (0.15)
brushite	15 (0.14)	23 (0.2)	38 (0.34)
Other species	300 (2.7)	-	503 (4.6)
struvite	3 (0.03)	9 (0.08)	12 (0.1)
bobierrite	2 (0.02)	0	2 (0.02)
calcite	9 (0.08)	12 (0.1)	21 (0.2)
sodium hydrogen urate	232 (2.1)	138 (1.25)	370 (3.4)
uric acid	43 (0.4)	24 (0.2)	67 (0.6)
ammonium urate	4 (0.04)	3 (0.03)	7 (0.06)
potassium urate	4 (0.04)	0	4 (0.04)
opaline silica	2 (0.02)	1 (0.01)	3 (0.03)
porphyrines	1 (0.01)	16 (0.15)	17 (0.15)
Total number of samples	11016 (100)	1291 (11.7)	-

ii. The *in vitro* approaches

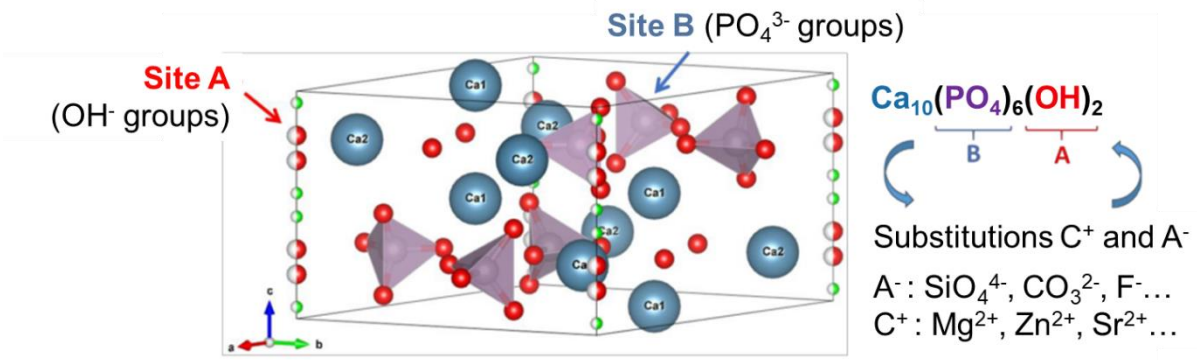

Figure 3. Crystal structure of a stoichiometric hydroxyapatite (hexagonal symmetry) with available sites for anionic (A and B sites) and cationic substitutions.

The hydroxyapatite ($Ca_{10}(PO_4)_6(OH)_2$, HAp) is a CaP mineral of great interest in the field of biomineralization. Stoichiometric HAp (*i.e.* ratio Ca/P = 1.67) is a crystalline structure often exhibiting a hexagonal symmetry (**Figure 3**). Standing for the main constituent in body parts such as bones and teeth, investigations have been carried out for tissue engineering[18] or dentistry[19]. However, HAp in human body is Ca deficient and therefore non-stoichiometric (*i.e.* Ca/P < 1.67) due to anionic and cationic substitutions[20]. As introduced in the previous section, RP is composed of carbonated HAp. An *in vitro* model system with similar morphological and chemical features would enable to understand the mechanisms of CaOx stone crystallization. Hereafter, we will present *three* different approaches (one from the literature and two from our research group) in an attempt to address the question. We will discuss the methodology, advantages and limitations of each strategy.

To investigate the formation of urinary stones *in vitro*, Achilles and collaborators used a FMCG crystallizer[21,22] (**Figure 4a** described in **Chapter 1** section **2.c.ii**). First, CaP spherulites were generated in an agar-agar gel matrix using NaCl (200 *mmol.L*$^{-1}$), Na_2HPO_4 (10 *mmol.L*$^{-1}$), NaH_2PO_4 (10 *mmol.L*$^{-1}$) and $CaCl_2$ (1.7 *mmol.L*$^{-1}$) at pH 6.8 – 6.9. As depicted in **Figure 4b**, CaP spherulites showed a size up to 200 *µm* in diameter. Furthermore, they exhibited a core (**Figure 4b-2**) of carbonated apatite surrounded by a shell (**Figure 4b-3**) of octacalcium phosphate ($Ca_8H_2(PO_4)_6{\cdot}5H_2O$, OCP). Subsequent overgrowth of CaOx crystals on CaP was conducted for 4 – 8 hours with NaCl (200 *mmol.L*$^{-1}$), $CaCl_2$ (2.0 *mmol.L*$^{-1}$), $Na_2C_2O_4$ (0.3 *mmol.L*$^{-1}$) and n-morpholino-ethanesulphonic acid (MES, 10 *mmol.L*$^{-1}$, pH 6.0). It induced the heterogeneous growth of COM crystals directly out of the sheet-like shell (**Figure 4c**). Additionally, these COM crystals exhibited a single morphology, the monoclinic prismatic one.

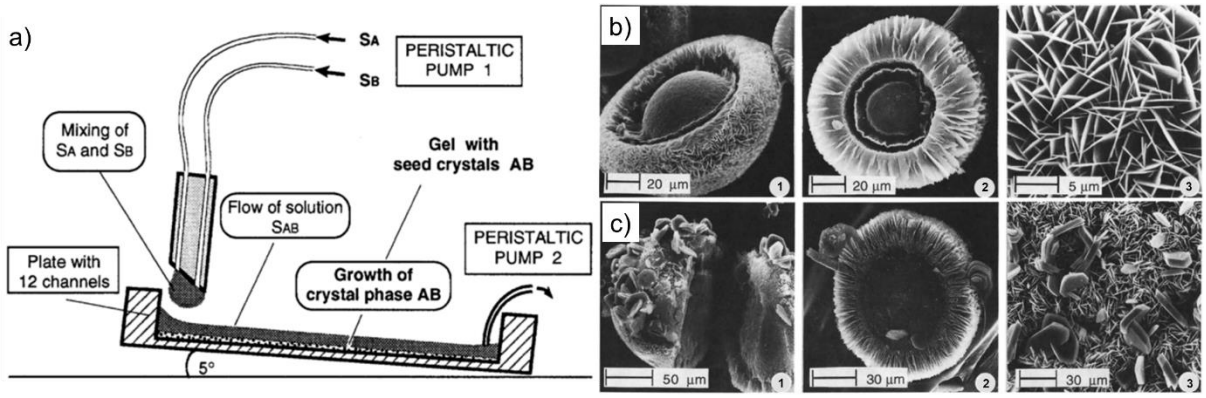

Figure 4. Formation of urinary stones *in vitro* using a FMCG crystallizer[21]: a) illustrative description of the *in vitro* crystallizer; b) CaP spherulites organized in a microcrystalline core and radially oriented sheet-like shell; c) subsequent overgrowth of CaOx crystals from the core-shell spherulites. Images are reproduced with permission from Springer.

Some aspects are noticeable regarding this first *in vitro* approach. On one hand, a FMCG crystallizer is a continuous-flow method that accounts for the presence of an organic matrix (herein, agar-agar). The CaP particles are organized in spherulites and permit CaOx crystallization after the passage of supersaturated solutions in calcium and oxalate. On the other hand, the *in vitro* crystallizer does not recreate the dimensions of the nephron. Moreover, the spherulites show a complex structure with two distinct crystalline phases (HAp and OCP) and are up to ≈ 40 times bigger than encountered in *in vivo* RP. We suspect that the agar-agar gel matrix is not inert with respect to CaP crystallization. Studies support that gel matrices control the nucleation, growth and orientation of crystal systems[23] and induce microporosity during insertion into the crystal lattice[24,25]. Nevertheless, the FMCG crystallizer emphasized on the reactive role of CaP spherulites in the genesis of CaOx formation.

As a *second* approach, we introduce a former study from our research group[26]. For simplicity, non-substituted HAp served as a model system to mimic RP. Worth pointing out, slight carbonate substitution could occur in HAp since water was not decarbonated prior to all syntheses (≈ 1% wt in CO_3^{2-}). Based on the work of Takemoto and collaborators[27], $Ca(NO_3)_2{\cdot}4H_2O$ (5.0 *mmol.L*$^{-1}$) and $(NH_4)_2HPO_4$ (3.0 *mmol.L*$^{-1}$, pH 10) were used to synthetize nanoparticles of HAp by a wet-chemical method. The phosphate solution was added under vigorous stirring to the calcium solution. After 24 hours aging, the precipitates were filtered, washed and dried at 100°C overnight. The powders were grinded and calcined at 450 – 550°C. Last, the samples were pelletized and annealed at 1100°C. XRD analysis *vs.* temperature ensured the efficiency of the heat treatment to obtain ≈ stoichiometric HAp (**Figure 5a**). SEM images enabled to estimate an average size of ≈ 300 *nm* of HAp particles (**Figure 5b**). Thereafter, HAp was soaked in a sodium oxalate acidic solution (10 *mmol.L*$^{-1}$, pH 3.7) in total absence of additional source of calcium. The approach was inspired from the work of Sethmann and collaborators who exposed HAp to oxalate solutions at various concentrations

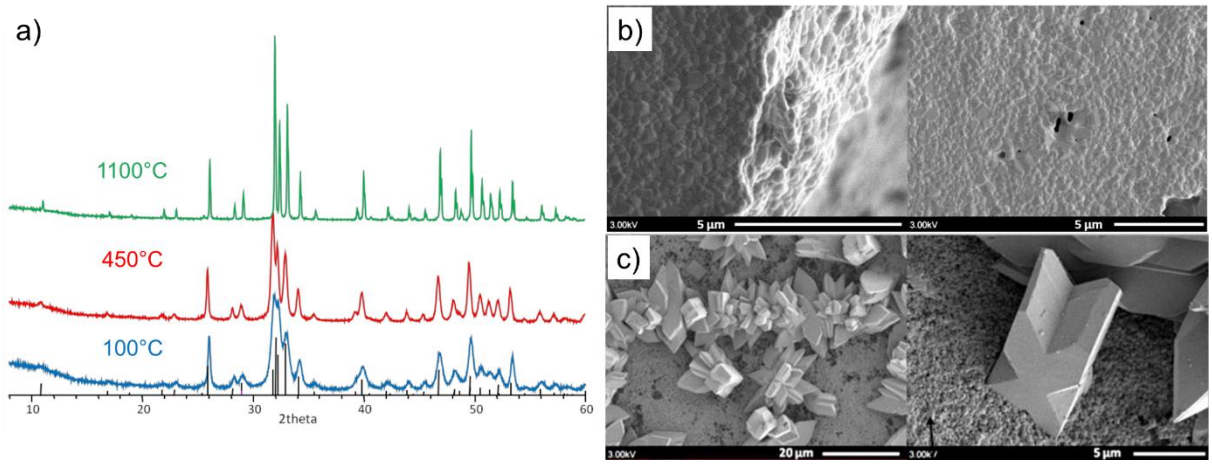

Figure 5. Investigation of the reactive role of stoichiometric hydroxyapatite regarding CaOx crystallization[26]: a) XRD patterns of nanoparticles of ≈ HAp *vs.* heat treatment; b) surface state of hydroxyapatite after pelleting; c) overgrowth of COM crystals at the surface of HAp platelets after partial dissolution of HAp in oxalate solution at $[Ox^{2-}]$ = 10 $mmol.L^{-1}$ (pH 3.7). Images are reproduced with kind permission from César Leroy.

and pH[28]. After 24 hours of soaking (**Figure 5c**), the surface of HAp showed the presence of COM crystals spotted under twins habit (right picture). Thereby, the partial dissolution of HAp in solution released Ca^{2+} ions for the heterogeneous CaOx crystallization at the RP model's surface. Regarding this strategy, the wet-chemical method combined with a heat treatment enabled to obtain a well-organized HAp. Moreover, the model system supported the reactive role of HAp with respect to the overgrowth of CaOx crystals. However, we want to point out that HAp from this study is a non-biomimetic apatite. Additionally, the twins morphology of COM crystals onto the RP model cannot be compared to *in vivo* observations. Albeit usually observed after *in vitro* synthesis in batch, these COM crystals have never been observed in "real life" kidney stones (refer to **Figure 1b**). Finally and most importantly, the batch crystallization does not account for the confined environment of the nephron.

The *third* and last strategy was investigated in the context of the present work. Aqueous solutions of $Ca(NO_3)_2{\cdot}4H_2O$ (5.0 $mmol.L^{-1}$, 1.0 $\mu L.min^{-1}$) and $(NH_4)_2HPO_4$ (3.0 $mmol.L^{-1}$, 1.0 $\mu L.min^{-1}$) were perfused in the collecting duct-on-a-chip device to induce the expected crystallization of HAp (**Figure 6a**). Similarly to CaOx crystallization in the continuous-flow micro-reactor, the co-laminar mixing of Ca^{2+} and HPO_4^{2-} ions led to the formation of a layer of precipitates onto the sealing glass coverslip (**Figure 6b**). Further examination showed that the layer's organization corresponded to spherulites (**Figure 6c**) while Energy-dispersive X-ray (EDS) analyses supported the formation of a CaP mineral (**Figure 6d**) with a ratio of Ca/P = 1.29 ± 0.03. The small amount of CaP crystals did not allow XRD analysis, therefore *Raman* spectroscopy was carried out to characterize the crystalline phase (**Figure 6e**).

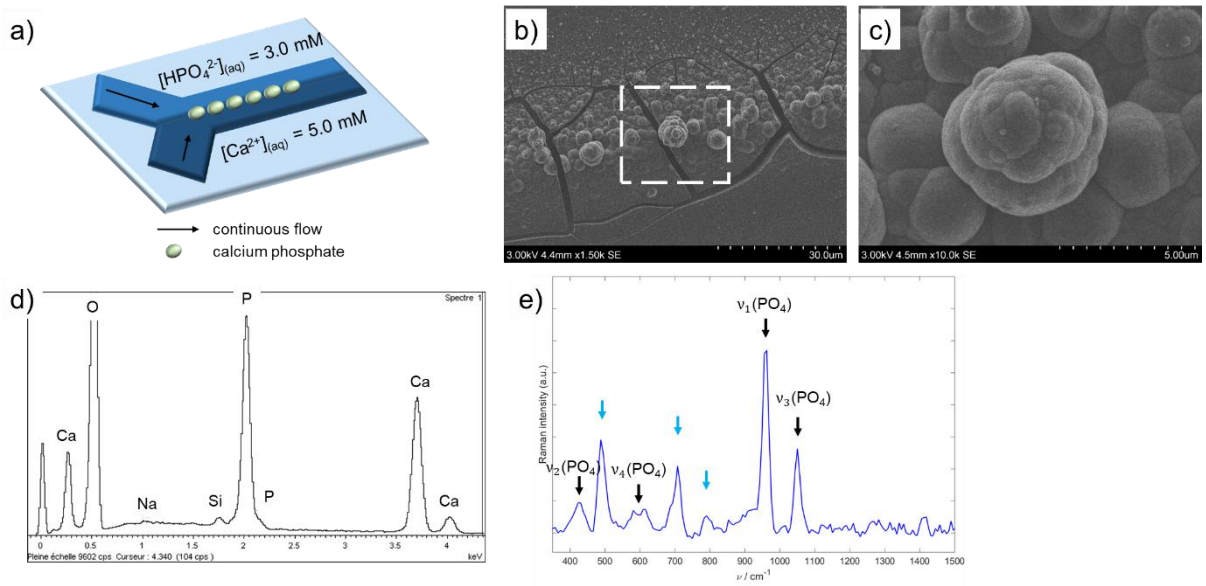

Figure 6. Towards the implementation of a CaP mineral in the collecting duct-on-a-chip device to investigate CaOx crystallization from a RP-like model: a) illustrative scheme of CaP precipitation from co-laminar mixing of $Ca(NO_3)_2$ and $(NH_4)_2HPO_4$; b) SEM image of the CaP layer onto the glass coverslip; c) magnified SEM image to support the organization in spherulites; d) Energy-dispersive X-ray analysis of CaP layer; e) *Raman* spectrum of the CaP spherulites with in black the peaks assigned to HAp and in blue, some unassigned peaks.

The *Raman* spectrum exhibited peaks at 447 ($\nu_2(PO_4)$), 600 ($\nu_4(PO_4)$), 961 ($\nu_1(PO_4)$) and 1050 ($\nu_3(PO_4)$) cm^{-1} assigned to HAp[29]. However, some peaks remained unassigned at ≈ 500, 700 and 800 cm^{-1} (blue arrows in **Figure 6e**). The first two unassigned peaks seemed to match the $\nu_4(HPO_4)$ bending mode of OCP[30] and the $\nu_3(NO_3)$ stretching mode of $Ca(NO_3)_2$[31], respectively. The crystallization of a CaP mineral could be conducted in the collecting duct-on-a-chip device. Yet, it did not lead to the expected formation of pure HAp. Indeed, the detection of a $Ca(NO_3)_2$ peak (*i.e.* initial precursor) using *Raman* spectroscopy showed the insufficient effectiveness of the co-laminar mixing of $Ca(NO_3)_2{\cdot}4H_2O$ and $(NH_4)_2HPO_4$ to induce complete HAp crystallization. The subsequent CaOx crystallization was attempted by injecting Ox^{2-} solution in the CaP-modified micro-reactor but was unsuccessful. The CaP layer was brittle and fragile and was "washed" away with the continuous flow of Ox^{2-} solution. Nonetheless, it seems possible to modify the glass surface with a CaP mineral and implement it into the micro-reactor.

Previous contributions have demonstrated that HAp is indeed a relevant candidate regarding CaOx-based stones crystallization. It is possible to investigate its reactive role in a batch crystallizer or a continuous flow crystallizer (*e.g.* FMCG). However, these RP-like models do not account for the proper features of "real life" RP, such as crystalline organization, chemical composition and most importantly, growth of CaOx-based kidney stones in a *confined* environment. Implementing the collecting duct-on-a-chip device with a mineral acting as a RP-like model system appears as a promising possibility. However, it requires the *in vitro* synthesis of a HAp mimicking a biological apatite and suitable for consecutive microfluidic investigations.

To this end, we propose a “two-step” protocol. First, the glass coverslip of the collecting duct-on-a-chip device (depicted in **Chapter 2**) will be modified with an apatitic layer. Then, the modified substrate will seal the microfluidic platform to act as an *in vitro* model of RP.

b. Towards an *in vitro* and biomimetic strategy

i. Crystallization of a biomimetic hydroxyapatite in Simulated Body Fluid solution

An *in vitro* and mimetic HAp has a great potential for the fabrication of biomaterials, *e.g.* HAp with close structure and morphology to bones for orthopedics. The utilization of an acellular Simulated Body Fluid (SBF) solution at ion concentrations, pH and temperature almost equal to those of the human blood plasma enabled to form a CaP rich layer on the surface of bioactive materials as proposed by Kokubo and collaborators[32] (**Figure 7**). On an apatite-wollastonite glass-ceramic, the authors demonstrated the *in vitro* formation of a carbonate-containing HAp layer (**Figure 7a**) organized in small crystallites (**Figure 7b**). In a later contribution, the same

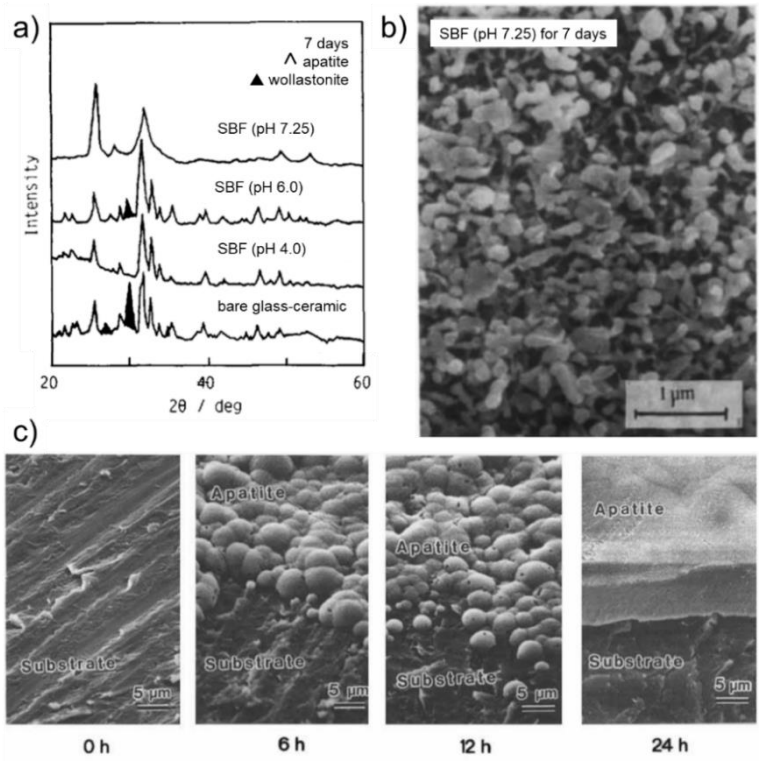

Figure 7. Overview of the Simulated Body Fluid (SBF) strategy developed by Kokubo and collaborators to induce the formation of carbonated HAp on various substrates[32,33]: a) XRD patterns of an apatite-wollastonite glass-ceramic soaked in SBF for 7 days against pH; b) SEM image of HAp formed on the glass-ceramic substrate after 7 days in SBF solution at pH 7.25; c) set of SEM images of poly-ether sulfone substrates placed on $CaO\text{-}SiO_2$ particles in SBF for 4 different periods followed by consecutive soaking in 1.5 SBF for 6 days. Figures are adapted with permission from John Wiley and Sons and Elsevier, respectively.

Table 2. Ion composition and associated concentrations in blood plasma, Simulated Body Fluid[32] (SBF) and 1.5 SBF[33] solutions (*mmol.L^{-1}*).

Ions	Na^+	K^+	Mg^{2+}	Ca^{2+}	Cl^-	HCO_3^-	HPO_4^{2-}	SO_4^{2-}
Blood plasma	142.0	5.0	1.5	2.5	103.0	27.0	1.0	0.5
SBF	142.0	5.0	1.5	2.5	147.8	4.2	1.0	0.5
1.5 SBF	213.0	7.5	2.3	3.8	223.0	6.3	1.5	0.8

research group showed that the synthesis protocol could be extended to various types of substrates[33]. For this to happen, an organic substrate (*e.g.* poly-ether sulfone) was set in contact with particles of CaO-SiO_2-based glass soaked in SBF solution to form apatite nuclei. Then, the substrate was soaked in a 1.5 SBF solution, *i.e.* a solution highly supersaturated with respect to apatite, to induce the *in situ* and fast growth of the HAp nuclei on the substrate (**Figure 7c**). Ion concentrations of blood plasma, SBF and 1.5 SBF solutions are given in **Table 2**, respectively. Furthermore, SBF and 1.5 SBF solutions are prepared from the successive dissolution of NaCl, $NaHCO_3$, KCl, K_2HPO_4, $MgCl_2{\cdot}6H_2O$, $CaCl_2$ and Na_2SO_4 salts in Tris-HCl buffer solution.

Nowadays, the surface functionalization with HAp mimicking a biological apatite is broadly conducted using the SBF strategy. In the context of our study, we adapted the synthesis protocol from Liu and collaborators[34]. We modified a glass coverslip according to the protocol presented in **Figure 8**. First, the glass substrate was immersed in a mixture solution of H_2SO_4:H_2O_2 (piranha solution) for one hour (**Figure 8a**), then rinsed once in distilled water and twice in acetone. The nucleation of CaP particles was carried out following a three-step procedure (**Figure 8b**). After oxidation, the glass coverslip was soaked in a $CaCl_2$ solution buffered at pH 7.4 with Tris-HCl buffer at room temperature. Then, an equal volume of K_2HPO_4 solution was slowly added dropwise and under stirring. Worth mentioning, calcium and phosphate containing solutions were prepared to respect the stoichiometric Ca/P = 1.67 for HAp. Finally, the reaction medium was stirred for 30 minutes vigorously. The procedure was repeated two more times before soaking the pre-deposited substrate in a 1.5 SBF solution buffered at pH 7.4 with Tris-HCl buffer at 37°C (**Figure 8c**). The image in **Figure 8d** illustrates how the coating in 1.5 SBF solution evolved at two distinct soaking times. Further characterizations have to be carried out to validate the deposit as a HAp layer exhibiting similar morphology and composition to biological apatite.

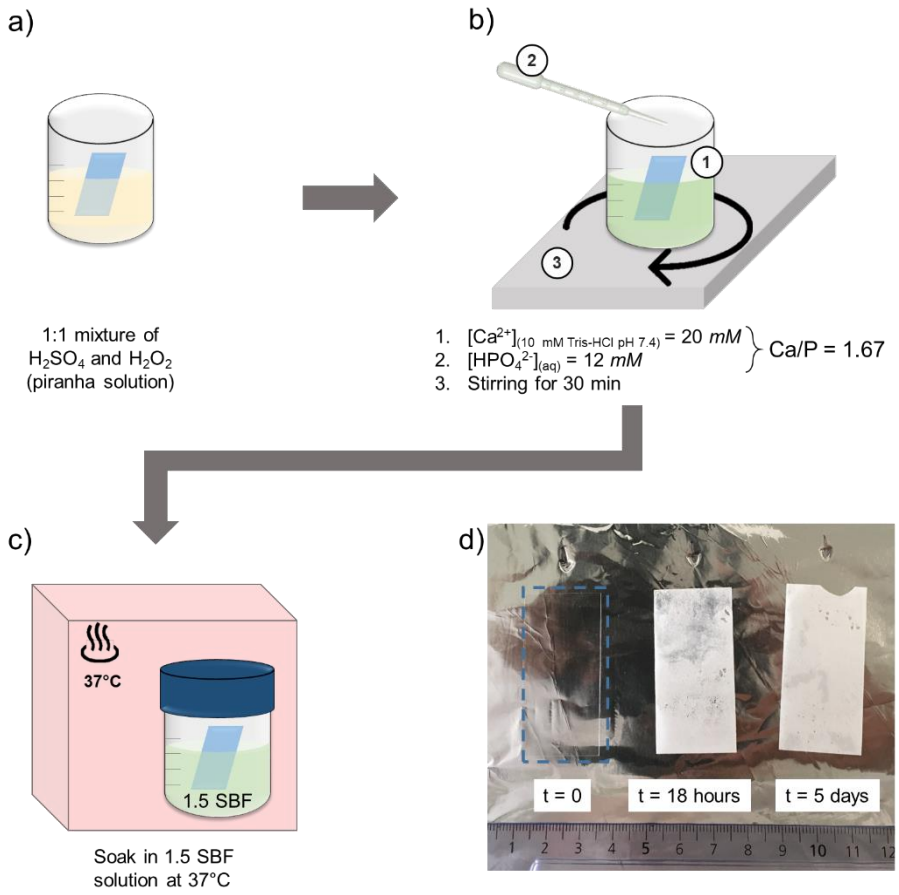

Figure 8. Illustrative description of the synthesis protocol to obtain a HAp layer mimicking a biological apatite using the SBF strategy. The protocol is adapted from Liu *et al.*[34]: a) oxidation of the glass substrate in piranha solution for one hour; b) CaP nucleation on the surface from a mixture of $CaCl_2$ and K_2HPO_4 solutions; c) HAp coating onto the glass substrate into 1.5 SBF solution buffered at pH 7.4 with Tris-HCl buffer at 37°C; d) coatings after 18 hours and 5 days soaking in 1.5 SBF solution.

ii. A non-stoichiometric hydroxyapatite to mimic the Randall's plaque

The morphological organization and chemical composition of the deposited layer on the glass substrate was investigated throughout the synthesis protocol. Images in **Figure 9** underline a noticeable evolution regarding the morphological organization. After oxidation of the bare glass coverslip (**Figure 9a**) and nucleation of CaP particles (**Figure 9b**), the substrate was soaked in 1.5 SBF solution for 5, 10, 18 hours and 5 days, respectively. As depicted in **Figures 9c-f**, a layer emerged to coat progressively the glass substrate in a multi-layered arrangement. Attention is drawn to **Figure 9e** and **Figure 9f** with a focus on the progressive growth of "cauliflower"-like structures. Complementary EDS analyses confirmed the formation of a CaP layer using the SBF strategy and quantified the evolution of the Ca/P ratio *vs.* time (**Table 3**). Noteworthy, CaP particles obtained from the mixing of $CaCl_2$ and K_2HPO_4 at molar ratio of Ca/P = 1.67 (*i.e.* **Figure 8b**) did not match the stoichiometric HAp ratio (Ca/P = 1.33 ± 0.03).

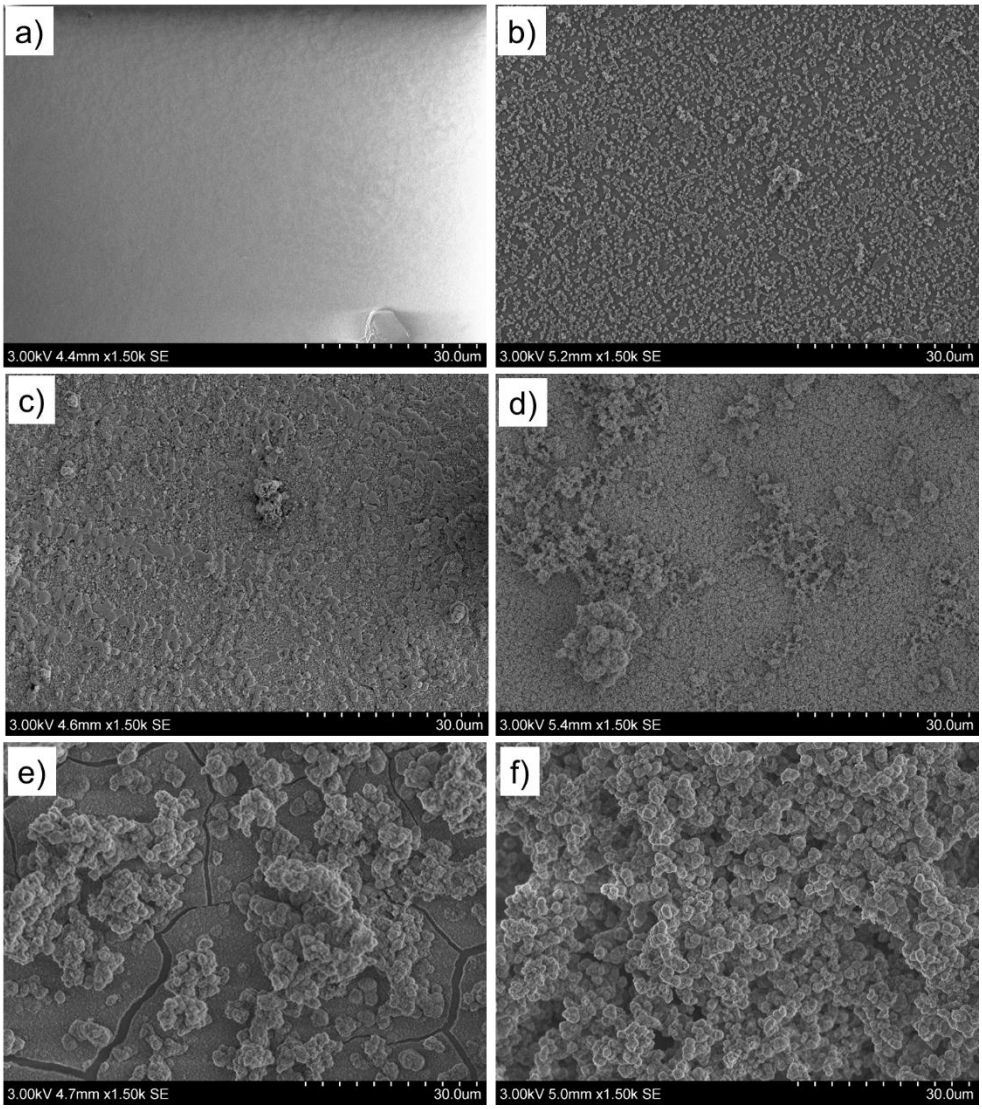

Figure 9. Time evolution of the surface of the glass coverslip using the SBF strategy: a) bare glass coverslip; b) after CaP nucleation from a mixture of $CaCl_2$ and K_2HPO_4 solutions; next images stand for glass substrate soaked for c) 5 hours, d) 10 hours, e) 18 hours and f) 5 days in 1.5 SBF solution buffered at pH 7.4 with Tris-HCl buffer at 37°C.

Table 3. Ca/P ratio of the HAp layers throughout the synthesis protocol in 1.5 SBF solution based on EDS analysis. Noteworthy, time in 1.5 SBF at 0 stands for CaP nucleation of the glass coverslip from a mixture of calcium chloride ($CaCl_2$) and potassium phosphate dibasic (K_2HPO_4).

Time in 1.5 SBF	0	5 hours	10 hours	18 hours	5 days
Ca / P	1.33 ± 0.03	1.33 ± 0.02	1.40 ± 0.02	1.40 ± 0.03	1.50 ± 0.03

When immersed in 1.5 SBF solution, the ratio slowly increased *vs.* time although it never reached Ca/P = 1.67. However, such low Ca/P ratio is usually reported in the literature with respect to the SBF strategy. When HAp grows from this complex ion solution, substitutions can occur as previously mentioned.

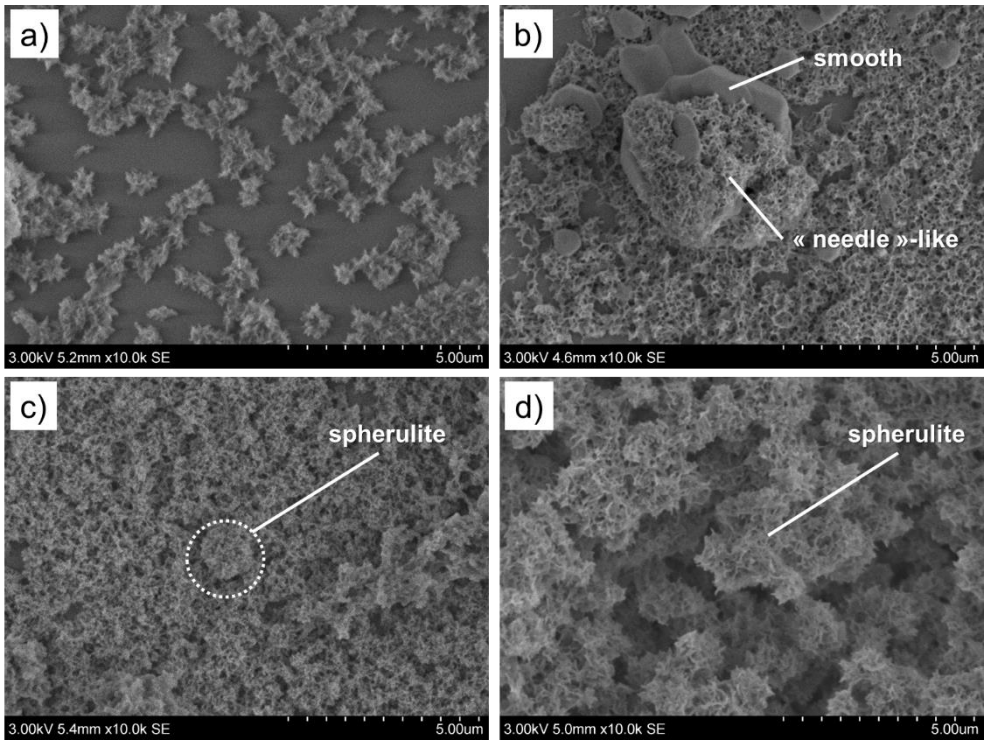

Figure 10. Magnified SEM images to depict the morphological organization of the deposited HAp layer after CaP nucleation (a), 5 hours (b), 10 hours (c) and 18 hours (d) soaking in 1.5 SBF solution buffered at pH 7.4 with Tris-HCl buffer at 37°C.

Therefore, a non-stoichiometric, calcium deficient and substituted HAp can be obtained.

Magnified SEM images in **Figure 10** gave further insights with respect to the structural organization of the layer. After CaP nucleation, rather isolated particles were observed on the surface of the glass coverslip (**Figure 10a**). These particles exhibited a vague spherical geometry organized in aggregates of ≈ 1.0 *µm*. After immersion in 1.5 SBF solution for 5 hours, the individual particles grew and connected to cover the surface (**Figure 10b**). Further examination of **Figure 10b** depicted a dual morphology with a dominant needle-like organization gradually overtaking a smooth looking structure. After 10 hours of immersion (**Figure 10c**), the substrate was evenly coated with the development of well-defined micrometric spherulites. This trend was consolidated after 18 hours of immersion with the coating organized in “pincushion”-like spherulites of diameter d ≈ 1.0 *µm* (**Figure 10d**).

XRD analysis of the modified glass substrate after immersion in 1.5 SBF solutions was conducted (**Figure 11a**). As the immersion time in 1.5 SBF solution increased, the CaP layer matched the pattern for poorly crystalline HAp. From 5 to 18 hours soaking, the diffraction patterns became similar to RP as illustrated in **Figure 2b**. However, 5 days in 1.5 SBF solution led to a different pattern. Two fine peaks at 2θ = 32° and 2θ = 45° were observed and likely corresponded to the (200) and (220) peaks of NaCl. Considering that sodium chloride is in greater amount compared to the other reagents in the acellular solution (**Table 2**), it is plausible

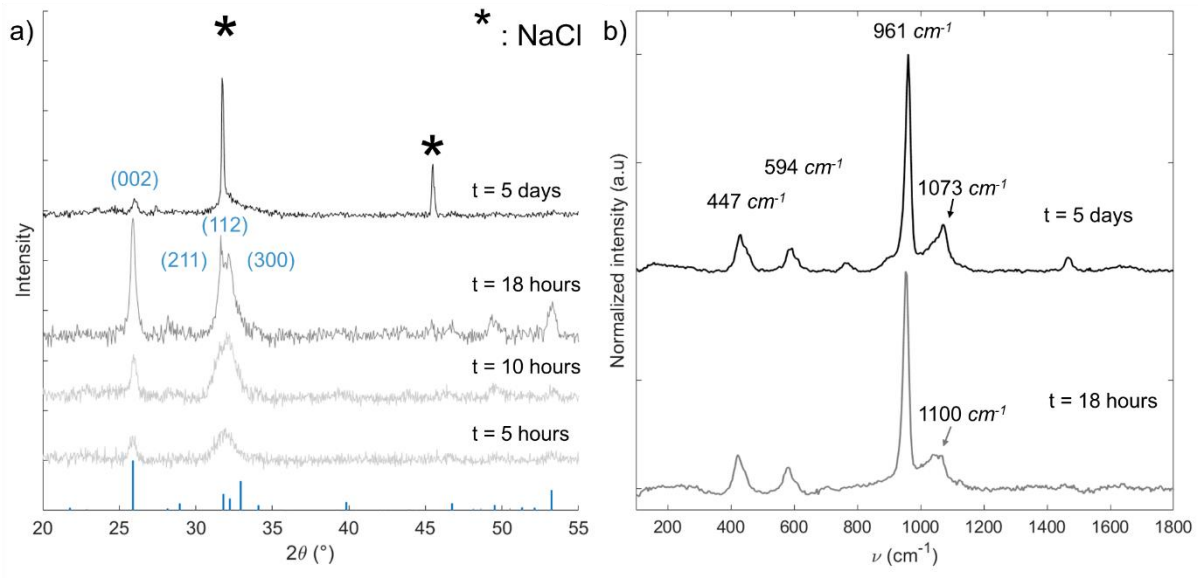

Figure 11. Surface characterization of HAp deposit on glass coverslip after immersion in 1.5 SBF solution: a) XRD patterns *vs.* time of apatitic layer (amorphous pattern from glass substrate has been removed). Reference pattern for HAp JCPDS 00-009-0432. (*) peaks correspond to the diffraction peaks of NaCl; b) *Raman* spectra showing the presence of the apatitic structure[29,35] (baselines corrected).

that after drying it crystallizes partially on the surface of the CaP layer. Yet, a noticeable shoulder was observed from 32 < 2θ < 35° and could be assigned with the overlap of HAp. Furthermore, the presence of a peak at 2θ = 26°, which stood for the (002) peak of HAp, strengthened the formation of HAp. One can wonder why NaCl is not visible on the series of SEM images in **Figure 9** and **Figure 10**. We could think that NaCl crystals did not precipitate under the well-described cubic morphology but maybe under smaller structures in close relationship with the spherulites. To support XRD analysis, *Raman* spectroscopy was carried out to confirm the formation of HAp (**Figure 11b**). After 18 hours and 5 days in 1.5 SBF solution, spectra demonstrated peaks at 447, 594 and 961 cm^{-1} assigned to HAp[29] with relatively broad peak between 1073 and 1100 cm^{-1}. According to Awonusi and collaborators, a peak around 1071 cm^{-1} can be assigned to a combination of $\nu_1(CO_3)$ vibrational mode with $\nu_3(PO_4)$ vibrational mode[35]. Prior to its use, no SBF solution degassing was done. Consequently, we demonstrated that the SBF strategy enabled the formation of a non-stoichiometric HAp, likely substituted with carbonate groups and referred to (hereafter) as the apatitic layer. Moreover, we point out the absence of "unassigned" peaks such as in **Figure 6e**. Therefore, we believe that the modified glass coverslip can serve as a suitable RP-like model system with respect to CaOx crystallization. Furthermore, the apatitic layer can be implemented in the microfluidic device to account for a confinement encountered in the nephron.

The Randall's plaque is a CaP deposit supposedly acting as a nidus for CaOx stone crystallization in the kidney. Chemical and morphological characterization support that the deposit consists of carbonated HAp[12] organized in spherulites of 1.0 to 5.0 μm in diameter[15]

and of poor crystallinity[17]. Noteworthy, some contributions tried to build up a RP-like model system to investigate its reactive role regarding CaOx stone crystallization[21,22,26]. However, the different models did not exhibit the proper features of the Randall's plaque (*i.e*. chemical composition and morphological organization). Moreover, the proposed approaches lacked accounting for the confinement and associated fluid-flow in the nephron. In a first attempt to address these issues, we tried to induce HAp crystallization directly in our collecting duct-on-a-chip device based on a former study in our research group[26]. On the sealing glass coverslip, the co-laminar mixing of $Ca(NO_3)_2{\cdot}4H_2O$ and $(NH_4)_2HPO_4$ resulted in a fragile CaP deposit, organized in spherulites and with a low ratio Ca/P = 1.29 ± 0.03. Moreover, *Raman* spectroscopy showed unassigned peaks in addition to those of HAp. In a second approach, we modified the glass coverslip with an apatitic layer *prior to implementation* in the collecting duct-on-a-chip device. To this end, we have utilized the nowadays broadly established SBF strategy[32,33] to synthesize biological-like apatites[34]. On a bare glass coverslip, we induced the pre-deposition of CaP nuclei from a mixture solution of $CaCl_2$ and K_2HPO_4 at a molar ratio Ca/P = 1.67. Afterwards, we induced the formation of an apatitic layer through immersion in a 1.5 SBF solution for several hours. After 18 hours, the deposit was organized in spherulites of d ≈ 1.0 *µm* in diameter with Ca/P = 1.40 ± 0.03 and showed evidence of substitutions and calcium deficiency. In consequence, we believe that the modified glass substrate can act as a suitable Randall's plaque model system. Once implemented in the microfluidic platform, it will enable to investigate the reactive role of such deposit with respect to heterogeneous crystallization of CaOx in the sole presence of oxalate ions.

2. The heterogeneous growth of calcium oxalate crystals

Using the SBF strategy enables to build up an *in vitro* Randall's plaque-like model exhibiting comparable chemical properties and morphological organization of the "real life" Randall's plaque (RP). If suitable to microfluidic implementation, such *in vitro* model system will inform on the reactive role of this CaP mineral regarding CaOx stones growth in the nephron. *In fine*, the RP-modified collecting duct-on-a-chip device will represent a step forward towards a biomimetic platform with respect to kidney stone disease. First, evidences have to be presented regarding the role of the RP-like model made of calcium deficient HAp in directing CaOx crystallization. Once confirmed, we will discuss the relevancy of inducing CaOx crystallization under microfluidic confinement compared to standard batch crystallization. Last, we will consider the influence of the dissolution rate of HAp layer with respect to heterogeneous CaOx crystallization by pH variation.

a. Calcium oxalate crystallization under micro-confinement

i. The Randall's plaque-like model: a growth support for calcium oxalate crystals

An *in vitro* CaP crystalline system can support subsequent CaOx crystallization as demonstrated by Achilles and collaborators[21] (**Figure 4c**) or our research group[26] (**Figure 5c**). In Achilles' contribution, the CaP spherulites were put in contact with a supersaturated solution *both* in Ca^{2+} *and* Ox^{2-} ions. Therefore, no clear evidence regarding the reactive role of the spherulites could be provided. Indeed, RP is suspected to trigger CaOx crystallization through the release of Ca^{2+} ions after partial dissolution of its apatitic structure. Prior investigations in our research group tended to support this mechanism[26]. However, CaOx crystal habit examination (*e.g*. twins shape as illustrated by left image in **Figure 5c**) did not match the pathological morphologies encountered *in vivo* preventing from considering the chemical system as biomimetic.

Using the SBF approach, we succeeded in modifying the surface state of a bare glass coverslip with an apatitic layer organized in spherulites. Acting as the RP-like model, we arbitrary decided to choose the apatitic layer that underwent immersion in 1.5 SBF solution for *18 hours*. Alike the contribution from our research group, the reactive role of the RP-like model to trigger CaOx crystallization was studied. Thereby, a piece of ≈ 0.5 × 0.5 cm^2 of the RP-like substrate was soaked in an oxalate solution (pH 7.36) in total absence of any additional source of Ca^{2+} ions for one week. For batch crystallization, two concentrations in Ox^{2-} ions were under scrutiny, *i.e.* $[Ox^{2-}]_{(aq)} = 0.40\ mmol.L^{-1}$ and $[Ox^{2-}]_{(aq)} = 100\ mmol.L^{-1}$, respectively.

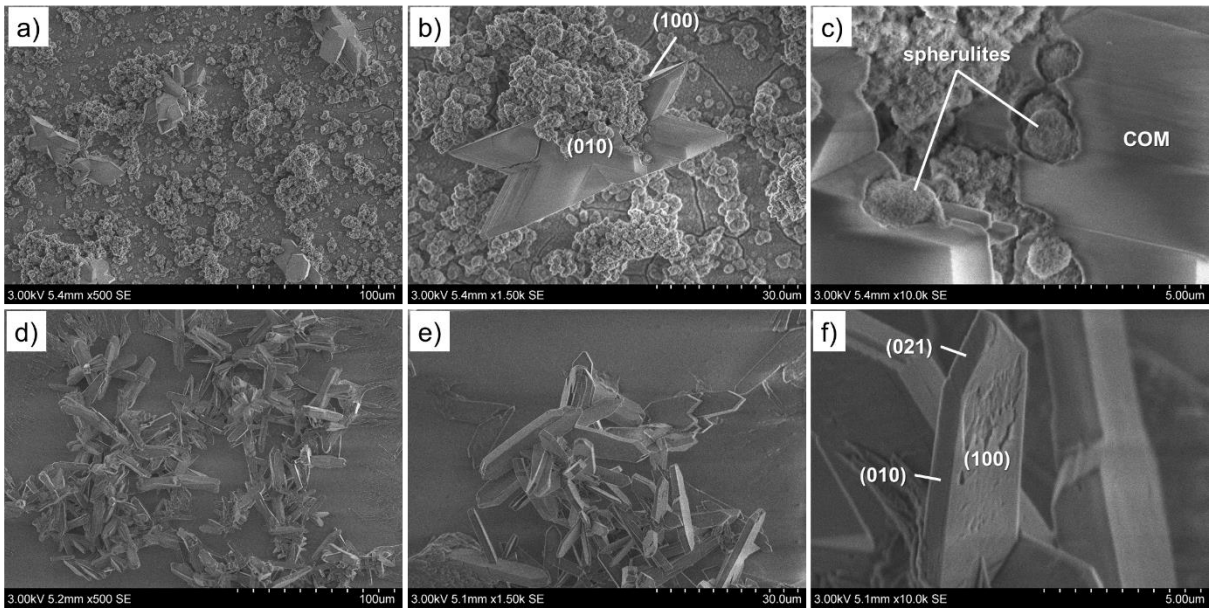

Figure 12. SEM images of the "heterogeneous" overgrowth of CaOx crystals from the RP-like substrate in batch crystallization for one week. The panel of images stands for after immersion in oxalate solution at $[Ox^{2-}]_{(aq)}$ = 0.40 *mmol.L*$^{-1}$ (**Figures 12a-c**) and at $[Ox^{2-}]_{(aq)}$ = 100 *mmol.L*$^{-1}$ (**Figures 12d-f**).

The first concentration in Ox^{2-} ions is equivalent to the urinary concentration of a patient diagnosed with moderate hyperoxaluria[36]. On the other hand, $[Ox^{2-}]_{(aq)}$ = 100 *mmol.L*$^{-1}$ is in no way physiological (but stands for the initial batch solution used for dilution). Herein, our aim is to assess that the apatitic layer serves as a calcium donor for the heterogeneous growth of CaOx crystals.

After one week of immersion in oxalate solutions, we observed the appearance of new crystals different from the HAp spherulites either at $[Ox^{2-}]_{(aq)}$ = 0.40 *mmol.L*$^{-1}$ (**Figures 12a-c**) or at $[Ox^{2-}]_{(aq)}$ = 100 *mmol.L*$^{-1}$ (**Figures 12d-f**). At condition akin to moderate hyperoxaluria, we observed the growth of well-defined crystals ranging up to 50 *µm* based on SEM examination (**Figure 12a**). Magnified images enabled to identify these crystals as COM crystals as shown in **Figure 12b** under twins morphology alike in section **1.a.ii**. Although not presented herein, *Raman* spectroscopy confirmed this assignment. Further examination showed spherulites embedded within the COM crystals (**Figure 12c**). This observation strongly suggested the progressive growth of COM crystals from the HAp spherulites through dissolution-recrystallization mechanisms. In an oxalate solution at $[Ox^{2-}]_{(aq)}$ = 100 *mmol.L*$^{-1}$, we observed the complete absence of the HAp spherulites at the expense of platelet-like crystals (**Figure 12d**). In-depth observation enlightened highly intertwined crystals of various sizes (**Figure 12e**) corresponding to monoclinic prismatic COM crystals (**Figure 12f**). The second concentration of interest in Ox^{2-} ions led to the total consumption of the *in vitro* RP-like substrate: it reinforced the spherulites' role to serve as a reactive material for CaOx crystallization. In absence of external Ca^{2+} ions source, the partial dissolution of the apatitic

layer in oxalate solution permitted the release of $Ca^{2+}_{(RP)}$ ions from the spherulites. At all concentrations in Ox^{2-} ions, the growth of CaOx crystals indicates that $[Ca^{2+}]_{(RP)} \times [Ox^{2-}]_{(aq)} \geq K_{sp(CaOx)}$. Consequently, batch crystallization supports the reactive role of the RP-like model for heterogeneous CaOx crystallization.

Nevertheless, two limitations regarding this approach are worth pointing out. First is the induction time for CaOx crystal growth with respect to the concentration in Ox^{2-} ions. Although underscoring dissolution-recrystallization mechanisms of the apatitic layer for COM crystal growth, batch crystallization is not appropriate for investigations *vs.* time. On one hand, one week (at least) is required to notice significant changes at $[Ox^{2-}]_{(aq)}$ = 0.40 $mmol.L^{-1}$. In contrary, $[Ox^{2-}]_{(aq)}$ = 100 $mmol.L^{-1}$ is associated to the total consumption of the apatitic layer after one week in solution. These experimental observations illustrate the lack of control over the diffusion of $Ca^{2+}_{(RP)}$ ions at the apatitic surface to attain sufficient $[Ca^{2+}]_{(RP)} \times [Ox^{2-}]_{(aq)}$ and to induce CaOx crystallization. Second and last issue is the morphology of CaOx crystals derived from the apatitic substrate. The growth of COM crystals in response to a large excess of Ox^{2-} ions is in accordance with hyperoxaluria conditions as observed by physicians[10]. Nonetheless, COM crystal twins morphology as depicted in **Figure 12b** (*i.e.* for $[Ox^{2-}]_{(aq)}$ = 0.40 $mmol.L^{-1}$) does not match pathological COM stones regarding neither the morphology nor the size range (**Figure 1b**). Monoclinic prismatic COM crystals as shown in **Figure 12f** are more similar in shape, although the crystals are too large and $[Ox^{2-}]_{(aq)}$ = 100 $mmol.L^{-1}$ is clearly unrealistic from the physio-pathologically point of view.

Herein, the apatitic substrate was introduced as a supportive matrix for CaOx crystallization. Batch crystallization showed that HAp spherulites served as a calcium donor when dissolving in oxalate solution. The released $Ca^{2+}_{(RP)}$ ions interacted with the Ox^{2-} ions in the solution to cause the growth of CaOx crystals from the apatitic layer. The resulting COM crystalline phase was in accordance with the excess of Ox^{2-} ions (hyperoxaluria). However, the observed crystal morphologies could not validate batch crystallization as a biomimetic approach to investigate heterogeneous growth of CaOx kidney stones as encountered in the nephron. To address the issue, we propose to adapt the microfluidic strategy described in **Chapter 2**. The corresponding results are subject to a publication and are presented in the coming part.

ii. Studying calcium oxalate growth from the Randall's plaque model under microfluidic considerations

The following work is aimed to be published as a scientific communication in ChemComm, journal of the Royal Society of Chemistry (RSC).

COMMUNICATION

Fast growth of calcium oxalate crystals on biomimetic Randall's plaque under microfluidic confinement

Received 00th January 20xx,
Accepted 00th January 20xx

DOI: 10.1039/x0xx00000x

Karol Rakotozandriny,[a,b] Florence Babonneau,[a] Ivan Lucas,[c] Emmanuel Letavernier,[d] Ali Abou-Hassan,[*b] and Christian Bonhomme,[*a]

The growth of kidney stones from carbonated hydroxyapatite nuclei called Randall's plaques remains poorly understood. The complexity is of both chemical and hydrodynamical nature. We tackle this fundamental question by synthesizing a dynamical interface involving an apatitic layer and growing calcium oxalate crystals under tuned microfluidic conditions (laminar flow, concentrations).

The global increase in kidney stone (KS) formers among the industrialized populations(1) has raised the urgent importance of understanding the idiopathic biomineralization of KS. Although known for being of strongly heterogeneous chemical composition,(2) a majority of KS are formed of calcium oxalate (CaOx) and non-negligible calcium phosphate (CaP) crystals. Further chemical characterization shows that CaOx stones can be found under two crystalline phases, the (stable) monohydrated whewellite ($CaC_2O_4.H_2O$, COM) and the (metastable) dihydrated weddellite ($CaC_2O_4.2H_2O$, COD). It is commonly assumed that CaOx stones can form by growing on CaP precipitate attached/associated with the renal papilla, a hypothesis first supported by Randall who correlated the presence of KS with the deposition of a CaP plaque (nowadays known as the Randall's plaque, RP).(3) A second assumption postulates that CaOx stones can originate from CaP tubular plugs in renal ducts of Bellini.(4) As potential mechanism for KS formation from RP, Xie *et al*.(5) proposed a phase transformation from amorphous CaOx clusters on RP (known to be a potential intermediate in biomineralization(6)) to crystalline CaOx stones. Moreover, studies regarding the micro-interface between CaOx stones and RP have given structural indications and have brought further support for the role of RP as a nucleus for stone crystallization.(7-9) Scanning electron microscopy (SEM) detailed the organization of RP in microspherules with attached COM crystals.(7)(8) In addition, chemical characterization has shown that RP presents various crystalline phases with a dominant (ill crystalline) carbonated hydroxyapatite (HAp) occurrence.(10,11) Hypotheses have been formulated to explain CaOx stones formation from RP as final response to: (i) high urine calcium concentration, (ii) reduced urine volume and, (iii) pH decrease leading to the loss of papillary epithelial integrity.(12,13) Recently, a study based on micro X-ray computed tomography has proposed that RP form due to dense aggregation of calcified nanoparticles of CaP at the tip of the papilla.(14)

To support *ex vivo* observations, a biomimetic model adapted to the CaOx crystal growth from RP would be of paramount importance. A few models *in bulk* have been reported in the literature. The mineralization of CaP microspherules has been demonstrated in an agar-agar matrix(15) and RP has been biomimicked using a Polymer-Induced Liquid-Precursor (PILP) process to later simulate stone formation.(16) Yet, both model systems lacked usually to account for: (i) the *µm size* and characteristic *morphology* of CaOx crystals observed in medical context, and (ii) the tubular confinement of the kidney and the associated specific hydrodynamics, *i.e*. the urinary *laminar* flow. Microfluidics, the technology of manipulating flows in channels with micrometric dimensions, has been established as a relevant method to biomimic living systems by recreating organs-on-chip including the microenvironment of nephrons.(17, 18) We provided a contribution to the field, by microengineering a 100 x 100 μm^2 "Y-shaped" microchannel and referred to it as a "collecting duct-on-a-chip" to recreate the conditions for crystallization of CaOx(19) and to study their associated growth kinetics. Albeit CaOx crystalline phases (COM, COD) matched medical observations, COM crystals usually precipitated under twin-shaped form (Fig. 2 in (19)) which has been never reported in pathological KS. In the present work, we used a bottom-up microfluidic approach in an attempt to study the implication of RP regarding CaOx stones formation. *The main goal is to obtain a synthetic "HAp/CaOx" interface comparable to RP/KS in terms of chemical phase, size and morphology*. Moreover, *fast CaOx growth* has to be achieved as *in situ* characterizations

[a] *Sorbonne Université, CNRS, Laboratoire de Chimie de la Matière Condensée de Paris, UMR 7574, Campus Jussieu, 4 place Jussieu F-75005 Paris.*
[b] *Sorbonne Université, CNRS, Laboratoire Physicochimie des Electrolytes et Nanosystèmes Interfaciaux, UMR 8234, Campus Jussieu, 4 place Jussieu F-75005 Paris.*
[c] *Sorbonne Université, CNRS, Laboratoire Interfaces et Systèmes Electrochimiques, UMR 8235, Campus Jussieu, 4 place Jussieu F-75005 Paris.*
[d] *AP-HP, Hôpital Tenon, Explorations Fonctionnelles Multidisciplinaires et Laboratoire des Lithiases, F-75020 Paris.*
† Footnotes relating to the title and/or authors should appear here.
Electronic Supplementary Information (ESI) available: [details of any supplementary information available should be included here]. See DOI: 10.1039/x0xx00000x

(X-ray diffraction, Raman) will be performed. We authorize the starting ionic concentrations to be non-physiological to decipher the involved physico-chemical processes. Therefore, we introduced an organic-free apatitic coating in the microfluidic platform to investigate its reactive role on the nucleation and growth of CaOx crystals. *In fine*, we hope that this novel model system will be considered as an *in vitro* "collecting duct-on-a-chip" platform for a broader understanding of the idiopathic stone formation and will provide a physico-chemical model capable of trustworthy diagnosis.

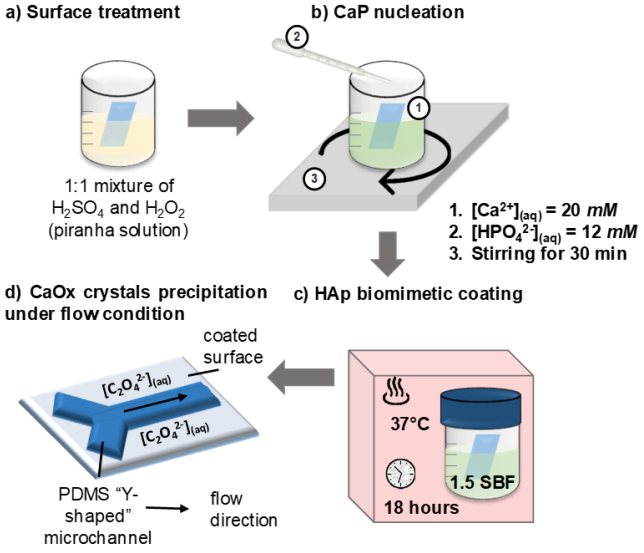

Fig.1 Schematic overview of the experimental protocol: (a) glass substrate treated in a 1:1 mixture of H_2SO_4 96% and H_2O_2 (30 % wt); (b) CaP nucleation induced from mixture of $CaCl_2$ and K_2HPO_4; (c) HAp coating onto the glass substrate for 18 hours at 37°C into 1.5 SBF solution buffered at pH 7.4 with 10 mM Tris-HCl; (d) microfluidic setup assembled with flow injected oxalates.

The formation of the apatitic layer was carried out onto a glass substrate following a modified protocol from Liu *et al.*[20] As summarized in Fig. 1, after the glass substrate was treated in piranha solution (Fig. 1a), CaP nucleation was initiated from a mixture of Ca^{2+} and HPO_4^{2-} aqueous solutions with a ratio Ca/P= 1.67 corresponding to the stoichiometry of HAp (Fig. 1b). As shown in Fig. 1c, the growth of the HAp coating was thereafter conducted by soaking the substrate into a solution matching in ion concentrations the so-called "1.5 Simulated Body Fluid (SBF)" solution[21] (composition given in Table S1). Then, the magnetic and reversible[22] microfluidic platform[19] was assembled and the channel inlets were connected to syringes filled with oxalate ($C_2O_4^{2-}$, Ox^{2-}) aqueous solution ($[Ox^{2-}]_{(aq)}$ = 0.1 *mol.L*$^{-1}$, pH 7.36 from $Na_2C_2O_{4(s)}$). Finally, $Ox^{2-}{}_{(aq)}$ solution was perfused at a continuous and total flow rate of 2.0 *µL.min*$^{-1}$ for 15 min to trigger CaOx crystallization (Fig. 1d).

SEM observations combined with Energy Dispersive X-rays (EDS) analyses characterized the growth of the CaP layer onto the substrate *vs.* time (Fig. S1, Table S2). After 18 h, the CaP layer was organized in aggregates of rather spherical particles (spherulites) with an average diameter ~ 1.0 – 2.0 *µm* (Fig. 2b). The organization and size of these spherulites are consistent with reported observations on RP[7,23-24] (Fig. 2a). X-ray diffraction analysis of the deposited layer (Fig. 2c) matched the pattern (JCPDS 00-009-0432) for poorly crystalline HAp (in contrast to reported HAp as synthetic biomedical composites[25]) with broader peaks often observed in the case of biological substituted hydroxyapatites, including RP.[11]

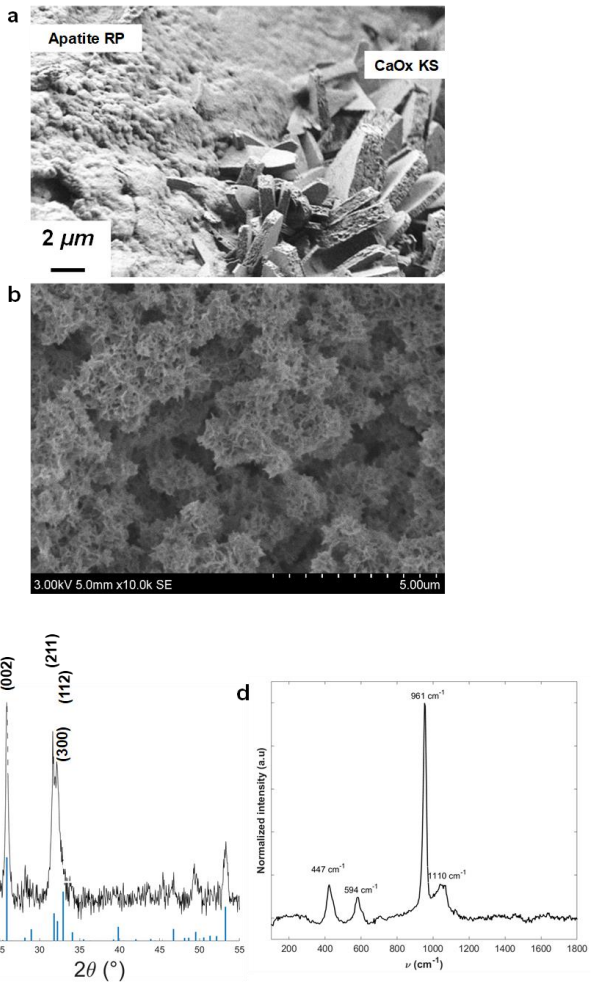

Fig. 2 Characterization of HAp coating: SEM images of (a) an interface between RP and COM kidney stone (reproduced from Bazin *et al.*[7] with permission of ACS); (b) spherulite organization of the apatitic layer after step (c) of the experimental protocol presented in Fig. 1; (c) XRD pattern of the apatitic layer (signal from glass substrate has been removed). Reference pattern of hydroxyapatite JCPDS 00-009-0432; (d) Raman spectrum with characteristic peaks of the apatitic structure (baseline corrected).

The poor crystallinity is due to the small size of the core crystallites and to non-stoichiometry, in agreement with the Ca/P ratio, 1.40 ± 0.03. Raman spectroscopy (Fig. 2d) supported the formation of HAp with peaks at 447, 594 and 961 *cm*$^{-1}$ assigned to $\nu_2(PO_4)$, $\nu_4(PO_4)$ and $\nu_1(PO_4)$ phosphate vibrations, respectively.[26] Additionally, carbonate substitution was suggested with the presence of a broad peak around 1110 *cm*$^{-1}$ that could combine $\nu_1(CO_3)$ carbonate with $\nu_3(PO_4)$ phosphate vibrations.[27] To estimate the extent of the apatitic layer to act as a calcium donor to induce

CaOx crystallization, the coated substrate was left in an oxalate aqueous solution ($[Ox^{2-}]_{(aq)}$ = 0.1 *mol.L*$^{-1}$) for two days (Figure S2).

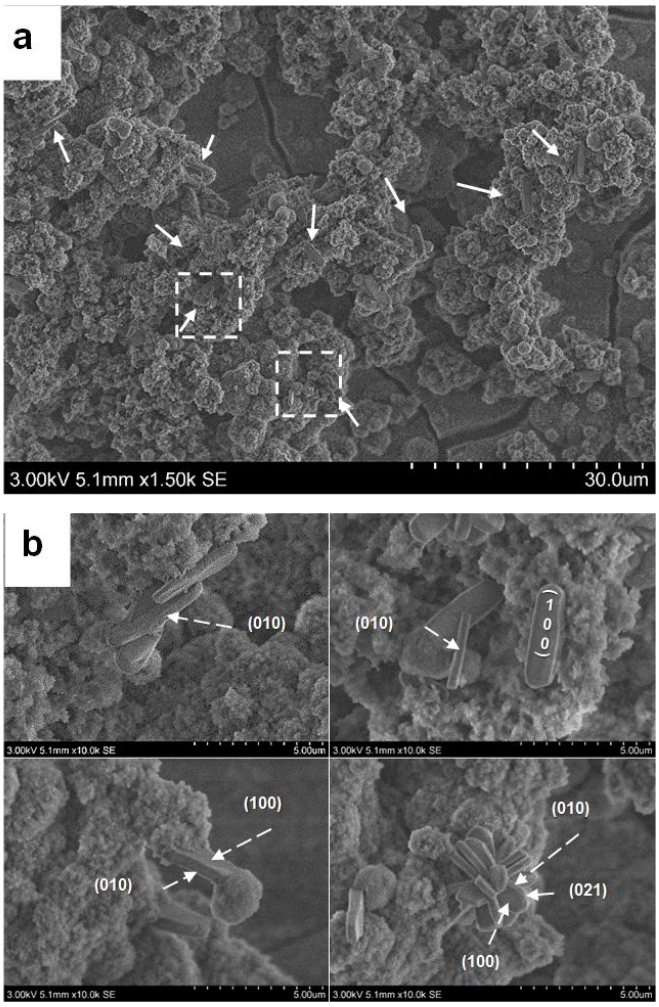

Fig. 3 SEM images of apatitic layer corresponding to the coating in "1.5 SBF" solution and exposed to 15 min continuous flow of $Ox^{2-}_{(aq)}$ at 0.1 *mol.L*$^{-1}$: (a) CaOx random crystallization onto the apatitic layer (white arrows); (b) magnified spots of previous image showing COM crystals embedded in the apatitic microspherules.

Based on crystal habits, SEM examination confirmed the growth of monoclinic-prismatic COM crystals ranging from 10 to 30 *µm*, in parallel with a complete dissolution of the apatitic layer (Fig. S2c). Therefore, in total absence of additional $Ca^{2+}_{(aq)}$ ions in the batch solution, it is concluded that the apatitic layer acts as a calcium donor. Following the release of $Ca^{2+}_{(aq)}$ ions, the solubility product was reached inducing precipitation (K_{sp}(COM) = 2.32 x 10^{-9}).[28] COM crystals exhibit similar morphology as observed *in vivo*[7] (Fig. 2a). Nevertheless, the average size of COM crystals is clearly not comparable to KS entrapped in RP. Moreover, the total dissolution of the apatitic layer – due to obvious lack of control over oxalate diffusion at the surface – did not permit to describe its reactive role regarding CaOx crystallization. To address the previous issue, the apatitic layer was exposed to the same oxalate aqueous solution once mounted in the microfluidic device (Figure 1d). After 15 min of $Ox^{2-}_{(aq)}$ continuous injection, microscale CaOx crystals randomly distributed onto the apatitic layer could be observed (white arrows in Fig. 3a). Magnified SEM images (Fig. 3b) confirmed the growth of CaOx crystals from spherulites and allowed to identify - based on crystal habits – mainly monoclinic-prismatic COM crystals of around 2.0 – 5.0 *µm*.

The shape and micrometric size range of the entrapped crystals were analogous to KS on RP reported in Fig.2a. More specifically, the specific "insertion" of COM crystals in HAp spherulites is well mimicked. The same conclusion holds for the very specific aggregation of COM crystals as shown in Fig. 3b, bottom right. As supported by reference spectrum in Fig. S3a, the formation of COM crystals was confirmed by Raman spectroscopy with characteristic peaks at 525, 896, 1466 and 1489 *cm*$^{-1}$ [19,29,30] in addition to those attributed to the apatitic layer (Fig. S3b). The constrained dimensions of the microchannel and the induced hydrodynamic flow of $Ox^{2-}_{(aq)}$ modulated the dissolution rate of the apatitic layer towards the controlled release of $Ca^{2+}_{(aq)}$ ions at its surface to favor crystal precipitation.[12] The convected $Ox^{2-}_{(aq)}$ ions diffused sufficiently at the apatitic layer surface to raise the local ionic product inducing COM crystallization. Compared to CaOx crystallization in batch, the use of a “collecting duct-on-a-chip” platform appeared as a fair compromise in terms of geometric and timescale considerations to study CaOx crystal growth onto the RP-like layer. Interestingly, the sole identification of COM crystalline phase is in clear accordance with clinical observations associating COM crystallization onto RP with hyperoxaluria[24] albeit the concentration in oxalate used in the present work was far beyond the minimum threshold for *in vivo* CaOx crystallization.[28] Nevertheless, the preliminary results presented herein enabled to propose a biomimetic RP modified “collecting duct-on-a-chip” platform as a suitable model approach regarding the reactive role of RP as a nucleation nuleus for CaOx crystals and to investigate the resulting interface (size, morphology) with respect to comparable *in vivo* KS.[7, 8, 10, 24]

To summarize, we successfully implemented a “collecting duct-on-a-chip” platform with an apatitic coating to mimic the role of a Randall’s plaque in the formation of CaOx kidney stones. We overcame the use of an organic matrix to avoid (as a first and simplified approach) its potential implication with respect to CaOx crystallization. Indeed, previous contributions reported on the role of organic matrices to control the growth of CaOx crystals[31] and to induce microporous crystalline structure due to insertion into mineral lattices.[32,33] For future investigations, components of the extra-cellular matrix such as collagen could be taken into account.[27] The spherulites organization of the layer was consistent with RP organization. COM crystals were consistent with clinical observations both in terms of overall crystal shape and size at the apatitic interface. Nonetheless, a few chemical and physical limitations did not permit to regard the system as fully biomimetic with respect to *in vivo* conditions. Although the concentration in $Ox^{2-}_{(aq)}$ ions perfused within the microfluidic system enabled the formation of COM crystals similar to *in vivo* CaOx stones, the oxalate concentration (*i.e.* $[Ox^{2-}]_{(aq)}$ = 0.1 *mol.L*$^{-1}$) remains unrealistic with respect to common hyperoxaluria conditions [34] and much larger

than the one used in our previous contribution[19] (*i.e.* $[Ox^{2-}]_{(aq)}$ = 0.4 *mmol.L*$^{-1}$). Even though the total flow rate of 2.0 *µL.min*$^{-1}$ matched our earlier work, it does not reflect strictly the laminar urinary flow within the collecting duct as well

(*i.e.* 10 *nL.min*$^{-1}$).[35] Here, we emphasize again that the targeted goal was to mimick realistically (and in a reasonable amount of time for further investigations, *i.e.* 15 min.) the "COM/RP" interface in terms of size, shape and morphology keeping in mind that all previous attempts (in batch) reported insofar in the literature failed.

The simultaneous decrease in both parameters (*i.e.* $[Ox^{2-}]_{(aq)}$ and flow rate) appears quite feasible, yet requires experimental setup enabling ultra-slow flow injection for sufficient duration of diffusion of the precursors. Currently, we are conducting ongoing experiments to work out the mentioned physico-chemical limitations. In a near future, we expect to present a further biomimetic platform matching realistic physiological conditions.

Conflicts of interest

Authors declare no conflict of interest. This work was supported by the doctoral school 397 “Physique et Chimie des Matériaux” (Sorbonne Université), the French state funds managed by the ANR within the Investissements d’Avenir programme ANR-11-IDEX-0004-02, and more specifically within the framework of the Cluster of Excellence MATISSE (Sorbonne Université). We also received technical support of “Institut Pierre-Gilles de Gennes” (Investissement d’Avenir programme ANR-10-EQPX-34). The authors also acknowledge LaBEx MICHEM (Sorbonne Université) for the use of nano/micro Raman facilities and Isabelle Génois for EDS analysis.

SI: Table S1. Chemical composition of "1.5 Simulated Body Fluid" (1.5 SBF) solution. **Table S2.** Elemental analyses of the apatitic layer obtained after coating. **Figure S1.** Quantification of Ca/P ratio of the apatitic layer onto the glass substrate *vs* time of coating in "1.5 SBF" solution from Energy Dispersive X-rays (EDS) analyses. **Figure S2.** In batch CaOx crystallization: (a) after coating of HAp onto the glass substrate, (b) after soaking in oxalate aqueous solution for two days, (c) then dried at room temperature and observed under SEM. **Figure S3.** Raman spectra of (a) reference COM crystal (squared markers) and (b) apatitic layer (rounded markers) exposed to 15 min continuous flow of $[Ox^{2-}]_{(aq)}$ = 0.1 *mol.L*$^{-1}$.

Notes and references

1 V. Romero, H. Akpinar, D.G. Assimos, *Reviews in Urology*, 2010, **12**, e86.
2 M. Daudon, *Ann. Urol*., 2005, **39**, 209.
3 A. Randall, *Annals of Surgery*, 1937, **105**, 1009.
4 A.P. Evan, J.E. Lingeman, F.L. Coe, J.H. Parks, S.B. Bledsoe, Y. Shao Y et al., *The Journal of Clinical Investigation*, 2003, **111**, 607.
5 B. Xie, T.J. Halter, B.M. Borah, G.H. Nancollas, *Crystal Growth & Design*, 2015, **15**, 204.
6 M. Hajir, R. Graf, W. Tremel W., *Chemical Communications*, 2014, **50**, 6534.
7 D. Bazin, M. Daudon, C. Combes, C. Rey C., *Chemical Reviews*, 2012, **112**, 5092.
8 E. Letavernier, D. Bazin, M. Daudon, *Comptes Rendus Chimie*, 2016, **19**, 1456.
9 E. Letavernier, G. Kauffenstein, L. Huguet, N. Navasiolava, E. Bouderlique, E. Tang et al., *Journal of the American Society of Nephrology*, 2018, **29**, 2337.
10 M. Daudon, D. Bazin, E. Letavernier E., *Urolithiasis*, 2015, **43**, 5.
11 S. Rouzière, D. Bazin, M. Daudon M., *Comptes Rendus Chimie*, 2016, **19**, 1404.
12 H.-G. Tiselius, *Urological Research*, 2011, **39**, 231.
13 A.P. Evan, F.L. Coe, J.E. Lingeman, Y. Shao, A.J. Sommer, S.B. Bledsoe et al., *The Anatomical Record*, 2007, **290**, 1315.
14 B.A. Sherer, L. Chen, M. Kang, A.R. Shimotake, S.V. Wiener, T. Chi et al., *Acta Biomaterialia*, 2018, **71**, 72.
15 W. Achilles , U. Jöckel, A. Schaper, M. Burk, H. Riedmiller, Scanning Microsc., 1995, **9**, 577.
16 A. Chidambaram, D. Rodriguez, S. Khan, L. Gower L., *Urolithiasis*, 2015, **43**, 77.
17 Z. Wei, P.K. Amponsah, M. Al-Shatti, Z. Nie, B.C. Bandyopadhyay, *Lab Chip*, 2012, **12**, 4037.
18 K.-J. Jang, K.-Y. Suh, *Lab Chip*, 2010, **10**, 36.
19 G. Laffite, C. Leroy, C. Bonhomme, L. Bonhomme-Coury, E. Letavernier, M. Daudon et al., *Lab Chip*, 2016, **16**, 1157.
20 Q. Liu, J. Ding, F.K. Mante, S.L. Wunder, G.R. Baran, *Biomaterials*, 2002, **23**, 3103.
21 M. Tanahashi, T. Yao, T. Kokubo, M. Minoda, T. Miyamoto, T. Nakamura et al., *Journal of the American Ceramic Society*, 1994, **77**, 2805.
22 M. Rasponi, F. Piraino, N. Sadr, M. Laganà, A. Redaelli, M. Moretti M., *Microfluidics and Nanofluidics*, 2011, **10**, 1097.
23 S.R. Khan, D.E. Rodriguez, L.B. Gower, M. Monga M., *The Journal of Urology*, 2012, **187**, 1094.
24 M. Daudon, O. Traxer, P. Jungers, D. Bazin, *AIP Conference Proceedings*, 2007, **900**, 26.
25 A.A. Chaudhry, S. Haque, S. Kellici, P. Boldrin, I. Rehman, F.A. Khalid et al., *Chemical Communications*, 2006, **21**, 2286.
26 S. Koutsopoulos, *Journal of Biomedical Materials Research Part A*, 2002, **62**, 600.
27 A. Awonusi, M.D. Morris, M.M.J. Tecklenburg, *Calcified Tissue International*, 2007, **81**, 46.
28 M. Daudon, E. Letavernier, V. Frochot, J.-P. Haymann, D. Bazin, P. Jungers, *Comptes Rendus Chimie*, 2016, **19**, 1504.
29 B. Bohner, G. Schuszter, O. Berkesi, D. Horváth, A. Tóth, *Chemical Communications*, 2014, **50**, 4289.
30 I. Petit, G.D. Belletti, T. Debroise, M.J. Llansola-Portoles, I.T. Lucas, C. Leroy et al., *ChemistrySelect*, 2018, **3**, 8801.
31 S. Bisaillon, R. Tawashi, *Journal of Pharmaceutical Sciences*, 1975, **64**, 458.
32 F. Nindiyasari, E. Griesshaber, L. Fernández-Díaz, J.M. Astilleros, N. Sánchez-Pastor, A. Ziegler et al., *Crystal Growth & Design*, 2014, **14**, 4790.
33 L. Chen, T. Ye, X. Jin, J. Ren, B. Huang, Z.-K. Xu et al., *CrystEngComm*., 2015, **17**, 8113.
34 M. Daudon, P. Jungers, O. Traxer, *Lithiase urinaire*, Lavoisier, Médecine Sciences publications; 2012.
35 P.D. Vize, A.S. Woolf, J.B.L. Bard, *The Kidney: From Normal Development to Congenital Disease*, Elsevier Science; 2003.

SUPPLEMENTARY INFORMATION

Fast growth of calcium oxalate crystals on biomimetic Randall's plaque under microfluidic confinement

Karol Rakotozandriny,[a,b] Florence Babonneau,[a] Ivan Lucas,[c] Emmanuel Letavernier,[d] Ali Abou-Hassan,[*b] and Christian Bonhomme,[*a]

[a.] *Sorbonne Université, CNRS, Laboratoire de Chimie de la Matière Condensée de Paris, UMR 7574, Campus Jussieu, 4 place Jussieu F-75005 Paris.*
[b.] *Sorbonne Université, CNRS, Laboratoire Physicochimie des Electrolytes et Nanosystèmes Interfaciaux, UMR 8234, Campus Jussieu, 4 place Jussieu F-75005 Paris.*
[c.] *Sorbonne Université, CNRS, Laboratoire Interfaces et Systèmes Electrochimiques, UMR 8235, Campus Jussieu, 4 place Jussieu F-75005 Paris.*
[d.] *AP-HP, Hôpital Tenon, Explorations Fonctionnelles Multidisciplinaires et Laboratoire des Lithiases, F-75020 Paris.*

Table S1. Chemical composition in Na^+, K^+, Ca^{2+}, Mg^{2+}, HCO_3^-, Cl^-, HPO_4^{2-} and SO_4^{2-} ions for 500 mL of "1.5 Simulated Body Fluid" (1.5 SBF) solution buffered at pH 7.4 with 10 mM Tris-HCl.

Precursors	NaCl	$NaHCO_3$	KCl	K_2HPO_4	$MgCl_2.6H_2O$	$CaCl_2$	Na_2SO_4
m (g)	6.0000	0.2614	0.2087	0.1306	0.2338	0.2108	0.0532

Table S2. Elemental analyses of the apatitic layer obtained after coating.

Element	O	Na	Mg	Al	Si	**P**	Cl	K	**Ca**	Ti
nucleation (A%)	58.31	5.99	n/a	1.87	26.26	**1.24**	0.29	3.26	**1.70**	1.08
18 hours (A%)	52.62	1.74	0.83	0.29	4.08	**15.73**	1.37	0.79	**22.56**	n/a
5 days (A%)	51.03	4.89	0.76	n/a	0.06	**13.93**	8.12	0.29	**20.92**	n/a

Figure S1. Quantification of Ca/P ratio of the apatitic layer onto the glass substrate *vs* time of coating in "1.5 SBF" solution from Energy Dispersive X-rays (EDS) analyses: SEM images (top) with corresponding EDS spectra (bottom).

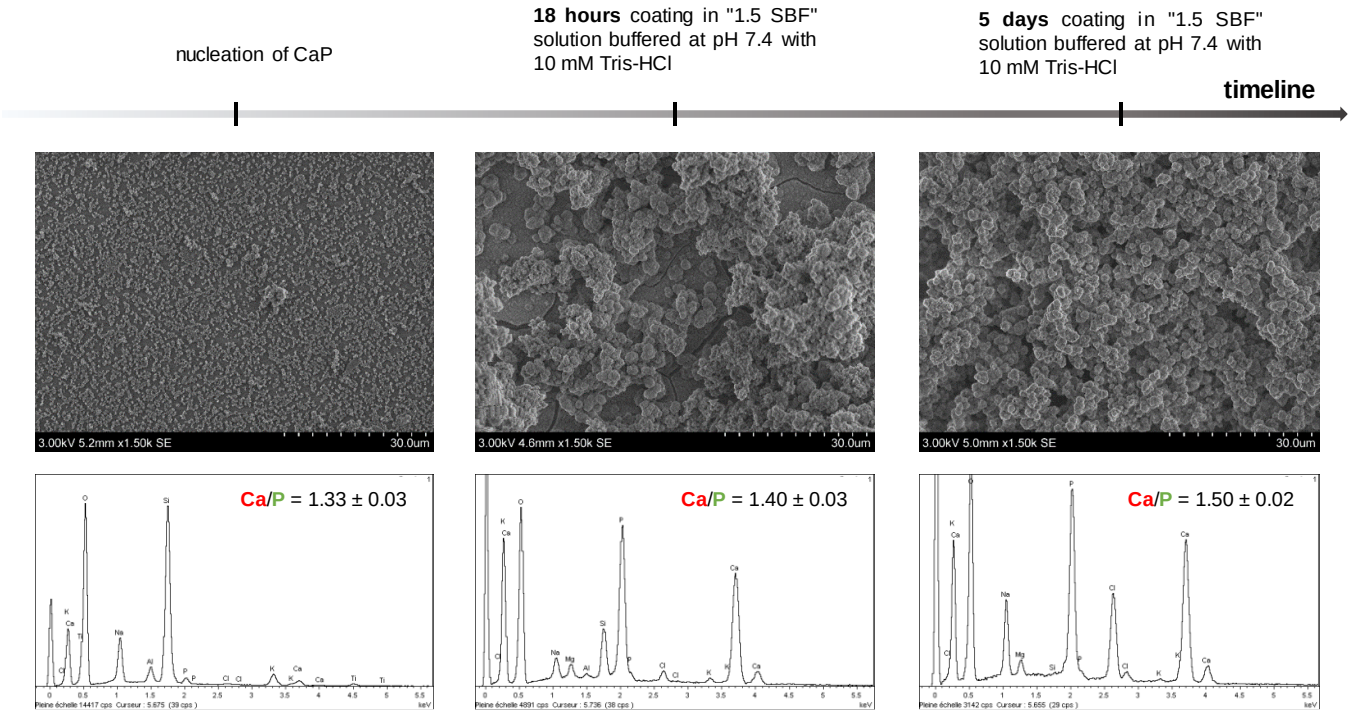

Figure S2. In batch CaOx crystallization: (a) after coating of HAp onto the glass substrate, (b) after soaking in oxalate aqueous solution for two days, (c) then dried at room temperature and observed under SEM.

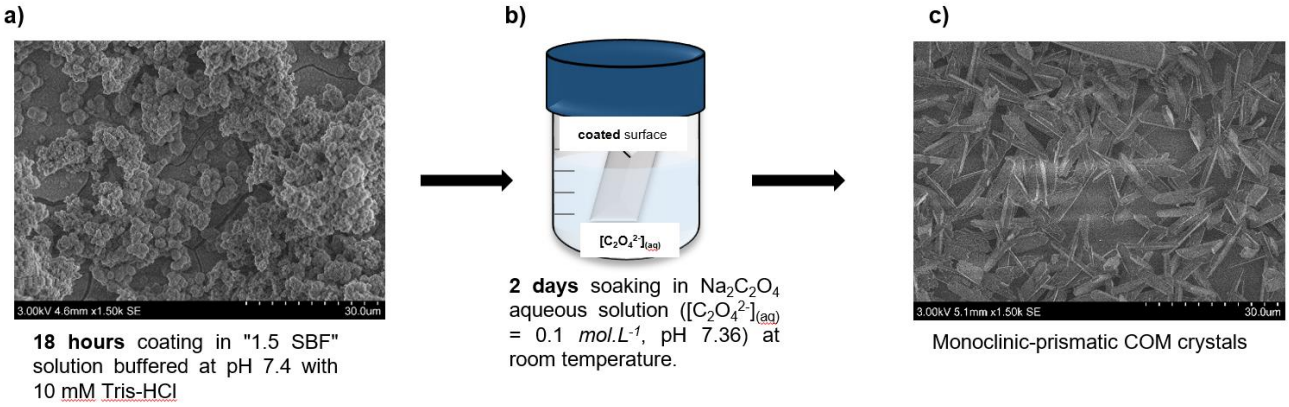

Figure S3. Raman spectra of (a) reference COM crystal (squared markers) and (b) apatitic layer (rounded markers) exposed to 15 min continuous flow of $[Ox^{2-}]_{(aq)}$ = 0.1 *mol.L*$^{-1}$ showing the presence of COM crystal. All spectra are baseline corrected.

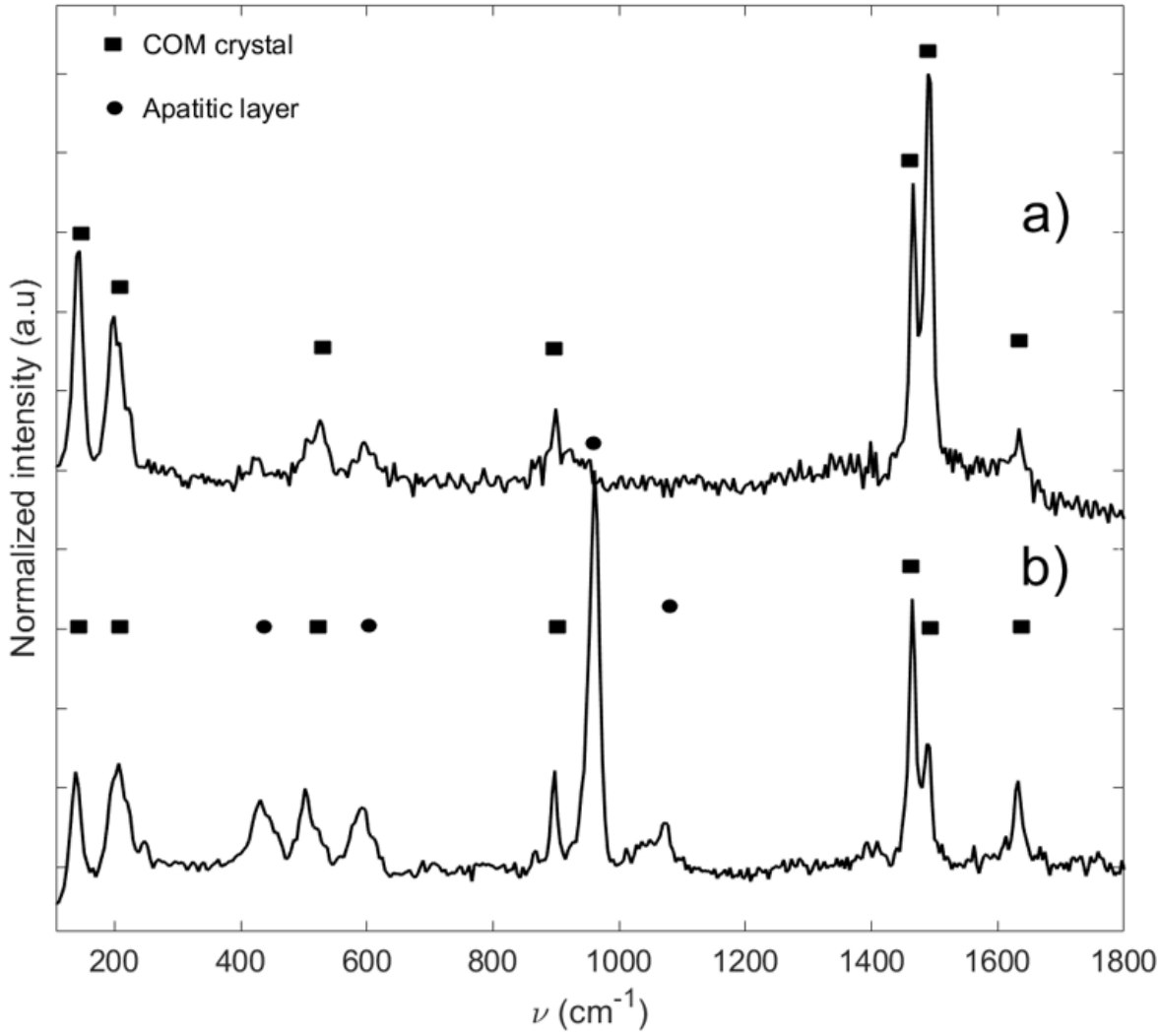

Implementing the collecting duct-on-a-chip device with the apatitic layer was more relevant for investigating CaOx stone growth from the Randall's plaque. Compared to batch crystallization, several advantages are worth pointing out. The microfluidic approach accounts for the micro-confinement akin to the nephron. Moreover, the controlled flow of Ox^{2-} ion permits the control over the ion diffusion at the apatitic surface. Consequently, the local diffusion of Ox^{2-} ions induced local dissolution of the apatitic layer, associated to local zones of supersaturation in $Ca^{2+}_{(RP)}$ and Ox^{2-} ions towards $[Ca^{2+}]_{(RP)} \times [Ox^{2-}]_{(aq)} \geq K_{sp(CaOx)}$. Interestingly, CaOx crystals derived from the dissolution-recrystallization process of RP-like substrate were fully consistent with the COM crystals observed *in vivo* under hyperoxaluria condition. Furthermore, the growing interface between HAp spherulites and COM crystals could be studied to inform on the organization between *in vivo* RP and CaOx kidney stone. Our first results are conclusive and room remains for improvements. A preliminary study is proposed to lower the Ox^{2-} concentration towards physio-pathological conditions. Furthermore, it is worth keeping in mind that *in vivo* Randall's plaque is strongly associated to the proteins (*e.g.* collagen) of the renal extra-cellular matrix (ECM). Therefore, the possible influence of such organic species cannot be neglected regarding CaOx stone formation. Likewise the development of the *in vitro* RP-like substrate, it would be interesting to think of an *in vitro* ECM model system associated to the collecting duct-on-a-chip device. Back to the RP-like model system, CaOx crystals growth depends on the dissolution-recrystallization of the apatitic layer. Therefore, investigating the influence of the apatitic layer's dissolution rate on CaOx crystallization is of prime importance.

b. The dissolution rate of the Randall's plaque-like model regarding calcium oxalate crystallization

i. The pH sensitivity of substituted hydroxyapatite

In response to the selective re-absorption and exchange of ions, the urine flowing through the nephron undergoes changes in urinary pH[37]. From initial pH 7.4, the pH value decreases first in *the proximal tubule* (pH 6.7 – 6.8), then increases again in the descending limb of *the loop of Henle* (pH 7.2) to reach finally pH 5.6 – 6.0 at the end of *the collecting ducts* (see **Chapter 1** section **1.a.i** for further description of the mentioned structures). Nevertheless, renal failure might occur and alter the normal pH ranges in the nephron.

Interestingly, several studies showed the pH sensitivity of different HAp materials with respect to their dissolution behavior in solution. For example, Ducheyne and collaborators demonstrated a higher solubility when measuring the concentration in free Ca^{2+} ions in solution at pH 7.3 of Ca-deficient (4.80 *ppm*) compared to stoichiometric (1.88 *ppm*) HAp[38].

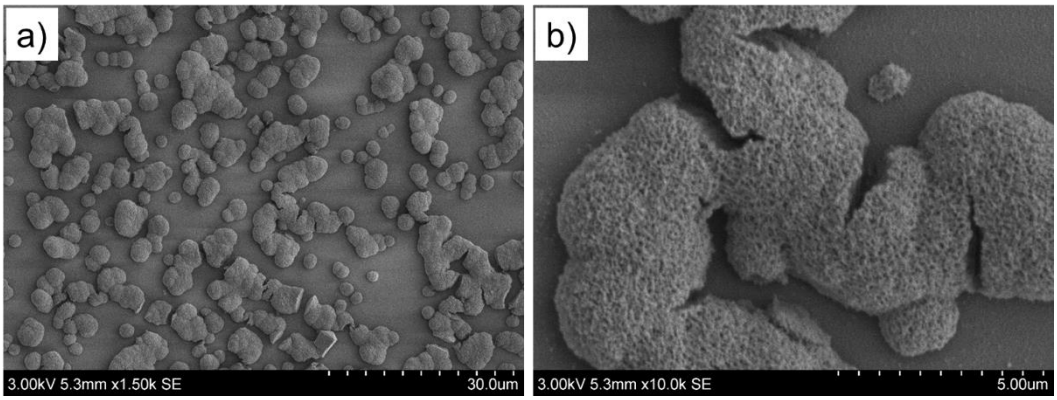

Figure 13. SEM images at two distinct magnifications of apatitic layer after subsequent exposure to a HCl solution at pH 4.5 for one week.

Table 4. Concentration in $Ca^{2+}_{(RP)}$ ions *from* the apatitic layer measured in the solution against the pH and the immersion time. Concentrations are given minus the nominal concentration at initial time (*i.e.* $[Ca^{2+}]_{t=0}$ = 5 and 4 *ppm* for deionized water and HCl solution, respectively). In absence of standard deviation, these measurements serve as qualitative indicators at best.

$[Ca^{2+}]_{(RP)}$	24 hours	48 hours	one week
pH 7.4 (*deionized water*)	14 *ppm*	21 *ppm*	21 *ppm*
pH 4.5 (*HCl*)	30 *ppm*	32 *ppm*	36 *ppm*

Furthermore, Hankermeyer *et al.* showed an increased dissolution rate of carbonated HAp in HCl solution[39]. Considering that the final urine might become as acidic as pH 4.5 *in case of a renal failure*[40], the stability of HAp-RP can be strongly modified, influencing the formation of CaOx kidney stones. To study HAp-COM crystallization reaction, Sethmann *et al.* investigated the release of Ca^{2+} ions from a bone substrate in various oxalate solutions with pH ranging from 4.5 to 7.5[28]. The results showed that the reaction was induced even under common urinary concentration in Ox^{2-} ions and pH (*e.g.* combined 0.25 $mmol.L^{-1}$ and pH 5.5).

If operated at lower pH, the RP-modified collecting duct-on-a-chip device would still stand for a biomimetic platform with respect to the kidney stone disease. As demonstrated in section **2.a**, the apatitic layer acted as a substrate for COM crystal growth through the release in $Ca^{2+}_{(RP)}$ ions at pH 7.36. Herein, we want to adapt our previous study at *pH 4.5*. First, we demonstrate a higher dissolution behavior of the apatitic substrate at the pH of interest.

Two pieces of ≈ 0.5 × 0.5 cm^2 from the same apatitic layer (as shown in **Figure 8d**) were soaked in two solutions (V = 1.0 *mL*) at two pH values, *i.e*. pH 7.4 and 4.5, respectively. The pH was adjusted using HCl. Afterwards, the concentration in $Ca^{2+}_{(RP)}$ ions was measured *vs.* time using a Ca^{2+} ion sensitive electrode for comparison purposes (**Table 4**). The results positively supported the influence of an acidic pH on the partial dissolution of the apatitic layer, even after 24 hours soaking. Interestingly, the equilibrium concentration in $Ca^{2+}_{(RP)}$ was

attained *almost* after 48 hours although at pH 4.5, $Ca^{2+}_{(RP)}$ continued to slightly increase. It is worth commenting the gap between the concentration in Ca^{2+} measured by Ducheyne *et al.*[38] and our value at comparable pH and time (*i.e.* 4.80 *vs.* 14 *ppm* at pH 7.4 after 24 hours, respectively). While we used the apatitic substrate as a Ca-deficient HAp model, the other group worked with *commercial* Ca-deficient phosphate tribasic ($Ca_{10-x}(HPO_4)_x(PO_4)_{6-x}(OH)_{2-2x}$, Ca/P = 1.61). Consequently, we presume a better crystallinity of their material (*i.e.* lesser solubility) compared to the SBF-issued apatitic layer.

After one week in HCl solution, SEM characterization was carried out for further evaluation (**Figure 13**). In **Figure 13a**, we assessed the dissolution of the apatitic layer with the clear loss of the "cauliflower"-like organization (see **Figure 9e** and magnified **Figure 10d**). Yet, patches of HAp remained with the exposure of the glass substrate beneath. Furthermore, we observed a "sponge"-like aspect at higher magnification (**Figure 13b**). Aside from supporting an enhanced dissolution at pH 4.5, we showed drastic morphological changes of the apatitic layer compared to its primary aspect.

ii. The calcium oxalate heterogeneous growth derived from the Randall's plaque-like substrate under acidic condition (*i.e.* pH 4.5)

Before implementation within the collecting duct-on-a-chip device, we assess once again that the apatitic layer acts as a supportive substrate to trigger CaOx crystallization at pH 4.5 (as in section **2.a.i**). Noteworthy, $Ox^{2-} \equiv C_2O_4^{2-}$ is the conjugate base of oxalic acid (at 25°C)

$$C_2O_4H_2 \rightleftharpoons C_2O_4H^- + H^+ \quad pK_a = 1.2$$

$$C_2O_4H^- \rightleftharpoons C_2O_4^{2-} + H^+ \quad pK_a = 4.3$$

Therefore, a piece of ≈ 0.5 × 0.5 *cm* of the apatitic layer was soaked in an oxalate solution at *pH 4.5* in total absence of external sources of Ca^{2+} ions for one week. Again, two concentrations in Ox^{2-} ions were studied, *i.e.* $[Ox^{2-}]_{pH\ 4.5} = 0.40\ mmol.L^{-1}$ and $[Ox^{2-}]_{pH\ 4.5} = 100\ mmol.L^{-1}$, respectively. After one week soaking in oxalate solution, we assessed the emergence of new crystals apart from the HAp spherulites either at $[Ox^{2-}]_{pH\ 4.5}$ = 0.40 $mmol.L^{-1}$ (**Figures 14a-b**) or at $[Ox^{2-}]_{pH\ 4.5}$ = 100 $mmol.L^{-1}$ (**Figures 14c-d**). The measurement of the concentration in free $Ca^{2+}_{(RP)}$ was attempted in the end, unsuccessfully. We hypothesized that the released $Ca^{2+}_{(RP)}$ ions reacted with Ox^{2-} ions for consecutive CaOx crystallization. Under moderate hyperoxaluria-like condition (*i.e.* $[Ox^{2-}]_{pH\ 4.5}$ = 0.40 $mmol.L^{-1}$), the apatitic spherulites were highly dissolved (background in **Figure 14a**) resulting in the exposure of the glass substrate underneath (alike in **Figure 13a**). In addition, COM crystals grew from the spherulites (likewise in **Figure 12b**)**.** Magnified SEM image detailed morphological changes on the spherulites (**Figure 14b**). After immersion in oxalate solution at pH 4.5, the spherulites lost their "pincushion" aspect and transform to

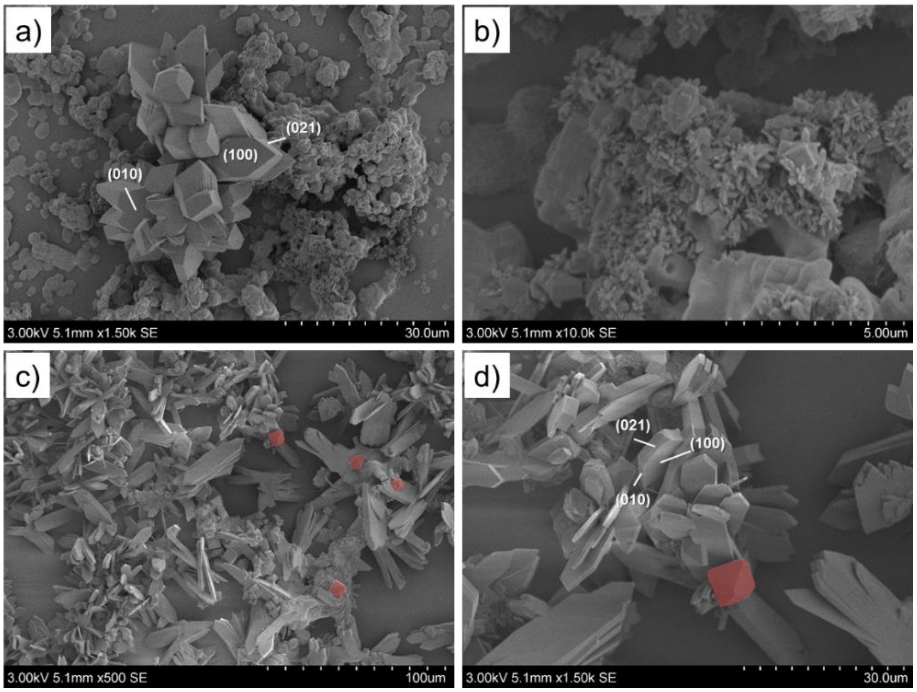

Figure 14. SEM images of CaOx crystals growth from the RP-like substrate in batch crystallization for one week *at pH 4.5*. The panel of images stands for after immersion in oxalate solution at $[Ox^{2-}]_{pH\ 4.5}$ = 0.40 *mmol.L*$^{-1}$ (**Figures 14a-b**) and at $[Ox^{2-}]_{pH\ 4.5}$ = 100 *mmol.L*$^{-1}$ (**Figures 14c-d**). Red "false-color" indicates the presence of bipyramid COD crystals.

aggregates. The inability to easily spot these aggregates using *Raman* spectroscopy limits their phase identification. Yet, we can suspect either a phase transformation from Ca-deficient HAp to another CaP mineral or the formation of CaOx crystals. At $[Ox^{2-}]_{pH\ 4.5}$ = 100 *mmol.L*$^{-1}$ (**Figures 14c-d**), we assessed the complete consumption of the apatitic spherulites at the expense of monoclinic prismatic COM crystal (as illustrated in **Figure 12e**). Surprisingly, occasional bipyramid COD crystals of ≈ 5 – 10 *µm* and associated to COM crystals were also identified (in red in the magnified image of **Figure 14d**). Using batch crystallization, we confirmed the use of the apatitic layer as a calcium donor for CaOx heterogeneous crystallization, even at more acidic conditions.

Afterwards, the RP-modified collecting duct-on-a-chip device was assembled and continuously perfused at Q_{tot} = 2.0 *µL.min*$^{-1}$ with solely oxalate solution at pH 4.5 (similarly to section **2.a.ii**). Les us recall that a total operating flow rate of 2.0 *µL.min*$^{-1}$ is associated to an average fluid velocity of $\bar{u}$ = 3.33 × 10^3 *µm.s*$^{-1}$, a Reynolds number of R_e = 0.37 and a Péclet number of P_e = 374 (see **Chapter 2** section **1.a.i** for definitions). The corresponding results are presented in **Figures 15** and **16** for oxalate solution at $[Ox^{2-}]_{pH\ 4.5}$ = 0.40 *mmol.L*$^{-1}$ and $[Ox^{2-}]_{pH\ 4.5}$ = 100 *mmol.L*$^{-1}$, respectively.

At the lowest concentration (*i.e.* 0.40 *mmol.L*$^{-1}$), we did not observe the growth of well-defined CaOx crystals from the "cauliflower"-like structures (**Figure 15a**). Nevertheless, **Figures 15b-d** enlightened morphological changes *after one hour* of continuous perfusion of

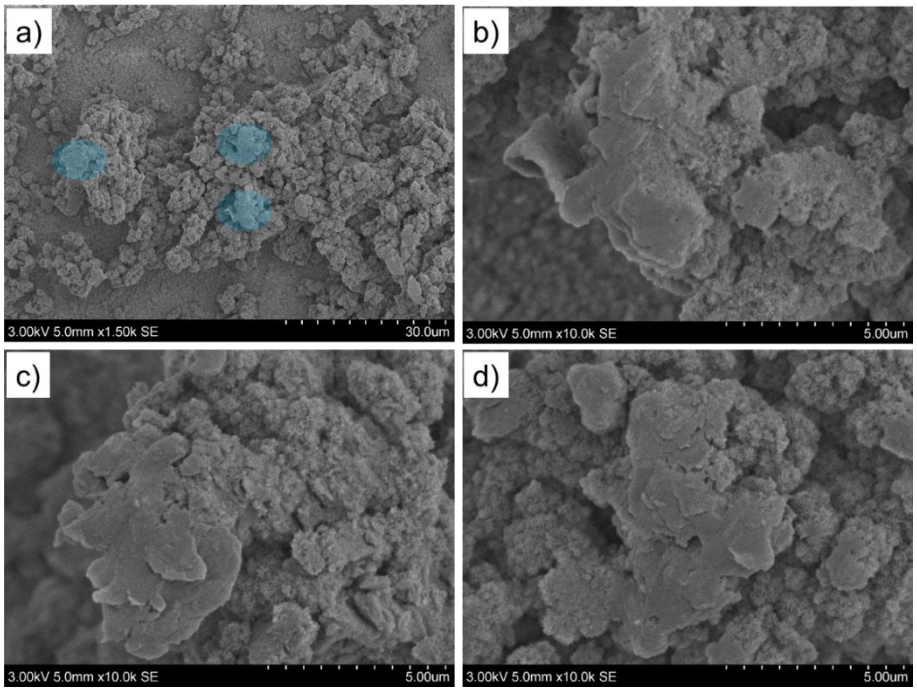

Figure 15. Series of SEM images depicting the RP-like substrate after consecutive exposure to continuous flow of oxalate solution at $[Ox^{2-}]_{pH\ 4.5}$ = 0.40 *mmol.L*$^{-1}$ in the collecting duct-on-a-chip device (Q_{tot} = 2.0 *µL.min*$^{-1}$ for *one hour*). Blue color in **Figure 15a** shows the respective locations of **Figures 15b-d**.

oxalate solution. The spherulites lost their pincushion-like morphology and exhibited smoother surface state. We conclude on the lowest concentration in Ox^{2-} ions to be insufficient under microfluidic conditions for CaOx crystals growth. This finding contrasted with the batch crystallization's results under acidic conditions (**Figure 14**). One hypothesis relies on a too limited exposure time of the RP-like substrate to the flowing oxalate solution. Indeed, we arbitrary set the contact time between the solution and the substrate to one hour. Since we assessed a morphological change with respect to the spherulites, we could suggest that a longer exposure might trigger CaOx crystallization. This would agree with Sethmann and collaborators[28] who induced COM crystal precipitation when soaking in batch a bone substrate for three days in oxalate solution at $[Ox^{2-}]_{pH\ 4.5}$ = 0.50 *mmol.L*$^{-1}$.

The RP-modified collecting duct-on-a-chip device presents more conclusive results when operating at $[Ox^{2-}]_{pH\ 4.5}$ = 100 *mmol.L*$^{-1}$ (**Figure 16**). Noteworthy, the series of images detail the same RP-like substrate after continuous perfusion of oxalate solution for 15 *min* but at two different locations in the microchannel, *i.e.* **Figures 16a-c** *vs.* **Figures 16d-f**. At such higher concentration in Ox^{2-} ions, the short perfusion time enabled heterogeneous CaOx crystallization derived from the apatitic substrate. Therefore, the acidic pH combined with $[Ox^{2-}]_{pH\ 4.5}$ = 100 *mmol.L*$^{-1}$ enabled the release of substantial amount of $Ca^{2+}_{(RP)}$ such as $[Ca^{2+}]_{(RP)} \times [Ox^{2-}]_{pH\ 4.5} \geq K_{sp(CaOx)}$. Alike batch crystallization at similar concentration in Ox^{2-} ions (**Figures 14c-d**), we observed the occasional presence of COD crystals over-expressing the

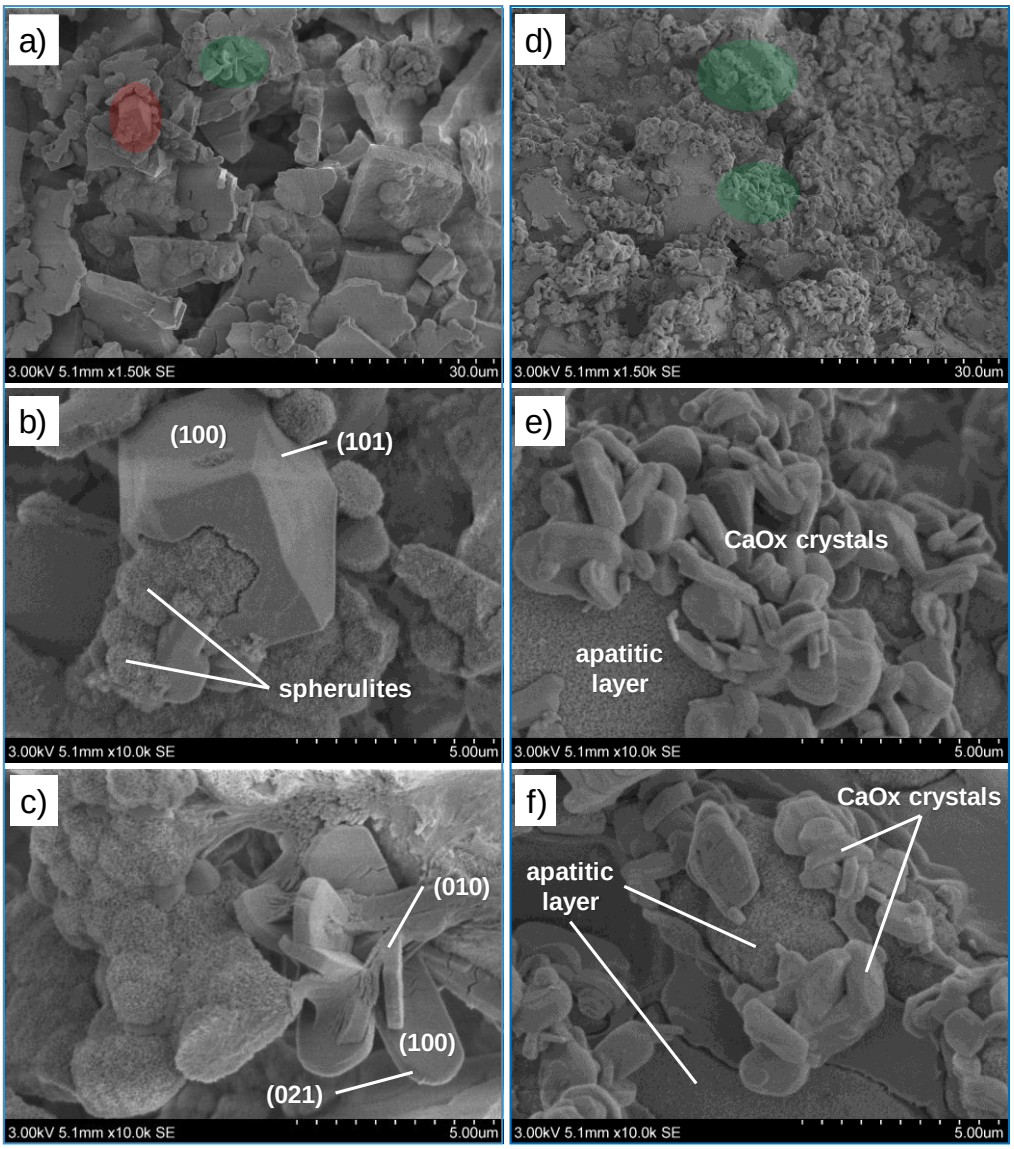

Figure 16. Set of SEM images depicting *two distinct zones* of the RP-like substrate after consecutive exposure to continuous flow of oxalate solution at $[Ox^{2-}]_{pH\ 4.5}$ = 100 *mmol.L*$^{-1}$ in the collecting duct-on-a-chip device (Q_{tot} = 2.0 *µL.min*$^{-1}$ for *15 min*). Red and green colors in **Figure 16a** and **Figure 16d** show the locations of **Figures 16b-c** and **Figures 16e-f**, respectively.

(100) crystallographic face (**Figure 16b**). Otherwise, platelet-like crystals grew on the apatitic layer (**Figures 16c-f**) that resembled monoclinic prismatic COM crystals. Once more, the spherulites entrapped in CaOx crystals (*e.g.* **Figure 16b**) supported the dissolution-recrystallization mechanism of RP towards the growth of CaOx crystals. In **Figures 16d-f**, we could note the growth of COM agglomerates under acidic condition. We know that low pH induces an enhanced dissolution of the apatitic layer and, in turn, a greater release in $Ca^{2+}_{(RP)}$ ions. Consequently, it "boosts" CaOx crystallization compared to the results presented in the publication for $[Ox^{2-}]_{(aq)}$ = *100 mmol.L*$^{-1}$ (section **2.a.ii**). It is interesting to note that agglomerates (with individual crystal sizing up to ≈ 2.0 µm) grew instead of enlarging CaOx crystals. Noteworthy, these CaOx agglomerates (*e.g.* **Figure 16e**) resemble the ones in **Figure 1b** as observed by Daudon and collaborators[5]. Nevertheless, we recall that $[Ox^{2-}]_{pH\ 4.5}$ = 100 *mmol.L*$^{-}$

[1] is not physio-pathologically realistic with respect to standard hyperoxaluria condition. We guess that similar results could be obtain for 0.40 *mmol.L*$^{-1}$ > $[Ox^{2-}]_{pH\ 4.5}$ > 100 *mmol.L*$^{-1}$ (*e.g.* at 1.0 *mmol.L*$^{-1}$ as investigated by Sethmann et al.[28]) and with a decrease in flow rate matching nephron-like flow conditions.

Due to poor crystallinity, substituted HAp demonstrated higher solubility (even more in acidic solution[39]) compared to stoichiometric HAp[38]. Knowing that the urine can become acidic in extreme cases[40], HAp-RP can be more sensitive to dissolution, release higher amounts of $Ca^{2+}_{(RP)}$ ions and consequently, boost the growth of CaOx-based kidney stones. Using a bone substrate as a RP model, Sethmann and collaborators investigated the influence of pH on the release of Ca^{2+} ions with respect to HAp to COM crystallization reaction[28]. The authors highlighted a dissolution-recrystallization mechanism of the bone surface towards the precipitation of COM crystals. To investigate kidney stone formation in closer conditions to the disease, we have operated the RP-modified collecting duct-on-a-chip device under acidic condition (*i.e.* pH 4.5). First, we demonstrated that $Ca^{2+}_{(RP)}$ ions released from the apatitic substrate was pH-sensitive (**Table 4**) and enabled CaOx crystals growth from the substrate under batch crystallization (**Figure 14**). Two concentrations in Ox^{2-} ion were under scrutiny and used, thereafter, to conduct CaOx crystallization at pH 4.5 and under microfluidic conditions. Although $[Ox^{2-}]_{pH\ 4.5}$ = 0.40 *mmol.L*$^{-1}$ reacted with the spherulites to induce morphological changes at their surfaces, it did not trigger heterogeneous CaOx crystallization (**Figure 15**). On the other hand, $[Ox^{2-}]_{pH\ 4.5}$ = 100 *mmol.L*$^{-1}$ demonstrated more conclusive results regarding the growth of COM crystals derived from the apatitic layer (**Figure 16**). Similarly to $[Ox^{2-}]_{(aq)}$ = 100 *mmol.L*$^{-1}$ at pH 7.36 (see section **2.a.ii**), monoclinic prismatic COM crystals appeared from the apatitic spherulites. However, COM crystals at pH 4.5 likely formed agglomerates (**Figure 16e**) while at pH 7.36, they were organized in aggregates of a few platelet-like crystals. Noteworthy, COD crystals were occasionally observed under combined very high concentration in Ox^{2-} ions and acidic pH 4.5 (**Figure 16b**). With respect to the CaOx crystalline phases and crystal habits, the results were comparable to medical observations[5] (**Figure 1b**). However, it is important to remember that $[Ox^{2-}]_{pH\ 4.5}$ = 100 *mmol.L*$^{-1}$ is far from being realistic even in pathological cases. Aside from the microfluidic advantage, we present as *proof-of-concept* that heterogeneous CaOx crystallization also can be investigated under urinary-like acidic conditions and under *microfluidic confinement*.

3. Conclusion

The Randall's plaque, a deposit made of Ca-deficient HAp, is found in the nephron (*i.e.* loop of Henle[11] and/or ducts of Bellini[12]) and is suspected to initiate the formation of CaOx-based kidney stones[2]. In-depth chemical characterization of such deposit showed that RP consists of

poorly crystalline carbonated HAp[5], organized in micro-spherulites (from 1.0 to 5.0 *µm*) strongly associated to proteins from the extra-cellular matrix (*e.g*. collagen)[15]. Unfortunately, medical studies accounting for the initiating role regarding CaOx crystallization were mainly based on *indirect* evidences. Therefore, the development of an *in vitro* model system of the RP would prove more than valuable to investigate its reactive role and to support the medical observations.

Noteworthy contributions from the literature attempted to build up such an *in vitro* RP model systems. Achilles and collaborators generated core-shell spherulites of apatite-octacalcium phosphate[21,22]. Our research group synthesized non-substituted HAp to serve as RP model[26]. Sethmann and collaborators used a piece of bone to act as a mimetic model of RP[28]. Interestingly, they all succeeded in inducing subsequent CaOx crystallization (although, in batch) either from Ca^{2+} and Ox^{2-} ions containing solutions or sole Ox^{2-} ions solutions at similar concentrations to stone promoting conditions. Their respective results supported the role of RP as a calcium donor through its partial dissolution to trigger CaOx crystallization. However, they all missed in accounting for the confinement and associated fluid-flow encountered in the nephron. Having access to these combined conditions would propose a physicochemical model mimicking further kidney stone disease.

In the present chapter, we presented a new strategy to build up an *in vitro* RP-like model system suitable for microfluidic investigation using the collecting duct-on-a-chip device described in **Chapter 2**.

Based on the work of Liu *et al*., we coated the sealing glass coverslip of the micro-reactor with an apatitic layer using the SBF strategy[34]. Briefly, the SBF strategy relies on the use of an acellular solution at ion concentrations, pH and temperature comparable to those of the human blood plasma to induce the formation of a Ca-deficient HAp layer on a substrate[32,33]. In-depth characterization showed that the apatitic layer issued from the SBF strategy consisted of poorly crystalline HAp (XRD analysis), likely substituted (*Raman* spectroscopy) and organized in micro-spherulites of ≈ 1.0 *µm* (SEM imaging).

To ensure that the apatitic layer acted as a calcium donor (i.e. release in $Ca^{2+}_{(RP)}$ ions), batch crystallization was conducted by immersion in two distinct Ox^{2-} ion containing solutions at 0.40 $mmol.L^{-1}$ and 100 $mmol.L^{-1}$ (pH 7.36), respectively. Both concentrations of interest supported the dissolution-recrystallization mechanisms of the apatitic layer towards COM crystal growth. Indeed, close examination enlightened the progressive growth of COM crystals from the apatitic spherulites. However, the obtained COM crystals' morphologies (*i.e.* twins shape usually obtained under batch crystallization[26]) and sizes (*i.e.* up to 50 µm) did not permit to validate the batch method as a mimetic technique with respect to kidney stone formation.

Thereafter, the apatitic layer was assembled within the micro-reactor to obtain a RP-modified collecting duct-on-a-chip device and continuously injected with an oxalate solution. The controlled flow of Ox^{2-} ions permitted the control over the diffusion of ions at the apatitic surface. In consequence, the local diffusion of Ox^{2-} ion induced local dissolution of the apatitic layer, associated to local zones of supersaturation in $Ca^{2+}_{(RP)}$ and Ox^{2-} ions leading to $[Ca^{2+}]_{(RP)} \times [Ox^{2-}]_{(aq)} \geq K_{sp(CaOx)}$ (*i.e*. CaOx crystallization). Interestingly, monoclinic prismatic COM crystals were obtained, in full agreement with the COM crystals observed by physicians under hyperoxaluria conditions[5,10]. Furthermore, the growing interface between HAp spherulites and COM crystals could be studied to inform on the organization between *in vivo* RP and CaOx kidney stone. COM crystals grew from the HAp spherulites, underlying the dissolution-recrystallization mechanisms of RP to promote the growth of CaOx-based kidney stones.

Last, we studied the influence of the pH on the apatitic layer's dissolution rate and, *in fine*, on CaOx crystallization. In response to renal failure, the becoming urine can experienced abnormal pH ranges with a direct impact on the dissolution of RP and subsequent formation of CaOx-based kidney stones. Alike Ducheyne and collaborators[38] and Hankermeyer and collaborators[39], we supported that the apatitic layer dissolved more in acidic solution (herein at pH 4.5). Under microfluidic confinement, the continuous flow of Ox^{2-} ions at $[Ox^{2-}]_{pH\ 4.5}$ = 100 $mmol.L^{-1}$ demonstrated the emergence of monoclinic prismatic COM crystals from the apatitic spherulites and organized in agglomerates. Occasionnally, (100) elongated COD crystals were observed under the combined confined and acidic conditions. It is worth pointing out that usually, this specific crystal morphology is obtained in presence of additives. *In fine*, we presented the RP-modified collecting duct-on-a-chip device as a suitable platform for the investigation of CaOx-based kidney stones growth from a RP-like substrate under abnormal acidic conditions.

Interestingly, this observation shows that CaOx crystallization in the collecting duct-on-a-chip device can be studied by varying the chemical conditions in the micro-reactor. Obviously, these chemical conditions have a noticeable impact on the resulting CaOx crystals, with respect to their crystalline phases and crystal morphologies. Therefore, it could be interesting to investigate the modulating effect of other external additives on CaOx crystallization using the microfluidic device. To address the question, the next chapter will deal with the influence of polyphenolic catechins from green tea on CaOx crystals.

References

(1) Daudon, M. [Epidemiology of nephrolithiasis in France]. *Ann Urol (Paris)* **2005,** *39* (6), 209.

(2) Daudon, M.; Jungers, P.; Bazin, D. Stone Morphology: Implication for Pathogenesis. *AIP Conference Proceedings* **2008,** *1049* (1), 199.

(3) Randall, A. The Origin and Growth of Renal Calculi. *Annals of Surgery* **1937,** *105* (6), 1009.

(4) Evan, A. P.; Coe, F. L.; Lingeman, J. E.; Shao, Y.; Sommer, A. J.; Bledsoe, S. B.; Anderson, J. C.; Worcester, E. M. Mechanism of Formation of Human Calcium Oxalate Renal Stones on Randall's Plaque. *The Anatomical Record* **2007,** *290* (10), 1315.

(5) Bazin, D.; Daudon, M.; Combes, C.; Rey, C. Characterization and Some Physicochemical Aspects of Pathological Microcalcifications. *Chemical Reviews* **2012,** *112* (10), 5092.

(6) Letavernier, E.; Bazin, D.; Daudon, M. Randall's plaque and kidney stones: Recent advances and future challenges. *Comptes Rendus Chimie* **2016,** *19* (11), 1456.

(7) Sherer, B. A.; Chen, L.; Kang, M.; Shimotake, A. R.; Wiener, S. V.; Chi, T.; Stoller, M. L.; Ho, S. P. A continuum of mineralization from human renal pyramid to stones on stems. *Acta Biomaterialia* **2018,** *71*, 72.

(8) Wesson, J. A.; Johnson, R. J.; Mazzali, M.; Beshensky, A. M.; Stietz, S.; Giachelli, C.; Liaw, L.; Alpers, C. E.; Couser, W. G.; Kleinman, J. G.et al. Osteopontin Is a Critical Inhibitor of Calcium Oxalate Crystal Formation and Retention in Renal Tubules. *Journal of the American Society of Nephrology* **2003,** *14* (1), 139.

(9) Mo, L.; Huang, H. Y.; Zhu, X. H.; Shapiro, E.; Hasty, D. L.; Wu, X. R. Tamm-Horsfall protein is a critical renal defense factor protecting against calcium oxalate crystal formation. *Kidney international* **2004,** *66* (3), 1159.

(10) Daudon, M.; Traxer, O.; Jungers, P.; Bazin, D. Stone Morphology Suggestive of Randall's Plaque. *AIP Conference Proceedings* **2007,** *900* (1), 26.

(11) Evan, A. P.; Lingeman, J. E.; Coe, F. L.; Parks, J. H.; Bledsoe, S. B.; Shao, Y.; Sommer, A. J.; Paterson, R. F.; Kuo, R. L.; Grynpas, M. Randall's plaque of patients with nephrolithiasis begins in basement membranes of thin loops of Henle. *The Journal of Clinical Investigation* **2003,** *111* (5), 607.

(12) Daudon, M.; Bazin, D.; Letavernier, E. Randall's plaque as the origin of calcium oxalate kidney stones. *Urolithiasis* **2015,** *43* (1), 5.

(13) Kuo, R. L.; Lingeman, J. E.; Evan, A. P.; Paterson, R. F.; Parks, J. H.; Bledsoe, S. B.; Munch, L. C.; Coe, F. L. Urine calcium and volume predict coverage of renal papilla by Randall's plaque. *Kidney international* **2003,** *64* (6), 2150.

(14) Tiselius, H.-G. The role of calcium phosphate in the development of Randall's plaques. *Urolithiasis* **2013,** *41* (5), 369.

(15) Khan, S. R.; Rodriguez, D. E.; Gower, L. B.; Monga, M. Association of Randall Plaque With Collagen Fibers and Membrane Vesicles. *The Journal of Urology* **2012,** *187* (3), 1094.

(16) Reid, D. G.; Jackson, G. J.; Duer, M. J.; Rodgers, A. L. Apatite in Kidney Stones is a Molecular Composite With Glycosaminoglycans and Proteins: Evidence From Nuclear Magnetic Resonance Spectroscopy, and Relevance to Randall's Plaque, Pathogenesis and Prophylaxis. *The Journal of Urology* **2011,** *185* (2), 725.

(17) Rouzière, S.; Bazin, D.; Daudon, M. In-lab X-ray fluorescence and diffraction techniques for pathological calcifications. *Comptes Rendus Chimie* **2016,** *19* (11), 1404.

(18) Rosa, A. L.; Beloti, M. M.; Oliveira, P. T.; Van Noort, R. Osseointegration and osseoconductivity of hydroxyapatite of different microporosities. *Journal of Materials Science: Materials in Medicine* **2002,** *13* (11), 1071.

(19) Sanosh, K. P.; Chu, M.-C.; Balakrishnan, A.; Lee, Y.-J.; Kim, T. N.; Cho, S.-J. Synthesis of nano hydroxyapatite powder that simulate teeth particle morphology and composition. *Current Applied Physics* **2009,** *9* (6), 1459.

(20) Cacciotti, I. In *Handbook of Bioceramics and Biocomposites*; Antoniac, I. V., Ed.; Springer International Publishing: Cham, 2016, DOI:10.1007/978-3-319-12460-5_7 10.1007/978-3-319-12460-5_7.

(21) Achilles, W.; Jöckel, U.; Schapers, A.; Ulshöfer, B.; Riedmiller, H. In *Urolithiasis 2*; Ryall, R.;Bais, R.;Marshall, V. R.;Rofe, A. M.;Smith, L. H.;Walker, V. R., Eds.; Springer US: Boston, MA, 1994, DOI:10.1007/978-1-4615-2556-1_55 10.1007/978-1-4615-2556-1_55.

(22) Achilles, W.; Jöckel, U.; Schaper, A.; Burk, M.; Riedmiller, H. In vitro formation of 'urinary stones': Generation of spherulites of calcium phosphate in gel and overgrowth with calcium oxalate using a new flow model of crystallization. **1995,** *9*, 577.

(23) Bisaillon, S.; Tawashi, R. Growth of Calcium Oxalate in Gel Systems. *Journal of Pharmaceutical Sciences* **1975,** *64* (3), 458.

(24) Chen, L.; Ye, T.; Jin, X.; Ren, J.; Huang, B.; Xu, Z.-K.; Chen, H.; Li, H. Gel network incorporation into single crystals grown by decomplexation method. *CrystEngComm* **2015,** *17* (42), 8113.

(25) Nindiyasari, F.; Griesshaber, E.; Fernández-Díaz, L.; Astilleros, J. M.; Sánchez-Pastor, N.; Ziegler, A.; Schmahl, W. W. Effects of Mg and Hydrogel Solid Content on the Crystallization of Calcium Carbonate in Biomimetic Counter-diffusion Systems. *Crystal Growth & Design* **2014,** *14* (9), 4790.

(26) Leroy, C. Ph.D thesis, Université Pierre et Marie Curie, 2016.

(27) Takemoto, S.; Kusudo, Y.; Tsuru, K.; Hayakawa, S.; Osaka, A.; Takashima, S. Selective protein adsorption and blood compatibility of hydroxy-carbonate apatites. *Journal of Biomedical Materials Research Part A* **2004,** *69A* (3), 544.

(28) Sethmann, I.; Grohe, B.; Kleebe, H.-J. Replacement of hydroxylapatite by whewellite: Implications for kidney-stone formation. *Mineralogical Magazine* **2014,** *78*, 91.

(29) Koutsopoulos, S. Synthesis and characterization of hydroxyapatite crystals: a review study on the analytical methods. *Journal of Biomedical Materials Research Part A* **2002,** *62* (4), 600.

(30) Fowler, B. O.; Markovic, M.; Brown, W. E. Octacalcium phosphate. 3. Infrared and Raman vibrational spectra. *Chemistry of Materials* **1993,** *5* (10), 1417.

(31) Liu, Y.; Zhu, T.; Zhao, D.; Zhang, Z. Investigation of the hygroscopic properties of $Ca(NO_3)_2$ and internally mixed $Ca(NO_3)_2/CaCO_3$ particles by micro-Raman spectrometry. *Atmospheric Chemistry and Physics* **2008,** *8* (23), 7205.

(32) Kokubo, T.; Kushitani, H.; Sakka, S.; Kitsugi, T.; Yamamuro, T. Solutions able to reproduce in vivo surface-structure changes in bioactive glass-ceramic A-W3. *Journal of Biomedical Materials Research* **1990,** *24* (6), 721.

(33) Tanahashi, M.; Yao, T.; Kokubo, T.; Minoda, M.; Miyamoto, T.; Nakamura, T.; Yamamuro, T. Apatite Coating on Organic Polymers by a Biomimetic Process. *Journal of the American Ceramic Society* **1994,** *77* (11), 2805.

(34) Liu, Q.; Ding, J.; Mante, F. K.; Wunder, S. L.; Baran, G. R. The role of surface functional groups in calcium phosphate nucleation on titanium foil: a self-assembled monolayer technique. *Biomaterials* **2002,** *23* (15), 3103.

(35) Awonusi, A.; Morris, M. D.; Tecklenburg, M. M. J. Carbonate Assignment and Calibration in the Raman Spectrum of Apatite. *Calcified Tissue International* **2007,** *81* (1), 46.

(36) Daudon, M.; Jungers, P.; Traxer, O. *Lithiase urinaire*; Lavoisier, Médecine Sciences publications, 2012.

(37) Khan, S. Where do the renal stones form and how? *Italian Journal of Mineral and Electrolyte Metabolism* **1996,** *10* (2), 75.

(38) Ducheyne, P.; Radin, S.; King, L. The effect of calcium phosphate ceramic composition and structure on in vitro behavior. I. Dissolution. *Journal of Biomedical Materials Research* **1993,** *27* (1), 25.

(39) Hankermeyer, C. R.; Ohashi, K. L.; Delaney, D. C.; Ross, J.; Constantz, B. R. Dissolution rates of carbonated hydroxyapatite in hydrochloric acid. *Biomaterials* **2002,** *23* (3), 743.

(40) Silbernagl, S.; Despopoulos, A. *Taschenatlas Physiologie*; Georg Thieme Verlag, 2007.

CHAPTER 4.

MODULATION OF CALCIUM OXALATE CRYSTALLIZATION BY ADDITIVES: THE EFFECT OF GREEN TEA

Chapter 4 Modulation of calcium oxalate crystallization by additives: the effect of green tea

Table of contents

1. Effect of green tea on calcium oxalate crystallization under microfluidic confinement

a. The catechins: polyphenolic compounds from green tea

Green tea (GT) is one of the most commonly drank beverage around the world. It is a complex brew containing caffeine, tannins, polyphenols[1] and even oxalates[2]. Such beverage was reported to have potential anti-oxidative and preventive effects on diseases such as atherosclerosis or Parkinson's disease due to a rich content in polyphenols[3-5]. Furthermore, studies on animal models supported preventive effects of GT on renal stones[6,7]. For example,

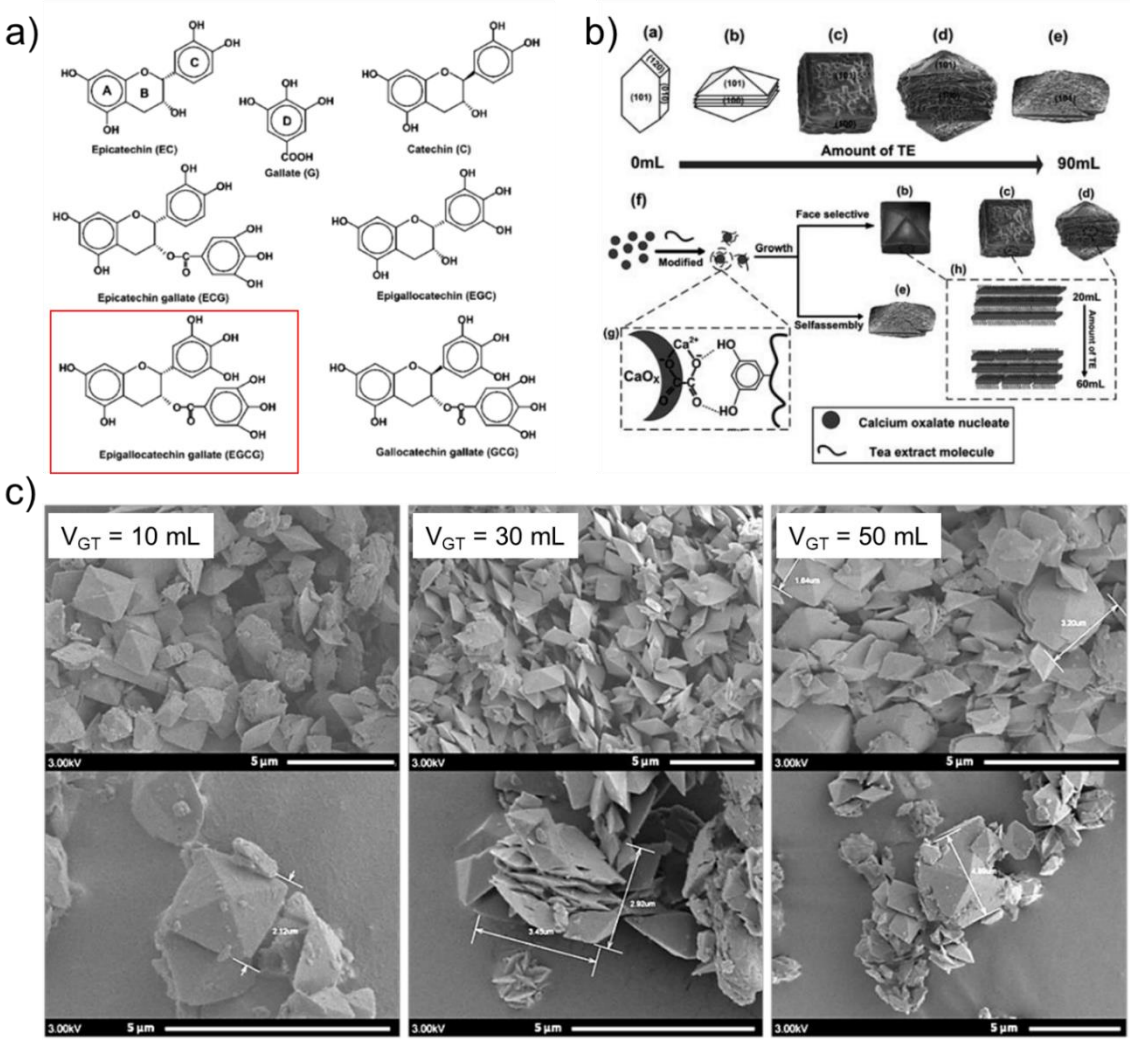

Figure 1. Modulation effect of catechins on CaOx crystallization: a) structures of main catechins of green tea extract. A, B, C and D are identifiers for the basic ring frame of polyphenols. An emphasize is made on EGCG (in red); b) schematic representation of CaOx crystals obtained at increasing amount of green tea extract (TE) with potential crystallization pathway. Figure is adapted from Chen *et al.*[8] with permission from RSC; c) SEM images of COD crystals obtained under batch syntheses *vs.* increasing volume of GT. Figures are reproduced with kind permission from César Leroy[9].

in vivo vs. in vitro studies pointed out that GT – especially polyphenolic epigallocatechin gallate (EGCG) – had an inhibitory effect on stone formation[7]. Medical observations at Tenon hospital (Paris, France) considered GT consumption for treating kidney stones due to its content in polyphenolic catechins (**Figure 1a**). Interestingly, these observations led to a patent application[10]. However, debates still animate the community regarding the beneficial impact of GT on kidney stones. Rodgers and colleagues stated that GT consumption did not reduce the risk factors for CaOx stone formation[11]. With respect to the content in oxalates, Rode *et al.* did not notice increased stone risk factors among patients drinking GT, although suffering from calcium excess in urine[12]. Therefore, no clear consensus exists about the relationship between GT consumption and CaOx kidney stone formation. Nevertheless, *in vitro* investigations demonstrated conclusive results. For instance, EGCG was found to decrease the binding of CaOx monohydrate (COM) crystals onto renal tubular cells[13]. Additionally, Chen *et al.*[8] concluded that catechins from GT were effective in preferentially directing CaOx crystallization from COM to COD (CaOx dihydrate) in batch syntheses (**Figure 1b**). The same results were also obtained by our research group[9]. Under batch syntheses, CaOx crystallization was induced by the dropwise addition of an aqueous oxalate solution at $[Ox^{2-}]_{(aq)}$ = 10.0 $mmol.L^{-1}$ in a GT solution containing Ca^{2+} ions at $[Ca^{2+}]_{\textbf{\textit{In Green Tea}}}$ = 10.0 $mmol.L^{-1}$ (GT brewed at 1.00 *g* of leaves in 100 *mL* of boiled millQ water at 100°C for 5 min). The results showed that the gradual increase in GT in the reaction medium favored the formation of COD compared to COM crystals (**Figure 1c**).

Knowing that COD exhibits poorer adhesion to renal epithelial cells[14] and is usually found in the urine of healthy persons[15], further investigations regarding GT's influence on CaOx crystallization still seem worth conducting. Herein, we aim at assessing the influence of GT extract on CaOx crystallization in the collecting duct-on-a-chip device with a close interest in the polyphenolic compounds. The confinement effect and its consequence on the resulting concentration gradients of Ox^{2-} and Ca^{2+} ions along with the nature of the injected precursor's solutions (aqueous, *i.e.* $Ox^{2-}_{(aq)}$ and $Ca^{2+}_{(aq)}$, or GT containing, *i.e.* $Ox^{2-}_{\textbf{(GT)}}$ and $Ca^{2+}_{\textbf{(GT)}}$) have been investigated regarding the crystal habits, crystalline phases and the influence of hydrodynamics on CaOx crystallization.

b. Calcium oxalate crystallization under co-laminar mixing of $Ca^{2+}_{(GT)}$ and $Ox^{2-}_{(GT)}$ in green tea solution.

i. Influence of the chemical environment on CaOx hydrates

To study the influence of catechins on CaOx crystallization, GT brew was prepared as follows: a mass m_{GT} = 1.00 *g* of green tea leaves was brewed for 5 min in V = 100 *mL* of boiled milliQ water at 100°C. Once cooled, the brew was washed in chloroform (repeated three times) to remove unwanted molecules (*e.g.* caffeine, pigments and other non-polar impurities) and to enable longer fridge storage in sealed bottle at 4°C. To verify the presence of catechins, UV-visible spectroscopy was carried out. Indeed, Atomssa and collaborators demonstrated that epigallocatechin gallate, epicatechin gallate, epigallocatechin and epicatechin (**Figure 1a**) exhibited maximal absorbance in water at 273.6, 276.8, 269.6 and 278.4 nm, respectively[16]. The UV-visible spectrum of a 100 times diluted aliquot of the brew showed maximal absorbance (A_{max} ≈ 0.1288) in the same wavelength range (*i.e.* 259 < λ_{max} ≈ 271 < 285 nm) and, therefore, supported the presence of catechins in the brew (**Figure 2**). Using an average molar absorption coefficient

$$\varepsilon_{average} = 0.25 \times (\varepsilon_{EGCG} + \varepsilon_{ECG} + \varepsilon_{EGC} + \varepsilon_{EC}) \approx 7523\ L.mol^{-1}.cm^{-1}$$

we estimated an approximate concentration in catechins of ≈ 1.71 *mmol.L*$^{-1}$ in the *undiluted* GT brew. The respective molar absorption coefficients of the catechins of interest were taken from this reference[16].

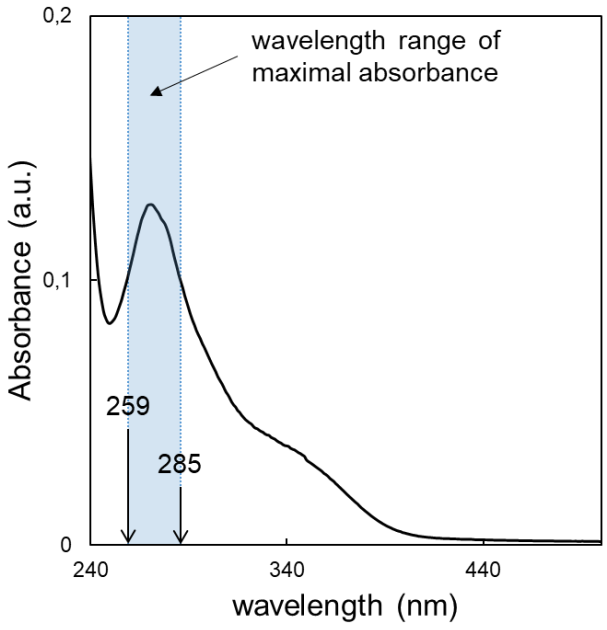

Figure 2. UV-visible spectrum of purified GT solution (1.00 *g*/ 100 *mL*) diluted 100 times.

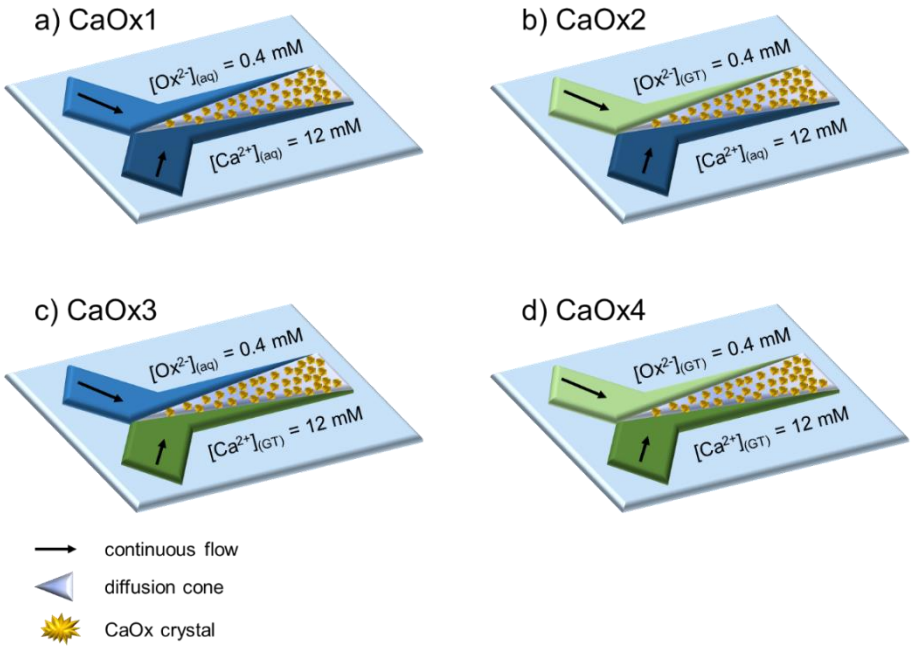

Figure 3. Schematic illustrations of the experimental conditions to study the effect of polyphenolic catechins from GT on CaOx crystallization in the collecting duct-on-a-chip device. CaOx crystallization is induced through the co-laminar mixing of either a) $Ox^{2-}_{(aq)}$ and $Ca^{2+}_{(aq)}$ ions (standard condition *a.k.a CaOx1*), b) $Ox^{2-}_{(GT)}$ and $Ca^{2+}_{(aq)}$ ions (*CaOx2*), c) $Ox^{2-}_{(aq)}$ and $Ca^{2+}_{(GT)}$ ions (*CaOx3*) or d) $Ox^{2-}_{(GT)}$ and $Ca^{2+}_{(GT)}$ ions (*CaOx4*). At all conditions, solutions are continuously injected in the microfluidic device at equal flow rates of Q = 1.0 $\mu L.min^{-1}$ for two hours.

Afterwards, calcium ($CaCl_2$) and oxalate ($Na_2C_2O_4$) precursors were separately dissolved in GT solution to prepare GT containing $Ca^{2+}_{(GT)}$ and $Ox^{2-}_{(GT)}$ solutions at $[Ca^{2+}]_{(GT)}$ = 12.0 $mmol.L^{-1}$ and $[Ox^{2-}]_{(GT)}$ = 0.40 $mmol.L^{-1}$, respectively. Worth mentioning, the sole GT brew could contain Ox^{2-} ions as demonstrated by Brzezicha-Cirocka and colleagues[2]. In first approach, we did not account for it during the study.

In the assembled collecting duct-on-a-chip device, the effect of polyphenolic compounds in GT on CaOx crystallization was investigated under different scenarii as described in **Figure 3**. The first experimental condition, *i.e. CaOx1* (**Figure 3a**), was extensively studied throughout **Chapter 2** and served as the *standard condition* (without any GT). Under the next three conditions, CaOx crystallization was induced through the co-laminar mixing of $Ox^{2-}_{(GT)}$ and $Ca^{2+}_{(aq)}$ ions (*CaOx2* in **Figure 3b**), $Ox^{2-}_{(aq)}$ and $Ca^{2+}_{(GT)}$ ions (*CaOx3* in **Figure 3c**) and $Ox^{2-}_{(GT)}$ and $Ca^{2+}_{(GT)}$ ions (*CaOx4* in **Figure 3d**), respectively. At all conditions, the precursors were continuously injected in the micro-reactor at equal flow rates of Q = 1.0 $\mu L.min^{-1}$ for two hours.

The SEM results corresponding to the four scenarii of interest are presented in **Figure 4**. First, we observed that CaOx crystal morphologies and crystalline phases strongly differed between *CaOx1* (**Figures 4a-b**), *CaOx2* (**Figures 4c-d**), *CaOx3* (**Figures 4e-f**) and *CaOx4* (**Figures 4g-h**). The series of images support the net effect of physicochemical conditions (and concentration gradients) on CaOx crystal formation. As already demonstrated in **Chapter 2**,

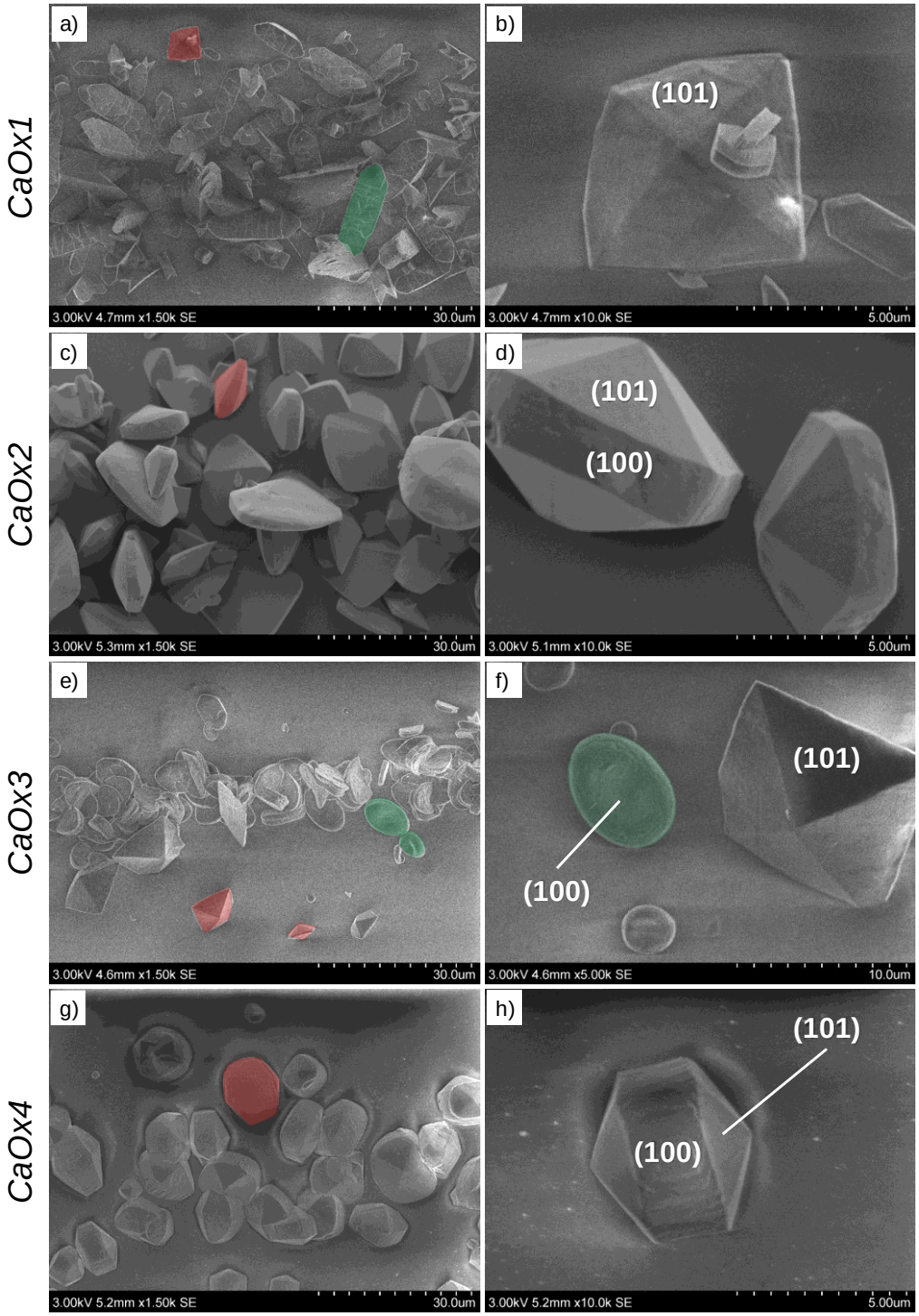

Figure 4. Scanning Electron Microscopy (SEM) images depicting the effect of green tea on CaOx crystallization in the collecting duct-on-a-chip device according to condition *CaOx1* (**Figures 4a-b**), *CaOx2* (**Figures 4c-d**), *CaOx3* (**Figures 4e-f**) and *CaOx4* (**Figures 4g-h**). See **Figure 3** for further description regarding the individual experimental conditions. Green and red "false-colors" point out some COM and COD crystals, respectively.

CaOx crystallization under *CaOx1* (*i.e.* in total absence of GT) resulted in a mixture of dominant COM crystals and rare flatted bipyramid COD crystals (**Figure 4b**).

In the presence of GT, we assessed a higher occurrence of COD crystals at all conditions (**Figures 4c-h**), sometimes with COM crystalline phase completely unreported (*e.g. CaOx2*

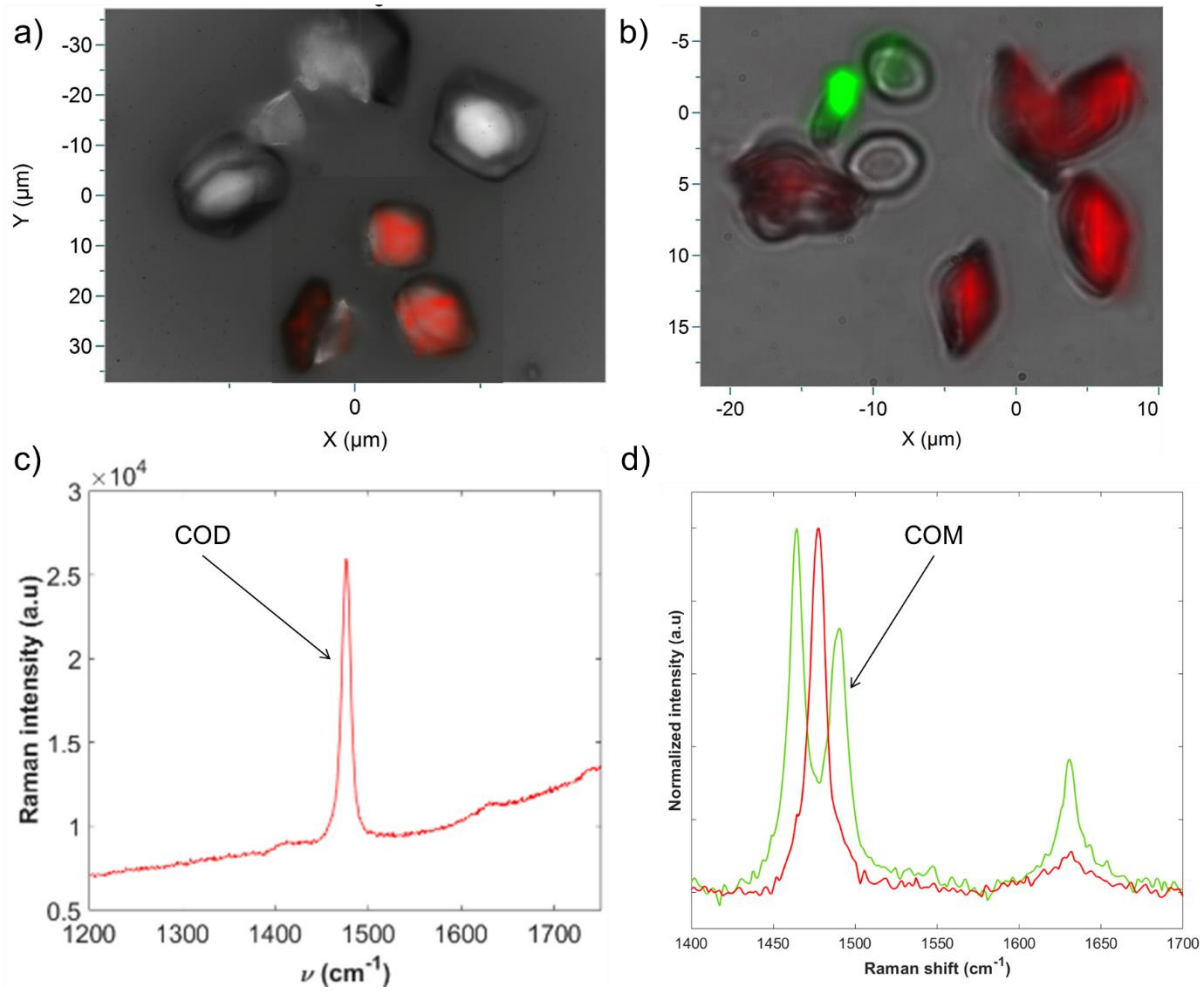

Figure 5. *Raman* mapping of CaOx crystals corresponding to a) *CaOx2* condition (mixing of $Ox^{2-}_{(GT)}$ and $Ca^{2+}_{(aq)}$ ions) and b) *CaOx3* condition (mixing of $Ox^{2-}_{(aq)}$ and $Ca^{2+}_{(GT)}$ ions); c-d) *Raman* spectra of COM crystal in green and COD crystals in red for *CaOx2* (c) and *CaOx3* (d), respectively. Similar "false-color" is used to discriminate COM from COD crystals on the micrographs.

and *CaOx4* conditions). The effect of GT on the morphology of CaOx crystals contrasted drastically whether it was first mixed in solution with $Ox^{2-}_{(GT)}$ ions or $Ca^{2+}_{(GT)}$ ions.

Under co-laminar mixing of $Ox^{2-}_{(GT)}$ and $Ca^{2+}_{(aq)}$ (*i.e. CaOx2*), only COD crystals sizing up to ≈ 20 *µm* were detected (**Figure 4c**). Compared to **Figure 4b**, COD crystals exhibited an elongated bipyramid habit with the over-expression of the (100) crystalline face (**Figure 4d**). Noteworthy, the crystalline phase was confirmed using *Raman* mapping as showed in red color in **Figure 5a**. Under *CaOx3* scenario, CaOx crystals precipitated in a mixture of COM (green) and occasional COD (red) crystals of maximum ≈ 15 *µm* (**Figure 4e**). Unlike *CaOx1* condition, COM crystals exhibited a single round-shaped morphology with concave (100) crystalline face (**Figure 4f**). Such crystal shape is unusual in *batch conditions* and in *absence of additives*. Yet, similar morphology was reported using batch syntheses in presence of osteopontin[17] as well as in urine of stone formers[18]. On the other hand, COD crystals were found under flatted bipyramid shape. Again, *Raman* mapping correlated the crystal habit to the crystalline phase

with green (red, respectively) color for COM (COD, respectively) crystals (**Figure 5b**). Last, *CaOx4* condition (*i.e.* co-laminar mixing of $Ox^{2-}_{(GT)}$ and $Ca^{2+}_{(GT)}$) presented comparable results to *CaOx2* condition (**Figure 4g**). No COM crystals were found after CaOx crystallization and COD crystals (up to ≈ 15 *µm*) showed solely the (100) elongated bipyramid morphology (**Figure 4h**) highly over-expressed (100) face compared to COD crystals in *CaOx2* scenario.

In agreement with Chen *et al.*[8], who assessed the effectiveness of GT to direct the crystallization of CaOx crystals from COM to COD, we came to the same conclusion. The chemical composition on either side of the liquid-liquid interface and, consequently, the corresponding concentration gradients within the microchannel directly affected the formation and habits of CaOx crystals. Let us recall from **Chapter 2** that $Ox^{2-}_{(aq)}$ and $Ca^{2+}_{(aq)}$ ions have comparable self-diffusion coefficients ($D_{Ox^{2-}}$ = 9.87 x 10^{-10} $m^2.s^{-1}$ and $D_{Ca^{2+}}$ = 7.92 x10^{-10} $m^2.s^{-1}$ in water at 25°C[19]). At $[Ox^{2-}]_{(aq)}$ = 0.4 $mmol.L^{-1}$ and $[Ca^{2+}]_{(aq)}$ = 12 $mmol.L^{-1}$, $Ca^{2+}_{(aq)}$ ions are transported faster through diffusion to the oxalate side rather than to the opposite (**Chapter 2** section **1.b.i**). Furthermore, depending on which side of the interface GT was found, Ca^{2+} and Ox^{2-} ions did not meet the same chemical environment upon diffusion. Under *CaOx2* condition (*i.e. GT on the oxalate-rich side*), (100) elongated COD crystal (**Figure 4d**) resulted from the mixing of $Ox^{2-}_{(GT)}$ and $Ca^{2+}_{(aq)}$ ions. This morphology was comparable with the one found in pathological case of severe hypercalciuria[18] and were also obtained after batch crystallization by Chen *et al.*[8] (**Figure 1b**). The authors supported the idea that H-bonds between the polyphenol groups of GT and the oxalate groups in CaOx crystals played a key role in the inhibition of COM crystal growth. However, it is worth mentioning that they first mixed GT with Ca^{2+} precursor unlike us. In the context of our work, we think that the potential interactions of polyphenols and Ox^{2-} ions in solution results in a lesser availability of Ox^{2-} ions. Consequently, it limits the self-diffusion of $Ox^{2-}_{(GT)}$ ions compared to free $Ox^{2-}_{(aq)}$ ions and leads to apparent higher hypercalciuria in the overall system. When *GT is on the calcium-rich side* of the liquid-liquid interface (*i.e. CaOx3*), a mixture of round-shaped COM and flatted bipyramid COD crystals was found (**Figure 4f**). Compared to the correlative study by Daudon and colleagues, this result is similar to the pathological case of combined hyperoxaluria and hypercalciuria[18]. Moreover, COM crystals interestingly exhibited a crystal habit previously reported in the literature in presence of osteopontin protein[17,20]. Osteopontin appears to preferentially adsorb on (100)/(121) edges and (100) face due to hydrophilic properties[20]. Regarding the polyphenol molecules from GT, their hydrophilic properties can confer preferential interactions with growing CaOx crystals and therefore, explain the final round-shaped morphology of COM crystals. The very last experimental condition, *i.e. CaOx4*, showed that $Ox^{2-}_{(GT)}$ ion's availability is the limiting step as in the case *CaOx2* case (**Figure 4g**).

In agreement with batch crystallization, we positively supported the influence of GT in favoring the formation of COD crystals rather than COM ones using the collecting duct-on-a-chip device. However, we showed that the chemical composition on either side of the liquid-liquid interface (*i.e.* "where" is GT) is an important factor with respect to CaOx crystalline phases, crystal habits and occurrence. While *CaOx2* and *CaOx4* conditions resulted in solely (100) elongated bipyramid COD crystals (**Figures 4d** & **h**), *CaOx3* condition rather favored occasional flatted bipyramid COD crystals among round-shaped COM crystals (**Figure 4f**).

ii. Modulation of the crystallization through hydrodynamics

In section **1.b.i**, the influence of GT polyphenolic compounds was investigated in the collecting duct-on-a-chip device under continuous-flow at Q = 1.0 *µL.min*$^{-1}$. This operating flow rate still remains 100 times higher when compared to a single collecting duct in the nephron (≈ 10 *nL.min*$^{-1}$)[21]. In **Chapter 2** section **2**, we underscored the key role of hydrodynamics in modulating CaOx crystallization. With respect to the chemical conditions, *i.e.* $[Ca^{2+}]_{(aq)} / [Ox^{2-}]_{(aq)} \gg 1$, it is expected to favor COD compared to COM crystals upon mixing of ion precursors[9]. *In absence of additives*, a decrease in flow rate enhanced $Ca^{2+}_{(aq)}$ and $Ox^{2-}_{(aq)}$ ion diffusion at the co-precipitation front compared to convection along the microchannel (see **Figure 12** in **Chapter 2** section **2.a.ii**). Consequently, complete mixing of $Ca^{2+}_{(aq)}$ and $Ox^{2-}_{(aq)}$ ions was achieved in the micro-reactor and induced the increasing incidence of COD crystals with respect to CaOx crystallization. However, mixing resulted from a slow homogenization of concentration gradients in $Ca^{2+}_{(aq)}$ and $Ox^{2-}_{(aq)}$ ions as demonstrated by the increasing induction time t_0 (prior to CaOx crystallization).

It is legitimate to wonder if the flow rate influences CaOx crystallization *in presence of GT*. In order to assess the role of hydrodynamics, the experimental conditions in **Figure 3** were once again investigated *vs.* flow condition (Q = 0.1 *µL.min*$^{-1}$ for 2.5 *hours*). **Table 1** compares the induction time t_0 along with the angle of diffusion cone α with respect to the flow conditions

Table 1. Comparison of the induction time (t_0) and the measured angle of the diffusion cone (α) *vs.* flow condition for all four scenarii (see **Figure 3**).

		1.0 *µL.min*$^{-1}$		0.1 *µL.min*$^{-1}$	
Co-laminar mixing of	**Designation**	**t_0** (*min*)	**α** (°)	**t_0** (*min*)	**α** (°)
$Ox^{2-}_{(aq)}$ and $Ca^{2+}_{(aq)}$	*CaOx1*	1.0 ± 0.5	3.4 ± 0.1	8.0 ± 0.5	5.2 ± 0.2
$Ox^{2-}_{(GT)}$ and $Ca^{2+}_{(aq)}$	*CaOx2*	1.9 ± 0.3	4.0 ± 0.2	10.8 ± 0.3	8.5 ± 0.1
$Ox^{2-}_{(aq)}$ and $Ca^{2+}_{(GT)}$	*CaOx3*	2.4 ± 0.3	3.1 ± 0.1	9.5 ± 0.4	5.8 ± 0.2
$Ox^{2-}_{(GT)}$ and $Ca^{2+}_{(GT)}$	*CaOx4*	2.9 ± 0.5	3.9 ± 0.2	8.5 ± 0.8	n/a

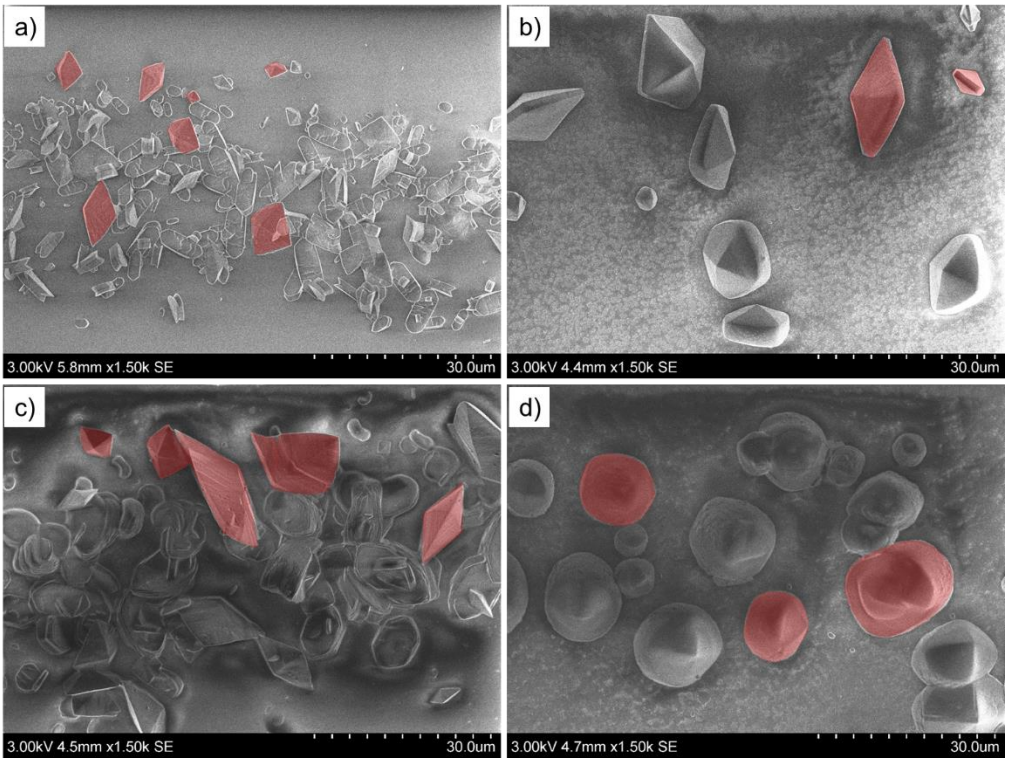

Figure 6. SEM images of CaOx crystals obtained under a) *CaOx1*, b) *CaOx2*, c) *CaOx3* and d) *CaOx4* conditions at flow rate Q = 0.1 *µL.min*$^{-1}$ for 2.5 *hours*. Refer to **Figure 3** for further description of the experimental conditions. Red "false-color" points out some of the COD crystals.

(*i.e*. Q = 1.0 *µL.min*$^{-1}$ and Q = 0.1 *µL.min*$^{-1}$). Worth reminding, these qualitative features describe the necessary time to start CaOx crystallization upon reagent contact (*i.e.* first crystal ≈ 1.0 *µm*) and the opening-angle of the CaOx precipitation cone after reaction.

Compared to *CaOx1* condition (*i.e.* absence of GT), CaOx crystallization is delayed at almost all conditions and regardless of the flow rate. GT altered the diffusion of Ca^{2+} and Ox^{2-} ions at their liquid-liquid interface and delayed CaOx crystallization. Noteworthy, the homogenization took longer in presence of GT, *e.g.* t_0(*CaOx1*) = 8.0 ± 0.5 *min vs.* t_0(*CaOx2*) = 10.8 ± 0.3 *min* at same flow rate. Moreover, low flow-condition widened the CaOx crystallization cone (*e.g.* 3.1° ± 0.1° *vs*. 5.8° ± 0.2° for *CaOx3* condition). Although the presence of GT altered the mixing of Ca^{2+} and Ox^{2-} ions, the decrease in flow rate still favored diffusion at the contact interface for it to occur closer to the channel's "Y-junction".

After assessing the combined influence of hydrodynamics and GT at the optical scale, CaOx crystals were characterized with respect to the crystalline phase and crystal habit (**Figure 6**). SEM micrographs correspond to *CaOx1* (**Figure 6a**), *CaOx2* (**Figure 6b**), *CaOx3* (**Figure 6c**) and *CaOx4* (**Figure 6d**) conditions at Q = 0.1 *µL.min*$^{-1}$, respectively. They have to be compared to **Figures 4a**, **4c**, **4e** & **4g** in the previous section.

At Q = 0.1 *µL.min*$^{-1}$, *CaOx1* and *CaOx3* conditions resulted in CaOx mixtures of COM and COD crystals (**Figures 6a** and **6c**, respectively). While COD crystals (in red) exhibit flatted bipyramid morphology regardless of the conditions, COM crystals in *CaOx3* condition showed smoother edges. On the other hand, *CaOx2* and *CaOx4* conditions resulted only in COD crystals (**Figures 6b** and **6d**, respectively). However, COD crystals from *CaOx4* condition (**Figure 6d**) did not exhibit the (100) elongated bipyramid morphology as in *CaOx2* (red in **Figure 6b**). Yet, the COD crystalline phase of these not clearly-defined structures was confirmed by using *Raman* spectroscopy (not presented herein). Regardless of the experimental conditions, CaOx crystalline phases at Q = 0.1 *µL.min*$^{-1}$ (**Figure 6**) matched adequately the ones at Q = 1.0 *µL.min*$^{-1}$ (**Figure 4**). The same observation could be made with respect to crystal habits, expect for *CaOx4* condition when comparing **Figures 4g** and **6d**. Finally, we demonstrated that the decrease in flow rate did not alter significantly CaOx crystallization with respect to the crystalline phases and the crystal morphologies. Consequently, the parameter of prime importance herein remained the modulating role of GT with respect to CaOx crystallization.

Green tea is one of the most popular beverage worldwide. Furthermore, interesting studies supported preventive effects regarding various diseases such as atherosclerosis, Parkinson's disease and even kidney stone formation[3-5,10]. With respect to CaOx crystals, *in vitro* investigations demonstrated the ability of polyphenolic catechins from green tea to inhibit stone formation[7], decrease COM crystal binding on renal cells[13] and even direct CaOx crystallization from COM to COD crystals[8]. Knowing that COD exhibits less adhesion to renal epithelial cells[14] and is usually found in the urine of healthy subjects[15], investigating the modulation effect of green tea with respect to CaOx crystals could provide a natural solution to treat and prevent kidney stones. Similarly to the work presented in **Chapter 2**, CaOx crystallization under co-laminar mixing of Ca^{2+} and Ox^{2-} ions was investigated *in presence of green tea* (GT). We demonstrated that GT favors COD crystalline phase with respect to COM crystals. Furthermore, we showed that COD crystals exhibit various morphologies (*i.e.* flatted or elongated bipyramid shapes) depending on the presence of GT either on the calcium-rich or the oxalate-rich side in the micro-reactor. Besides, we studied the influence of hydrodynamics on CaOx crystallization in presence of additives. We showed that a decrease in flow rate did not interfere with CaOx crystalline phases and overall crystal morphologies. This late result emphasized the dominant role of GT with respect to CaOx crystallization in the collecting duct-on-a-chip device.

2. Calcium oxalate crystallization from the apatitic layer mimicking the Randall's plaque: a preliminary study in presence of green tea

a. Heterogeneous calcium oxalate crystallization in green tea solution

In the nephron, the Randall's plaque (RP) is a calcium deficient hydroxyapatite deposit suspected to initiate the formation of CaOx-based kidney stones[22-24]. In **Chapter 3**, we presented an apatitic layer (**Figure 7a**) suitable for microfluidic investigations of the RP reactive role regarding CaOx crystallization. In the RP-modified collecting duct-on-a-chip device, the controlled flow of an oxalate solution induced *local dissolution* of the apatitic layer. The associated release in $Ca^{2+}_{(RP)}$ ions generated *local zones of supersaturation* such as $[Ca^{2+}]_{(RP)} \times [Ox^{2-}]_{(aq)} \geq K_{sp(CaOx)}$ for CaOx crystallization. Monoclinic prismatic COM crystals (*i.e.* platelet-shaped crystals) grew from the apatitic spherulites, supporting the *dissolution-recrystallization* mechanisms of RP for the growth of CaOx crystals.

In the previous section, we demonstrated the modulating effect of GT to direct CaOx crystallization from COM to COD crystals under co-laminar mixing of Ca^{2+} and Ox^{2-} ions. Herein, we investigated the effect of GT on CaOx crystallization in the *RP-modified* collecting duct-on-a-chip device.

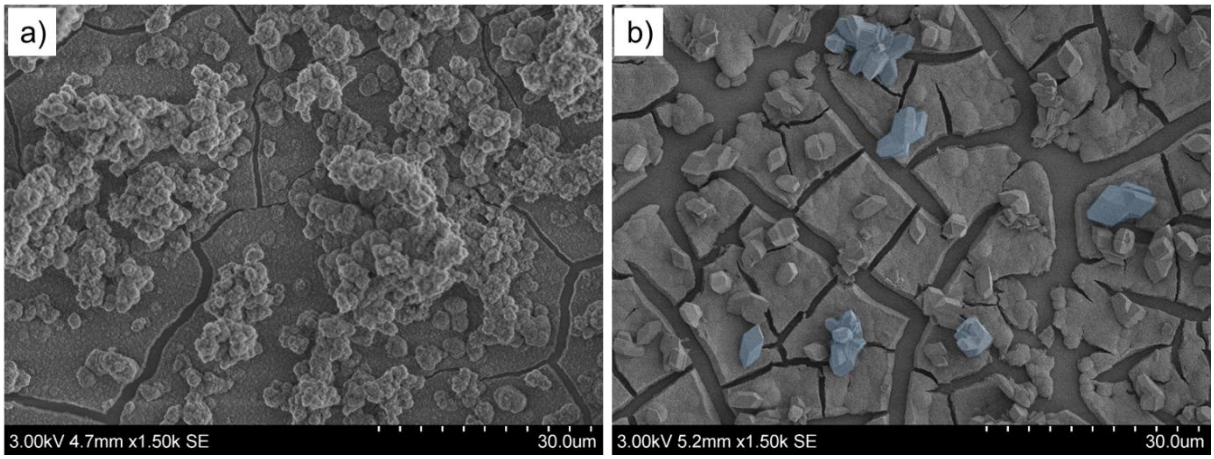

Figure 7. SEM images of the apatitic layer a) as described in **Chapter 3** section **1.b**; b) after immersion in a green tea solution (1.00 *g* of green tea leaves / 100 *mL* of milliQ water) for one week. Blue "false-color" points out some CaOx crystals that grew from the apatitic layer.

First, batch crystallization was carried out alike in **Chapter 3** section **2.a.i**. Before adding $Ox^{2-}_{(GT)}$ ions in the medium, a piece of ≈ 0.5 × 0.5 *cm²* from the apatitic layer was soaked *in GT for one week* (V_{GT} = 1.0 *mL*, pH 7.4). **Figure 7b** shows that GT was not inert with respect to the apatitic layer. Indeed, new crystals of ≈ 10 – 15 *µm* (some in blue) grew on the substrate and exhibited the morphologies of COM crystals obtained under syntheses in batch[9]. The growth of CaOx crystals in sole presence of GT underlined that the brew we used initially contained Ox^{2-} ions in sufficient amount to trigger crystallization.

After assessing the effect of *GT only*, we studied the heterogeneous CaOx crystallization on the apatitic layer in presence of GT containing oxalate solutions. Alike in **Chapter 3** section **2.a.i**, the calcium donor role of the apatitic layer was under scrutiny and, therefore, no additional source of Ca^{2+} ions was added. To conduct the study, pieces of ≈ 0.5 × 0.5 *cm²* from the apatitic layer were immersed in solutions (V_{GT} = 1.0 *mL*) *for one week*. Two concentrations in $Ox^{2-}_{(GT)}$ ions were used, *i.e.* $[Ox^{2-}]_{(GT)}$ = 0.40 *mmol.L*$^{-1}$ and $[Ox^{2-}]_{(GT)}$ = 0.10 *mol.L*$^{-1}$, respectively. Noteworthy, $Na_2C_2O_4$ was dissolved in GT to obtain these respective concentrations. We did not account for the nominal amount of Ox^{2-} ions already present in GT. Furthermore, we studied the potential influence of the pH to modulate CaOx crystallization in presence of GT. Prior to the dissolution of the oxalate precursor, GT brew was adjusted to pH 4.5 with HCl.

After one week immersion in oxalate solutions, we observed new crystals apart from the apatitic spherulites either at $[Ox^{2-}]_{(GT)}$ = 0.40 *mmol.L*$^{-1}$ (**Figures 8a-d**) or at $[Ox^{2-}]_{(GT)}$ = 0.10 *mol.L*$^{-1}$ (**Figures 8e-h**). Further examinations highlighted the growth of COD crystals at all concentrations and pH values, exhibiting either the flatted bipyramid shape (**Figures 8b** and **8d**) or the (100) elongated bipyramid shape (**Figures 8f** and **8h**).

Under the combined conditions of $[Ox^{2-}]_{(GT)}$ = 0.40 *mmol.L*$^{-1}$ and pH 4.5 (**Figure 8c**), we noticed a higher dissolution of the spherulites compared to pH 7.36 (**Figure 8a**). This confirmed the pH-sensitivity of the apatitic layer, as already demonstrated in **Chapter 3** section **2.b.i**, even in GT along with the growth of flatted bipyramid COD crystals.

At $[Ox^{2-}]_{(GT)}$ = 0.10 *mol.L*$^{-1}$ and regardless of the pH value, we observed the complete disappearence of the apatitic layer (**Figures 8e-h**) replaced by crystals exhibiting a sheet-like habit (in blue in **Figures 8f** and **8h**). Based on the crystal morphology[25,26], we suspected a phase transformation from Ca-deficient HAp to octacalcium phosphate ($Ca_8H_2(PO_4)_6{\cdot}5H_2O$, OCP) but in absence of in-depth chemical characterization we could not be certain. Therefore, *Raman* spectroscopy will be conducted in a near future to identify the crystalline phase. Yet, we did not exclude this hypothesis since existing contributions in the literature already

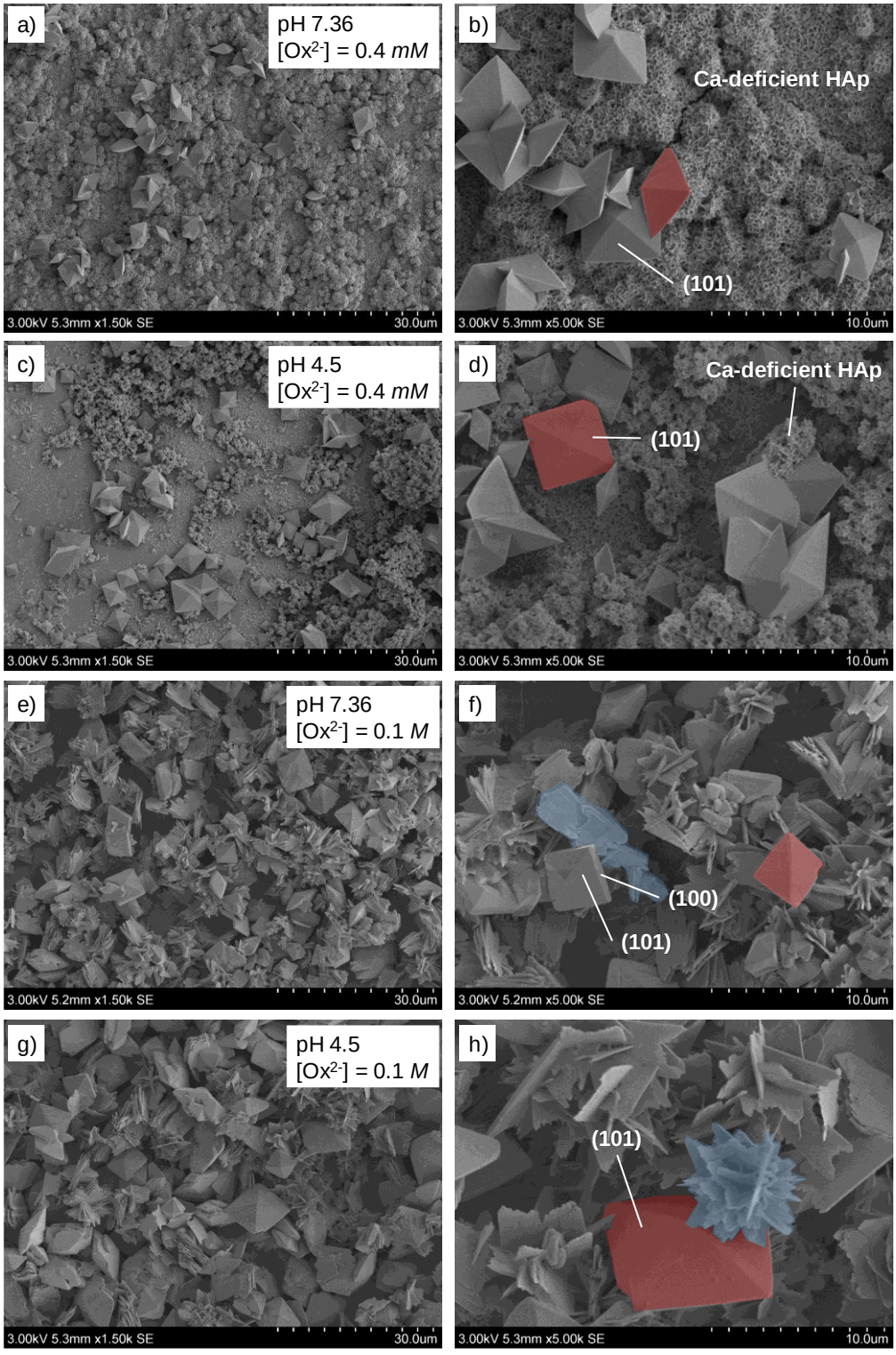

Figure 8. SEM images of the heterogeneous growth of CaOx crystals from the apatitic layer after immersion in GT solutions containing Ox^{2-} ions (from $Na_2C_2O_4$ precursor) for one week. Red and blue "false-colors" indicate the presence of some bipyramid COD crystals and sheet-like structures, respectively. **Figures 8a-d** correspond to the apatitic layer soaked in a GT solution containing $Ox^{2-}_{(GT)}$ ions at $[Ox^{2-}]_{(GT)}$ = 0.40 *mmol.L*$^{-1}$ and pH 7.36 (**Figures 8a-b**) or pH 4.5 (**Figures 8c-d**). **Figures 8d-h** correspond to the apatitic layer soaked in a GT solution containing $Ox^{2-}_{(GT)}$ ions at $[Ox^{2-}]_{(GT)}$ = 0.10 *mol.L*$^{-1}$ and pH 7.36 (**Figures 8e-f**) or pH 4.5 (**Figures 8g-h**).

investigated the reverse phase transformation, *i.e.* from OCP to apatite[27,28]. Therefore, a large concentration in $Ox^{2-}_{(GT)}$ ions induced the growth of (100) elongated bipyramid COD crystals along with the phase transformation of the apatitic layer to a sheet-like structure.

In this section, we supported the role of the apatitic layer as a calcium donor for CaOx crystallization in presence of GT. The dissolution-recrystallization of the apatitic spherulites led to the growth of COD crystals at all concentrations in $Ox^{2-}_{(GT)}$ ions and all pH values. Once again, we showed the influence of GT to direct CaOx crystallization from COM to COD crystals. At $[Ox^{2-}]_{(GT)} = 0.40$ *mmol.L*$^{-1}$ we observed the growth of flatted bipyramid COD crystals from the spherulites. At $[Ox^{2-}]_{(GT)} = 0.10$ *mol.L*$^{-1}$ COD crystals exhibited (100) elongated bipyramid shapes. Moreover, the emergence of sheet-like shaped crystals at the highest concentration in $Ox^{2-}_{(GT)}$ ions suggested the phase transformation of the apatitic spherulites to another calcium phosphate phase (probably OCP).

b. Preliminary investigation under microfluidic confinement

Albeit presented as a preliminary study, the following experimental results open the way to the investigation of CaOx crystallization within the collecting duct-on-a-chip device under multi-physicochemical conditions. Throughout the present work, we studied various parameters suspected to influence CaOx crystallization. In **Chapter 2**, the influence of the microfluidic confinement such as encountered in the collecting duct was under scrutiny. Under the co-laminar mixing of Ca^{2+} and Ox^{2-} ions, we showed that the CaOx crystals were fairly comparable to *in vivo* observations. In **Chapter 3**, we investigated the reactive role of an apatitic layer (*i.e.* acting as a model system for RP) to promote, through dissolution-recrystallization, the growth of CaOx crystals. Compared to standard investigations in batch, we supported the relevancy of studying the key role of an apatitic layer as a calcium donor under microfluidic confinement. The controlled flow of sole Ox^{2-} ions within the micro-reactor induced the partial dissolution of the apatitic layer (*i.e.* release in $Ca^{2+}_{(RP)}$) towards local zones of supersaturation (*i.e.* $[Ca^{2+}]_{(RP)} \times [Ox^{2-}]_{(aq)} \geq K_{sp(CaOx)}$). Under a large excess of Ox^{2-} ions, COM crystals grew from the apatitic spherulites under crystal morphologies comparable to *in vivo* observations. In **Chapter 4** section **1**, we studied the modulating influence of catechins from GT on CaOx crystals. Under microfluidic confinement, we supported that GT directed CaOx crystallization from COM to COD crystals.

Herein, we aimed at combining all the features we investigated at once in the collecting duct-on-a-chip device with respect to CaOx crystallization. Therefore, the microfluidic platform was assembled with an apatitic layer to form the RP-modified collecting duct-on-a-chip device.

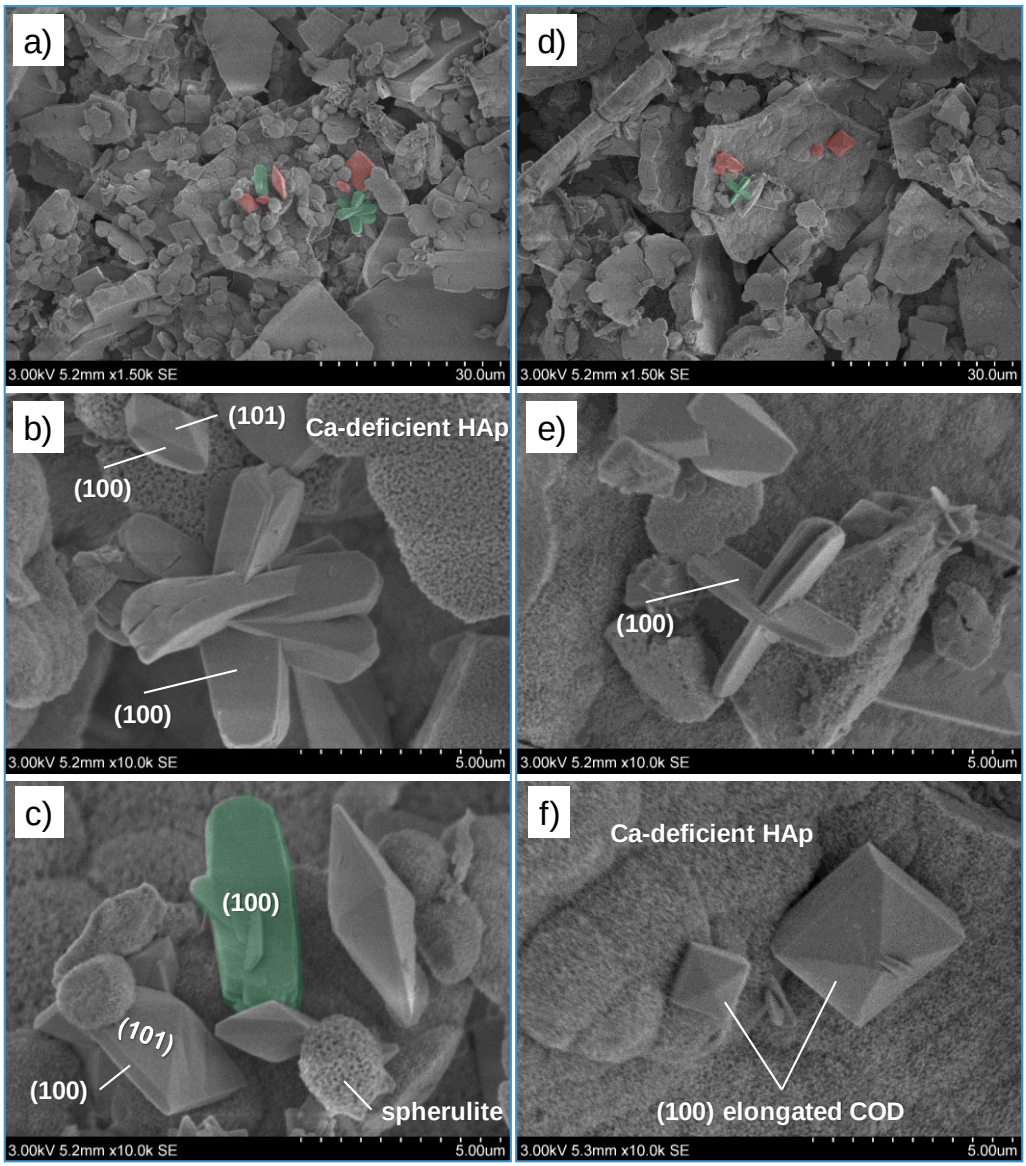

Figure 9. SEM images depicting *two distinct zones* of the apatitic layer after consecutive exposure to continuous flow of oxalate solution at $[Ox^{2-}]_{(GT)}$ = 0.10 *mol.L*$^{-1}$ and *pH 4.5* in the collecting duct-on-a-chip device (Q_{tot} = 2.0 *µL.min*$^{-1}$ for *15 min*). Red and green colors in **Figure 9a** and **Figure 9d** show the locations of COD (red) and COM (green) crystals in the magnified images in **Figures 9b-c** and **Figures 9e-f**, respectively.

Afterwards, GT solution containing Ox^{2-} ions at $[Ox^{2-}]_{(GT)}$ = 0.10 *mol.L*$^{-1}$ and pH 4.5 was continuously perfused within the micro-reactor at Q_{tot} = 2.0 *µL.min*$^{-1}$ for 15 *min* (**Figure 9**). These parameters were chosen among the ones depicted in **Figure 8** based on the previous results throughout the present work. The series of images details the same apatitic layer (after continuous perfusion of oxalate solution) but at two different locations in the microchannel, *i.e.* **Figures 9a-c** *vs.* **Figures 9d-f**. Furthermore, the green and red "false-colors" aim at easing the identification of COM and COD crystals, respectively.

After the consecutive perfusion of Ox^{2-} ions at $[Ox^{2-}]_{(GT)}$ = 0.10 *mol.L*$^{-1}$, in presence of GT and at pH 4.5, we observed the growth of CaOx crystals from the apatitic layer in a mixture of COM and COD crystals (**Figures 9a** and **9d**). Closer examination showed that COM crystals mainly exhibited platelet-like habits (**Figures 9b**, **9c** and **9e**) while COD crystals grew principally under the (100) elongated bipyramid shape (**Figures 9c** and **9f**). It was interesting to notice that the flow of $Ox^{2-}_{(GT)}$ ions in presence of GT did not induce the sole growth of COD crystals from the apatitic layer in the microfluidic platform. However, the (100) elongated COD crystals were comparable to the ones obtained under crystallization in batch (**Figures 8g-h**). Compared to batch conditions, we did not notice the suspected phase transformation of the apatitic spherulites to the “sheet-like” structure. Once again, the microfluidic confinement supported the controlled diffusion of Ox^{2-} ions at the apatitic surface for a more controlled reactivity between $Ca^{2+}_{(RP)}$ and $Ox^{2-}_{(GT)}$ ions.

As a future perspective, we showed the feasibility of the multi-physicochemical investigation of CaOx crystallization in the collecting duct-on-a-chip device. Therefore, the RP-modified micro-reactor was continuously perfused with a GT solution containing Ox^{2-} ions at $[Ox^{2-}]_{(GT)}$ = 0.10 *mol.L*$^{-1}$, pH 4.5 and in absence of any additional source of calcium. We demonstrated that CaOx crystals grew from the apatitic layer in a mixture of platelet-like COM crystals and mainly (100) elongated bipyramid COD crystals. At comparable chemical conditions but in batch, we assessed the presence of COM crystals but we did not notice the suspected phase transformation of the apatitic spherulites to a still unclearly characterized “sheet-like” structure. This preliminary study supported the strong potential of the collecting duct-on-a-chip device to investigate CaOx crystallization under even more complex chemical environments.

3. Conclusion

In the present chapter, we investigated the modulating effect of GT on CaOx crystallization by using the collecting duct-on-a-chip device. Two aspects were under scrutiny to evaluate the potential of the microfluidic platform with respect to kidney stone disease.

First we studied the co-laminar mixing of Ca^{2+} and Ox^{2-} ions in presence of GT. We showed that GT enabled to direct CaOx crystallization from COM to COD crystals as observed under batch conditions. However, we demonstrated the importance of the presence of GT either on the calcium-rich or the oxalate-rich side in the micro-reactor regarding CaOx crystalline phases and shapes. COM crystals mainly exhibited round-shaped morphorlogy. On the other hand, COD crystals showed flatted bipyramid shape or (100) elongated bipyramid morphology. The later crystal shape is generally observed in complete absence of additives.

As a second and last example, we combined all features from the present work at once. The RP-modified collecting duct-on-a-chip device was continuously perfused with a GT containing Ox^{2-} ions in large excess (i.e. $[Ox^{2-}]_{(GT)}$ = 0.10 *mol.L*$^{-1}$) and at pH 4.5 at Q_{tot} = 2.0 *µL.min*$^{-1}$ for 15 *min*. It aimed at attempting CaOx crystallization under multi-physicochemical conditions to open the way to future perspectives. At similar chemical (batch) conditions, the apatitic layer served as a supportive matrix for the growth of (100) elongated COD crystals. Additionally, the apatitic spherulites seemed to undergo phase transformation from Ca-deficient HAp to another CaP crystalline phase (exhibiting a “sheet-like” structure). Under microfluidic confinement, we observed the growth of a mixture of COM and COD crystals from the apatitic layer. COM crystals mainly exhibited a platelet-like morphology while COD were observed under the (100) elongated bipyramid shape. Furthermore, we did not notice the presence of “sheet-like” crystals. The controlled flow at the apatitic surface enabled a more controlled reactivity between $Ca^{2+}_{(RP)}$ and $Ox^{2-}_{(GT)}$ ions for CaOx crystallization. Furthermore, the presence of GT favored the formation of COD crystals compared to COM crystals. To conclude, we supported the use of the collecting ducto-on-a-chip device to investigate CaOx crystallization under various physicochemical conditions, all aiming at mimicking the potential stone promoting conditions encountered in the nephron.

References

(1) Kazimierczak, R.; Hallmann, E.; Rusaczonek, A.; Rembiałkowska, E. Polyphenols, tannins and caffeine content and antioxidant activity of green teas coming from organic and non-organic production. *Renewable Agriculture and Food Systems* **2015,** *30* (03), 263.

(2) Brzezicha-Cirocka, J.; Grembecka, M.; Szefer, P. Oxalate, magnesium and calcium content in selected kinds of tea: impact on human health. *European Food Research and Technology* **2016,** *242* (3), 383.

(3) Frassetto, L.; Kohlstadt, I.; H., M. P. In *Advancing Medicine with Food and Nutrients, Second Edition*; CRC Press, 2012, DOI:10.1201/b13694-30 10.1201/b13694-30.

(4) Engelhardt, U. H. In *Reference Module in Chemistry, Molecular Sciences and Chemical Engineering*; Elsevier, 2013, DOI:10.1016/B978-0-12-409547-2.02784-0 10.1016/B978-0-12-409547-2.02784-0.

(5) Dogliotti, E.; Vezzoli, G.; Nouvenne, A.; Meschi, T.; Terranegra, A.; Mingione, A.; Brasacchio, C.; Raspini, B.; Cusi, D.; Soldati, L. Nutrition in calcium nephrolithiasis. *Journal of Translational Medicine* **2013,** *11* (1), 109.

(6) Itoh, Y.; Yasui, T.; Okada, A.; Tozawa, K.; Hayashi, Y.; Kohri, K. Preventive Effects of Green Tea on Renal Stone Formation and the Role of Oxidative Stress in Nephorlithiasis. *The Journal of Urology* **2005,** *173* (1), 271.

(7) Jeong, B. C.; Kim, B. S.; Kim, J. I.; Kim, H. H. Effects of green tea on urinary stone formation: an in vivo and in vitro study. *Journal of endourology* **2006,** *20* (5), 356.

(8) Chen, Z.; Wang, C.; Zhou, H.; Sang, L.; Li, X. Modulation of calcium oxalate crystallization by commonly consumed green tea. *CrystEngComm* **2010,** *12* (3), 845.

(9) Leroy, C. Ph.D thesis, Université Pierre et Marie Curie, 2016.

(10) Benzerara, Y.; Daudon , M.; Bazin , D.; Haymann, J. P.; Rode, J. In *WIPO*; A61K 31/353 (2006.01), A61P 13/04 (2006.01) ed., 2015; Vol. WO/2015/025294

(11) Rodgers, A.; Mokoena, M.; Durbach, I.; Lazarus, J.; de Jager, S.; Ackermann, H.; Breytenbach, I.; Okada, A.; Usami, M.; Hirose, Y.et al. Do teas rich in antioxidants reduce the physicochemical and peroxidative risk factors for calcium oxalate nephrolithiasis in humans? Pilot studies with Rooibos herbal tea and Japanese green tea. *Urolithiasis* **2016,** *44* (4), 299.

(12) Rode, J.; Bazin, D.; Dessombz, A.; Benzerara, Y.; Letavernier, E.; Tabibzadeh, N.; Hoznek, A.; Tligui, M.; Traxer, O.; Daudon, M.et al. Daily Green Tea Infusions in Hypercalciuric Renal Stone Patients: No Evidence for Increased Stone Risk Factors or Oxalate-Dependent Stones. *Nutrients* **2019,** *11* (2).

(13) Kanlaya, R.; Singhto, N.; Thongboonkerd, V. EGCG decreases binding of calcium oxalate monohydrate crystals onto renal tubular cells via decreased surface expression of alpha-enolase. *JBIC Journal of Biological Inorganic Chemistry* **2016,** *21* (3), 339.

(14) Sheng, X.; Ward, M. D.; Wesson, J. A. Crystal surface adhesion explains the pathological activity of calcium oxalate hydrates in kidney stone formation. *Journal of the American Society of Nephrology* **2005,** *16* (7), 1904.

(15) He, J. Y.; Deng, S. P.; Ouyang, J. M. Morphology, Particle Size Distribution, Aggregation, and Crystal Phase of Nanocrystallites in the Urine of Healthy Persons and Lithogenic Patients. *IEEE Transactions on NanoBioscience* **2010,** *9* (2), 156.

(16) Atomssa, T.; Gholap, A. Characterization and determination of catechins in green tea leaves using UV-visible spectrometer. *Journal of Engineering and Technology Research* **2015,** *7* (1), 22.

(17) Langdon, A.; Grohe, B. The osteopontin-controlled switching of calcium oxalate monohydrate morphologies in artificial urine provides insights into the formation of papillary kidney stones. *Colloids and Surfaces B: Biointerfaces* **2016,** *146*, 296.

(18) Daudon, M.; Letavernier, E.; Frochot, V.; Haymann, J.-P.; Bazin, D.; Jungers, P. Respective influence of calcium and oxalate urine concentration on the formation of calcium oxalate monohydrate or dihydrate crystals. *Comptes Rendus Chimie* **2016,** *19* (11), 1504.

(19) Buffle, J.; Zhang, Z.; Startchev, K. Metal Flux and Dynamic Speciation at (Bio)interfaces. Part I: Critical Evaluation and Compilation of Physicochemical Parameters for Complexes with Simple Ligands and Fulvic/Humic Substances. *Environmental Science & Technology* **2007,** *41* (22), 7609.

(20) Grohe, B.; Taller, A.; Vincent, P. L.; Tieu, L. D.; Rogers, K. A.; Heiss, A.; Sorensen, E. S.; Mittler, S.; Goldberg, H. A.; Hunter, G. K. Crystallization of Calcium Oxalates Is Controlled by Molecular Hydrophilicity and Specific Polyanion-Crystal Interactions. *Langmuir* **2009,** *25* (19), 11635.

(21) Vize, P. D.; Woolf, A. S.; Bard, J. B. L. *The Kidney: From Normal Development to Congenital Disease*; Elsevier Science, 2003.

(22) Daudon, M.; Bazin, D.; Letavernier, E. Randall's plaque as the origin of calcium oxalate kidney stones. *Urolithiasis* **2015,** *43* (1), 5.

(23) Bazin, D.; Daudon, M.; Combes, C.; Rey, C. Characterization and Some Physicochemical Aspects of Pathological Microcalcifications. *Chemical Reviews* **2012,** *112* (10), 5092.

(24) Evan, A. P.; Coe, F. L.; Lingeman, J. E.; Shao, Y.; Sommer, A. J.; Bledsoe, S. B.; Anderson, J. C.; Worcester, E. M. Mechanism of Formation of Human Calcium Oxalate Renal Stones on Randall's Plaque. *The Anatomical Record* **2007,** *290* (10), 1315.

(25) Achilles, W.; Jöckel, U.; Schapers, A.; Ulshöfer, B.; Riedmiller, H. In *Urolithiasis 2*; Ryall, R.;Bais, R.;Marshall, V. R.;Rofe, A. M.;Smith, L. H.;Walker, V. R., Eds.; Springer US: Boston, MA, 1994, DOI:10.1007/978-1-4615-2556-1_55 10.1007/978-1-4615-2556-1_55.

(26) LeGeros, R. Z. Preparation of octacalcium phosphate (OCP): A direct fast method. *Calcified Tissue International* **1985,** *37* (2), 194.

(27) LeGeros, R. Z.; Daculsi, G.; Orly, I.; Abergas, T.; Torres, W. Solution-mediated transformation of octacalcium phosphate (OCP) to apatite. *Scanning Microsc* **1989,** *3* (1), 129.

(28) Iijima, M.; Kamemizu, H.; Wakamatsu, N.; Goto, T.; Doi, Y.; Moriwaki, Y. Transition of octacalcium phosphate to hydroxyapatite in solution at pH 7.4 and 37°C. *Journal of Crystal Growth* **1997,** *181* (1), 70.

General conclusion and perspectives

The global increase in prevalence of the kidney stone disease has raised the importance to understand the biomineralization processes responsible for its occurrence. In-depth chemical characterizations already showed the hybrid nature of kidney stones. Mainly composed of CaOx crystals (CaOx monohydrate COM and/or CaOx dihydrate COD crystalline phases), renal calculi also exhibit other inorganic and organic species such as CaP crystals or proteins, for example.

Towards a better understanding of the kidney stone disease, countless approaches have been explored (from *ex vivo* to *in vitro* studies) with a focus on CaOx stones. With respect to *in vitro* investigations, static and/or continuous-flow techniques attempted to address the physicochemical conditions accountable for the formation of these CaOx concretions. Nevertheless, these methods failed at studying the potential influence of the renal micro-confinement and associated urinary laminar-flow on the genesis of kidney stones.

To overcome these issues, we decided to rely on the **microfluidic** technology with an in-depth focus on the **nephron-on-a-chip** technology. We built up a continuous-flow microchannel mimicking the dimensions of a single collecting duct and referred to it as the **collecting duct-on-a-chip** device. This robust microfluidic platform enabled us to investigate CaOx crystallization under a large panel of physicochemical conditions suspected to influence the crystal growth.

In the collecting duct-on-a-chip device, we studied CaOx crystallization under the co-laminar mixing of Ca^{2+} and Ox^{2-} ions at matching concentrations of patients diagnosed with combined hypercalciuria ($[Ca^{2+}]_{(aq)}$ = 12.0 *mmol.L*$^{-1}$, 1.0 *µL.min*$^{-1}$) and moderate hyperoxaluria ($[Ox^{2-}]_{(aq)}$ = 0.40 *mmol.L*$^{-1}$, 1.0 *µL.min*$^{-1}$) and compared the results to medical observations. Indeed, such urinary concentrations in calcium and oxalate were associated to a higher occurrence of COD crystals with respect to COM ones among stone formers. The crystal examination under microfluidic conditions showed that CaOx precipitated in mixtures of predominant COM and rare COD crystals, both exhibiting various shapes and sizes. However, the flow rate of 1.0 *µL.min*$^{-1}$ was not “mimetic” with respect to the urinary flow in a single collecting duct (≈ 10 *nL.min*$^{-1}$). Therefore, we studied the influence of hydrodynamics on CaOx crystallization in the microfluidic device. The decrease in overall flow rates induced a higher homogenization of the concentration gradients in Ca^{2+} and Ox^{2-} ions within the microchannel. It enhanced the mixing of Ca^{2+} and Ox^{2-} ions towards a higher occurrence of COD crystals. The strongest asset of using the collecting duct-on-a-chip device was to study the ***in situ*** and ***in real time*** growth kinetics of CaOx crystals to propose insights regarding the enlargement of

kidney stones *in vivo*. Our experimental findings supported a growth behavior of CaOx crystals under confinement following two distinct regimes. First, the emerging crystal grew *vs.* time in response to the supersaturation in Ca^{2+} and Ox^{2-} ions according to a surface-reaction kinetics (*i.e.* growth $\propto t^{1/2}$). Once the crystal reached a critical size, the growth kinetics was limited by the transport rate of ions into the CaOx matrix (*i.e.* growth $\propto t^{1/3}$). For thorough understanding of the experimental findings, we collaborated with Pr. Ágota Tóth and Pr. Dezső Horváth (University of Szeged, Hungary) to numerically investigate CaOx crystallization under microfluidic confinement. Their *in-house* code presented promising results regarding the physics and hydrodynamics involved in the reactivity of CaOx crystals under confinement as encountered in the nephron.

In the kidney, the growth of CaOx-based stones is highly suspected to be initiated by a calcium deficient HAp deposit, known as the Randall's plaque. Through its partial dissolution, such deposit released Ca^{2+} ions in the nephron for the consecutive formation of CaOx stones. To explore this common belief and test the proposed assumptions in the literature, we presented **a new strategy** to build up an *in vitro* apatitic layer exhibiting comparable chemical and morphological features of the Randall's plaque (*i.e.* Ca-deficient HAp organized in micro-spherulites). The most important aspect was to obtain a model system **suitable for microfluidic investigations** in order to study its reactive role with respect to CaOx crystallization under confinement. We demonstrated that a controlled and continuous flow of solely $Ox^{2-}_{(aq)}$ ions ($[Ox^{2-}]_{(aq)}$ = 0.10 *mol.L*$^{-1}$, total flow rate 2.0 *µL.min*$^{-1}$) induced the local dissolution of the apatitic layer, towards local zones of supersaturation in $Ca^{2+}_{(RP)}$ and $Ox^{2-}_{(aq)}$ ions for $[Ca^{2+}]_{(RP)} \times [Ox^{2-}]_{(aq)} \geq K_{sp(CaOx)}$ (*i.e*. CaOx crystallization). Interestingly, platelet-like COM crystals were obtained in full agreement with medical observations for hyperoxaluria conditions. Furthermore, we demonstrated that COM crystals grew from the HAp spherulites, underlying the dissolution-recrystallization mechanisms of the Randall's plaque to promote the growth of kidney stones. In an attempt to mimic further the complexity of the nephron, we also studied the influence of the pH on the apatitic layer's dissolution and, *in fine*, on CaOx crystallization. In conclusion, the collecting duct-on-a-chip device was suitable to investigate the formation of CaOx crystals under abnormal and acidic urine-like conditions.

Finally, we explored the modulating effect of polyphenolic catechins from a green tea (GT) solution on CaOx crystals in the collecting duct-on-a-chip device. We demonstrated the role of GT to direct CaOx crystallization from COM to COD crystals. Under co-laminar mixing of Ca^{2+} and Ox^{2-} ions, we showed the importance of the presence of GT on the calcium-rich side or the oxalate-rich side of the mixing interface. Indeed, we demonstrated that GT has a decisive influence on the occurrence of either COM or COD crystalline phases and on the resulting crystal morphologies. While COM crystals exhibited round-shaped morphology with a concave

(100) crystalline face, COD crystals grew under flatted or (100) elongated bipyramid morphologies. Additionally, we studied the combined influence of the apatitic layer and a GT solution containing $Ox^{2-}_{(GT)}$ ions on CaOx crystallization under confinement. After the continuous injection of solely $Ox^{2-}_{(GT)}$ ions ($[Ox^{2-}]_{(GT)}$ = 0.10 *mol.L*$^{-1}$, pH 4.5, total flow rate 2.0 *µL.min*$^{-1}$), we observed the growth of CaOx crystals from the apatitic spherulites. CaOx crystal examination detailed the formation of a mixture of platelet-like COM and (100) elongated bipyramid COD crystals. Once again, the controlled flow of $Ox^{2-}_{(GT)}$ solution at the apatitic surface enabled to control the reactivity between $Ca^{2+}_{(RP)}$ and $Ox^{2-}_{(GT)}$ ions with respect to CaOx crystallization. Interestingly, this physicochemical approach supported the use of the microfluidic device to investigate CaOx crystallization under **more complex conditions** with respect to the kidney stone disease.

To conclude, we would like to emphasize on the **multi-disciplinary** (physics, chemistry, material science, microfluidics…) and highly **exploratory** aspects of this research project. With the objective of contributing to the understanding of urolithiasis, we proposed a robust microfluidic device mimicking the micro-confinement and urinary laminar-flow of a single collecting duct to investigate CaOx crystallization. The collecting duct-on-a-chip device enabled us to explore glimpses of the hydrodynamics and the chemistry involved in the formation of CaOx crystals. The platform was suitable for physicochemical implementations and permitted *in situ* multi-scale characterizations. We are confident that the present work will set the stage for further explorations using the microfluidic device. Indeed, room remains for improvements and modifications up to the day we succeed in offering a platform fully capable of accounting for the kidney stone disease.

From the design point of view of the platform, let us recall that the device is made of a microchannel casted in a piece of PDMS and assembled with a glass coverslip. A straight microchannel is the simplest design with respect to the multi-structural organization of the nephron. A more complex design, including a loop for example, would explore CaOx crystallization in other parts of the nephron (*e.g.* the loop of Henle). Similarly to the introduction of an apatitic layer, it could be highly interested to modify the device with an extra-cellular matrix-like material (*e.g.* Matrigel^{TM}) and thereafter, renal cells. Additionally, re-absorption and exchange of ions occur throughout the nephron. Accounting for such phenomena in the platform would provide valuable information on the mechanisms of kidney stone formation. From the characterization point of view, we believe that investigating CaOx crystallization under microfluidic conditions and *in situ Raman* spectroscopy would inform on the chemical reactivity (*i.e.* nucleation and growth mechanisms). Indeed, debates still animate the community regarding the potential growth of CaOx crystals from a transient amorphous phase. However, the current attained spatial resolution of the optic microscopy prevented us to

support – or not – this idea. A similar idea would be to adapt the microfluidic reactor for *in situ* NMR microimaging as proposed by Renslow and colleagues who imaged biofilms in a microchannel (Analyst, 2017, **142**, 2363). These are some projects we have been thinking about in the hope that, in a near future, the collecting duct-on-a-chip device will serve the biomedical community as, for example, a predictive platform for suitable and reliable diagnosis.

Appendix

a. Fabrication of the microfluidic platform

i. Technical design and requirements

To match the 100 *µm* diameter of the collecting duct, the design of a microchannel was considered that had to meet the following features:

- "Y-shaped" microchannel exhibiting two inlets and one outlet
- Square section of 100 x 100 *µm*
- 2.5 cm in length from Y-junction

With respect to the requirements, a microchannel was first 3-D modeled using Autodesk Inventor® (computer-aided design software) and the resulting metallic mold was micro-machined at the technical platform of the Institut Pierre-Gilles de Gennes (**Figure 1a**).

ii. Microfluidic assembly

Being affordable, transparent to a large range of wavelength and already used in microfluidics as polymer material for biological studies, polymethylsiloxane (PDMS, Sylgard 184, Dow Corning©) was selected to cast the channel. Futhermore, PDMS could be made magnetic to enable facile and reversible sealing/unsealing of the complete microfluidic assembly using magnets[1,2]. Therefore, the microchannel was casted in light transparent PDMS windowed by magnetic PDMS according to the following protocol: first, PDMS mixed with curing agent in 10:1 weight ratio was degassed, poured onto the metallic mold and cured at 70°C for 2 hours in an oven. Thereafter, magnetic PDMS (*i.e.* iron carbonyl powder loaded PDMS in 1:1 weight ratio) mixed with curing agent in 20:1 weight ratio was degassed, poured into a cut-off window around the transparent PDMS-based microchannel and cured at 70°C for 2 hours in an oven. Once cooled, the overall material was delicately peeled off the mold and the inputs/outputs punched. Finally, the microfluidic platform was assembled with (from top to bottom) the PDMS-based microchannel, a glass coverslip closing the channel bottom and neodymium magnets to reversibly seal the device (**Figure 2b**).

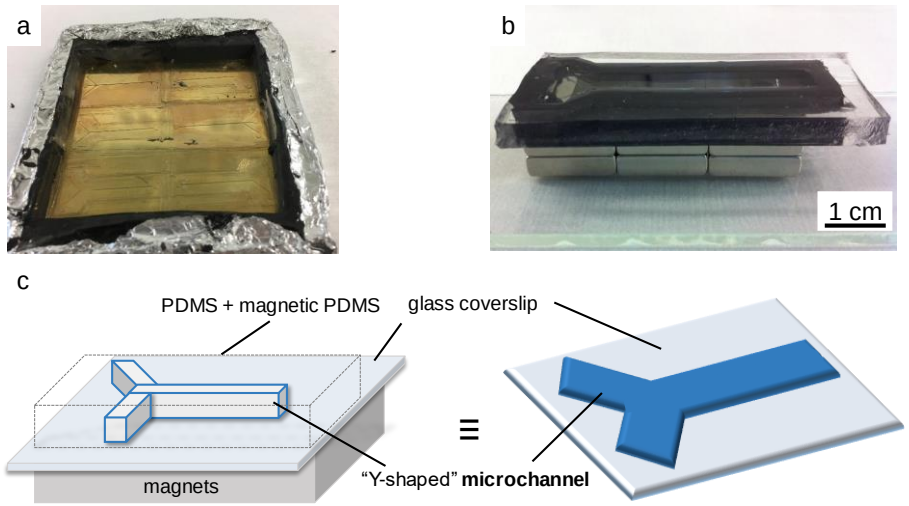

Figure 1. Design and fabrication of the microfluidic platform: a) metallic mold used as a model to cast the Y-shaped microchannel; b) fully assembled microfluidic device; c) schematic representation of the platform from the side point of view (right) and simplified (left).

b. Calcium oxalate crystallization under co-laminar mixing of Ca^{2+} and Ox^{2-} ions

i. $CaCl_2$ and $Na_2C_2O_4$ in solution

In accordance with medical observations promoting CaOx crystallization, we set calcium and oxalate ionic concentrations to pathological hypercalciuria ($[Ca^{2+}]_{(aq)}$ = 12.0 *mmol.L*$^{-1}$) and moderate hyperoxaluria ($[C_2O_4^{2-}]_{(aq)}$ = 0.4 *mmol.L*$^{-1}$) with precursors in aqueous solution prepared as follows:

- Aqueous solution in Ca^{2+} ion: anhydrous calcium chloride ($CaCl_{2(s)}$, 110.98 *g.mol*$^{-1}$, Sigma-Aldrich) was used as Ca^{2+} ions donor. A first batch solution of $[Ca^{2+}]_{(aq)}$ = 0.1 *mol.L*$^{-1}$ was prepared by dissolving $m(CaCl_{2(s)})$ = 5.55 *g* in V_{water} = 500 *mL* of deionized water and when needed diluted in deionized water to reach $[Ca^{2+}]_{(aq)}$ = 12.0 *mmol.L*$^{-1}$ in aqueous solution.
- Aqueous solution in $C_2O_4^{2-}$ ion: sodium oxalate ($Na_2C_2O_{4(s)}$, 134.00 *g.mol*$^{-1}$, Sigma-Aldrich) was used as $C_2O_4^{2-} \equiv Ox^{2-}$ ions donor. A first batch solution of $[Ox^{2-}]_{(aq)}$ = 0.1 *mol.L*$^{-1}$ was prepared by dissolving $m(Na_2C_2O_{4(s)})$ = 6.7 *g* in V_{water} = 500 *mL* of deionized water and when needed diluted in deionized water to reach $[Ox^{2-}]_{(aq)}$ = 0.4 *mmol.L*$^{-1}$ in aqueous solution.

ii. Microfluidic setup

CaOx crystallization from Ca^{2+} and Ox^{2-} ions as sole precursors was induced by co-laminar flow of previously cited precursors. For this purpose, two syringes individually filled with precursor in aqueous solution were loaded onto a syringe-pump (kd Scientific or CETONI) and

connected to the inlets of the microfluidic platform. Then, Ca^{2+} and Ox^{2-} ions were infused at the same flow rate $Q_{Ca}^{2+} = Q_{Ox}^{2-}$ (either µL.min^{-1} or nL.min^{-1}) at room temperature for a time duration dependent to the instructed flow rate. At the end, mixing solution was collected at the microchannel outlet and the microfluidic platform was disassembled to retrieve the glass coverslip onto which CaOx crystals precipitated. Afterwards, crystals were delicately rinsed with deionized water and ethanol and dry at ambient air before undergoing further analysis otherwise stored at 4°C to limit phase transition.

c. Synthesis of an apatitic layer to mimic the Randall's plaque

i. 10 mM Tris-Hcl buffer at pH 7.4

First, a batch solution of **1 M** Tris-HCl buffer at pH 7.4 was prepared as follows: a mass m_{Tris} = 12.1 *g* of Tris(hydroxymethyl)aminomethane was dissolved in V = 80.0 *mL* of milliQ water. The pH value of the solution was adjusted by the slow dropwise addition of V_{HCl} ≈ 6 – 7 mL of HCl. Finally, milliQ water was added to obtain a final volume of $V_{\mathbf{1M\ Tris\text{-}HCl}}$ = 100 mL of the buffer solution.

Afterwards, a volume $V_{\mathbf{1M\ Tris\text{-}HCl}}$ = 1.0 *mL* of 1 M Tris-HCl buffer at pH 7.4 was diluted in 99.0 *mL* of milliQ water to obtain $V_{\mathbf{10mM\ Tris\text{-}HCl}}$ = 100 *mL* of the final **10 mM** Tris-HCl buffer at pH 7.4.

ii. 1.5 SBF solution buffered in 10 mM Tris-HCl buffer at pH 7.4

The 1.5 SBF (Simulated Body Fluid) solution was prepared from the successive dissolution of NaCl, $NaHCO_3$, KCl, K_2HPO_4, $MgCl_2{\cdot}6H_2O$, $CaCl_2$ and Na_2SO_4 salts in Tris-HCl buffer solution (see).

Table 1. Chemical composition of 1.5 SBF solution in 10 mM Tris-HCl buffer at pH 7.4

Precursor	**NaCl**	**$NaHCO_3$**	**KCl**	**K_2HPO_4**	**$MgCl_2.6H_2O$**	**$CaCl_2$**	**Na_2SO_4**
m (g)	6.0000	0.2614	0.2087	0.1306	0.2338	0.2108	0.0532

iii. Synthesis protocol of the apatitic layer

A glass coverslip was coated with an apatitic layer using a modified protocol from Liu *et al*.[3]:

- Glass substrate was oxidized in a 1:1 mixture of sulfuric acid (H_2SO_4, VWR) and hydrogen peroxide (H_2O_2 30 %, VWR) for 1 hour at room temperature, rinsed with deionized water and with acetone twice.
- CaP nucleation was then initiated onto the glass substrate. First, the substrate was immersed in 15 mL of [Ca^{2+}] = 20 mmol.L^{-1} at room temperature ($CaCl_{2(s)}$ buffered at ph

7.4 with 10 mM Tris-HCl), then 15 mL of $[HPO_4^{2-}]_{(aq)}$ = 12 mmol.L^{-1} ($K_2HPO_{4(s)}$, Sigma-Aldrich) was slowly dropped on the glass substrate/$CaCl_2$ mixture and the final mixture was stirred for 30 min. This deposition process was carried three times in total.

- Biomimetic coating was carried in freshly prepared 1.5 SBF by dissolving $NaCl_{(s)}$, $NaHCO_{3(s)}$, $KCl_{(s)}$, $K_2HPO_{4(s)}$, $MgCl_2.6H_2O_{(s)}$, $CaCl_{2(s)}$ and $Na_2SO_{4(s)}$ in 10 mM Tris-HCl buffered at pH 7.4. Glass substrate was immersed in 80 mL of 1.5 SBF in a polystyrene bottle and placed for several hours at 37°C in an oven.

In the end, the nephron-on-a-chip platform was assembled and ready for further uses.

d. Polyphenolic catechins and CaOx crystal modutation

We bought loose green tea (GT) from a Chinese retailer in the 13th arrondissement of Paris and used it along our various experiments.

- Green tea solution: m(GT) = 1.0 g of tea leaves were brewed for 5 min in 100 mL of milliQ water firstly boiled at 100°C. Then, tea solution was filtered and washed three times consecutively in V = 100 mL of chloroform for purification purpose. When not used, tea solution was stored at 4°C out of direct sunlight for 1 month of sustainability (**Figure 2**).

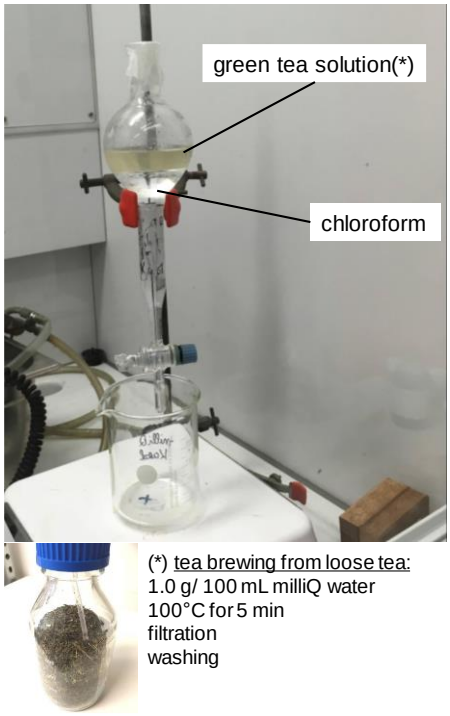

Figure 2. Setup for green tea purification using chloroform solvent.

- Ca^{2+} and Ox^{2-} ions in tea solution: ionic precursors in tea solution were prepared as follows.

For Ca^{2+} at $[Ca^{2+}]_{(GT)}$ = 12.0 *mmol.L*$^{-1}$ in tea solution, a mass m($CaCl_2$) = 0.1332 *g* is dissolved in V_{GT} = 100 *mL*.

For Ox^{2-} at $[Ox^{2-}]_{(GT)}$ = 0.10 *mol.L*$^{-1}$ in tea solution, a mass m($Na_2C_2O_4$) = 1.34 *g* is dissolved in V_{GT} = 100 *mL*.

For Ox^{2-} at $[Ox^{2-}]_{(GT)}$ = 0.40 *mmol.L*$^{-1}$ in tea solution, a volume $V_{GT}(Ox^{2-})$ = 0.4 *mL* of an oxalate solution at $[Ox^{2-}]_{(GT)}$ = 0.10 *mol.L*$^{-1}$ is diluted in V_{GT} = 99.6 *mL* of green tea to obtain a final volume of 100 *mL*.

e. Characterization techniques

i. X-Ray Diffraction

The structural characterization of the samples was conducted by using a powder diffractometer Bruker D8 Advance. The different X-ray diffractions patterns were measured using Cu-Kα radiation at 1.5406 Å. Typical diffractograms were collected from 10° < 2θ < 60° with steps of 0.03° and a scanning speed of 0.5 s/point in loop mode for 30 min. The backgrounds of the patterns were subtracted using the EVA software.

ii. Raman spectroscopy

Raman spectroscopy is a technique used to observe vibrational, rotational and other low-frequency modes in a system. In chemistry, it is a commonly used method to highlight structural fingerprint of molecules of interest. Relying on inelastic scattering of an excited system due to an incident monochromatic light (usually a laser in the visible, near infrared or near ultraviolet ranges), the resulting shift in energy gives information about the vibrational modes in the system. In addition of being a fast, non-invasive and non-destructive characterization method, Raman spectroscopy is progressively integrated for microfluidic investigations and referred to as Raman-microfluidic systems to probe materials at diverse interfaces (*e.g.* liquids and/or solids)[4]. Herein, all Raman measurements were carried out at the laboratory LISE (UMR 8235, Sorbonne Université) using a LabRAM HR Evolution spectrometer (λ = 532 nm, Andor CCD detector, hole 70). Materials underwent characterization without further preparation after synthesis.

iii. Scanning Electron Microscopy and Energy Dispersive X-Ray Spectroscopy

Scanning Electron Micrsocopy (SEM) enables the observation of crystal morphologies at microscale dimensions giving in-depth access to the microstructure of our materials of interest with respect to the experimental conditions. Therefore, Hitachi S-3400 apparatus was used to

scan the surface sample with a focused beam of electrons accelerated at V_{acc} = 3.0 kV. After synthesis, samples did not necessarily require further preparation (*i.e.* gold coating) to undergo surface scanning and micrographs were acquired at several magnification ranges to demonstrate the microstructure of our materials. Furthermore, SEM technique could be coupled to Energy Dispersive X-Ray Spectroscopy (EDS) to highlight the elemental composition of our materials. In that purpose, the materials (coated with a carbon layer) were stimulated with a high-energy beam of electron (V_{acc} = 10.0 kV) to collect the emission of characteristic X-rays for chemical characterization.

- Calcium oxalate crystals: with respect to the experimental conditions, SEM allowed to view the overall CaOx crystals obtained after co-laminar flow of precursors in solution. Moreover, micrographs described CaOx crystals regarding the diversity in size and crystal habit. In association with Raman spectroscopy, electron microscopy enabled to correlate each crystal habit encountered with either whewellite or weddellite phases. For this material, no EDS analysis was carried the technique being not quantitative with respect to carbon and oxygen.
- Synthesis of an apatitic layer to mimic the Randall's plaque: at each step of the protocol, SEM enabled to view the overall structure of the material along with an in-depth characterization of the microscale organization. Complementary EDS analysis provided quantitative information regarding the elemental composition of the material, especially in terms of Ca/P ratio to ensure the stoichiometry of the *in vitro* RP.

iv. In situ and in real time monitoring of CaOx crystallization

At controlled temperature, controlled pH and under stirring, batch crystallization of co-precipitated and supersaturated solutions in Ca^{2+} and Ox^{2-} ions induces instantaneous formation of CaOx crystals. Yet interesting for easy and mass production of bulk material, batch crystallization does not enable control over the diffusion phenomena responsible for *in vivo* CaOx crystallization. In that purpose, microsize dimensions associated with microfluidic approach offer better control over molecular diffusion and most importantly observable timescale to access *in situ* information about the kinetics of CaOx crystal growth. By adapting the microfluidic model system under a light microscope (Leica) coupled to a camera (Fuji X100F), we monitored the crystallization of CaOx crystals under co-laminar flow of calcium and oxalate ions in real time (**Figure 3**). Within the microchannel, a section located approximately 300 µm away from the Y-junction was observed under a 40x magnification objective. Thereafter, pictures of the section were taken at periodic time (Δt = 5 s) starting from the moment the section was filled with the precursors in solution and for a time duration dependent to the instructed flow rate. Pictures were edited into a timelapse video using

Windows Movie Maker software, analyzed with ImageJ® software to obtain data related to CaOx crystal growth and processed thanks to Matlab software.

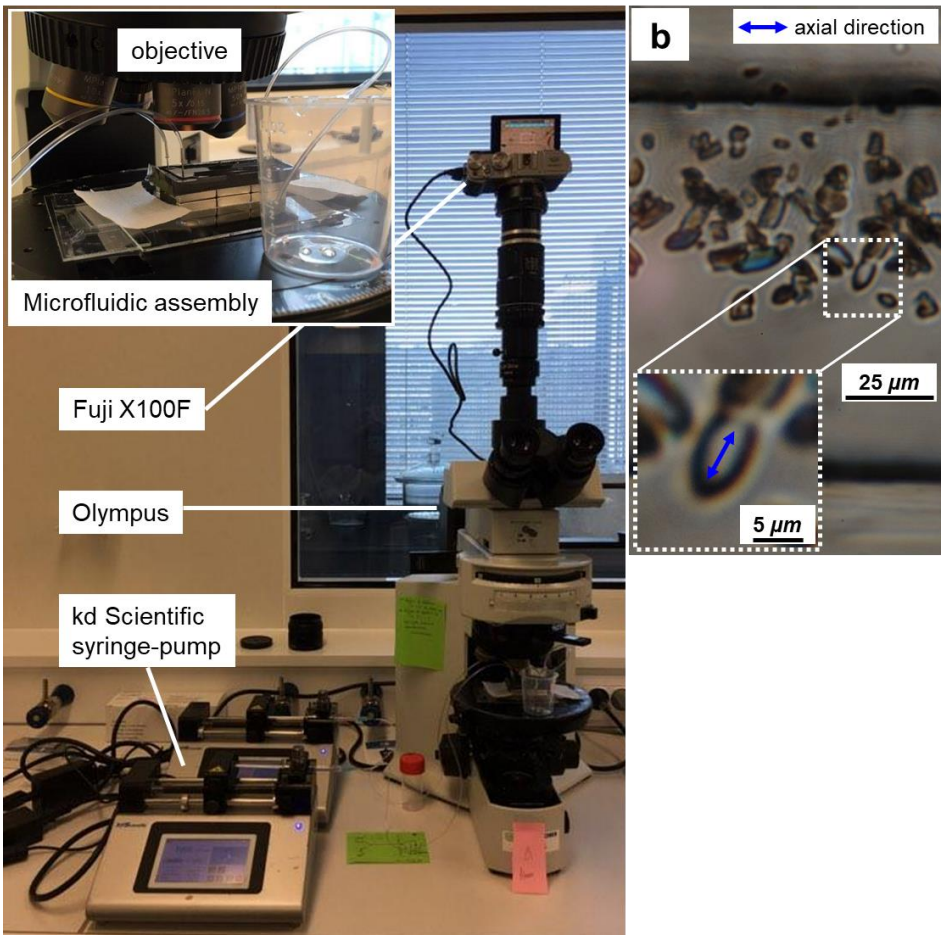

Figure 3. Experimental setup for in situ and in real time monitoring of CaOx crystallization.

References

(1) Rasponi, M.; Piraino, F.; Sadr, N.; Laganà, M.; Redaelli, A.; Moretti, M. Reliable magnetic reversible assembly of complex microfluidic devices: fabrication, characterization, and biological validation. *Microfluidics and Nanofluidics* **2011,** *10* (5), 1097.

(2) Tsao, C.-W.; Lee, Y.-P. Magnetic microparticle-polydimethylsiloxane composite for reversible microchannel bonding. *Science and Technology of Advanced Materials* **2016,** *17* (1), 2.

(3) Liu, Q.; Ding, J.; Mante, F. K.; Wunder, S. L.; Baran, G. R. The role of surface functional groups in calcium phosphate nucleation on titanium foil: a self-assembled monolayer technique. *Biomaterials* **2002,** *23* (15), 3103.

(4) Chrimes, A. F.; Khoshmanesh, K.; Stoddart, P. R.; Mitchell, A.; Kalantar-zadeh, K. Microfluidics and Raman microscopy: current applications and future challenges. *Chemical Society Reviews* **2013,** *42* (13), 5880.